

DIGITAL ACCESS TO SCHOLARSHIP AT HARVARD
DASH.HARVARD.EDU

HARVARD LIBRARY


Studies of neutrinos in high definition with LArTPC

Citation

Kubota, Shion. 2025. Studies of neutrinos in high definition with LArTPC. Doctoral Dissertation, Harvard University Graduate School of Arts and Sciences.

Link

https://dash.harvard.edu/handle/1/42720715

Terms of use

This article was downloaded from Harvard University's DASH repository, and is made available under the terms and conditions applicable to Other Posted Material (LAA), as set forth at

https://harvardwiki.atlassian.net/wiki/external/NGY5NDE4ZjgzNTc5NDQzMGIzZWZhMGFlOWI2M2EwYTg

Accessibility

https://accessibility.huit.harvard.edu/digital-accessibility-policy

Share Your Story

The Harvard community has made this article openly available.
Please share how this access benefits you. Submit a story

HARVARD
Kenneth C. Griffin

GRADUATE SCHOOL
OF ARTS AND SCIENCES

THESIS ACCEPTANCE CERTIFICATE

The undersigned, appointed by the

Department of Physics

have examined a dissertation entitled

Studies of neutrinos in high definition with LArTPC

presented by Shion Kubota

candidate for the degree of Doctor of Philosophy and hereby certify that it is worthy of acceptance.

Signature _____

Typed name: Prof. Roxanne Guenette (Univ. of Manchester)

Signature _____

Typed name: Prof. John Doyle

Signature _____

Typed name: Prof. Carlos Argüelles-Delgado

Date: May 21, 2025

Studies of neutrinos in high definition with LArTPC

a dissertation presented
by
Shion Kubota
to
The Department of Physics

in partial fulfillment of the requirements
for the degree of
Doctor of Philosophy
in the subject of
Physics

Harvard University
Cambridge, Massachusetts
May 21 2025

©2025 Shion Kubota
All rights reserved.

Studies of neutrinos in high definition with LArTPC

Abstract

Neutrinos, among the most elusive particles in the Standard Model, hold the potential to illuminate fundamental questions in particle physics and cosmology, including the mechanism of neutrino mass generation and the search for physics beyond the Standard Model. The Deep Underground Neutrino Experiment (DUNE) is poised to address these challenges through a comprehensive program of precision neutrino oscillation measurements, nucleon decay searches, and astrophysical neutrino detection, leveraging a high-intensity neutrino beam and massive Liquid Argon Time Projection Chambers (LArTPCs) across a 1300 km baseline.

This dissertation presents contributions to two critical aspects of DUNE's detector development and physics potential. First, it details the performance and deployment of the Digital Wire Analyzer (DWA), an advanced quality assurance tool designed to ensure the mechanical and electrical integrity of Anode Plane Assemblies (APAs) in the DUNE Far Detector. The DWA enables precise, automated verification of wire tension, continuity, and isolation, safeguarding the fidelity of charge readout in large-scale LArTPCs. Validation studies demonstrate that the DWA achieves high accuracy and reliability across thousands of channels, with tension measurements consistent with traditional methods but delivered at significantly greater speed and scalability. Its successful integration into production workflows has established the DWA as a cornerstone technology for ensuring APA quality throughout DUNE's construction.

Second, this work explores the development and application of Q-Pix, a novel pixel-based readout technology offering true three-dimensional, self-triggering capabilities for next-generation LArTPCs. Through hardware characterization and simulation studies, the potential of Q-Pix to enhance low-energy neutrino detection is evaluated, with a focus on supernova and solar neutrino signals. The results demonstrate significant improvements in event reconstruction, background rejection, and energy threshold reduction compared to traditional wire-based systems, highlighting Q-Pix as a transformative approach for future DUNE modules and beyond.

Together, these efforts advance the precision and scope of neutrino detection, contributing to the realization of "high-definition" neutrino physics with liquid argon detectors.

Contents

Title Page **i**

Copyright **ii**

Abstract **iii**

Table of Contents **iv**

List of Figures **vi**

List of Tables **ix**

Abbreviations **x**

Dedication **xii**

Acknowledgments **xiii**

1 Introduction **1**
- 1.1 Historical Context and the Role of Neutrinos . . . 2
- 1.2 The Discovery of Neutrinos . . . 3
- 1.3 The Discovery of Neutrino Mass . . . 7
- 1.4 Neutrino Oscillation . . . 9
- 1.5 Theory of Mass . . . 19
- 1.6 Open Questions in Neutrino Physics . . . 23

2 Deep Underground Neutrino Experiment (DUNE) **30**
- 2.1 Physics of DUNE . . . 32
- 2.2 DUNE experiment . . . 38
- 2.3 LArTPC . . . 45
- 2.4 Implementation in DUNE: Far Detector Modules . . . 50

3 Digital Wire Analyzer **59**
3.1 QA/QC of APA . . . 60
3.2 DWA Principle . . . 62
3.3 DWA Hardware . . . 67
3.4 DWA Firmware . . . 75
3.5 DWA Software . . . 78
3.6 Performance Analysis . . . 85
3.7 Summary . . . 94

4 Q-Pix **98**
4.1 Challenges of wire-based technology . . . 99
4.2 Simulation Study of 2D vs. 3D Readout Geometries . . . 102
4.3 Q-Pix Principle . . . 105
4.4 Q-Pix Schematic Designs . . . 106
4.5 Q-Pix Hardware Development . . . 110

5 Q-Pix Supernovae studies **126**
5.1 Supernova explosion . . . 127
5.2 Supernovae Neutrinos . . . 129
5.3 Simulation Framework for Supernova Neutrino Studies . . . 133
5.4 Performance of Q-Pix Readout for Supernova Neutrino Detection . . . 142
5.5 Summary . . . 167

6 Solar studies with Q-Pix **169**
6.1 Fusion Processes and Solar Neutrinos . . . 170
6.2 Experimental Consideration . . . 176
6.3 Solar Neutrino Prediction . . . 178
6.4 Background Prediction . . . 180
6.5 Results . . . 200
6.6 Summary . . . 221

7 Conclusion **224**

List of Figures

1.1 Feynman diagram of neutrinoless double beta decay 22
1.2 Neutrino mass orderings 24

2.1 CP violation sensitivity in $\nu_\mu \to \nu_e$ oscillation maxima 33
2.2 Oscillation probabilities for $\nu_\mu \to \nu_e$ and $\bar{\nu}_\mu \to \bar{\nu}_e$ 34
2.3 Sensitivity to neutrino mass ordering 35
2.4 Sensitivity to leptonic CP violation 35
2.5 Overview of the DUNE experiment 39
2.6 Schematic of the LBNF beamline 39
2.7 DUNE beam energy spectra at the Far Detector 40
2.8 Near Detector complex configurations 42
2.9 DUNE Far Detector caverns and cryostat layout 44
2.10 APA operation in a single-phase LArTPC 48
2.11 Photograph of a full-scale APA module 53
2.12 Photograph of a full-scale CRP module 56

3.1 Laser-based wire tension measurement setup 62
3.2 Resonance response of a test wire 66
3.3 DWA unit and test stand setup 67
3.4 Block diagram of the DWA system 68
3.5 Front panel of the DWA power distribution box 69
3.6 DWA analog and relay boards 70
3.7 DWA relay switch matrix configurations 73
3.8 DWA probe boards and APA headboard connection 75
3.9 Effectiveness of the MNS algorithm 78
3.10 DWA GUI for scan configuration and monitoring 79
3.11 DWA GUI status and scan configuration panels 80
3.12 Effect of Savitzky–Golay filtering on amplitude scan 83
3.13 Processed tension plots in the DWA GUI 84
3.14 DWA test stand for APA validation 86
3.15 DWA continuity and isolation test results 87

3.16 Signal amplitude versus wire length . . . 88
3.17 High-resolution DWA tension scans . . . 89
3.18 Relative tension difference between fast and laser scans . . . 91
3.19 Signal envelope extraction for SNR analysis . . . 92
3.20 SNR versus wire length . . . 93
3.21 Comparison of DWA and laser tension measurements . . . 95

4.1 Degenerate track configuration in wire-based LArTPC . . . 100
4.2 Efficiency and purity of ν_e CC selection . . . 103
4.3 Efficiency and purity of NC π^0 selection . . . 104
4.4 Efficiency and purity of ν_μ CC selection . . . 105
4.5 Q-Pix charge digitization schemes . . . 107
4.6 Waveform reconstruction using RTDs . . . 109
4.7 Q-Pix front-end demonstration setup . . . 112
4.8 Input current vs. reset frequency in Q-Pix prototype . . . 113
4.9 Simulated vs. measured Q-Pix reset waveforms . . . 114
4.10 System diagram of TPC and SAQ electronics . . . 115
4.11 Simulated charge cloud and radial profiles . . . 116
4.12 Measured transverse diffusion with Q-Pix . . . 117
4.13 Q-Pix PB schematic and prototype . . . 118
4.14 Calibration of nanoampere current source . . . 121
4.15 PB response to different input currents . . . 121
4.16 Calibration curve of the PB prototype . . . 122
4.17 UTAH TPC schematic and photograph . . . 123

5.1 Stages of core-collapse supernova mechanism . . . 129
5.2 Historic communication of SN1987A detection . . . 131
5.3 Simulated supernova neutrino emission spectra . . . 135
5.4 Stacked energy spectrum of supernova ν_e interactions . . . 136
5.5 Simulated energy and timing distributions for supernova signal and background . . . 139
5.6 Simulated Q-Pix current profiles and resets . . . 142
5.7 Supernova energy reconstruction before and after correction . . . 144
5.8 Supernova reconstruction efficiency vs. neutrino energy . . . 145
5.9 Supernova event ID efficiency and purity vs. cluster time window . . . 148
5.10 Event ID efficiency and purity vs. number of resets . . . 150
5.11 Q-Pix data rates vs. reset threshold . . . 151
5.12 Number of resets before and after clustering for SN burst . . . 155
5.13 Supernova burst trigger efficiency vs. number of ν_e interactions . . . 156
5.14 True ν energy vs. angle difference for ν_e CC and ES events . . . 158
5.15 Electron track reconstruction with RANSAC for supernova event . . . 160

5.16 Angle correlation between neutrino and electron vs. neutrino energy . . 162
5.17 Reconstructed vs. true electron direction before and after correction . . 163
5.18 Reconstructed neutrino directions from supernova interactions 164
5.19 Angular resolution for supernova pointing 165

6.1 Solar neutrino energy spectra by source 173
6.2 Proton–proton chain and solar neutrino sources 174
6.3 Detector model used for solar neutrino study 177
6.4 True and reconstructed energy spectra of B8 and hep neutrinos 180
6.5 Neutrino interaction cross sections on ^{40}Ar 180
6.6 Decay chains of ^{219}Rn and ^{220}Rn 186
6.7 Decay chain of ^{222}Rn from the ^{238}U series 187
6.8 Gamma spectrum from alpha-capture in argon 189
6.9 Simulated energy spectrum of neutrons 194
6.10 External gamma-ray spectrum at LAr surface 197
6.11 Simulated energy spectra and sensitivity for solar neutrino detection . . 200
6.12 Gamma survival probability vs. LAr shielding thickness 204
6.13 Energy spectra and sensitivity in low-background scenario 205
6.14 Angular distributions in solar neutrino pseudo-experiment 207
6.15 Log-likelihood ratio distributions for solar signal detection 209
6.16 Directional sensitivity vs. energy with and without fiducialization . . . 210
6.17 Scintillation time profile for alpha and electron signals in LAr 213
6.18 Pulse-shape discrimination between electrons and alpha-induced gammas 214
6.19 Delayed gamma production and light yield from solar ν_e CC events . . 216
6.20 Detection significance for solar CC events with delayed-light tagging . . 219
6.21 Q-Pix data rates for solar signals and backgrounds 220

List of Tables

1.1 Summary of major neutrino oscillation experiments 18

2.1 Water Cherenkov vs. LArTPC comparison 51

4.1 3D network classification accuracy on validation set 102
4.2 Comparison of the Reset and Replenishment Schemes in Q-Pix 110

5.1 Predicted supernova event rates in liquid argon 136
5.2 Radiogenic background sources for supernova study 138
5.3 Simulation parameters for Q-Pix study 142
5.4 Comparison of data rates: DUNE projective vs. Q-Pix 152

6.1 Composition of cavern rock and lining materials 179
6.2 Expected solar ν_e interactions by channel 179
6.3 Summary of internal background sources 182
6.4 Summary of external background processes 193
6.5 Summary of solar neutrino background sources 199
6.6 Expected signal and background events using light coincidence 218

List of Abbreviations

Abbreviation	Full Term	Page
AC	Alternating Current	62
APA	Anode Plane Assembly	31
ARM	Advanced RISC Machine	75
ArgoNeuT	Argon Neutrino Teststand	45
ASIC	Application-Specific Integrated Circuit	53
BPF	Bandpass Filter	70
BSM	Beyond the Standard Model	32
CAD	Computer-Aided Design	85
CAPTAIN	Cryogenic Apparatus for Precision Tests of Argon Interactions with Neutrinos	99
CC	Charged Current	7
CDF	Cumulative Distribution Function	207
CNO	Carbon-Nitrogen-Oxygen (cycle)	172
CIR	Charge-Integrate/Reset	105
CISC	Complex Instruction Set Computer	76
CNN	Convolutional Neural Network	102
COTS	Commercial Off-The-Shelf	111
CP	Charge-Parity	3
CRP	Charge Readout Plane	44
CUORE	Cryogenic Underground Observatory for Rare Events	x
CUPID	CUORE Upgrade with Particle IDentification	27
DAC	Digital to Analog Converter	70
DC	Direct Current	62
DONuT	Direct Observation of Nu Tau	5
DP	Dual Phase	156
DUNE	Deep Underground Neutrino Experiment	18
DWA	Digital Wire Analyzer	54
ECSN	Electron-Capture Supernova	128
ERP	Ending Reset Point	160
ES	Elastic Scattering	136
EXO-200	Enriched Xenon Observatory-200	190
FD	Far Detector	31
FPGA	Field-Programmable Gate Array	70
GALLEX	Gallium Experiment	8
GAr	Gaseous Argon	41
GLoBES	General Long Baseline Experiment Simulator	134
GONG	Global Oscillations Network Group	174
GUTs	Grand Unified Theories	21
GUI	Graphical User Interface	79
HALO	Helium and Lead Observatory	153
HD	Horizontal Drift	52
HNL	Heavy Neutral Lepton	38
HV	High Voltage	69
ICARUS	Imaging Cosmic And Rare Underground Signals	45
IMB	Irvine-Michigan-Brookhaven detector	131
JUNO	Jiangmen Underground Neutrino Observatory	24
KamLAND	Kamioka Liquid Scintillator Antineutrino Detector	153
KATRIN	Karlsruhe Tritium Neutrino Experiment	25
KM3NeT	Cubic Kilometre Neutrino Telescope	153
kpc	Kiloparsec	134
kton	Kiloton	31
LAr	Liquid Argon	3
LArIAT	Liquid Argon In A Testbeam	99

Abbreviation	Full Term	Page
LArTPC	Liquid Argon Time Projection Chamber	28
LBNF	Long-Baseline Neutrino Facility	38
LBNL	Lawrence Berkeley National Laboratory	227
LEP	Large Electron-Positron Collider	5
LEGEND	Large Enriched Germanium Experiment for Neutrinoless $\beta\beta$ Decay	27
LHC	Large Hadron Collider	2
LSND	Liquid Scintillator Neutrino Detector	27
MARLEY	Model of Argon Reaction Low Energy Yields	137
MiniBooNE	Mini Booster Neutrino Experiment	27
MNS	Mains Noise Suppression	74
MSW	Mikheyev–Smirnov–Wolfenstein Effect	14
ND	Near Detector	32
NEXT	Neutrino Experiment with a Xenon TPC	27
nEXO	next Enriched Xenon Observatory	27
NMOS	N-type Metal-Oxide Semiconductor	111
NOνA	NuMI Off-axis ν_e Appearance	17
NSI	Non-Standard Interaction	37
PCA	Principal Component Analysis	163
PB	Pill Box	117
PDB	Power Distribution Box	67
PCB	Printed Circuit Board	55
PMNS	Pontecorvo-Maki-Nakagawa-Sakata Matrix	13
PMT	Photomultiplier Tube	49
pp	Proton-Proton (chain)	171
PRISM	Precision Reaction Independent Spectrum Measurement	42
PSD	Pulse Shape Discrimination	211
QA	Quality Assurance	52
QC	Quality Control	52
QPixG4	Q-Pix Geant4	188
R&D	Research and Development	43
RANSAC	Random Sample Consensus	159
RMS	Root Mean Square	82
RTD	Reset Time Difference	108
SAQ	Simplified Analog Q-Pix	113
SAND	System for on-Axis Neutrino Detection	42
SiPM	Silicon Photomultiplier	53
SLoMo	Sanford Underground Low background Module	176
SNEWS	SuperNova Early Warning System	143
SNB	Supernova Burst	154
SoC	System on a Chip	75
SOHO	Solar and Heliospheric Observatory	174
SOM	System on a Module	69
SP	Single Phase	156
SSM	Standard Solar Model	173
SBN	Short-Baseline Neutrino program	28
SRP	Starting Reset Point	160
SURF	Sanford Underground Research Facility	31
T2K	Tokai to Kamioka	17
TPC	Time Projection Chamber	27
UAr	Underground Argon	176
UTA	University of Texas at Arlington	118
UTAH TPC	UTA-Harvard TPC	123
VGA	Variable Gain Amplifier	72
VD	Vertical Drift	54
VUV	Vacuum Ultraviolet	46
$0\nu\beta\beta$	Neutrinoless Double Beta Decay	22

TO MY たからもの – MY PARENTS
Thank you for making me believe
I could become anything and
reach beyond what is seen.
With love and gratitude.

Acknowledgments

"*Not all treasure is silver and gold, mate.*"
—*Captain Jack Sparrow, Pirates of the Caribbean*

There are many kinds of treasure, and during this Ph.D., I've found the most meaningful ones in people —those who offered guidance when I was lost, encouragement when I doubted myself, and laughter when I needed it most. This journey was shaped as much by equations and experiments as it was by friendship, mentorship, and unwavering support. What follows is a small attempt to express a very large gratitude.

First of all, I would like to thank my supervisor, Roxanne Guenette, who welcomed me into her research group even before I began my Ph.D. Back then, I was still an undergraduate at Mount Holyoke College, commuting to Harvard every weekend on the Peter Pan bus. From those early days, you offered me the chance to step into the world of research and begin shaping a path of my own. Later, when you moved to Manchester, I followed you and moved to Manchester across "the pond". That decision opened up new opportunities —it allowed me to grow as an independent researcher and to begin building international collaborations, especially with the European research community and CERN. The path we took was unconventional, but it taught me a great deal, and I'm grateful for the experiences it made possible.

My committee members, John Doyle and Carlos Argüelles-Delgado, have also had a lasting impact on my academic journey. Even while I was based far from campus, their mentorship reminded me of my roots in the Harvard Physics community. Their thoughtful questions consistently challenged me to think beyond my usual frameworks —not just to solve problems, but to question the assumptions behind them. Whether through feedback on presentations or seemingly simple but deeply incisive comments, they helped me stretch my thinking in directions I wouldn't have reached on my own, and encouraged me to approach problems with broader perspective and deeper curiosity.

I'm also deeply thankful to my collaborators in the group, especially Anyssa and Miguel. As postdocs, they brought deep experience and perspective to our work together, and I learned a great deal from both of them—not just about hardware and cryogenics, but also about navigating challenges with persistence and good humor. With Anyssa, I made more trips to Daresbury than I can count, all in the name of

the DWA project—a project that kept us constantly engaged with new puzzles. From our peak-finding marathons to our lunch explorations at the lab café, those days were filled with both determination and laughter. And with Miguel, I had the unforgettable experience of spending a summer in Texas—flying out from Manchester together, learning cryogenics for Q-Pix, and surviving both cockroach encounters and relentless heat waves. Introducing you to American staples like Walmart and Jersey Mike's added some cultural flavor to the mix, and your good humor made even the hottest days feel lighter.

I'm grateful to my collaborators on both the DWA and Q-Pix projects. For the DWA, I especially thank John, Nathan, James, Matt, and Graham. Taking this project from a concept to a working system was a journey full of challenges, learning, and teamwork. I gained so much from working alongside you. For Q-Pix, I want to thank Jonathan, Varghese, and Kevin from the University of Texas at Arlington. Even though I wasn't a student there, you welcomed me to UTA and gave me the chance to dive into the hardware side of the project. Your mentorship and generosity enabled me to gain critical hands-on experience, and I'm deeply grateful for the opportunity to learn and contribute.

I'm also thankful to the organizations that supported me along the way. The Grew Bancroft Foundation, the Ezoe Memorial Recruit Foundation, the Masason Foundation, and the Mitsui Mirai Challenger's Audition program not only provided financial support but also believed in the potential of young researchers to shape the future. Their encouragement gave me the freedom to pursue bold ideas, take risks, and grow as both a scientist and a communicator. I'm thankful not only for their resources, but for the communities they foster—full of driven, curious people who continue to inspire me.

I also wish to thank those who personally believed in the vision behind my research. I am especially grateful to Miyashita-san, whose generous support made it possible to explore new directions and ideas that might not have been possible otherwise. I also thank my patrons on the *esse-sence* program for offering not only funding, but a platform that encourages creativity and exploration beyond traditional academic boundaries. Your support has been instrumental in helping me carry this work from concept to completion.

When I arrived in the U.S. in 2015 with minimal English skills and a suitcase full of uncertainty, I never imagined I' d one day be writing a physics PhD dissertation —let alone from Harvard. So much of what made that improbable journey possible began at Mount Holyoke College. I'm forever thankful for the people I met there, where this path truly began. Kerstin, my first physics professor, introduced me to particle physics and changed the course of my life. The documentary *Particle Fever*, which she showed in class, opened my eyes to the wonder and scale of the field, and I haven't looked away since. To Neal and Spencer —thank you for being there when I felt overwhelmed or unsure I could continue in physics. Your open doors and steadfast support reminded me that I belonged. To Sam, my philosophy professor —thank you for helping me see the world beyond physics and for believing in my ability to hold questions that don't

always have answers. And to my physics friends at Mount Holyoke —you showed me what it means for women to support each other in science. That solidarity shaped the scientist I've become, and it's a strength I will carry forward.

While I was at Mount Holyoke, I was also supported in ways that extended far beyond campus. When classes and academics became overwhelming, I would often head into Boston to visit my friends at the Boston sharehouse —a place that became my second home. To Kaoru-chan, Katano-kun, Kensho-san, Kubonao, Masa, Rikuo, Takashima, and Yuuki-san —thank you for the endless laughter and chaotic game nights, from *Quiplash* to *Smash Brothers*. I still can't believe that all of us, who once spent weekends shouting at the TV and laughing until 2 a.m., are now doing such amazing things around the world. Coming back to the sharehouse almost every weekend recharged me in ways I didn't even realize at the time, and those memories will always stay with me.

After graduating from Mount Holyoke, I moved to Boston to work as a research fellow with Roxanne before officially beginning my PhD. Just as I started the program, the COVID-19 pandemic hit —and like so many others, I found myself navigating graduate school in isolation, without the usual rhythms of campus life. Despite that unusual beginning, I was lucky to build friendships that carried me through with Felipe, Ashley, Neeraj, Jordan, and Greg. You came into my life through different paths — our cohort, quarantine times, and shared research spaces —and your support helped me stay grounded. Even though I spent most of my PhD far from campus, our connection reminded me that I was still part of a community.

After spending the first part of my PhD in Boston, life took an unexpected turn —to Manchester. Moving to a new country in the middle of a PhD wasn' t something I had planned for, and I wasn' t sure what I was walking into. But I can' t talk about my time in Manchester without mentioning Helena. As a postdoc in the Guenette group at Harvard, you were the only person I moved with —and having someone familiar by my side made all the difference. Your presence was grounding and reassuring, and reminded me that I wasn't alone in the leap. From our post-work pints to weekend hangouts, you brought a sense of comfort and sisterhood that I looked forward to week after week. Your resilience, warmth, and quiet kindness brought so much joy into my life and made Manchester feel, unexpectedly, like home.

Shortly after I moved to Manchester, I traveled to Italy and had a conversation that would shift the course of my path with my friend, Yamato-san. A Paralympian and entrepreneur, you've been part of my life for over a decade, and your support has never wavered. During that trip, when I shared my doubts about staying in academia, you believed in me without hesitation. You told me I shouldn' t give up, and started introducing me to people across disciplines and industries. Through those conversations, I discovered my passion for science outreach —something that has since become a core part of who I am as a scientist. Thank you for helping me find not just my path, but also my voice.

As I neared the finish line of this Ph.D., the thesis writing became its own mountain

to climb—mentally, emotionally, and everything in between. During this time, I had the unwavering support of Zach and Lissa (and of course, Jasper, Jiren, Badger, and Naji). Thank you for being such good sports, for your daily doses of encouragement, and for offering the breaks and distractions I didn't know I needed. You made those final months feel lighter.

And throughout so much of this journey —through relocations, revisions, and every phase in between —I had the support of my partner, Dr. Chris Macias. When we met at the DUNE collaboration meeting at CERN in 2023, I never imagined we'd end up here, sharing not just physics, but life. Since then, we've traveled across Europe, taken in beautiful landscapes, tried incredible food, and learned how to slow down and enjoy it all. You've shown me what true resilience looks like in a researcher. You've become a role model to me —someone who has carved out success in science while proudly representing a minority community in physics. Having gone through a Ph.D. yourself, you understood the journey better than anyone, and supported me in every possible way. I truly couldn't have done this without you.

Lastly, to my parents, Mami and Toshiro Kubota. From the moment I was born, you made sure I knew I was loved, and that no dream was ever too far out of reach. When I left Japan in 2015, alone and unsure, speaking only fragments of English, you let me go—not because it was easy, but because you believed in what might be waiting on the other side. Since then, your quiet strength has followed me across every border, through every challenge, always reminding me where I came from. Today, with a Ph.D. in hand, named as Forbes 30 Under 30 Asia and MIT Technology Review Japan' s Innovators Under 35, I still see the girl who once clung to your hands at the airport, unsure of the world ahead. I may have grown, but I am still the same girl who loves her parents more than words can say. This degree is not mine alone. It carries your sacrifices, your hopes, and the unwavering belief you never stopped giving me. I carry your love in everything I do, and I always will.

Somewhere, something incredible is
waiting to be known.

Carl Sagan

1

Introduction

Long before I traced neutrinos through liquid argon, I was trained as a classical flautist. I spent years immersed in melody and rhythm, unaware that the music I loved was governed by principles I had yet to discover. When I could no longer play due to braces, I found myself drawn instead to the physics that made those harmonics possible. Beneath the melody was fluid dynamics, beneath the harmony was interference, and beneath it all, a universe governed by laws even more elegant than the music they made possible.

What began as a search for harmony in sound soon became a search for harmony in nature itself. That search finds its most comprehensive expression, so far, in the Standard Model of particle physics.

1.1 Historical Context and the Role of Neutrinos

Developed in the 1970s, the Standard Model provides a quantum field theory description of all known fundamental particles and their interactions, excluding gravity [1]. It describes the electromagnetic, weak, and strong forces within a single theoretical framework based on a gauge symmetry structure. Matter particles are grouped into three generations of quarks and leptons, while interactions are mediated by gauge bosons: gluons for the strong force, $W^{\pm}$ and Z^0 bosons for the weak force, and the photon for electromagnetism. The Higgs mechanism explains how particles acquire mass through spontaneous symmetry breaking, giving rise to the massive W and Z bosons and generating masses for charged fermions via their interactions with the Higgs field. The discovery of the Higgs boson on July 4, 2012, at the Large Hadron Collider (LHC) provided strong validation for the Standard Model, completing its particle content. It remains one of the most successful and precisely tested frameworks in the history of physics [2].

Yet even in its empirical triumphs, the Standard Model remains incomplete. It cannot explain the observed matter-antimatter asymmetry of the universe, the nature of dark matter, or, most intriguingly, the non-zero masses of neutrinos. Neutrinos occupy a special place in this story. Nearly massless, electrically neutral, and weakly interacting, they were first introduced to preserve the conservation of energy and momentum in beta decay. In 1930, Wolfgang Pauli postulated the neutrino to resolve this discrepancy,

famously writing [3], "I have done a terrible thing. I have postulated a particle that cannot be detected." It would take more than two decades for neutrinos to be confirmed experimentally. Since then, neutrino physics has evolved from a theoretical curiosity into a powerful probe of new physics.

Today, neutrinos serve as one of the most sensitive instruments for exploring physics beyond the Standard Model. Their weak interactions, flavor oscillations, and potential Charge Parity (CP)-violating properties make them central to some of the most pressing questions in particle physics and cosmology. But what makes neutrinos especially powerful is not their abundance—it is their subtlety. They speak in the softest tones, interacting rarely, eluding detection, leaving only the faintest traces in their wake. Observing them demands more than just technological sophistication—it requires precision, patience, and a system finely tuned to respond only when the rare and meaningful occurs. This thesis is situated at that frontier, focused on the development of novel detection techniques for observing neutrinos in high definition with Liquid Argon (LAr) —technology designed not to overwhelm the data with constant measurement, but to remain sensitive to the faint, fleeting signals that emerge when silence speaks.

1.2 The Discovery of Neutrinos

The neutrino, initially postulated by Pauli to salvage conservation laws, has become one of the most elusive and illuminating particles in physics. This section traces the key experimental milestones in the detection of neutrino flavors and their properties—laying the groundwork for the revolutionary realization that neutrinos have mass.

The first direct detection of neutrinos was achieved by Fred Reines and Clyde Cowan in 1955, through the observation of inverse beta decay at the Savannah River nuclear

reactor [4]. Their first experiment, conducted in 1953, used a nuclear reactor at Hanford as a source of electron antineutrinos, which they attempted to detect via the inverse beta decay reaction:

$$p + \bar{\nu}_e \rightarrow n + e^+. \tag{1.1}$$

They employed a liquid scintillator to detect two gamma rays: one at 511 keV from positron-electron annihilation, and another at 9 MeV from neutron capture a few microseconds later. However, this early attempt was unsuccessful due to overwhelming background from cosmic rays and radioactive decays.

In 1955, they improved the experiment by increasing the detector size from 300 liters to 10 tons and switching to a more powerful reactor at the Savannah River Plant. They also added lead shielding to suppress cosmic ray interactions and doped the water with cadmium to enhance neutron detection: cadmium has a high cross section for thermal neutron capture and emits a distinctive gamma-ray cascade upon capture, providing a delayed coincidence signal crucial for identifying inverse beta decay events. This improved setup successfully confirmed the existence of neutrinos and demonstrated their weakly interacting nature [5]. Reines was awarded the Nobel Prize in Physics in 1995 for this work. Cowan had unfortunately passed away earlier and was therefore ineligible.

Soon after, in 1962, muon neutrinos were discovered by Leon Lederman, Melvin Schwartz, and Jack Steinberger [6]. They developed a high-energy muon neutrino beam by directing a proton beam at a beryllium target, which produced mesons that decayed into (anti)muons and muon (anti)neutrinos. This ν_μ beam was then directed into a spark chamber placed behind iron shielding to observe interactions characteristic of muon neutrinos.

The tau neutrino was finally detected in 2001 by the Direct Observation of the Nu

Tau (DONuT) experiment [7], following decades of indirect evidence for its existence. This was one of the most technically demanding neutrino experiments to date, for two main reasons. First, producing a tau neutrino beam requires significantly higher energies than those needed for electron or muon neutrinos. Second, the tau lepton produced via charged-current tau neutrino interactions has a lifetime of only 2.9×10^{-13} s, decaying almost instantaneously into charged pions, a muon, or an electron. Identifying tau neutrino interactions therefore requires sub-millimeter spatial resolution to resolve the characteristic kink of the tau decay. The DONuT collaboration addressed these challenges using a high-energy proton beam to produce tau neutrinos, and a hybrid detector consisting of steel-emulsion targets interleaved with scintillating fiber trackers. Researchers scanned these emulsion plates by hand under microscopes, searching for a sign: a sudden kink in a track, a whisper of a tau's final moment. Four tau neutrino events were ultimately identified from around 3500 interactions recorded[8].

Beyond its technical achievement, the DONuT experiment also represents a uniquely human facet of particle physics: the act of peering into emulsion with the naked eye, searching frame by frame for the unseen. It evokes a form of science that is as much devotion as it is deduction. For those who study it, one cannot help but imagine the moment of discovery—the researcher at the microscope, witnessing a kinked track for the first time, standing at the very edge of human knowledge. These are the moments that define not just experimental breakthroughs, but the very spirit of physics. It is this quiet, hands-on pursuit of understanding that continues to inspire my work, and reminds me that even the most fleeting signals can carry the weight of discovery.

In parallel, experiments at the Large Electron-Positron Collider (LEP) studied Z

boson decays through the process

$$e^+e^- \to Z \to \nu\bar{\nu} \tag{1.2}$$

to determine the number of light neutrino flavors [9]. Precision measurements showed that the number of light active neutrino species, those that couple to the Z boson, is 2.9840±0.0082, consistent with three flavors. This established the framework of three massless, weakly interacting neutrinos in the Standard Model.

Despite this apparent completeness, the Standard Model still leaves important questions unanswered. One such issue is the absence of right-handed neutrinos. In 1956, Chien-Shiung Wu's experiment on beta decay demonstrated maximal parity violation, consistent with the emission of right-handed antineutrinos [10]. The following year, Maurice Goldhaber's experiment studying the decay of ^{152}Eu showed that all neutrinos are left-handed [11]—a result naturally explained if neutrinos are massless.

At the time, these findings supported the Standard Model's structure, which included only left-handed neutrinos and right-handed antineutrinos. However, the later discovery of neutrino mass challenged this picture. A massive fermion must possess both left- and right-handed components, yet the Standard Model contains no right-handed neutrino field and thus no way to endow neutrinos with mass via the standard Higgs mechanism. This absence, once considered an elegant simplification, became a profound inconsistency—one that points to physics beyond the Standard Model.

The resolution to this puzzle emerged not from theoretical constructs, but from experimental anomalies. In particular, measurements of solar and atmospheric neutrinos revealed flavor transformations—oscillations—that implied non-zero neutrino masses and thus signaled new physics. These discoveries are discussed in the next section.

1.3 The Discovery of Neutrino Mass

While early experiments confirmed the existence of three neutrino flavors, they also revealed anomalies that hinted at physics beyond the Standard Model. Foremost among these was the solar neutrino deficit observed by Ray Davis in 1968—a result that ultimately led to the discovery that neutrinos have non-zero mass [12]. In this experiment, he built a detector deep underground at the Homestake Mine to measure the flux of solar neutrinos. At the time, scientists were developing theoretical models of solar fusion. John Bahcall, a theoretical astrophysicist, calculated the expected solar neutrino flux based on these models, and Davis aimed to confirm this prediction [13].

The experiment used 380,000 liters of perchloroethylene and targeted the charged-current (CC) interaction of electron neutrinos:

$$\nu_e + {}^{37}\mathrm{Cl} \rightarrow {}^{37}\mathrm{Ar} + e^{-}. \tag{1.3}$$

Counting the number of ^{37}Ar atoms produced using Germanium detectors, Davis observed a significant deficit—about one-third of the predicted flux. This discrepancy became famously known as the solar neutrino problem.

Similar discrepancies between theoretical predictions and measured values were observed in other experiments. One notable example was the Kamiokande experiment, originally constructed to search for proton decay using a large water Cherenkov detector in the Kamioka Mine, Japan. In 1989, Kamiokande confirmed the solar neutrino deficit through real-time detection of ^{8}B neutrinos [14]. Later, in 1992, the same detector reported an unexpected deficit in atmospheric muon neutrinos compared to theoretical predictions, a result known as the atmospheric neutrino anomaly [15]. Complementing

these findings, the Gallium Experiment (GALLEX) at Gran Sasso began operations in 1991 and observed a similar shortfall in solar neutrino flux, particularly targeting low-energy neutrinos from the pp-chain [16].

In 1998, the Super-Kamiokande experiment provided the first compelling evidence for neutrino oscillations by observing a deficit of upward-going muon neutrinos compared to downward-going ones—an effect consistent with distance-dependent flavour transformation of atmospheric neutrinos [17]. Utilizing a large water Cherenkov detector located in the Kamioka Mine, Super-Kamiokande demonstrated that neutrinos change flavour as they propagate through the Earth.

Subsequently, in 2002, the Sudbury Neutrino Observatory (SNO) resolved the long-standing solar neutrino problem by directly measuring both CC and neutral-current (NC) interactions using a heavy water Cherenkov detector [18]. The CC interaction is sensitive exclusively to electron neutrinos, while the NC interaction is equally sensitive to all active neutrino flavours. These interactions are represented as:

$$\begin{aligned} &\text{CC:} \quad \nu_e + d \to p + p + e^- \\ &\text{NC:} \quad \nu_\ell + d \to p + n + \nu_\ell \end{aligned} \tag{1.4}$$

Here, d denotes deuterium, and ℓ represents any active neutrino flavour (e, μ, τ).

SNO's CC interaction measurements revealed a significant deficit of electron neutrinos, consistent with earlier solar neutrino experiments. However, their crucial NC measurements demonstrated that the total flux of all neutrino flavors matched solar model predictions. This resolved the solar neutrino problem by providing definitive evidence that electron neutrinos from the Sun undergo flavor oscillations into muon and tau neutrinos en route to Earth, directly confirming neutrino flavor conversion and the existence of neutrino mass. Specifically, the electron neutrino flux detected via CC in-

teractions aligned with the deficits seen by experiments like Homestake, while the total neutrino flux from NC interactions was in excellent agreement with Bahcall's theoretical predictions.

Takaaki Kajita from Super-Kamiokande and Arthur B. McDonald from SNO were awarded the 2015 Nobel Prize in Physics for these groundbreaking discoveries.

These complementary results from solar and atmospheric neutrino experiments provided compelling evidence that neutrinos undergo flavor transitions in flight. Since such transitions are only possible if neutrinos have distinct, non-zero masses, these observations signaled the need for new theoretical frameworks that extend beyond the Standard Model. The following section introduces the quantum mechanical foundation of neutrino oscillation, explaining how this phenomenon directly implies that neutrinos possess non-zero mass.

1.4 Neutrino Oscillation

The observation that neutrinos change flavour as they propagate implies that their flavour eigenstates are not identical to their mass eigenstates. This phenomenon, known as neutrino oscillation, is only possible if neutrinos have mass. This section outlines the theoretical foundation of this effect, beginning with the simplified two-flavour case and extending to the full three-flavour framework relevant to modern experiments.

1.4.1 Two-Flavour Neutrino Oscillation Formalism

Although neutrino oscillations in nature involve three flavours, significant insight can be gained by first considering a simplified two-flavour system. Let us assume two flavour eigenstates, ν_α and ν_β, related to two mass eigenstates, ν_1 and ν_2, via a unitary mixing

matrix parametrized by a single mixing angle θ:

$$\begin{pmatrix} \nu_\alpha \\ \nu_\beta \end{pmatrix} = \begin{pmatrix} \cos\theta & \sin\theta \\ -\sin\theta & \cos\theta \end{pmatrix} \begin{pmatrix} \nu_1 \\ \nu_2 \end{pmatrix}. \tag{1.5}$$

A neutrino produced in a pure flavour state $|\nu_\alpha\rangle$ at time $t = 0$ can be expressed in terms of mass eigenstates as:

$$|\nu(0)\rangle = |\nu_\alpha\rangle = \cos\theta|\nu_1\rangle + \sin\theta|\nu_2\rangle. \tag{1.6}$$

Since mass eigenstates propagate independently, their time evolution is given by:

$$|\nu_i(t)\rangle = e^{-iE_j t}|\nu_i\rangle, \quad (j = 1, 2). \tag{1.7}$$

Thus, the state at time t evolves as:

$$|\nu_\alpha(t)\rangle = \cos\theta e^{-iE_1 t}|\nu_1\rangle + \sin\theta e^{-iE_2 t}|\nu_2\rangle. \tag{1.8}$$

The probability of detecting the neutrino as flavour ν_β at time t is given by:

$$P(\nu_\alpha \to \nu_\beta(t)) = |\langle\nu_\beta|\nu_\alpha(t)\rangle|^2. \tag{1.9}$$

Using $|\nu_\beta\rangle = -\sin\theta|\nu_1\rangle + \cos\theta|\nu_2\rangle$, the transition amplitude becomes:

$$\begin{aligned}
A(\nu_\alpha \to \nu_\beta(t)) &= \langle \nu_\beta | \nu_\alpha(t) \rangle \\
&= (-\sin\theta\langle\nu_1| + \cos\theta\langle\nu_2|)(\cos\theta\, e^{-iE_1 t}|\nu_1\rangle + \sin\theta\, e^{-iE_2 t}|\nu_2\rangle) && (1.10)\\
&= -\sin\theta\cos\theta e^{-iE_1 t} + \cos\theta\sin\theta e^{-iE_2 t} && (1.11)\\
&= \sin\theta\cos\theta\left(e^{-iE_2 t} - e^{-iE_1 t}\right), && (1.12)
\end{aligned}$$

and the corresponding probability is:

$$\begin{aligned}
P(\nu_\alpha \to \nu_\beta(t)) &= |A(\nu_\alpha \to \nu_\beta(t))|^2 \\
&= |\cos\theta\sin\theta e^{-iE_1 t}(e^{-i\Delta E t} - 1)|^2 && (1.13)\\
&= \cos^2\theta\sin^2\theta(2 - e^{-i\Delta E t} - e^{i\Delta E t}) && (1.14)\\
&= \frac{\sin^2 2\theta}{4} 2(1 - \cos(\Delta E t)) && (1.15)\\
&= \frac{\sin^2 2\theta}{2} 2\sin^2\left(\frac{\Delta E t}{2}\right) && (1.16)\\
&= \sin^2 2\theta\, \sin^2\left(\frac{\Delta E\, t}{2}\right), && (1.17)
\end{aligned}$$

where $\Delta E = E_2 - E_1$.

For a neutrino mass eigenstate ν_i, the exact energy-momentum relation is given by:

$$E_i = \sqrt{p^2 + m_i^2}, \tag{1.18}$$

where E_i is the total energy, p is the momentum (assumed approximately equal for all mass eigenstates), and m_i is the mass of the i-th eigenstate.

In the relativistic limit, where $m_i^2 \ll p^2$, the square root can be expanded using a

binomial approximation:

$$E_i = p\sqrt{1+\frac{m_i^2}{p^2}} \simeq p\left(1+\frac{m_i^2}{2p^2}\right). \tag{1.19}$$

This yields:

$$E_i \simeq p + \frac{m_i^2}{2p}. \tag{1.20}$$

Since highly relativistic neutrinos satisfy $E \simeq p$, we can rewrite this as:

$$E_i \simeq E + \frac{m_i^2}{2E}. \tag{1.21}$$

Therefore,

$$\Delta E = E_2 - E_1 \simeq \frac{m_2^2 - m_1^2}{2E} = \frac{\Delta m_{21}^2}{2E}, \tag{1.22}$$

where $\Delta m_{21}^2 = m_2^2 - m_1^2$ is the mass-squared difference.

Finally, assuming $t \simeq L$ (the distance traveled) and using natural units ($\hbar = c = 1$), the oscillation probability becomes:

$$P(\nu_\alpha \to \nu_\beta) = \sin^2 2\theta \sin^2\left(\frac{\Delta m_{21}^2 L}{4E}\right). \tag{1.23}$$

Restoring conventional units yields the practical form:

$$P(\nu_\alpha \to \nu_\beta) = \sin^2 2\theta \sin^2\left(1.267\,\frac{\Delta m_{21}^2\,[\mathrm{eV}^2]\cdot L\,[\mathrm{km}]}{E\,[\mathrm{GeV}]}\right). \tag{1.24}$$

This expression reveals the characteristic oscillatory behaviour of neutrinos. The amplitude of the oscillation is governed by the mixing angle θ, while the frequency depends on the mass-squared difference Δm_{21}^2, the neutrino energy E, and the baseline L over

which the neutrino propagates. Crucially, if all neutrino masses were equal—or zero—Δm^2_{21} would become zero, and no probability of flavour change ($P(\nu_\alpha \to \nu_\beta)$) would be zero as well. Thus, the observation of neutrino oscillations provides unambiguous evidence that at least two neutrino mass eigenstates possess distinct, non-zero masses, marking a clear departure from the original Standard Model, which assumes massless neutrinos. While oscillation experiments are sensitive only to differences in mass squared, current global fits and theoretical considerations suggest that all three neutrino mass states are likely non-zero, though the absolute mass scale remains undetermined.

1.4.2 Three-Flavour Framework and Oscillation Parameters

While the two-flavour model captures the essence of neutrino oscillation, a complete description of the phenomenon requires all three active neutrino flavours. In the three-flavour framework, the flavour and mass eigenstates are related by the 3×3 Pontecorvo–Maki–Nakagawa–Sakata (PMNS) matrix [19]:

$$\begin{pmatrix} \nu_e \\ \nu_\mu \\ \nu_\tau \end{pmatrix} = \begin{pmatrix} U_{e1} & U_{e2} & U_{e3} \\ U_{\mu 1} & U_{\mu 2} & U_{\mu 3} \\ U_{\tau 1} & U_{\tau 2} & U_{\tau 3} \end{pmatrix} \begin{pmatrix} \nu_1 \\ \nu_2 \\ \nu_3 \end{pmatrix}. \tag{1.25}$$

The PMNS matrix can be parameterized by three mixing angles θ_{12}, θ_{13}, and θ_{23}, and one Dirac CP-violating phase δ_{CP}. A common decomposition is:

$$U_{\mathrm{PMNS}} = \begin{pmatrix} 1 & 0 & 0 \\ 0 & c_{23} & s_{23} \\ 0 & -s_{23} & c_{23} \end{pmatrix} \begin{pmatrix} c_{13} & 0 & s_{13}e^{-i\delta_{\mathrm{CP}}} \\ 0 & 1 & 0 \\ -s_{13}e^{i\delta_{\mathrm{CP}}} & 0 & c_{13} \end{pmatrix} \begin{pmatrix} c_{12} & s_{12} & 0 \\ -s_{12} & c_{12} & 0 \\ 0 & 0 & 1 \end{pmatrix}, \tag{1.26}$$

where $s_{ij} \equiv \sin\theta_{ij}$ and $c_{ij} \equiv \cos\theta_{ij}$.

Each mixing angle and mass-squared difference governs neutrino oscillations within specific energy and baseline regimes. The parameters θ_{12} and Δm^2_{21} dominate solar neutrino oscillations and long-baseline reactor experiments, where the characteristic mass-squared difference of $\sim 7.4\times10^{-5}$ eV^2 matches the relevant L/E scales. The mixing angle θ_{23} and the larger mass-squared difference $|\Delta m^2_{32}| \sim 2.5 \times 10^{-3}$ eV^2 primarily govern atmospheric neutrino oscillations and are probed by long-baseline accelerator experiments. The mixing angle θ_{13}, once thought to be vanishingly small, has been measured to be non-zero, enabling sensitivity to CP violation through the complex phase δ_{CP}. If δ_{CP} is significantly different from zero or π, it would signal CP violation in the lepton sector—an intriguing feature that may offer indirect insights into the matter–antimatter asymmetry of the universe via mechanisms such as leptogenesis.

1.4.3 Matter Effects

While the vacuum oscillation framework describes neutrino propagation in empty space, neutrinos often traverse dense media such as the Sun, the Earth, or supernovae, where the presence of matter modifies their evolution. This modification, known as the Mikheyev–Smirnov–Wolfenstein (MSW) effect [20], alters the effective oscillation parameters and can lead to dramatic enhancements in flavour conversion under specific conditions.

In matter, electron neutrinos interact with ambient electrons via both CC and NC interactions, while muon and tau neutrinos experience only NC interactions. The resulting asymmetry induces an effective potential energy for electron neutrinos relative to the other flavours. This additional energy enters the neutrino Hamiltonian in the flavour basis and modifies the propagation dynamics.

In the two-flavour approximation, the effective Hamiltonian in vacuum is given by:

$$H_{\text{vac}} = \frac{\Delta m^2}{4E} \begin{pmatrix} -\cos 2\theta & \sin 2\theta \\ \sin 2\theta & \cos 2\theta \end{pmatrix}, \tag{1.27}$$

where Δm^2 is the mass-squared difference, θ is the vacuum mixing angle, and E is the neutrino energy. In a medium with electron number density N_e, an additional matter-induced potential appears for electron neutrinos:

$$V_{\text{CC}} = \sqrt{2} G_F N_e, \tag{1.28}$$

where G_F is the Fermi constant. This potential enters the total Hamiltonian as:

$$H_{\text{matter}} = H_{\text{vac}} + \begin{pmatrix} V_{\text{CC}} & 0 \\ 0 & 0 \end{pmatrix}. \tag{1.29}$$

While neutrinos propagate as eigenstates of the total Hamiltonian, the presence of a flavour-dependent potential in matter redefines these propagation eigenstates relative to their vacuum counterparts. The MSW effect captures how this modification, arising from coherent forward scattering of electron neutrinos, alters flavour evolution compared to vacuum oscillations.

Diagonalizing this total Hamiltonian yields modified oscillation parameters in matter: an effective mixing angle θ_m and an effective mass-squared difference Δm^2_m. These quantities fully determine the oscillation probability in a matter-rich environment and

are given by:

$$\sin^2 2\theta_m = \frac{\sin^2 2\theta}{\left(\cos 2\theta - \frac{2\sqrt{2}G_F N_e E}{\Delta m^2}\right)^2 + \sin^2 2\theta}, \tag{1.30}$$

$$\Delta m^2_m = \Delta m^2 \sqrt{\left(\cos 2\theta - \frac{2\sqrt{2}G_F N_e E}{\Delta m^2}\right)^2 + \sin^2 2\theta}. \tag{1.31}$$

These expressions directly reflect how the matter potential distorts both the mixing structure and the oscillation frequency compared to their vacuum values.

A particularly striking feature of the MSW effect arises when the matter potential satisfies the so-called resonance condition:

$$\frac{2\sqrt{2}G_F N_e E}{\Delta m^2} = \cos 2\theta. \tag{1.32}$$

At this point, the effective mixing angle reaches $\theta_m = \pi/4$, corresponding to maximal mixing—even if the vacuum mixing angle θ is small. This condition marks the point of most efficient flavour conversion: neutrinos produced in a pure flavour state can undergo nearly complete transformation into another flavour over the course of propagation. Physically, this occurs because the flavour states become equal mixtures of the instantaneous mass eigenstates in matter, maximizing the interference that drives oscillations.

This resonance mechanism is particularly important in solar neutrino physics. Neutrinos produced in the Sun's core propagate through a smoothly varying electron density profile as they travel outward. If the density changes slowly enough—a condition known as adiabaticity—the neutrino remains in its instantaneous matter eigenstate. When this eigenstate evolves from one dominated by electron flavour into one dominated by an-

other flavour, nearly complete conversion occurs. This MSW-driven transformation explains the observed suppression of electron neutrinos detected on Earth, as confirmed by solar neutrino experiments such as SNO and Super-Kamiokande.

A similar mechanism operates in the extreme environment of a core-collapse supernova. In this case, neutrinos are produced in enormous numbers and across all flavours, emerging from regions with electron densities many orders of magnitude higher than in the Sun. As they travel outward through the exploding stellar envelope, the rapidly decreasing matter density enables multiple MSW resonances to occur at different radii, each corresponding to distinct mass-squared splittings (Δm^2_{21} and Δm^2_{31}). These resonances can drive flavour conversion through both the solar and atmospheric mass scales, and depending on the ordering and adiabaticity, they can significantly alter the flavour composition of the neutrino signal observed on Earth. Moreover, in supernovae, neutrino-neutrino interactions introduce an additional nonlinear effect known as collective oscillation, which can interplay with MSW-driven transitions and lead to even more complex spectral features.

Beyond astrophysical environments, the MSW effect also plays a crucial role in terrestrial long-baseline accelerator experiments. As beam neutrinos traverse the Earth's crust—typically over distances of hundreds to thousands of kilometers—the matter-induced potential introduces a difference between neutrino and antineutrino oscillation probabilities. This arises because the sign of the matter potential flips for antineutrinos, and the oscillation probabilities depend on the sign of the mass-squared difference Δm^2_{31}. As a result, the degree of matter-induced enhancement or suppression differs between neutrinos and antineutrinos, and this asymmetry provides a handle on determining the neutrino mass ordering. Experiments such as NuMI Off-axis ν_e Appearance (NOvA) experiment and Tokai to Kamioka (T2K) experiment, and future efforts like Deep Un-

derground Neutrino Experiment (DUNE) and Hyper-Kamiokande, leverage this matter effect as a key sensitivity lever in their measurement programs.

1.4.4 Experimental Approaches and Parameter Sensitivities

Oscillation experiments aim to determine the six fundamental parameters of the three-flavour framework: the two mass-squared differences (Δm^2_{21}, Δm^2_{31}), three mixing angles (θ_{12}, θ_{13}, θ_{23}), and the CP-violating phase δ_{CP}. Different experimental approaches probe these parameters across varying baselines and energy regimes. Table 1.1 summarizes the primary sensitivities of each experimental class.

Experiment	**Type**	**Status**	**Dominant Sensitivity**	**Secondary Sensitivity**
KamLAND	Reactor (Long-baseline)	Past	θ_{12}, Δm^2_{21}	θ_{13}
K2K	Accelerator	Past	θ_{23}, $\lvert\Delta m^2_{31}\rvert$	—
MINOS	Accelerator	Past	θ_{23}, $\lvert\Delta m^2_{31}\rvert$	θ_{13}
Daya Bay	Reactor (Short-baseline)	Current	θ_{13}	$\lvert\Delta m^2_{31}\rvert$
RENO	Reactor (Short-baseline)	Current	θ_{13}	$\lvert\Delta m^2_{31}\rvert$
Double Chooz	Reactor (Short-baseline)	Current	θ_{13}	$\lvert\Delta m^2_{31}\rvert$
Super-Kamiokande	Solar / Atmospheric	Current	θ_{12}, Δm^2_{21}; θ_{23}, $\lvert\Delta m^2_{31}\rvert$	Mass ordering, θ_{13}
Borexino	Solar	Current	θ_{12}, Δm^2_{21}	θ_{13}
IceCube	Atmospheric	Current	θ_{23}, $\lvert\Delta m^2_{31}\rvert$	Mass ordering
T2K	Accelerator	Current	θ_{13}, δ_{CP}	θ_{23}, Mass ordering
NOνA	Accelerator	Current	θ_{13}, Mass ordering	δ_{CP}, θ_{23}
JUNO	Reactor (Medium-baseline)	Future	Mass ordering, Δm^2_{21}, θ_{12}	θ_{13}
Hyper-Kamiokande	Solar / Atmospheric / Accelerator	Future	θ_{23}, $\lvert\Delta m^2_{31}\rvert$, δ_{CP}	Mass ordering, θ_{13}
DUNE	Accelerator	Future	Mass ordering, δ_{CP}, θ_{23}	θ_{13}

Table 1.1: Summary of major neutrino oscillation experiments, categorized by type and status, along with their dominant and secondary sensitivities to oscillation parameters.

Together, these experiments have established the existence of neutrino oscillations and measured most of the mixing parameters with increasing precision. However, key unknowns remain—including the neutrino mass ordering, the octant of θ_{23}, and the value

of δ_{CP}. These open questions provide the central motivation for the next generation of long-baseline experiments such as DUNE and Hyper-Kamiokande, which will be discussed in subsequent chapters.

1.5 Theory of Mass

The discovery of neutrino oscillations implies that neutrinos possess non-zero mass. However, in the framework of the Standard Model, neutrinos remain massless due to the absence of right-handed neutrino fields. Fermion masses in the Standard Model arise from Yukawa interactions of the form:

$$\mathcal{L}_{\mathrm{Yukawa}} = -y_f \bar{L} H f_R + \mathrm{h.c.}, \tag{1.33}$$

where L is the left-handed fermion doublet, H is the Higgs field, and f_R is the corresponding right-handed singlet. For charged leptons and quarks, both left- and right-handed components exist, allowing such mass terms. In contrast, since no right-handed neutrino ν_R has been observed yet, no analogous Yukawa coupling can be written for neutrinos. As a result, neutrinos are massless by construction within the Standard Model. Explaining the origin and smallness of neutrino mass thus requires an extension of the Standard model and has far-reaching implications for particle physics and cosmology.

1.5.1 Dirac versus Majorana Neutrinos

A fundamental question in neutrino physics is whether neutrinos are Dirac or Majorana particles. If neutrinos are Dirac fermions—like electrons or quarks—they require the existence of a right-handed neutrino field, ν_R, which does not participate in Standard Model gauge interactions. This gauge-singlet field allows neutrinos to acquire mass

through the same mechanism as other fermions: a Yukawa coupling to the Higgs field. The corresponding term in the Lagrangian is

$$\mathcal{L}_{\text{Dirac}} = -y_\nu \bar{L}\tilde{H}\nu_R + \text{h.c.}, \tag{1.34}$$

where y_ν is the neutrino Yukawa coupling, L is the lepton doublet, and $\tilde{H}$ is the conjugate Higgs field. After electroweak symmetry breaking, this interaction generates a Dirac mass for the neutrino:

$$m_D = y_\nu v, \tag{1.35}$$

where $v \approx 246$ GeV is the Higgs vacuum expectation value. Reproducing the observed sub-eV neutrino masses requires the Yukawa coupling y_ν to be exceptionally small, approximately 10^{-12} [21, 22]. This value is many orders of magnitude smaller than the Yukawa couplings of other fermions, such as the electron ($y_e \sim 10^{-6}$). Such extreme suppression appears unnatural, as the Standard Model provides no underlying reason for why the neutrino's coupling to the Higgs field should be so disproportionately weaker than that of all other particles. This disparity motivates the exploration of alternative mass generation mechanisms, such as the seesaw mechanism, which can naturally explain the smallness of neutrino masses without requiring anomalously fine-tuned parameters.

Alternatively, if neutrinos are Majorana particles, meaning they are identical to their antiparticles, their mass can arise through mechanisms that violate lepton number conservation. Remarkably, it is possible to generate such a mass term without introducing new particles beyond the Standard Model, by constructing an effective interaction involving only existing fields. This interaction, known as the Weinberg operator, is suppressed by a high energy scale associated with physics beyond the Standard Model.

After electroweak symmetry breaking, the Weinberg operator [23] leads to a neutrino mass proportional to v^2/Λ, where v is the Higgs vacuum expectation value and Λ represents the characteristic scale of new physics responsible for lepton number violation. The observed smallness of neutrino masses—on the order of sub-eV—implies that Λ must lie near 10^{14} GeV [22]. This energy scale is intriguingly close to that predicted by Grand Unified Theories (GUTs), suggesting a potential link between the origin of neutrino mass and the unification of fundamental forces.

1.5.2 Seesaw Mechanisms

A well-known realization of the Weinberg operator is provided by the seesaw mechanism [24], which offers a natural explanation for the smallness of neutrino masses. In this framework, heavy particles—introduced through extensions of the Standard Model —couple to the light neutrinos. As a result, neutrino masses are suppressed by the ratio of the electroweak scale to a much larger mass scale associated with new physics. This elegant mechanism captures the essence of why neutrino masses are many orders of magnitude smaller than those of charged fermions.

Several variants of the seesaw mechanism exist, differing in the types of heavy particles involved—such as heavy right-handed neutrinos or scalar and fermionic triplets —but they all share the common feature that light neutrino masses emerge due to the presence of high-scale states that effectively decouple at low energies. While the detailed dynamics depend on the specific model, the generic prediction is that observing tiny neutrino masses today points toward physics at energy scales potentially linked to grand unification or other beyond Standard Model phenomena.

1.5.3 Implications

Mass-generating mechanisms often violate lepton number, leading to experimentally testable consequences. The most prominent example is neutrinoless double beta decay ($0\nu\beta\beta$), a hypothetical process in which two neutrons transform into two protons and two electrons without emitting neutrinos. This process, illustrated in Figure 1.1, violates lepton number conservation and can only occur if neutrinos are Majorana particles. A discovery of $0\nu\beta\beta$ would not only provide definitive evidence for the Majorana nature of neutrinos, but also offer sensitivity to the absolute neutrino mass scale through the decay rate.

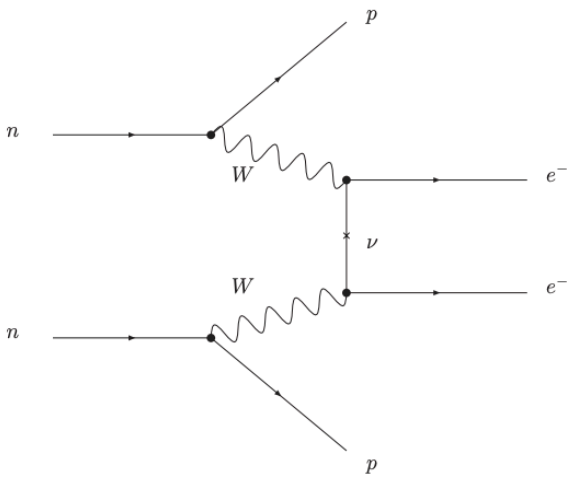


Figure 1.1: Feynman diagram of neutrinoless double beta decay ($0\nu\beta\beta$), where a virtual Majorana neutrino mediates the process, allowing two neutrons to decay into two protons and two electrons without neutrino emission. Figure taken from [25].

The high scale associated with the seesaw mechanism also provides a natural framework for leptogeneesis, wherein the decays of heavy Majorana neutrinos in the early universe generate a lepton asymmetry. As first outlined by Sakharov [26], the dynamical generation of a matter–antimatter asymmetry requires three conditions to be satisfied:

violation of baryon (or lepton) number, violation of C and CP symmetries, and a departure from thermal equilibrium. In leptogenesis, these criteria are naturally met [27, 28]: heavy Majorana neutrino decays violate lepton number and, if CP-violating phases are present in the neutrino sector, produce an excess of leptons over anti-leptons. Since these decays occur out of equilibrium in the cooling early universe, the generated lepton asymmetry is preserved and partially converted into a baryon asymmetry through non-perturbative sphaleron processes. This mechanism offers a compelling explanation for the observed matter-antimatter imbalance and links neutrino mass generation to one of the fundamental questions in cosmology.

In summary, while the origin of neutrino mass lies beyond the Standard Model, its experimental consequences are accessible to current and next-generation neutrino experiments. These efforts form the backbone of a broader program to probe the nature of mass and symmetry in the universe.

1.6 Open Questions in Neutrino Physics

The discovery of neutrino oscillations has opened a rich and ongoing field of inquiry into the fundamental properties of neutrinos. While the phenomenon confirms that neutrinos are massive and mix, several critical questions remain unresolved. Addressing these open problems is essential not only for completing the neutrino sector but also for understanding the broader implications for particle physics, cosmology, and the origin of mass.

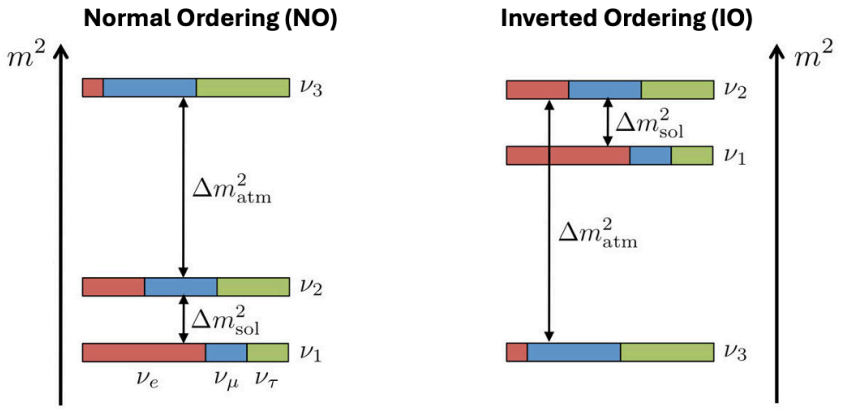


Figure 1.2: Illustration of the two possible neutrino mass orderings: normal ordering (NO) where $m_3 > m_2 > m_1$, and inverted ordering (IO) where $m_2 > m_1 > m_3$. The vertical axis represents mass-squared, and the colored bars indicate the flavour composition of each mass eigenstate.

1.6.1 Neutrino Mass Ordering

Oscillation experiments are sensitive to mass-squared differences, but not to the absolute mass values. As a result, it remains unknown whether the third mass eigenstate is the heaviest (normal ordering, $m_3 > m_2 > m_1$) or the lightest (inverted ordering, $m_2 > m_1 > m_3$) as illustrated in Figure 1.2.

Upcoming and ongoing long-baseline experiments, such as DUNE [29] and Jiangmen Underground Neutrino Observatory (JUNO) [30], aim to determine the ordering with high precision by leveraging matter effects and interference patterns in neutrino oscillations.

1.6.2 CP Violation in the Lepton Sector

Another major open question is whether neutrino oscillations violate the CP symmetry. The Dirac CP-violating phase δ_{CP} in the PMNS matrix governs this phenomenon, which

manifests as a difference in oscillation probabilities between neutrinos and antineutrinos. A non-zero δ_{CP} could provide a crucial ingredient for explaining the matter-antimatter asymmetry of the universe via leptogenesis. Present data from T2K [31] and NOνA [32] suggest a preference for significant CP violation [33, 34], but the uncertainties remain large. Definitive measurements are a central goal of the next generation of accelerator-based experiments, especially DUNE and Hyper-Kamiokande. Note that the Dirac phase δ_{CP} affects oscillation probabilities and can be measured in long-baseline experiments, whereas potential Majorana phases—if neutrinos are Majorana particles—do not influence oscillations and must be probed via processes like $0\nu\beta\beta$.

1.6.3 Absolute Neutrino Mass Scale

While oscillation experiments are sensitive to differences in squared masses, they provide no information about the absolute mass scale of neutrinos. Determining this absolute scale remains one of the most elusive goals in fundamental physics, with direct implications for cosmology, particle theory, and the overall structure of the lepton sector. Three complementary experimental approaches are currently pursued, each probing a different aspect of neutrino mass.

The most direct and model-independent method is kinematic: precise measurements of the electron energy spectrum near the endpoint of beta decay can reveal the effective electron neutrino mass. The most sensitive experiment of this kind is KATRIN (Karlsruhe Tritium Neutrino), which uses a high-luminosity windowless gaseous tritium source and an ultra-precise electrostatic spectrometer over 70 meters in length to examine the endpoint of tritium beta decay. With its unprecedented energy resolution and control of systematics, KATRIN currently places an upper bound of $m_\nu < 0.8$ eV at 90% confidence level [35]. Beyond the physics reach, KATRIN represents a technolog-

ical masterpiece—combining cryogenic pumping, high-voltage stability, and ultra-high vacuum at massive scale—and stands as a landmark of modern experimental neutrino physics.

A second avenue is offered by cosmological observations. Neutrinos contribute to the energy density of the universe and influence the formation of large-scale structure. Their masses suppress small-scale clustering and alter the evolution of density perturbations, leaving measurable imprints on the cosmic microwave background. Recent results from Planck, combined with baryon acoustic oscillation and lensing data, constrain the sum of neutrino masses to $\sum m_\nu \lesssim 0.12$ eV [36].

A third and more indirect method involves $0\nu\beta\beta$. If neutrinos are Majorana particles, this process could occur in certain nuclei, providing sensitivity to the effective Majorana mass $m_{\beta\beta}$—a coherent sum over neutrino masses weighted by the elements of the PMNS matrix and potential Majorana phases. Experiments that target neutrinoless double beta decay will be explained in more details in the next subsection.

Together, these approaches offer synergistic insight into the absolute neutrino mass scale and its ordering. A consistent picture across all three methods would help distinguish between normal and inverted hierarchies and test the degree to which neutrino masses are hierarchical, quasi-degenerate, or indicative of physics beyond the minimal three-flavour framework.

1.6.4 Majorana or Dirac Nature

A fundamental open question in neutrino physics is whether neutrinos are Majorana or Dirac particles. If neutrinos are Majorana, they are identical to their antiparticles, and lepton number is violated. The most sensitive experimental probe of this is $0\nu\beta\beta$. Observation of this process would unambiguously confirm the Majorana nature of neutrinos,

establish lepton number violation, and provide information on the absolute neutrino mass scale through the effective Majorana mass term $m_{\beta\beta}$.

Several next-generation experiments are actively pursuing this goal with increasing sensitivity. Among these, the NEXT (Neutrino Experiment with a Xenon TPC) program [25] offers a particularly promising approach, employing high-pressure xenon gas time projection chambers to combine excellent energy resolution with topological reconstruction of electron tracks. This capability provides powerful background rejection, a key requirement in $0\nu\beta\beta$ searches. NEXT is designed to search for $0\nu\beta\beta$ in ^{136}Xe with sensitivity to half-lives beyond 10^{26} years, and its modular design allows for scalable upgrades toward ton-scale detectors in future phases.

Other leading experiments include Large Enriched Germanium Experiment for Neutrinoless $\beta\beta$ Decay (LEGEND) [37], which uses high-purity germanium detectors enriched in ^{76}Ge; CUORE Upgrade with Particle IDentification (CUPID) [38], a bolometric detector targeting ^{100}Mo; and next Enriched Xenon Observatory (nEXO) [39], a proposed liquid xenon Time Projection Chamber (TPC) also studying ^{136}Xe. Although no confirmed observation of $0\nu\beta\beta$ has yet been made, these efforts are rapidly advancing the experimental frontier and will play a crucial role in determining the Majorana or Dirac nature of neutrinos in the coming decade.

1.6.5 Sterile Neutrinos and Anomalies

Beyond the established three-flavour framework, several short-baseline anomalies and cosmological tensions have motivated the hypothesis of sterile neutrinos—additional neutral fermions that do not interact via the weak force but can mix with active neutrinos. Although Liquid Scintillator Neutrino Detector (LSND) [40] and Mini Booster Neutrino Experiment (MiniBooNE) [41] observed excess events consistent with sterile

neutrino oscillations at the ∼1 eV scale, subsequent searches by Micro Booster Neutrino Experiment (MicroBooNE) have not confirmed these signals [42], leading to tension in global fits. New precision efforts, such as the Fermilab Short-Baseline Neutrino (SBN) program [43], aim to conclusively address this possibility.

1.6.6 Unification and High-Energy Implications

The smallness of neutrino masses may be a low-energy window into physics at much higher scales, such as grand unification or string theory. Many seesaw models operate at scales near 10^{14} GeV, suggesting that neutrinos could serve as a bridge to otherwise inaccessible energy regimes. Although these connections remain speculative, they provide theoretical motivation for studying the flavour structure of the neutrino sector and the pattern of mixing angles.

1.6.7 Conclusion and Outlook

Neutrinos remain among the most enigmatic particles in the Standard Model. Addressing the open questions outlined in this chapter—such as the mass ordering, CP violation, absolute mass scale, and Majorana nature—requires a comprehensive experimental program spanning reactor, solar, atmospheric, and accelerator-based neutrino sources.

Among these efforts, DUNE is uniquely positioned to deliver decisive answers to some of those questions. With its long-baseline configuration, precision Liquid Argon Time Projection Chamber (LArTPC) detectors, and high-intensity neutrino beam from Fermilab, DUNE will probe CP violation, resolve the mass ordering, and test the three-flavour paradigm with unprecedented sensitivity. Moreover, its capabilities ex-

tend beyond oscillation physics, offering the potential to detect supernova and solar neutrinos, search for proton decay, and explore beyond-Standard-Model phenomena.

The next chapter introduces the DUNE experiment in detail, outlining its scientific goals, experimental design, and anticipated contributions to our understanding of neutrinos and the fundamental structure of the universe.

The whole of science is nothing more than
a refinement of everyday thinking—done together.

Albert Einstein

2

Deep Underground Neutrino Experiment (DUNE)

Some experiments hum quietly in the background of discovery—DUNE, however, begins with a symphony. It is a flagship endeavor in neutrino physics, composed on a scale never before attempted: a beamline stretching 1300 kilometers across the Earth, a network of liquid argon detectors buried deep underground, and an experimental design

crafted to probe some of the most profound unanswered questions in particle physics and cosmology. From the origin of matter's dominance over antimatter, to the ordering of neutrino masses, to the tantalizing possibility of proton decay, DUNE is designed not merely to listen, but to resolve—with clarity, with depth, and with force.

Much like a conductor shaping the dynamics of a performance, DUNE's configuration orchestrates its physics reach: a high-intensity, wide-band neutrino beam generated at Fermilab; a long-baseline trajectory to the Sanford Underground Research Facility (SURF); and precision detection via modular LArTPCs at both ends of the beam line, poised to capture even the faintest traces of interaction. The far detector, with a fiducial mass of 40 kilo-tons (ktons) of liquid argon, offers the scale necessary to collect rare events with high statistical power. This design enables DUNE to disentangle the overlapping melodies of CP violation and matter effects—unraveling the subtle interplay of neutrino oscillations.

Within the global symphony of neutrino research, DUNE contributes a distinctive and resonant movement. Alongside complementary experiments such as Hyper-Kamiokande and JUNO, it distinguishes itself through its extended baseline and high-resolution imaging capabilities. These features enable a diverse physics program, spanning precision oscillation measurements, astrophysical neutrino detection, and searches for physics beyond the Standard Model.

This chapter provides an overview of DUNE's scientific goals, experimental design, and core technologies, with particular emphasis on the modular architecture of the Far Detector (FD) and the role of the Anode Plane Assemblies (APAs) in the first detector module. The APA-based design establishes the foundation for the following chapters, which delve into the quality assurance protocols and the ongoing development of advanced readout systems that build upon this technological framework.

2.1 Physics of DUNE

Two primary objectives of DUNE are to establish the neutrino mass ordering and to investigate the existence of CP violation in the leptonic sector, both achieved through high-precision measurements of neutrino oscillation parameters. These goals are instrumental in testing the three-flavor neutrino oscillation paradigm and in furthering our understanding of the fundamental symmetries governing particle interactions.

Beyond these core objectives, DUNE's scientific program encompasses a broad spectrum of studies. This includes measurements of low-energy neutrinos from supernova burst and the sun, and searches for physics beyond the Standard Model (BSM), such as proton decay, and dark matter interactions. Furthermore, the Near Detector (ND) will facilitate a complementary physics program, enabling precise measurements of neutrino cross sections and nuclear effects.

To realize these objectives, DUNE leverages simultaneous fitting of the energy spectra of neutrinos and antineutrinos ($\nu_\mu \to \nu_\mu$, $\bar{\nu}_\mu \to \bar{\nu}_\mu$, $\nu_\mu \to \nu_e$, $\bar{\nu}_\mu \to \bar{\nu}_e$) detected in FD. This approach allows for concurrent determination of all relevant oscillation parameters, with specific spectral features through the asymmetry between neutrino and antineutrino appearance.

2.1.1 Beamline Physics

At the heart of DUNE's long-baseline oscillation program is its ability to leverage a high-intensity (1.2 MW, planned to be upgraded to 2.4 MW), wide-band neutrino beam directed over a 1300 km baseline from Fermilab to the FD at SURF. This baseline is deliberately optimized to span both the first and second oscillation maxima, as illustrated in Figure 2.1, thereby enhancing sensitivity to subdominant effects such as CP violation

and matter-induced asymmetries. The combination of long baseline and broad energy coverage allows DUNE to probe the fundamental parameters governing neutrino flavor transformation with unprecedented precision.

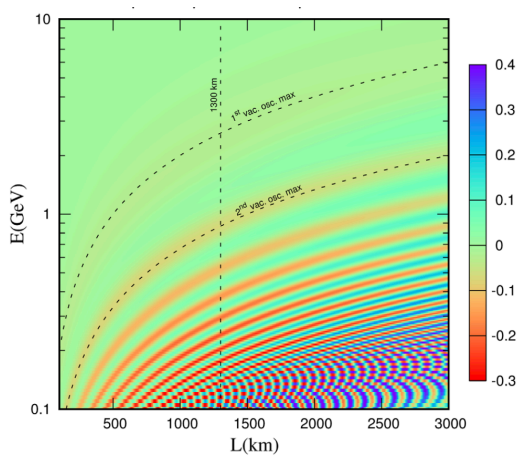


Figure 2.1: Difference in $\nu_\mu \to \nu_e$ oscillation probability between $\delta_{\text{CP}} = +\pi/2$ and $\delta_{\text{CP}} = -\pi/2$ as a function of baseline (L) and neutrino energy (E), highlighting CP violation sensitivity regions. The dashed curves indicate the locations of the first and second vacuum oscillation maxima. Figure adapted from [44].

A critical feature of DUNE's design is its sensitivity to matter effects, arising from coherent forward scattering as neutrinos propagate through Earth's crust. These interactions modify the effective oscillation probabilities, enhancing or suppressing the $\nu_\mu \to \nu_e$ appearance channel depending on the neutrino mass ordering and beam mode (neutrino or antineutrino). This intrinsic asymmetry provides a robust handle for determining whether the mass ordering follows the normal or inverted ordering. Figure 2.2 demonstrates the distinct energy-dependent behavior of neutrino and antineutrino appearance probabilities under varying values of the CP-violating phase δ_{CP}.

DUNE's dual-mode beam operation is essential for disentangling matter-induced asymmetries from intrinsic CP-violating effects governed by δ_{CP}. By precisely measuring both appearance and disappearance channels across a wide energy spectrum,

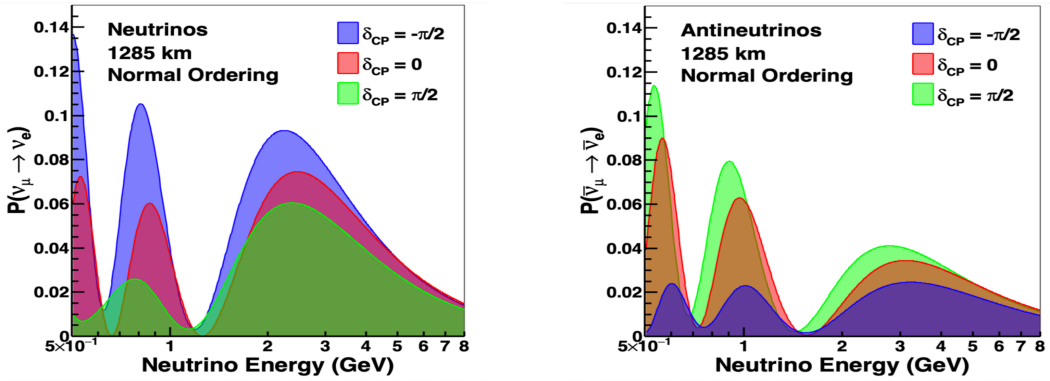


Figure 2.2: Oscillation probabilities $P(\nu_\mu \rightarrow \nu_e)$ (left) and $P(\bar{\nu}_\mu \rightarrow \bar{\nu}_e)$ (right) as functions of neutrino energy for a baseline of 1285 km under normal mass ordering. The bands correspond to representative values of $\delta_{CP} = -\pi/2$ (blue), 0 (red), and $\pi/2$ (green), illustrating the interplay between CP violation and matter effects.[45]

DUNE can resolve parameter degeneracies that have limited the sensitivity of previous experiments.

This capability translates into a world-leading sensitivity to both the neutrino mass ordering and leptonic CP violation. As shown in Figure 2.3, DUNE is projected to determine the mass ordering with greater than 5σ significance over most values of δ_{CP} within a few years of operation. Figure 2.4 presents the expected significance for establishing CP-violating effects across possible true values of δ_{CP}, demonstrating DUNE's ability to surpass the 5σ discovery threshold for a substantial fraction of parameter space after a decade of operation.

Through this comprehensive approach, DUNE complements shorter-baseline and narrow-band experiments, establishing itself as a cornerstone in the global effort to elucidate the fundamental properties of neutrinos and to explore physics beyond the Standard Model.

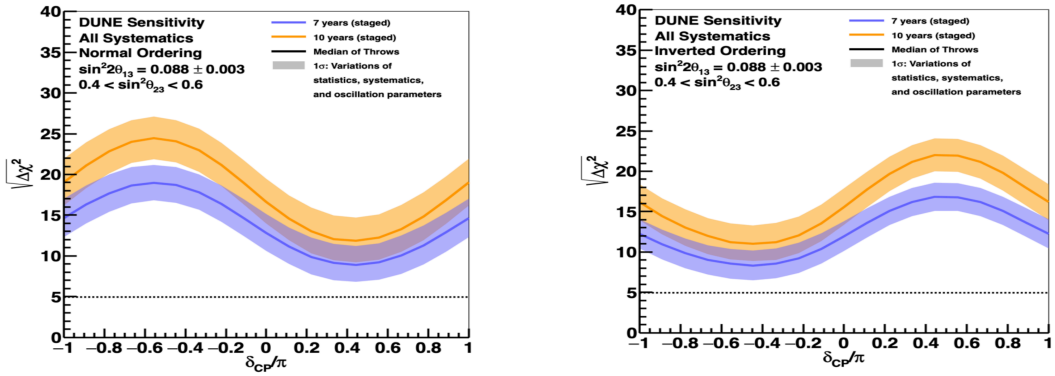


Figure 2.3: Projected sensitivity to neutrino mass ordering as a function of δ_{CP}, assuming (left) normal and (right) inverted mass ordering. The vertical axis shows $\sqrt{\Delta\chi^2}$, with shaded bands indicating 1σ variations due to statistical, systematic, and oscillation parameter uncertainties. Results are shown for 7-year (blue) and 10-year (orange) exposures.[45]

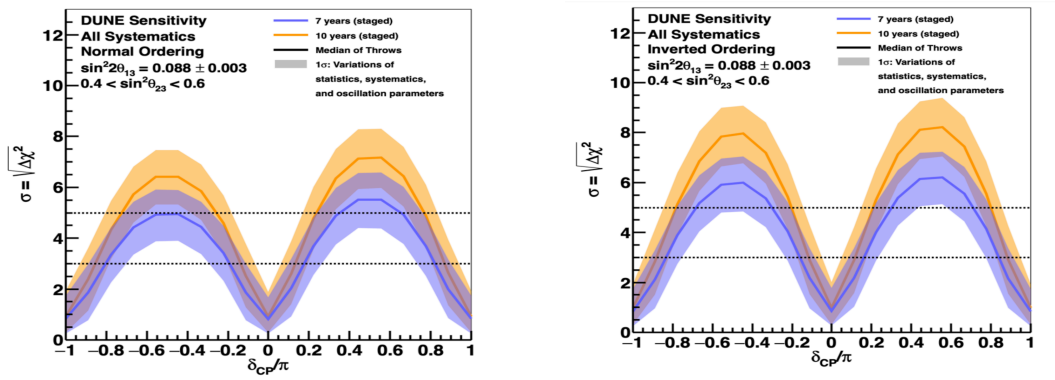


Figure 2.4: Expected sensitivity to leptonic CP violation as a function of δ_{CP}, assuming (left) normal and (right) inverted mass ordering. The vertical axis shows significance $\sigma = \sqrt{\Delta\chi^2}$. Results are shown for staged exposures of 7 years (blue) and 10 years (orange), with shaded bands representing 1σ uncertainties.[45]

2.1.2 Low-Energy Neutrino Physics

In addition to its long-baseline oscillation program, DUNE offers exceptional sensitivity to low-energy neutrinos from astrophysical sources, most notably those emitted during core-collapse supernovae. The 40 kt fiducial mass of liquid argon across the FD modules, combined with fine-grained tracking and calorimetric capabilities, enables DUNE to serve as a premier observatory for galactic supernova neutrinos.

DUNE is uniquely positioned to detect the early burst of electron neutrinos (ν_e) produced during the neutronization phase of a core-collapse event via charged-current interactions on argon:

$$\nu_e + {}^{40}\mathrm{Ar} \rightarrow e^- + {}^{40}\mathrm{K}^*. \tag{2.1}$$

This sensitivity to the ν_e channel complements water Cherenkov detectors, which primarily observe $\bar{\nu}_e$ through inverse beta decay. As a result, DUNE provides critical information on the flavor composition and time structure of the supernova neutrino flux, offering insights into both astrophysical dynamics and neutrino properties under extreme conditions.

While supernova neutrino detection represents a key component of DUNE's low-energy physics program, the experiment also holds potential for observing solar neutrinos through similar interaction channels. Achieving competitive sensitivity in this domain requires enhanced background mitigation strategies, including radiopure detector components, active veto systems, and potentially a dedicated low-threshold module. These prospects are the subject of ongoing research and development within the collaboration.

A detailed discussion of supernova neutrino detection capabilities, including expected event rates and flavor sensitivity, is presented in Chapter 5. Solar neutrino detection

prospects and associated background studies are addressed in Chapter 6.

2.1.3 Physics Beyond the Standard Model

Beyond its primary mission to investigate neutrino oscillations, DUNE serves as a powerful instrument for probing BSM physics. The combination of a large fiducial mass (40 kton), deep underground placement, and high-resolution detection capabilities enables sensitive searches for rare processes and exotic phenomena that could reveal new fundamental physics.

At the forefront of DUNE's BSM program is the search for baryon number violation, most notably through proton decay [46]. GUTs predict that protons are unstable, with favored decay channels depending on the theoretical framework. While water Cherenkov detectors such as Hyper-Kamiokande are optimized for detecting modes like $p \to e^+\pi^0$, DUNE's liquid argon technology offers unique sensitivity to channels involving kaons, particularly $p \to K^+\bar{\nu}$. In this mode, the low-momentum K^+ is invisible in water due to falling below the Cherenkov threshold, but it produces a distinctive, trackable signature in liquid argon. With this capability, DUNE is expected to probe proton lifetimes beyond 10^{34} years for such channels, providing critical complementarity to other global searches.

In addition to baryon number violation, DUNE offers a broad platform to explore other BSM scenarios [46, 47]. Precision measurements of neutrino oscillations allow for tests of the existence of sterile neutrinos, through potential deviations from the three-flavor framework. The experiment's sensitivity to matter effects over its long baseline (1300 km) enables searches for non-standard interactions (NSI) that could alter neutrino propagation in ways not predicted by the Standard Model. Furthermore, DUNE's intense neutrino beam and versatile detection systems create opportunities to search

for signatures of heavy neutral leptons (HNLs) or particles associated with dark sectors, which could manifest through rare interactions in or near the detectors. Through this diverse range of exploratory physics, DUNE extends its impact far beyond precision tests of established neutrino properties, positioning itself as a discovery machine capable of addressing some of the most profound open questions in particle physics.

DUNE's comprehensive physics program—spanning precision measurements of neutrino oscillations, detection of low-energy astrophysical neutrinos, and searches for rare processes and physics beyond the Standard Model—relies critically on its innovative experimental design. The following section outlines the key components of this design, including the neutrino beamline, near detector complex, and the modular liquid argon-based far detector, which together enable DUNE to achieve its ambitious scientific objectives.

2.2 DUNE experiment

The DUNE experiment consists of three main components: a new high-intensity neutrino beam produced at Fermilab, the ND located 574 m downstream of the neutrino source, and the FD situated 1300 km away at SURF. An overview of this long-baseline configuration is illustrated in Figure 2.5. The following section provides a detailed description of each of these components.

2.2.1 Neutrino Beam

The neutrino beam for DUNE is produced by the Long-Baseline Neutrino Facility (LBNF) [49] at Fermilab, which delivers a high-intensity, wide-band beam optimized for long-baseline oscillation studies. Protons accelerated to energies between 60 and

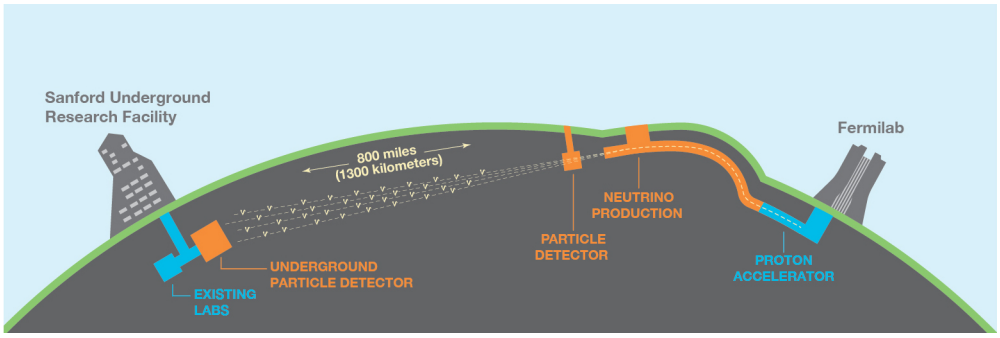


Figure 2.5: Schematic overview of the DUNE experiment. A high-intensity proton beam at Fermilab produces a neutrino beam directed towards the Near Detector complex. The neutrinos then travel 1300 km through the Earth to the Far Detector located deep underground at SURF. Image taken from [48].

120 GeV by the Main Injector are directed onto a graphite target, initiating hadronic cascades that predominantly generate charged pions and kaons. These secondary mesons are focused by a system of pulsed magnetic horns, which select particles of the desired charge to control the neutrino or antineutrino content of the beam. Figure 2.6 illustrates the schematic overview of the beamline configuration.

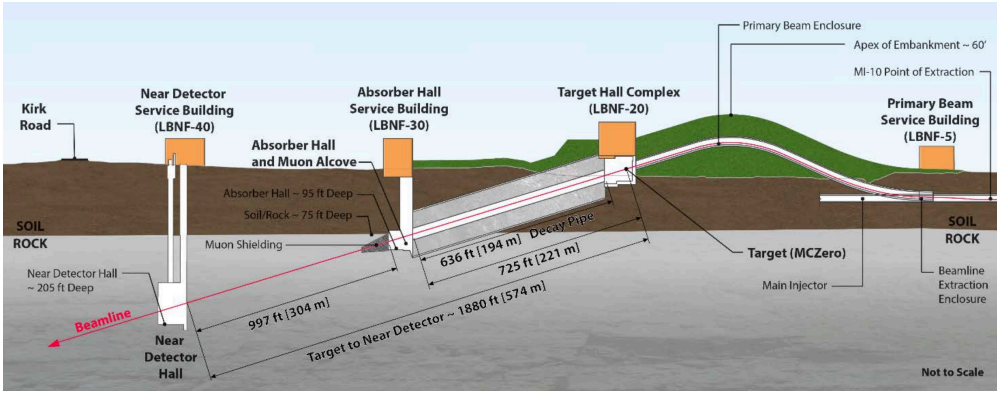
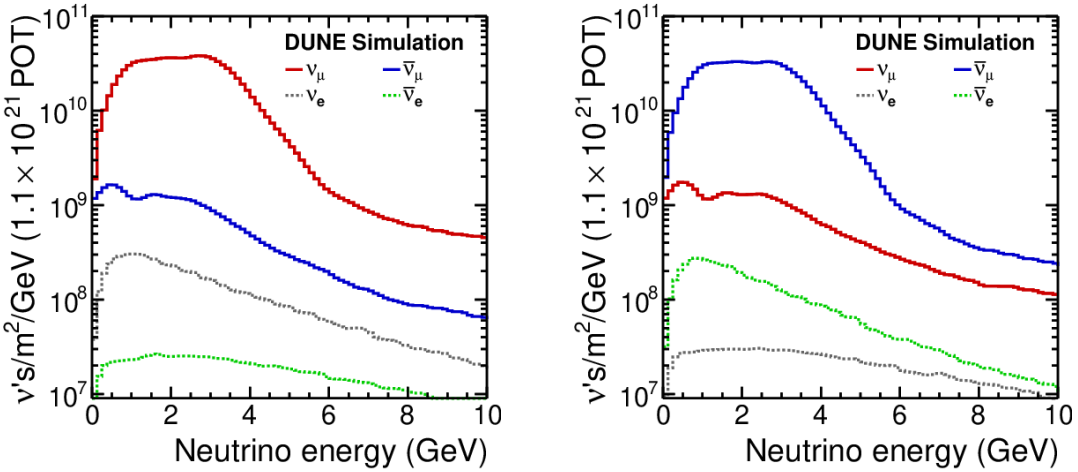


Figure 2.6: Schematic layout of the LBNF beamline at Fermilab. Protons from the Main Injector are extracted and directed to the target station, where meson production and focusing occur. The mesons decay in flight within the decay pipe, producing a neutrino beam that passes through an absorber system before reaching the Near Detector Hall. The configuration supports flexible operation in both neutrino and antineutrino modes. Image taken from [49].

The focused mesons enter a helium-filled decay pipe, where they decay in flight to produce a collimated beam of muon neutrinos or antineutrinos, depending on the horn polarity. Downstream of the decay region, a hadron absorber and shielding system remove residual protons, mesons, and muons, ensuring that primarily neutrinos continue toward the Near and Far Detectors.

The LBNF beamline is designed for flexibility, allowing adjustments to the focusing system and proton energy to tune the neutrino energy spectrum. The default configuration centers the flux around 2.5 GeV, aligning with the first oscillation maximum for the 1300 km baseline, while maintaining a broad energy profile to access both the first and second oscillation maxima. Figures 2.7 illustrate the expected neutrino flux at FD for forward horn current and reverse horn current modes.



(a) Forward Direction **(b)** Reverse Direction

Figure 2.7: Simulated energy spectra of the DUNE beam at the Far Detector for (a) neutrino mode (Forward Horn Current) and (b) antineutrino mode (Reverse Horn Current). The fluxes are shown for muon neutrinos (ν_μ), muon antineutrinos ($\bar{\nu}_\mu$), electron neutrinos (ν_e), and electron antineutrinos ($\bar{\nu}_e$). The beam is optimized to peak near 2.5 GeV, covering both the first and second oscillation maxima.[45]

Comprehensive monitoring systems, including hadron and muon monitors down-

stream of the decay region, provide real-time characterization of the beam profile and intensity. Additionally, ND complex plays a critical role in constraining the initial neutrino flux and composition, enabling precise extrapolation to FD and control of systematic uncertainties in oscillation measurements.

The LBNF beamline has been designed not only to meet the immediate requirements of DUNE's oscillation program but also to accommodate future upgrades, ensuring long-term flexibility for evolving physics goals.

2.2.1.1 Near Detector Complex

The DUNE Near Detector complex plays a pivotal role in constraining systematic uncertainties associated with neutrino flux predictions and interaction cross-sections. Located approximately 574 m downstream of the LBNF target station, the Near Detector characterizes the unoscillated neutrino beam with high precision, providing essential input for extrapolating measurements to FD and enabling accurate determination of oscillation parameters.

To address the diverse challenges of neutrino interaction modeling and flux normalization, ND comprises a suite of complementary subsystems. The primary component, ND-LAr, is a modular liquid argon time projection chamber designed to replicate the target material and detection technology of FD. This ensures that neutrino-argon interactions are studied in an environment closely matched to that of the oscillation measurement, minimizing detector-related biases.

Adjacent to ND-LAr is ND-GAr, a high-resolution gaseous argon (GAr) time projection chamber surrounded by a magnet and calorimeter system. ND-GAr enhances particle tracking, momentum resolution, and charge identification, particularly for low-energy particles and those exiting the ND-LAr volume. This capability is crucial for

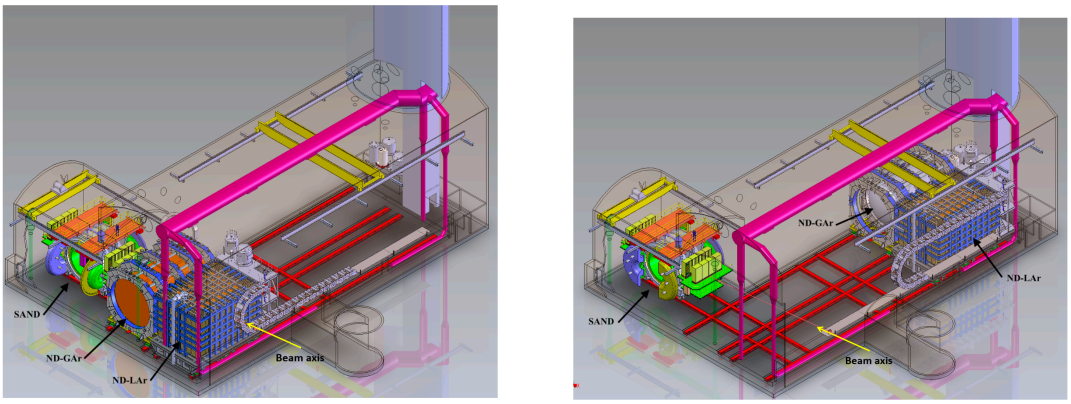


Figure 2.8: Near Detector complex with different configuration. Schematics are shown for the case where ND-GAr and ND-LAr are placed on axis (left), and ND-GAr and ND-LAr are placed off axis (right). Figures taken from [45].

precise reconstruction of complex final states and for studying nuclear effects in neutrino interactions.

Completing the system is System for on-Axis Neutrino Detection (SAND), a permanent on-axis detector that continuously monitors the stability of the neutrino beam during data-taking periods, while ND-LAr and ND-GAr are in off-axis positions.

A distinctive feature of the Near Detector design is the ND-Precision Reaction Independent Spectrum Measurement (PRISM) approach, which allows lateral movement of the ND-LAr and ND-GAr detectors across a range of off-axis positions. By sampling the neutrino beam at different angles, ND-PRISM effectively provides measurements under varying neutrino energy spectra without altering the underlying neutrino interaction kinematics. This technique enables a powerful constraint on the relationship between neutrino energy and observed final states, significantly reducing model dependencies in oscillation analyses. The operational principle of ND-PRISM is illustrated in Figure 2.8, showing how the detectors traverse different off-axis positions to achieve spectral variation.

Together, these components form an integrated system that ensures precise characterization of the neutrino beam and interaction dynamics. ND complex is thus essential to achieving DUNE's goal of high-precision oscillation measurements by providing robust control over the dominant sources of systematic uncertainty.

2.2.2 Far Detector Concept

The DUNE FD, located 1.5 kilometers underground at SURF in Lead, South Dakota, serves as the cornerstone of the experiment's long-baseline oscillation program and rare-event searches. Positioned at the end point of the 1300 km baseline from Fermilab, the FD is designed to observe neutrino interactions after oscillation effects have developed, providing sensitivity to key phenomena such as CP violation, mass ordering, and potential signals of physics beyond the Standard Model. Its deep underground location suppresses backgrounds, further enabling detection of low-energy neutrinos from astrophysical sources and rare-process searches like proton decay.

The FD employs a modular architecture, consisting of four independent cryostats, each housing a LArTPC with a fiducial mass of approximately 10 kilotons. This phased deployment strategy allows for the integration of proven technologies in the initial modules while accommodating innovative designs in later stages as detector Research and Development (R&D) progresses.

A schematic overview of the underground caverns and cryostat infrastructure is shown in Figure 2.9, highlighting the scale of the detector halls and supporting systems. Each cryostat utilizes membrane cryostat technology to contain the vast volumes of liquid argon required for high-statistics neutrino detection, with precision-engineered internal structures to support the TPC components and maintain uniform electric fields over multi-meter drift distances.

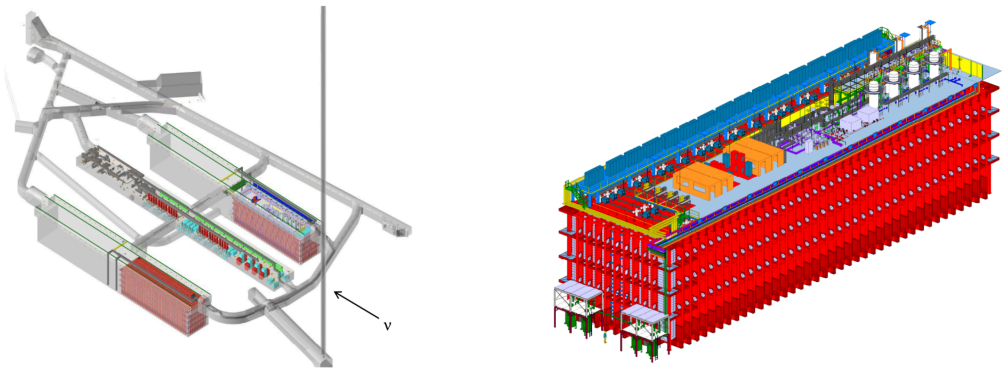


Figure 2.9: Left: Underground caverns for the DUNE Far Detector and cryogenics systems at SURF. The drawing shows the cryostats (red) for the first two FD modules at the 4850-foot level. Right: Schematic of a cryostat housing a 10 kt FD module, illustrating scale and supporting infrastructure.[50]

While all four modules share the foundational LArTPC detection principle, their specific implementations reflect a trajectory of technological evolution. The first module adopts a single-phase horizontal drift design utilizing APAs, providing a robust and well-characterized starting point. The second module introduces a vertical drift configuration with Charge Readout Planes (CRPs), aimed at increasing active volume, enhancing mechanical efficiency and exploring alternative readout geometries. The configurations for the third and fourth modules remain under active development, with ongoing R&D investigating advanced concepts such as pixel-based charge readout and further optimization for low-energy neutrino detection.

This modular and adaptive design philosophy ensures that DUNE not only addresses its immediate physics goals but also remains flexible to incorporate emerging technologies. The core detection technique—LArTPC—is discussed in detail in the following section, providing the basis for understanding the implementation strategies adopted across the Far Detector modules.

2.3 LArTPC

LArTPC [51, 52] represents a transformative advancement in neutrino detection technology, offering unprecedented spatial resolution, calorimetric precision, and topological event reconstruction. Originating from the time projection chamber concept introduced by David Nygren [53], the adaptation of this technique to cryogenic liquid argon has enabled detectors that combine large active volumes with fine-grained imaging—capabilities essential for addressing modern challenges in neutrino physics and rare-event searches.

The choice of liquid argon as a detection medium is driven by its uniquely favorable physical properties, as well as its availability and affordability. Its high density allows for compact, fully active detectors with substantial target mass, while its chemical inertness and noble gas electron structure ensure excellent charge transport characteristics. Moreover, argon's intrinsic scintillation properties provide a complementary optical signal, enhancing timing resolution and background discrimination. These attributes collectively position LArTPCs as ideal instruments for detailed studies of neutrino interactions, precision oscillation measurements, and searches for processes beyond the Standard Model.

Over the past two decades, LArTPC technology has matured through a series of experimental milestones, including Imaging Cosmic And Rare Underground Signals (ICARUS) [54], Argon Neutrino Teststand (ArgoNeuT) [55], and MicroBooNE [56], demonstrating both the feasibility and scientific potential of this approach. Building on this foundation, large-scale implementations such as ProtoDUNE [57] have validated the scalability of LArTPCs to multi-kiloton detectors, paving the way for their central role in next-generation experiments like DUNE.

The subsequent sections explore the fundamental operating principles of LArTPCs, their capabilities in particle identification, and their place within the broader landscape of neutrino detection technologies.

2.3.1 Operating Principles of LArTPCs

When a charged particle traverses liquid argon, it interacts with a high-density medium (1.4 g/cm^3), providing a relatively high probability of interaction within a relatively compact detector volume—an essential feature for neutrino detection. Along its path, the particle ionizes the argon atoms, liberating electrons, and excites atoms, leading to the formation of excimers. The decay of these excimers produces abundant scintillation photons in the vacuum ultraviolet (VUV) range, predominantly at 128 nm. Importantly, liquid argon is transparent to its own scintillation light, allowing these photons to propagate over large distances without significant attenuation. Efficient detection of prompt scintillation light is critical for determining the absolute interaction time (t_0), which in turn enhances spatial resolution along the drift axis.

An externally applied uniform electric field—500 V/cm in DUNE—guides the liberated ionization electrons toward the anode. This is made possible by argon's high dielectric strength, which allows stable operation under strong electric fields without risk of electrical breakdown. A critical factor enabling precise charge transport in liquid argon is its noble element nature. As a noble element, argon possesses a fully filled outer electron shell, making it chemically inert and highly resistant to forming bonds or attracting free electrons. This closed-shell configuration ensures that ionization electrons generated by traversing particles are not readily captured by argon atoms themselves. Instead, in ultra-pure conditions, these electrons can drift freely over several meters without significant loss. This property is fundamental to achieving long electron drift

distances in LArTPCs. Unlike materials with partially filled electron shells or polar molecules, where free electrons could be easily captured or scattered, argon provides an environment where the ionization charge remains intact, preserving detailed spatial and calorimetric information throughout the drift. However, because even trace amounts of electronegative impurities can disrupt this ideal behavior, rigorous purification is essential to fully exploit argon's electron-preserving characteristics.

The ionization electrons are subsequently collected or induce signals on finely segmented readout structures. In single-phase designs, such as those employing APAs shown in Figure 2.10, the anode consists of multiple layers of wires oriented at distinct angles (e.g., U, V, and X planes). This configuration captures several two-dimensional projections of the ionization pattern. By combining these projections with the measured drift time—referenced to the prompt scintillation light signal (t_0)—the full three-dimensional trajectory of the charged particle can be reconstructed with millimeter-scale precision. Alternative designs, such as CRPs in vertical drift configurations, employ segmented electrodes arranged at multiple orientations to achieve the same fundamental reconstruction principle.

Through this combination of high-density target material, long-range charge transport, precise spatial readout, and optical detection, LArTPCs function as fully active, high-resolution detectors capable of detailed event imaging. Figure 2.10 illustrates the working principle of LArTPC described above.

In addition to these core operational features, LArTPCs inherently provide strong particle identification capabilities. The fine-grained tracking, combined with measurements of energy loss per unit length (dE/dx) and event topology, enables effective differentiation between particle species. This includes the ability to distinguish electrons from photons originating in the neutrino interaction, such as those from π^0 decay, as

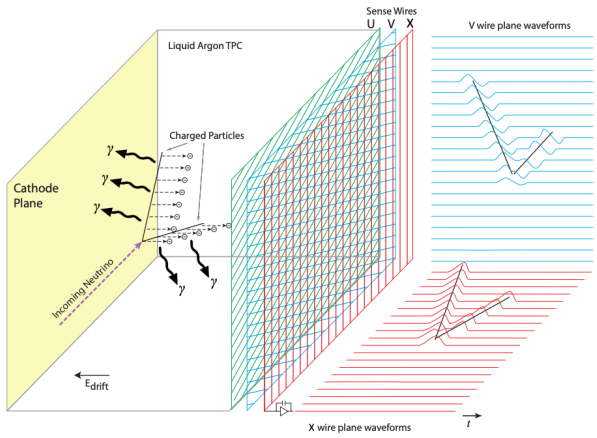


Figure 2.10: Schematic of APA operation in a single-phase LArTPC. Ionization electrons drift toward the APA under an applied electric field, inducing signals on the U and V wire planes before being collected on the X plane. The resulting waveforms (right) provide multiple two-dimensional projections, which, combined with drift time, enable full 3D reconstruction of charged particle trajectories.

well as to identify stopping protons via Bragg peak signatures and reconstruct complex hadronic final states. These intrinsic strengths are critical for reducing backgrounds in neutrino oscillation analyses and enhancing sensitivity to rare processes such as proton decay. While detailed reconstruction techniques lie beyond the scope of this overview, the role of LArTPCs in delivering precise event characterization remains central to their application in modern neutrino physics.

While LArTPCs offer a unique combination of fine-grained tracking, calorimetry, and particle identification within a fully active volume, they represent one approach within a broader landscape of neutrino detection technologies. Among these, Water Cherenkov detectors—such as Super-Kamiokande and its successor Hyper-Kamiokande —have played a foundational role in neutrino physics for decades. The complementary strengths and design philosophies of LArTPCs and Water Cherenkov detectors illustrate

how diverse experimental strategies are employed to address overlapping and distinct scientific goals. A comparative perspective highlights not only the motivations behind DUNE's adoption of LArTPC technology, but also how it fits within the global effort to advance neutrino research.

2.3.2 Advantages for Neutrino Physics

In the landscape of modern neutrino detection technologies, two approaches have emerged as dominant and complementary: Water Cherenkov detectors, exemplified by experiments such as Super-Kamiokande and Hyper-Kamiokande, and LArTPCs, as adopted by DUNE. Each technology offers distinct strengths, shaped by its underlying detection principles and optimized for different physics goals.

Water Cherenkov detectors operate by capturing Cherenkov light emitted when charged particles exceed the speed of light in water, with photomultiplier tubes (PMTs) lining the detector volume to record these signals. This method enables the construction of massive, cost-effective detectors with excellent sensitivity to high-energy neutrinos and clean identification of simple event topologies, such as single-ring muon or electron events. Hyper-Kamiokande, for example, leverages this capability with a fiducial mass exceeding 200 kilotons to pursue studies of atmospheric neutrinos, proton decay, and astrophysical sources.

In contrast, LArTPCs provide fine-grained, three-dimensional imaging through the detection of ionization charge and scintillation light within a dense, fully active liquid argon volume. This enables precise reconstruction of complex interaction topologies, detailed calorimetry, and robust particle identification—particularly in distinguishing electrons from photons, a critical feature for reducing neutral current π^0 backgrounds in ν_e appearance measurements. Furthermore, LArTPCs excel in tracking hadronic

final states, offering superior energy resolution and deeper insight into neutrino-nucleus interaction dynamics compared to the more integrated light signals of Water Cherenkov detectors.

While Water Cherenkov detectors benefit from scalability to extremely large volumes and low-energy thresholds suited for detecting solar neutrinos and certain proton decay modes (e.g., $p \to e^+\pi^0$), LArTPCs are optimized for precision studies where detailed event reconstruction is essential. The intrinsic timing from scintillation light, combined with millimeter-scale spatial resolution, allows effective background rejection and makes LArTPCs particularly powerful for both accelerator-based programs and rare-event searches.

For DUNE, the adoption of LArTPC technology is driven by capabilities such as precision measurements of oscillation parameters, sensitivity to CP violation, determination of neutrino mass ordering, and searches for proton decay modes favored by Grand Unified Theories—such as $p \to K^+\bar{\nu}$—all benefit from the detailed imaging and calorimetric performance that LArTPCs provide. Moreover, DUNE complements global efforts, such as Hyper-Kamiokande, by offering a contrasting detection strategy that broadens the overall sensitivity of the neutrino physics community.

A summary comparison of the key features of Water Cherenkov detectors and LArTPCs is presented in Table 2.1, highlighting how each technology addresses distinct aspects of neutrino detection.

2.4 Implementation in DUNE: Far Detector Modules

The modular design of the DUNE FD reflects a strategic approach to balancing technological maturity with innovation. While all four modules share the foundational

Feature	Water Cherenkov Detectors	Liquid Argon TPCs
Detection Principle	Cherenkov light emission detected by PMTs	Ionization charge drift and scintillation light detected via charge readout and photodetectors
Typical Medium	Ultra-pure water	Ultra-pure liquid argon
Spatial Resolution	∼10s of cm (limited by PMT coverage and light scattering)	Millimeter-scale precision via charge readout
Calorimetry	Indirect (based on total light yield)	Direct measurement via ionization charge (dE/dx)
Particle Identification	Effective for simple topologies (muon vs. electron ring separation); limited for complex or hadronic events	Detailed hadronic tracking, complex topology reconstruction
Energy Threshold	∼5–7 MeV (Cherenkov threshold)	MeV-scale, limited by electronic noise and backgrounds
Detector Mass	Highly scalable to 100+ kilotons	Modular scalability; typical modules order of kilotons
Best Suited For	Atmospheric and solar neutrinos, proton decay ($p \to e^+\pi^0$), supernova bursts	Precision oscillation physics, e/γ discrimination, proton decay ($p \to K^+\bar{\nu}$), detailed interaction studies
Examples	Super-Kamiokande, Hyper-Kamiokande	ICARUS, MicroBooNE, ProtoDUNE, DUNE

Table 2.1: Comparison between Water Cherenkov detectors and LArTPCs in neutrino physics applications.

detection principle of LArTPC, each embodies a distinct implementation that leverages advancements in detector engineering, scalability, and performance optimization.

The first module adopts a single-phase horizontal drift configuration based on APAs, representing the most established and well-characterized LArTPC design. The second module, while also using horizontal drift, introduces a vertical drift architecture utilizing CRPs, designed to increase active volume, improve mechanical efficiency, and explore alternative readout geometries. The configurations for the third and fourth modules remain under active development, with ongoing R&D focused on enhancing low-energy sensitivity, background reduction, and advanced charge readout technologies such as

pixel-based systems.

This section details the design philosophies, operational principles, and motivations behind each module, with particular emphasis on the horizontal drift APA-based module, which serves as the technological foundation for DUNE's initial physics program and the focus of subsequent quality assurance (QA) and quality control (QC) efforts discussed in this thesis.

2.4.1 First Module: Anode Plane Assemblies

The first DUNE Far Detector module employs a single-phase LArTPC design with Horizontal Drift (HD), centered around APAs. This configuration, validated through extensive prototyping in experiments such as ICARUS [54], MicroBooNE [56], and ProtoDUNE-SP [57], represents the most mature and reliable implementation of LArTPC technology at scale. Its selection reflects a balance of proven performance, mechanical stability, and scalability—key factors in meeting DUNE's initial physics objectives.

In this design, ionization electrons produced by neutrino interactions drift horizontally over several meters under a uniform electric field of 500 V/cm, directed toward the APA surfaces. Each APA consists of a stainless steel frame supporting a grounded (G) plane followed by three layers of precisely tensioned wires arranged in U, V, and X orientations. The G plane, closest to the drift volume, shapes the local electric field and shields the induction planes from the bulk drift potential, ensuring clean signal formation. The X plane then collects charge directly, while the U and V planes, angled at $\pm 30°$ relative to vertical, register induction signals. This multi-plane architecture captures distinct two-dimensional projections of the ionization pattern. When combined with drift time information—enhanced by scintillation light detection, this enables trajectories to be

reconstructed in three dimensions, as shown in Figure 2.10.

Each APA measures approximately 6 meters in height and 2.3 meters in width. Multiple APAs are tiled to form continuous anode walls within the cryostat, ensuring full coverage of the active volume. Figure 2.11 shows a photograph of a fully assembled APA undergoing inspection, offering a view of an actual production unit.



Figure 2.11: Photograph of a DUNE APA during QA inspection. The APA measures approximately 6 meters in height and 2.3 meters in width. The presence of myself provides a sense of scale, illustrating the modular construction used to tile multiple APAs within the FD cryostat.

To ensure low-noise signal acquisition, the readout electronics are operated within the cryogenic environment. Cold ASICs (Application-Specific Integrated Circuits) mounted directly on the APA frames perform pre-amplification, shaping, and digitization of wire signals, minimizing input capacitance and thermal noise. Embedded within the APA structure, photon detection systems capture scintillation light using wavelength-shifting light guides coupled to silicon photomultipliers (SiPMs), providing the t_0 information

for drift-time-based reconstruction and background rejection.

Mechanical precision is critical to APA performance, particularly in maintaining uniform wire tension to prevent sagging or breakage during thermal cycling and operation. To this end, rigorous QA/QC protocols are implemented throughout production, including wire tension measurements, electrical continuity tests, and structural inspections. Specialized diagnostic tools, such as the Digital Wire Analyzer (DWA), have been developed to enable efficient, high-throughput verification of wire integrity—an aspect explored in detail in the following chapter.

The APA-based single-phase module forms the technological backbone of DUNE's initial deployment, providing a robust, well-characterized platform for precision oscillation measurements, low-energy neutrino detection, and rare-event searches. Its established design not only supports DUNE's early physics program but also serves as a reference point for the evolution of detector technologies in subsequent modules.

2.4.1.1 Second Module: Charge Readout Planes

The second DUNE Far Detector module introduces a single-phase Vertical Drift (VD) LArTPC design utilizing CRPs, marking a significant evolution in detector architecture. By relocating the readout planes to the top and bottom of the cryostat, this configuration increases the active volume relative to the total cryostat volume, while also enhancing scalability and mechanical efficiency. At the same time, it preserves compatibility with the reconstruction principles established in the first module, ensuring continuity in physics performance.

In the VD design, a central cathode divides the detector horizontally, creating two symmetric vertical drift regions where ionization electrons migrate upward and downward under a uniform electric field of approximately 500 V/cm. This field strength

yields the same electron drift velocity as in the horizontal drift configuration of the first module, ensuring comparable charge transport and reconstruction performance. However, achieving this field over the vertical drift distances requires applying a significantly higher cathode voltage—an engineering challenge that represents a technological milestone in large-scale LArTPC design. The vertical layout also reduces the horizontal footprint of the anode planes, enabling a more compact and mechanically stable geometry—an important consideration for multi-kiloton detectors.

At the top and bottom of the active volume, CRPs serve as the charge collection interfaces. Each CRP consists of perforated printed circuit boards (PCBs) embedded with segmented electrodes arranged in three orientations, typically $\pm 30^\circ$ and 90°. Like the APA-based system, this projective readout captures multiple two-dimensional views of the ionization trails left by charged particles. When combined with drift time information—enhanced by scintillation light detection—the full three-dimensional event topology is reconstructed with high precision. This shared reconstruction methodology is consistent in data interpretation across both horizontal and vertical drift modules.

The CRP approach departs from traditional wire-based designs by employing rigid PCB structures, eliminating challenges associated with wire tensioning, sagging, or breakage. Such design choice enhances mechanical robustness, simplify construction, and offer improved uniformity in signal response across large detector areas. Structurally, the CRPs are supported by modular frameworks: the upper CRPs are suspended from the cryostat ceiling, while the lower CRPs rest on posts on the cryostat floor. This arrangement facilitates precise alignment, ease of installation for ProtoDUNE, and long-term mechanical stability within the cryogenic environment. An example of the CRP installation setup is shown in Figure 2.12 shows colleagues alongside the support framework inside the cryostat during installation, providing a view of the full-scale CRP

units.

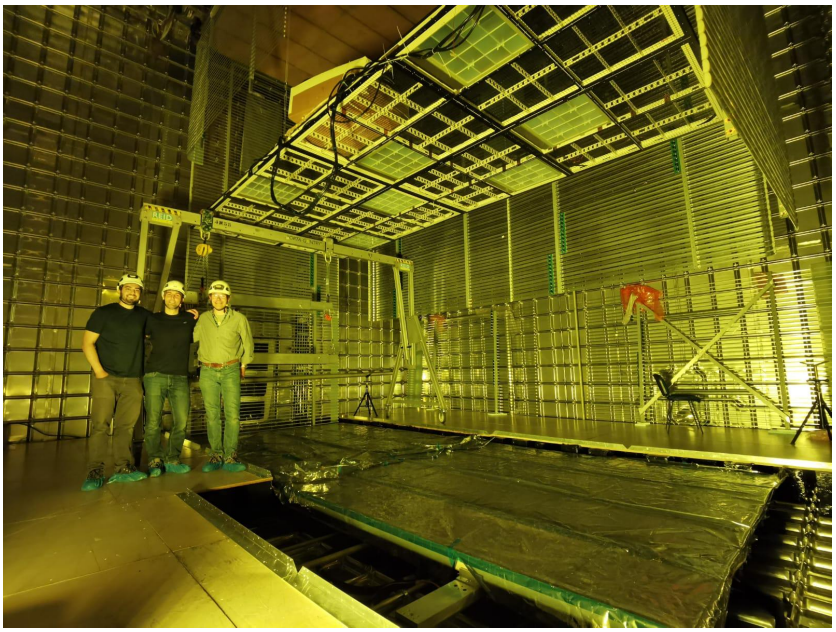


Figure 2.12: Photograph of a full-scale CRP module for the Far Detector. The upper CRP modules are shown suspended from the ceiling structure.

By adopting vertical drift and CRP technology, the second module aims to increase active volume efficiency, streamline large-scale LArTPC construction, and validate alternative readout solutions. These innovations not only contribute to DUNE's diverse physics program—spanning oscillation studies and rare-event searches—but also serve as a testbed for future advancements in liquid argon detector design.

2.4.2 Third and Fourth Modules: Modules of Opportunity

The designs of the third and fourth DUNE Far Detector modules remain deliberately adaptable, reflecting both the rapid evolution of LArTPC technology and DUNE's commitment to integrating advancements that address challenges observed in earlier modules. While the single-phase APA design of the first module provides a stable and

well-characterized foundation, it also exposes inherent limitations of wire-based readout systems—such as high channel density, ambiguities from projective geometries, and difficulties in reconstructing complex or overlapping event topologies. The vertical drift configuration of the second module introduces mechanical and readout improvements but leaves open opportunities for further optimization in areas like pattern recognition, low-energy sensitivity, and large-scale scalability.

Envisioned as "modules of opportunity," the third and fourth modules are intended to serve as platforms for deploying innovative detection technologies aligned with DUNE's expanding physics objectives. A primary focus of ongoing R&D is the development of pixel-based charge readout systems, such as Q-Pix or LArPix, which offer true three-dimensional, self-triggering capabilities. By replacing traditional anode planes with pixelated readouts, these systems aim to eliminate reconstruction degeneracies inherent to two-dimensional projections, enhance spatial resolution, and improve identification of complex event topologies—particularly in dense hadronic environments or low-energy neutrino interactions.

Beyond charge readout advancements, these modules may incorporate enhanced photon detection systems, novel drift configurations, or low-background design strategies to extend DUNE's sensitivity to rare processes and astrophysical neutrino sources. In particular, improved granularity and lower detection thresholds are critical for precision studies of supernova and solar neutrinos, where resolving faint, localized energy depositions can reveal subtle features of neutrino spectra and time profiles.

The third and fourth modules thus represent not only an extension of DUNE's core scientific program but also a strategic investment in the future of LArTPC technology. By serving as testbeds for next-generation detector concepts, these modules will inform the design of future large-scale neutrino experiments, ensuring that DUNE remains at

the forefront of both discovery potential and technological innovation.

While DUNE's FD modules represent a triumph of large-scale engineering, their performance ultimately depends on the precision of individual components. In the first module, APAs must function with the accuracy of a finely tuned instrument, where thousands of wires work in harmony to ensure reliable charge readout. Maintaining this precision requires rigorous QA and QC throughout production. The following chapter introduces the tools and methods developed to meet this challenge, with a focus on the DWA—a system designed to efficiently verify the mechanical and electrical integrity of every APA wire while fabricating and before it takes its place in DUNE's detector ensemble.

Great things are not done by impulse,

but by a series of small things brought together.

Vincent van Gogh

3

Digital Wire Analyzer

A LArTPC is much like a grand instrument, finely tuned to capture the whisper of invisible particles. At its heart, the APA resembles the strings of a harp or a grand piano, where each wire is meticulously engineered to play a crucial role in detecting ionization signals left behind by passing neutrinos. Just as a musician carefully tunes every string to ensure the harmony of a performance, every APA wire must be precisely tensioned and electrically sound to maintain the integrity of the signals. A single mis-

tuned string can distort a melody—likewise, a wire that is improperly setup can interfere with signal reconstruction, compromising the physics data collected by the detector.

To ensure that every string in this neutrino instrument is in perfect condition, rigorous quality control measures are essential. Just as a luthier inspects and tunes each string on a piano before a performance, specialized diagnostic tools are used to verify the tension, continuity, and isolation of every APA wire before installation. These ensure the precision of the detector, so that it is ready to capture nature's most elusive notes —the rare interactions of neutrinos.

3.1 QA/QC of APA

To ensure the reliable operation of APAs described in Subsection 2.4.1, several wire characteristics must be tightly controlled. For instance, the electrical path formed by each wire must remain continuous from the front-end electronics through to its full length. Discontinuities can arise from wire breakage, poor soldering at the readout interface, or interruptions in the PCB trace. Additionally, wires must be electrically isolated from their surroundings to maintain sensitivity to ionization electrons without introducing leakage currents or noise. These properties are typically verified using off-the-shelf instruments such as multimeters.

However, the wire tension—arguably the most critical characteristic—lacks such a convenient measurement tool. If the tension is too high, thermal contraction in liquid argon may cause the wire to snap. Broken wires risk shorting across other layers, which could damage the detector. If the tension is too low, wires may sag under gravity or become susceptible to mechanical vibrations. This leads to distortions in the APA's geometry, resulting in non-uniform electric fields and misreconstruction of particle tracks.

Vibrating wires also introduce additional electronic noise.

Previous studies have determined that an optimal wire tension of 6.86 N balances these effects [58, 56]. This value minimizes breakage during cooldown while limiting sag to less than 0.5 mm for the 5 m-long U and V wires.

The standard method for measuring tension involves exciting the wire and measuring its natural frequency, which is related to tension by

$$T = 4\lambda L^2 {f_0}^2 d, \tag{3.1}$$

where λ is the linear mass density, L is the length, and f_0 is the fundamental frequency. Various excitation techniques have been explored—mechanical [59, 60], electromagnetic [61, 62, 63, 64, 65], and electrical [66, 67, 68, 69, 70, 71, 72, 73].

Currently, the most widely used method is mechanical excitation, with the frequency measured via a laser-reflection system. This method was implemented in the MicroBooNE experiment [59], as shown in Figure 3.1. A laser diode and a photodetector are positioned in a V-shaped configuration, adjacent to each other and angled toward the wire. When the wire is plucked, it vibrates at its natural frequency, modulating the intensity of the reflected laser light captured by the photodetector. The resulting signal is Fourier-transformed, and the resonance frequency appears as a peak, as seen in the right panel of the Figure 3.1. The first and second harmonics are clearly visible.

Although effective, this method is labor-intensive and time-consuming—posing a significant challenge for a detector on the scale of DUNE. Each APA comprises nearly 3000 wires arranged in multiple overlapping planes, amounting to approximately one million wires across the entire experiment [29]. After assembly, wires in inner planes are no longer physically accessible, making laser-based tensioning impractical for full

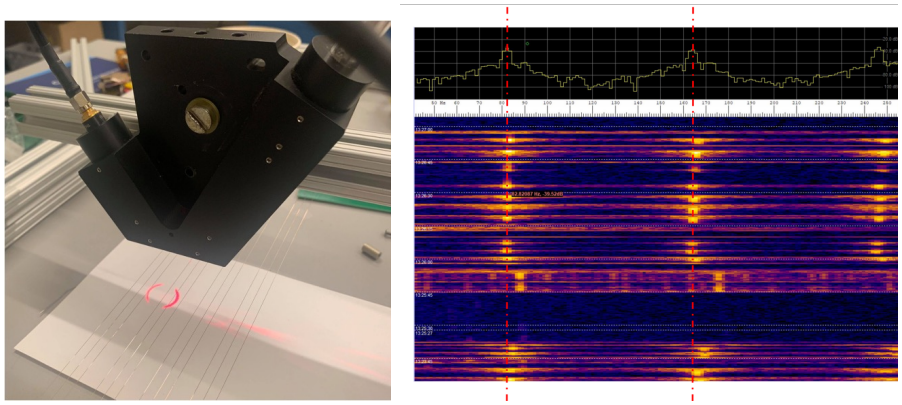


Figure 3.1: Apparatus used for laser-based tension measurement (left) and its Fourier-transformed frequency spectrum (right).

APA quality control.

To address these limitations, the DWA was developed [74]—a digital device capable of simultaneously measuring the tension of up to eight wires, with full automation and minimal operator intervention, both during and after production.

3.2 DWA Principle

In the method employed by the DWA, tested wires are excited via electromagnetic forces, generated by two equally spaced and parallel neighboring wires [75]. These neighboring wires are biased with a combination of alternating current (AC) and direct current (DC) voltages. The applied stimulus voltages can be expressed as

$$V_{\pm}(t) = V_{\mathrm{AC}} \sin(\omega t) \pm V_{\mathrm{DC}}, \tag{3.2}$$

where $\omega = 2\pi f$, and the signs correspond to the two neighboring wires—one is biased with V_+ and the other with V_-. This results in a voltage difference of $2V_{\mathrm{DC}}$ across the

gap between the two stimulus wires, creating a constant electric field at the location of the test wire. Simultaneously, the V_{AC} components capacitively couple to the test wire. Together, these effects produce a time-varying force at frequency f on the test wire.

When the excitation frequency f matches the natural frequency of the wire, the system enters mechanical resonance. The test wire undergoes an amplified oscillatory displacement, which can be modeled as a damped harmonic oscillator. The amplitude of the oscillation near resonance is given by

$$A(\omega) = \frac{A_0}{\sqrt{(\omega_0^2 - \omega^2)^2 + (\gamma\omega)^2}}, \tag{3.3}$$

where A_0 is a constant proportional to the applied driving force—scaling with both V_{AC} and V_{DC} in Equation 3.2. The parameter γ represents a damping coefficient, and $\omega_0 = 2\pi f_0$ is the angular frequency corresponding to the wire's natural frequency. This equation describes the response of a driven, damped harmonic oscillator. The amplitude remains small when the driving frequency ω is either much lower or much higher than the natural frequency ω_0, but it reaches a maximum when $\omega = \omega_0$. At resonance, the expression simplifies to:

$$A(\omega_0) = \frac{A_0}{\gamma\omega_0}, \tag{3.4}$$

highlighting that the peak amplitude is inversely proportional to both the damping coefficient γ and the natural frequency ω_0. A smaller damping factor results in a sharper, more pronounced amplitude peak, which improves the precision with which the resonance frequency—and thus the wire tension—can be extracted. The width of the peak also provides insight into energy loss mechanisms in the wire, such as material damping or mechanical coupling to the support structure. This sharp resonance behav-

ior is crucial to the sensitivity of the DWA, as it enables precise identification of the natural frequency.

As the test wire oscillates transversely between two adjacent stimulus wires, the capacitances between them—denoted $C_+(t)$ and $C_-(t)$—undergo small modulations due to the varying distances. Let the instantaneous displacement of the test wire be described by a sinusoidal function $x(t) = A_\omega \sin(\omega t)$, where A_ω is the oscillation amplitude and ω is the angular frequency. Assuming the amplitude is much smaller than the pitch d separating the wires (i.e., $A_\omega \ll d$), the distance to the right and left stimulus wires becomes $d - x(t)$ and $d + x(t)$, respectively.

For small oscillations, the mutual capacitance between wires can be approximated as inversely proportional to their separation. Expanding $1/(d \pm x(t))$ to first order in $x(t)/d$, the time-varying capacitances become:

$$C_\pm(t) \approx \frac{C}{1 \mp \frac{x(t)}{d}} \approx C\left(1 \pm \frac{x(t)}{d}\right) = C\left(1 \pm \frac{A_\omega}{d}\sin(\omega t)\right), \tag{3.5}$$

where C is the nominal capacitance at the equilibrium distance d. Introducing the dimensionless parameter

$$a(\omega) \equiv \frac{A_\omega}{d}, \tag{3.6}$$

which satisfies $a(\omega) \ll 1$, the capacitance modulation can be written compactly as

$$C_\pm(t) = C\left(1 \pm a(\omega)\sin(\omega t)\right), \tag{3.7}$$

capturing the leading-order effect of the wire's oscillation on the capacitive coupling.

The combination of these time-varying capacitances and voltages induces a current in the test wire. This current, $I(t)$, is the sum of two components from the neighboring

wires, $I_+(t)$ and $I_-(t)$, which is given by

$$\begin{aligned} I_\pm(t) &= \frac{d}{dt}(C_\pm V_\pm) \\ &= \frac{d}{dt}\left[C\left(1 \pm a(\omega)\sin(\omega t)\right)\left(V_{\mathrm{AC}}\sin(\omega t) \pm V_{\mathrm{DC}}\right)\right] \\ &= \frac{d}{dt}\Big[CV_{\mathrm{AC}}\sin(\omega t) \pm Ca(\omega)V_{\mathrm{AC}}\sin^2(\omega t) \pm CV_{\mathrm{DC}} + Ca(\omega)V_{\mathrm{DC}}\sin(\omega t)\Big] \\ &= C\omega\cos(\omega t)\left(V_{\mathrm{AC}} + a(\omega)V_{\mathrm{DC}}\right) \pm 2Ca(\omega)V_{\mathrm{AC}}\omega\sin(\omega t)\cos(\omega t) \\ &= \omega C\cos(\omega t)\left(V_{\mathrm{AC}} + a(\omega)V_{\mathrm{DC}}\right) \pm \omega Ca(\omega)V_{\mathrm{AC}}\sin(2\omega t) \end{aligned} \tag{3.8}$$

and thus,

$$\begin{aligned} I(t) &= I_+(t) + I_-(t) \\ &= 2\omega C\cos(\omega t)\left(V_{\mathrm{AC}} + a(\omega)V_{\mathrm{DC}}\right) \\ &= 2\omega\cos(\omega t) \times a'(\omega) \end{aligned} \tag{3.9}$$

where $a'(\omega)$ represents a composite amplitude factor incorporating the voltage and capacitance dependencies. This induced current I(t) derived in Equation 3.9 is only significant when the drive frequency ω is the wire's resonance. Therefore, it appears as a strong short bipolar waveform in the frequency scan, serving as the key signature for identifying the wire's natural frequency, shown in Figure 3.2.

In practice, the DWA system applies these time-varying voltages to the neighboring stimulus wires and continuously monitors the current induced on the adjacent test wires. The resonance signature is identified by sweeping the frequency and locating the bipolar peak.

To maximize measurement coverage, a minimal repeating unit of four wires is arranged in a specific sequence: a stimulus wire biased at V_+, followed by a test wire, then a stimulus wire biased at V_-, and finally a second test wire. This pattern ensures

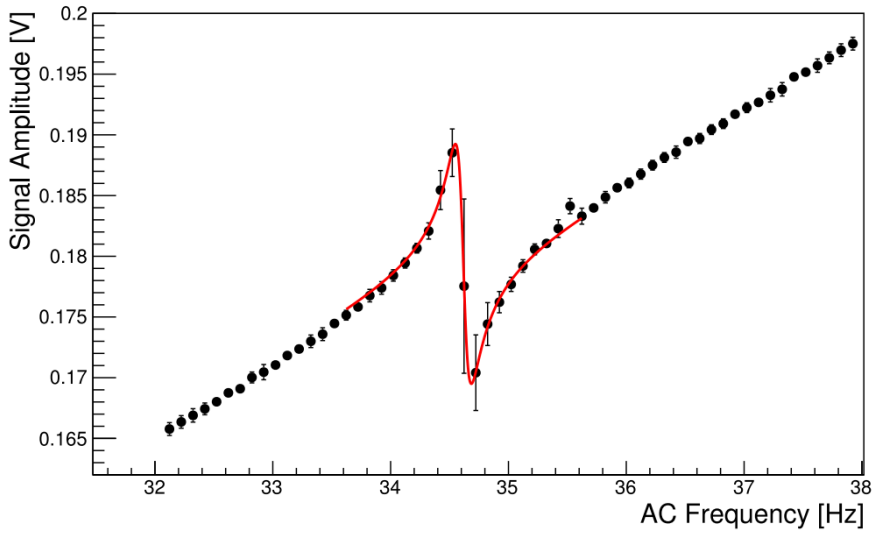


Figure 3.2: Resonance response of a test wire showing a bipolar current peak, fitted with the model described by Equation 3.9. Figure taken from [75].

that each test wire is symmetrically placed between two wires with a $2V_{\mathrm{DC}}$ differential. The method is scalable by reassigning wire roles—stimulus wires can become test wires in subsequent measurements, and vice versa. In this way, all wires on a plane can be sequentially measured without repositioning hardware.

An important feature of this method is that it implicitly verifies both the electrical continuity and isolation of the wires under test. Since the induced current is proportional to the test wire's capacitance—which depends on the effective electrical length—any discontinuity or break in the wire distorts the signal. Similarly, if the test wire is not electrically isolated, its potential may be constrained by an unintended connection to a neighboring wire or ground. Depending on which wires are active in the scan, this can result in an unusually high and flat amplitude across the frequency range or a distorted response lacking a clear resonance peak—both signatures are used to flag isolation failures. As such, the DWA provides a comprehensive diagnostic tool for wire

tension, continuity, and isolation—all without requiring physical access to the wires, offering a significant advantage over previous methods relying on manual multimeter probing.

3.3 DWA Hardware

The DWA system consists of two primary components: the power distribution box (PDB) and the DWA unit (Figure 3.3 left). A flexible flat ribbon cable, known as the flex cable, maintains the electrical connection between the APA and the DWA unit, as shown in the right image of Figure 3.3. The overall system architecture is summarized in Figure 3.4.

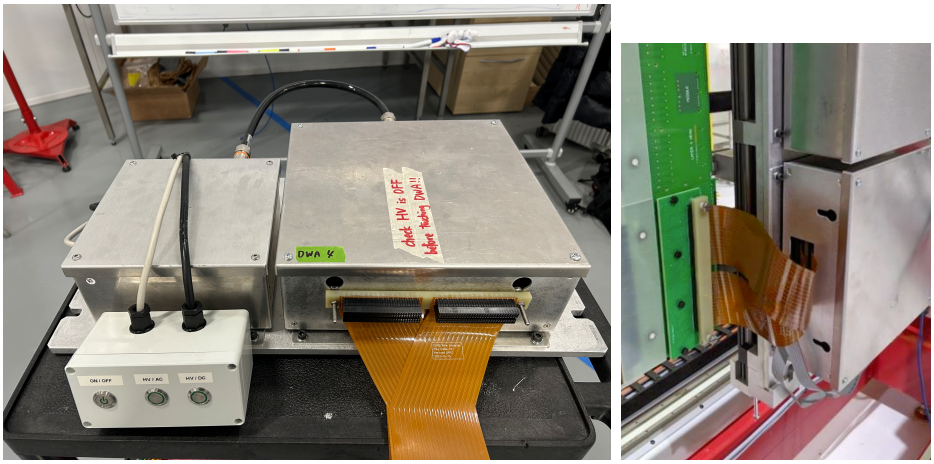


Figure 3.3: Left: Photograph of the DWA unit. The power distribution box (PDB, left), optional remote controller (front left), DWA enclosure (right), and the flex cable emerging from the front of the DWA are visible. Right: Photograph showing the DWA in operation, with the flex cable connecting the DWA to the APA headboard mounted on a vertical test stand.

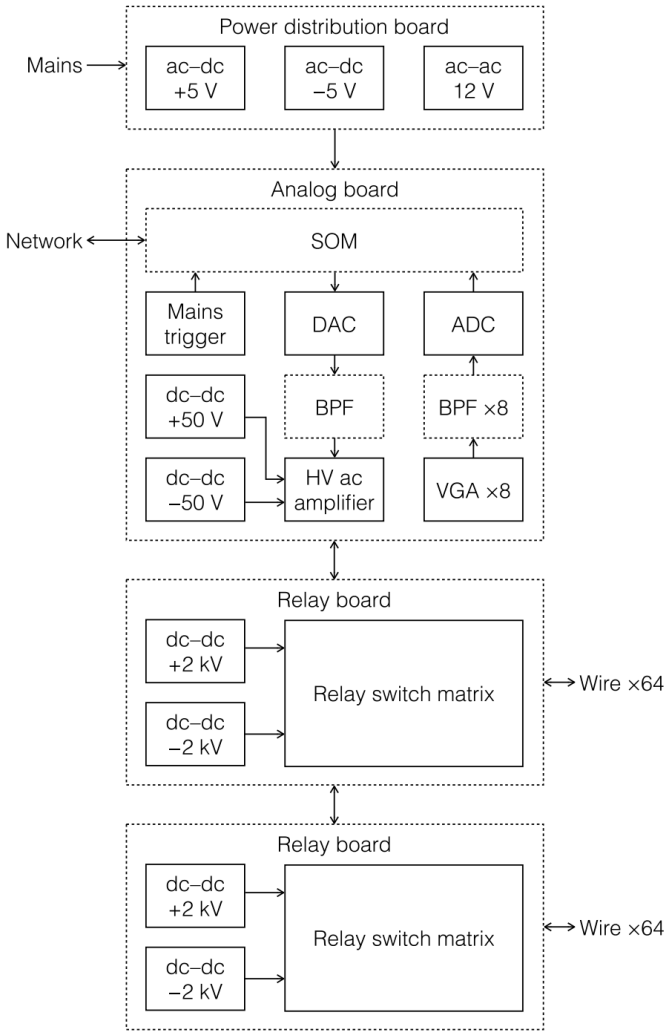


Figure 3.4: System-level block diagram of the DWA. The system consists of a power distribution box, an analog board containing control and signal processing electronics, and multiple relay boards interfacing with the APA wires. Arrows indicate power and signal flow between modules.

3.3.1 Power Distribution Box

The power distribution box houses an AC–DC converter that supplies the necessary power to operate the DWA system, converting mains voltage into regulated ±5 V DC lines. The input voltage is user-configurable for either 120 V or 230 V AC, depending

on regional standards. Three power buttons—controlling the main power, HV DC, and HV AC—are located on the side panel, along with three status LEDs labeled “Network”, “Activity”, and “Error”, which reflect the operational status of the system, as can be seen in Figure 3.5.

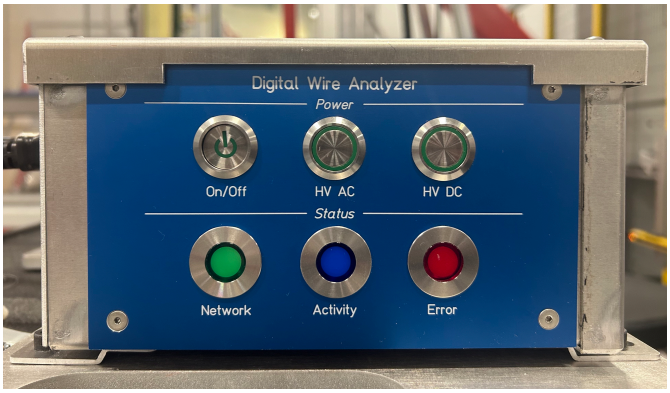


Figure 3.5: Front panel of the power distribution box (PDB) of the DWA system. The top row contains three power buttons for controlling main power, high-voltage AC (HV AC), and high-voltage DC (HV DC). The bottom row displays three status LEDs indicating network connection (green), activity (blue), and system errors (red).

The PDB enclosure functions as a Faraday cage, shielding the electronics from electromagnetic interference produced by the AC power source. An umbilical cable containing 20 individual signal and power lines connects the PDB to the DWA unit, supplying power while also returning system status signals to the PDB to drive user feedback LEDs.

3.3.2 Overview of the DWA Unit

The DWA unit integrates all functional modules required for stimulus generation, routing, measurement, and noise filtering. Internally, it includes the analog board, which generates high-voltage stimulus and processes current responses from the wires; commercial system-on-module (SOM) that integrates the Field Programmable Gate Array

(FPGA), which controls frequency sweeps, signal acquisition, and communication; the bandpass filter (BPF) boards, which isolate signals of interest while rejecting out-of-band noise; and the relay boards, which manage high-voltage routing to and from the APA wires. These components are organized into a compact form optimized for test stand use. Figure 3.6 shows the analog and relay boards used in the system.

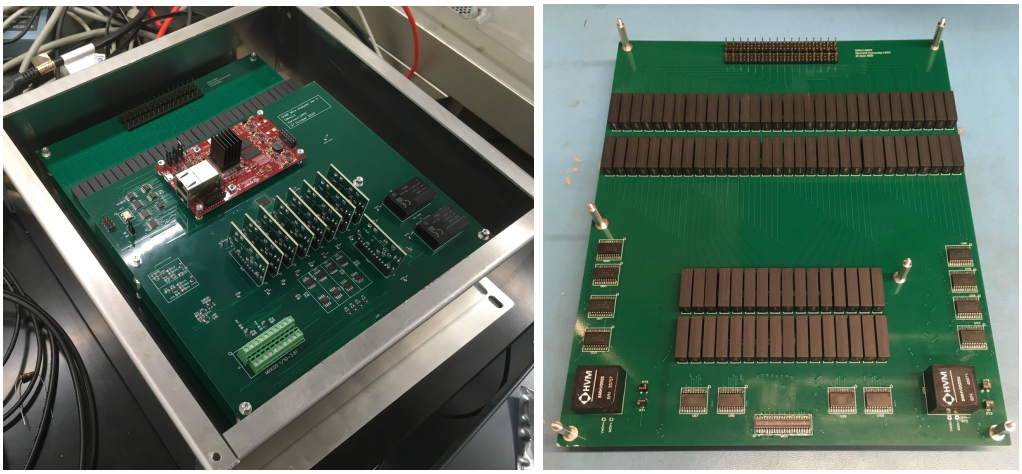


Figure 3.6: Left: photograph of the DWA unit with the top cover removed. The analog board can be seen mounted on top, featuring the red SOM, Avnet MicroZed, hosting FPGA. The vertical daughterboards are the BPF boards. Right: photograph of a DWA relay board. The black rectangular components are high-voltage reed relays that form the switch matrix for routing stimulus and readout signals to APA wires.

3.3.2.1 Analog Signal Generation and Amplification

The analog board serves as the core of the signal chain, handling both stimulus generation and readout amplification. It generates a high-voltage sinusoidal AC signal, which is swept over a predefined frequency range to excite the APA wires under test. The signal generation begins with a square wave produced by a digital-to-analog converter (DAC), which is then shaped into a sine wave using a switched-capacitor on the BPF

with a quality factor of approximately 10. This filtering step is essential for removing harmonics and producing a clean sinusoidal waveform.

The resulting sine wave is amplified using a high-voltage operational amplifier with a fixed gain of 18, powered by DC–DC converters. The use of a high-amplitude AC signal enhances the detectability of the small capacitive currents induced by the vibrating wire, improving the signal-to-noise ratio. Once generated, the amplified signal is passed to the relay boards for routing to the appropriate APA wires.

3.3.2.2 Relay Boards and High-Voltage Switching

The relay boards enable the dynamic switching of the high-voltage stimulus signals and measurement lines. Each relay board can test up to 128 wires by selecting which wires are biased and which are read out, without manual intervention. The stimulus voltages—V_{AC} and $\pm V_{\mathrm{DC}}$—are delivered to the relay boards, where the DC voltages are generated by onboard DC–DC converters powered by a +5 V line. The DC levels are adjustable via potentiometers.

High DC voltages increase the amplitude of the bipolar resonance response, though their upper limit is constrained by the voltage tolerance of connected hardware. For APA testing, the headboards are rated for 500 V in accordance with IPC-2222 [76], and the DWA's $\mathrm{HV_{DC}}$ is set accordingly.

Stimulus voltages are distributed through a switch matrix composed of high-voltage reed relays. These relays offer low open-circuit capacitance (approximately 1 pF), high isolation resistance, and sufficient breakdown voltage, and also include integrated magnetic shielding. These properties minimize crosstalk and allow dense placement on the printed circuit board.

The switch matrix architecture consists of bus relays and wire relays. Each bus line

connects to two bus relays and four wire relays. A relay board contains 16 such bus lines, totaling 32 bus relays and 64 wire relays per board. One of the two bus relays delivers the stimulus voltage (V_+ or V_-), while the other is used to read out the response signal. Each of the four wire relays selects one of the connected wires for routing to the bus. Only one bus relay per line is active at any given time. This structure enables any wire to be assigned as either a stimulus or measurement wire by switching the relays, allowing all wires in the array to be tested through a series of role swaps.

The dynamic switching scheme is illustrated in Figure 3.7, which shows two consecutive relay configurations used to measure alternating groups of wires. In each scan, one set of wires is connected to the variable gain amplifier (VGA) readout while neighboring wires are biased with high voltage to induce motion. The roles are then reversed in the next scan. This structure allows every wire in a densely packed array to be tested using only a limited number of channel lines. On the left side of the Figure 3.7, the relay-level logic shows which relays are active; on the right, the corresponding wire-level connections are visualized, highlighting how the switching pattern enables complete coverage.

3.3.2.3 VGA and Signal Conditioning

Once the current induced on the test wire is routed to the analog board, it is converted to a voltage by a resistor and then amplified using a VGA. The VGA is implemented using an operational amplifier in a non-inverting configuration. A digital potentiometer serves as the feedback resistor, allowing the gain to be adjusted dynamically up to a maximum value of 21. The resistor that converts current to voltage, connected to the inverting input, forms a high-pass RC filter with the inherent capacitance of the wire system. This filter has a cutoff frequency given by $f_c = 1/(2\pi RC)$. If the resonance

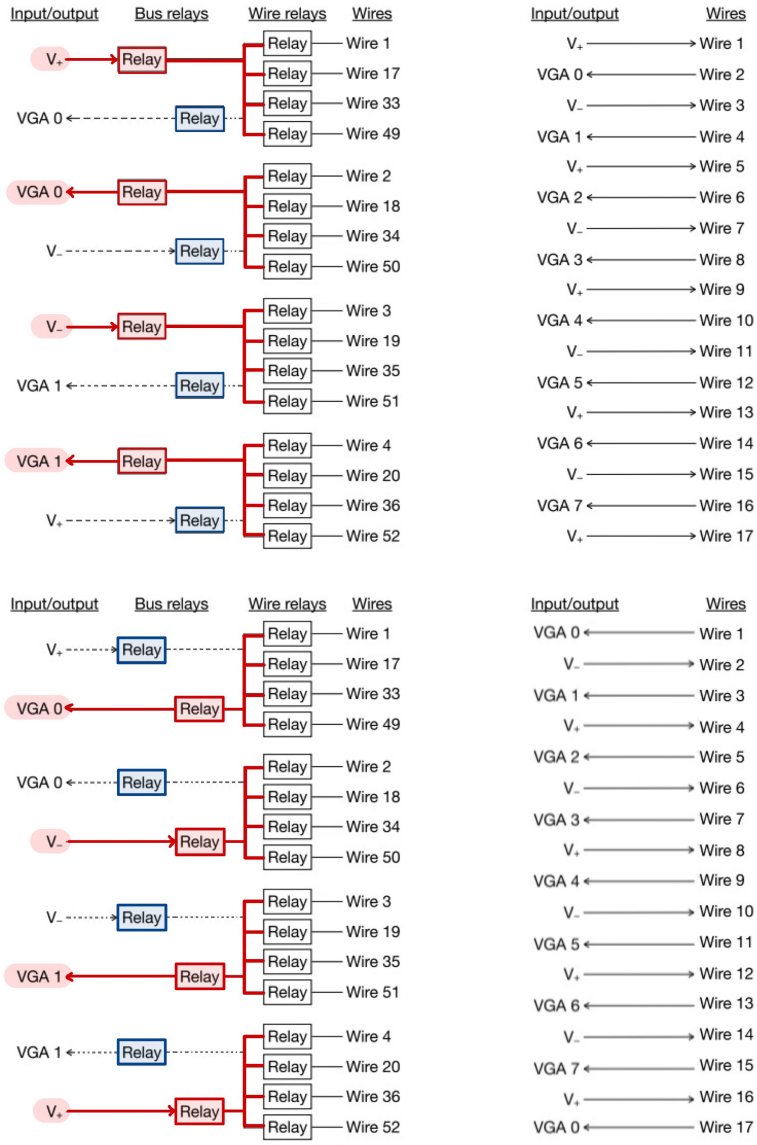


Figure 3.7: Relay switch matrix configurations used in two consecutive DWA scans. Top: The first configuration, where wires such as 2, 18, 34, and 50 are connected to VGA readout channels, and adjacent wires (e.g., 1 and 3) are biased with V_+ and V_- to induce wire motion. Bottom: The second configuration, where roles are swapped: the wires previously biased are now measured, and vice versa. Red lines highlight the active connections formed through bus and wire relays, while blue boxed relays indicate inactive lines. On the right, physical grouping of the first 17 wires are shown for each configuration, with relays omitted. By alternating relay states in this manner, the DWA is able to test all wires while keeping each measured wire sandwiched between two biased neighbors. The diagram is adapted and modified from [74] for clarity.

frequency f_0 of the wire is well below f_c, the signal is heavily attenuated and difficult to detect. Conversely, if f_0 is much higher than f_c, the filter enters a unity-gain regime in which small capacitance variations no longer modulate the gain, rendering the resonance undetectable. To ensure that the resonance signal is both present and amplified, the resistor value is selected based on the expected capacitance of the APA wires.

3.3.3 Noise Filtering and Mains Subtraction

Since APA wires can behave as antennas, the system is susceptible to electromagnetic interference from nearby electrical equipment. To mitigate broadband noise, each of the eight amplified signals from the VGAs is passed through a dedicated bandpass filter. The filtered analog signals are digitized using an eight-channel, 16-bit ADC. These digitized signals are then processed by the SOM, which performs real-time filtering and feature extraction. More details on SOM will be discussed in Section 3.4.

One prominent noise source is the mains voltage, which introduces periodic interference at either 50 Hz or 60 Hz, depending on the region. This is particularly problematic when the mains frequency is close to the resonance frequency being measured. To address this, the firmware includes an active mains noise subtraction (MNS) algorithm. The system uses an AC–AC transformer to step down the mains voltage to 12 V AC. This is then converted into a square wave, providing a synchronized timing reference for noise subtraction. The square wave allows precise phase tracking of the mains interference, enabling the firmware to filter out the corresponding noise components from the digitized data. Further details on the MNS algorithm are presented in Section 3.4.

3.3.4 Connection to APA

The DWA system connects to the APA via two polyimide flex cables—one per relay board (Figure 3.3)—and custom probe boards that interface with the APA headboards (Figure 3.8).

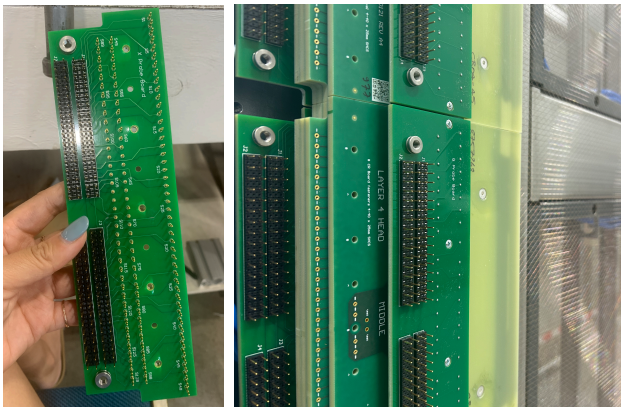


Figure 3.8: Left: photograph of the DWA probe board used to interface with APA headboards. Right: probe boards connected to the APA headboards during testing. The topmost board is the G-layer probe board, attached to its corresponding G-layer headboard. Below it are stacked headboards for the X, U, and V layers, with their shared probe board connected at the bottom.

The X, U, and V layers share a common probe board, while the G layer uses a dedicated one. The flex cables, chosen for their high dielectric strength and flexibility, allow dense high-voltage routing while accommodating various test stand geometries.

3.4 DWA Firmware

The DWA utilizes a commercial SOM, the Avnet MicroZed, which is based on the Xilinx Zynq-7020 system-on-chip (SoC). This SoC integrates a FPGA with a dual-core Advanced RISC Machine (ARM) processor. ARM processors are power-efficient microprocessors designed for high-performance embedded applications. They are based on a Reduced Instruction Set Computing (RISC) architecture, which executes a streamlined

set of instructions to achieve faster processing and lower power consumption compared to Complex Instruction Set Computing (CISC) architectures.

The SOM connects to the DWA hardware through two 100-pin connectors, providing digital control over key components such as the DAC, BPFs, relays, and ADC. Configuration and control commands are transmitted via Ethernet from a laptop to the SOM, enabling remote setup and automation of frequency sweeps and data acquisition. This automation is implemented as a finite-state machine (FSM), where the firmware transitions between a defined set of operational states in response to input conditions.

3.4.1 Measurement Control and Configuration

The firmware running on the FPGA governs the automated measurement process according to a predefined configuration received from the host system. This configuration includes parameters such as the frequency range, frequency step size, and dwell time at each frequency. These values determine the behavior of the relays, the timing of the waveform generation, and the data acquisition protocol. When a sweep is initiated, the relay switch matrix is activated according to the defined sequence, and the stimulus frequency begins at the minimum value. The system then increments through frequency steps until the maximum frequency is reached. The step size directly impacts the frequency resolution and thus the accuracy of the resonance detection.

To ensure accurate signal capture, the firmware allows the user to define the settling time of the wire before each measurement. This ensures that any mechanical ringing from the previous excitation has dissipated before new data is acquired. If this time is too short, residual oscillations can distort the voltage amplitude measured at subsequent frequencies.

The amplitude of the excitation signal is controlled by adjusting the DAC output,

which in turn scales the high-voltage AC amplitude. Meanwhile, the gain of the readout signal is tuned via a digital potentiometer controlling the VGA. The total number of ADC samples collected per frequency step is determined by the product of two configurable values: the number of AC cycles per frequency point, and the number of ADC samples per cycle. This approach allows flexible tuning of data resolution and noise rejection.

3.4.2 Mains Noise Subtraction

In addition to programmable signal control, the firmware also implements an active noise mitigation strategy, MNS, to suppress interference from the 50 Hz or 60 Hz mains voltage. This technique is critical when the stimulus frequency is close to the mains frequency or its harmonics.

The MNS process begins by recording the ambient noise prior to the application of any stimulus voltage. This so-called noise scan is conducted at the beginning of each sweep, and the resulting ADC samples are stored in memory. During the actual measurement, the noise samples are subtracted from the corresponding signal samples in real time. To ensure phase alignment between the noise and signal scans, a trigger signal—described earlier in Section 3.3.2—is used to synchronize both recordings.

To enhance the fidelity of the noise model, the firmware oversamples the mains noise by a factor of 8 relative to the signal sampling rate. This high-resolution noise trace captures small fluctuations more effectively, but it also increases memory usage. To manage this, noise scans are only taken at 1 Hz intervals across the frequency sweep, compared to the $\frac{1}{256}$ Hz step intervals used in the signal measurement. Linear interpolation is used to estimate the noise at intermediate frequencies not directly sampled. This technique reduces the amplitude of the mains noise in the signal by approximately

an order of magnitude.

Figure 3.9 illustrates the effectiveness of the MNS method. In this measurement, no stimulus voltage was applied, and the signal arises entirely from ambient noise filtered by the bandpass filter. The residual noise at the mains frequency is comparable to that of its second harmonic, but remains small enough to avoid interfering with resonance detection.

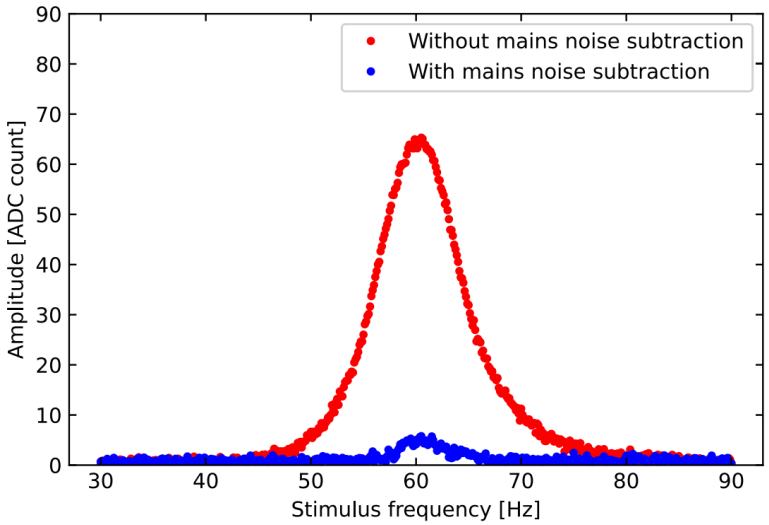


Figure 3.9: Demonstration of the effectiveness of the MNS algorithm. The plot shows the measured amplitude as a function of stimulus frequency without any applied signal voltage, isolating the response due to ambient noise. The red trace shows the result without noise subtraction, exhibiting a strong peak at 60 Hz corresponding to mains interference. The blue trace shows the result after applying MNS, which suppresses the 60 Hz peak by nearly an order of magnitude. This demonstrates the ability of the DWA firmware to significantly reduce environmental noise near the mains frequency, preventing false resonance identification. Taken from [74].

3.5 DWA Software

We have developed custom software to configure the DWA firmware, control scans, receive data, identify wire resonances, and calculate wire tensions. The graphical user

interface (GUI), shown in Figure 3.10, organizes these functions into multiple tabs, each serving a specific purpose.

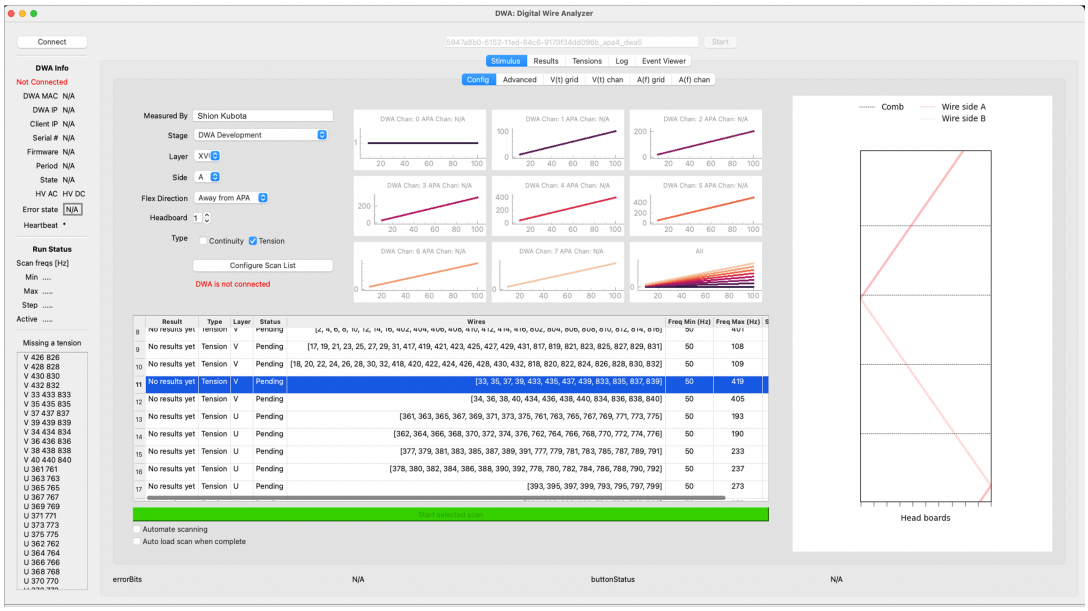


Figure 3.10: Screenshot of the DWA GUI during scan configuration and data collection. The left panel displays real-time status information, including scan progress and missing measurements. The top-center plots show signal evolution for each DWA channel. On the right, a visual representation of the APA headboard layout helps identify which wires are selected. The software also supports automatic scanning and resonance-based tension extraction.

3.5.1 DWA Configuration

Once the GUI is launched and the DWA system is connected via Ethernet, communication is established with the device. Upon successful connection, a green indicator appears as can be seen in the left image of Figure 3.11, and a heart icon in the information tab begins to pulse, signifying an active connection. The interface also displays the connection status and the activation state of high-voltage sources. By default, the green indicators for “HV AC” and “HV DC” are disabled; these only appear when their respective sources are explicitly turned on.

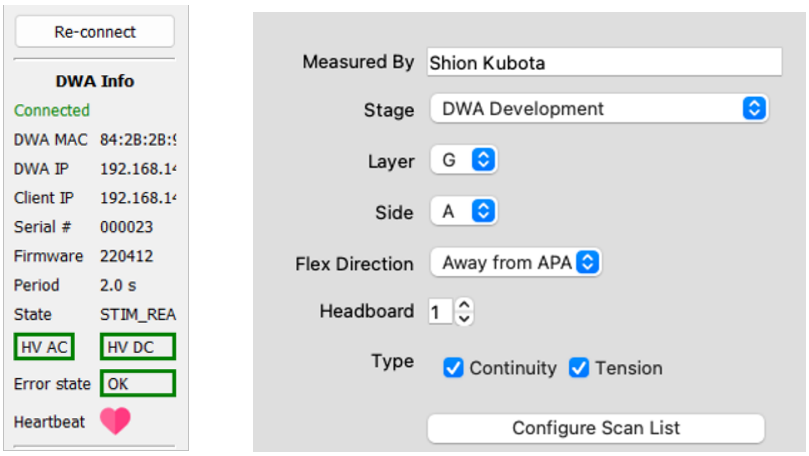


Figure 3.11: Screenshots of the DWA GUI. Left: The information panel confirms successful connection to the DWA system. The green status labels for "HV AC" and "HV DC" indicate that the high-voltage sources are turned on, and the heart icon pulses to reflect active communication. Right: Configuration panel used to define the scan conditions, including APA layer, headboard location, flex cable orientation, and scan types (continuity and/or tension). The example shown here is set for a G layer tension and continuity scan on headboard 1.

Following a successful connection, scan parameters can be entered through the *Stimulus* tab as seen in the right image of Figure 3.11. The user specifies the APA layer, side, and headboard to be tested, and the software internally calculates the wire lengths for each APA channel based on this input. Additionally, the flex cable direction can be specified as "Toward APA" or "Away from APA", depending on its physical orientation. This option is particularly useful when working around faulty relays. By toggling the cable orientation and repeating the scan, two distinct mappings between DWA relays and APA wires can be accessed, increasing fault tolerance in data acquisition.

The scan mode can also be selected depending on the type of measurement. For continuity and isolation tests, a fast scanning mode is available that disables DC high voltage and uses a coarser frequency step. This reduces scan time and is particularly useful for quick validation of electrical connections.

Once configuration is complete, clicking the "Configure Scan List" button generates the scan sequence and updates the interface accordingly.

3.5.2 Data Acquisition and Monitoring

The DWA can measure 8 APA wires per scan. During scan configuration, the full set of APA channels is divided into sequential subsets, each corresponding to a scan. A visual representation of the APA is displayed on the right side of the interface shown in Figure 3.10, where red lines indicate the wires currently under test. Solid lines represent wires on Side A, while dashed lines represent their counterparts on Side B. The horizontal lines represent the comb placed to confine the movement of wires. This visualization updates in real time as scans progress.

Two checkboxes beneath the scan list enable automation: "Automate scanning" begins the next scan in the sequence without user input, and "Auto load scan when complete" loads the corresponding results tab immediately after each scan finishes. These features enhance measurement throughput and streamline user interaction.

The *Stimulus* tab also displays real-time voltage data received via User Datagram Protocol (UDP) from the ADC, plotted for each of the 8 scanned channels across stimulus frequency.

Within the *Results* tab, the *Wires* sub-tab shows outcomes of continuity and isolation tests. Continuity is assessed by comparing measured amplitude to a reference case in which no wire is connected. If the signal profile matches the disconnected case, the wire is likely broken. Isolation is evaluated by checking whether the wire's signal exceeds a threshold level; a large signal suggests coupling to another wire or component.

3.5.3 Resonance Detection and Tension Refinement

For scans designed to measure wire tension, the *Wires* sub-tab also displays the calculated tension for each wire. Identifying the fundamental resonance frequency involves several signal processing steps.

First, a cumulative sum of the amplitude spectrum is computed as a function of frequency. This integral helps suppress noise and makes dominant features in the frequency domain more prominent.

To isolate the sharp resonance features, a baseline model is constructed using a Savitzky–Golay filter [77]. This method fits a third-order polynomial over a sliding window of approximately 3 Hz in width, generating a smoothed version of the cumulative spectrum that captures only the slowly varying background trend. Crucially, this smoothed output does not preserve narrow resonant peaks—it models only the baseline behavior. The baseline output from the Savitzky–Golay filter is then subtracted from the original cumulative signal. This subtraction yields a high-pass-filtered waveform in which broad structures are removed and narrow resonance peaks are retained. The result is a cleaned signal optimized for peak detection, as shown in Figure 3.12. The left and right images show the cumulative amplitude spectrum before and after the baseline removal, which signifies the resonant features.

To evaluate whether the processed signal contains resonances or only noise, a sliding root-mean-square (RMS) window is applied to the resulting data to calculate a local signal-to-noise ratio. If the RMS ratio exceeds a threshold (typically 4), the scan is identified as containing significant resonant features.

For resonance detection, the first derivative of the signal is computed to identify rising

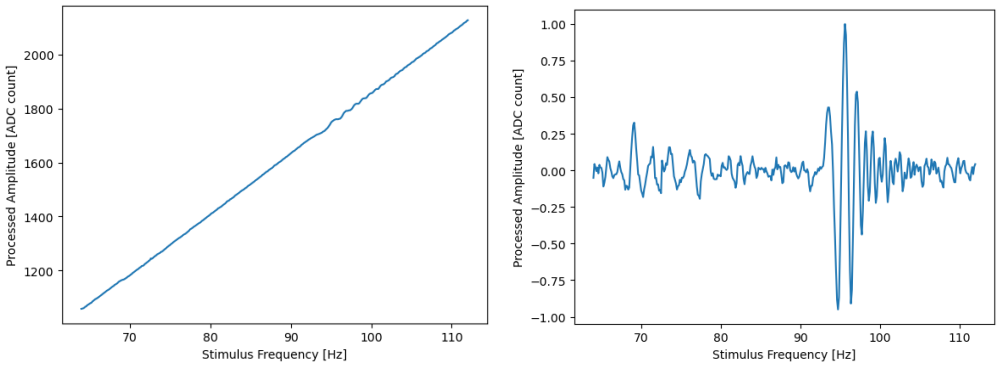


Figure 3.12: Amplitude scan before (left) and after (right) signal processing with a Savitzky–Golay filter. The resulting waveform on the right reveals narrow resonance peaks more clearly, enabling accurate detection and tension extraction.

and falling edges. A Pythagorean sum is then calculated as

$$P(f) = \sqrt{A(f)^2 + S(f)^2}, \tag{3.10}$$

where $A(f)$ is the amplitude and $S(f)$ is the slope at frequency f. This enhanced signal accentuates narrow resonant features, even those with modest amplitudes.

Candidate peaks are then selected using an adaptive thresholding method that dynamically responds to local signal-to-noise conditions. Peaks that are too close together, too small, or duplicated are removed. The initial rise of each peak is then localized by tracking the onset of rapid amplitude increase.

Each detected peak is matched to the nearest expected resonance using a grid search over a small frequency window. The quality of each match is scored using a cost function that includes proximity to expected frequency, amplitude consistency, and smoothness across channels. The lowest-cost assignment is selected to identify the wire's fundamental resonance frequency.

With the fundamental frequency identified, the wire tension is calculated using Equa-

tion 3.1, assuming the wire length and linear mass density are preconfigured. This process is repeated for each wire, enabling rapid, accurate, and scalable tension measurement across the APA.



Figure 3.13: Screenshot of the *Processed Plots* sub-tab in the *Results* tab of the DWA GUI, showing extracted resonance waveforms and calculated tensions for eight wire segments. Each plot displays amplitude versus stimulus frequency for one DWA channel. Colored vertical bars indicate the resonance frequencies identified by the algorithm, which are typically aligned with the first major peak. The colors correspond to different wire segments and match the identifiers shown beneath each plot. Dashed vertical lines indicate the expected resonance frequency for nominal tension (6.5 N), helping the user validate results. Some segments display multiple peaks due to comb spacing, which introduces nodal structure along the wire. If the vertical bars do not seem to be placed at the peak, users can drag them to manually align them with all observable resonance peaks; tension values are automatically updated in the interface. Alternatively, tensions can be adjusted directly by editing the values in the text boxes below each plot.

This full view of the resonance spectrum provides intuitive, interactive tools for refining the analysis. Multiple resonance peaks per wire segment may occur due to asymmetrically spaced nodes created by the APA comb structure. In these cases, a single

resonance does not fully represent the wire's mechanical behavior, and correct tension measurement requires aligning all vertical bars with the set of observed peaks for that segment.

Users can conveniently click and drag the vertical bars directly in the plots to adjust peak placement, or edit the values manually in the corresponding fields. These tools enable efficient and accurate refinement of automated results, especially for complex geometries or low signal-to-noise cases. Figure 3.13 shows an example of this post-processing interface.

3.6 Performance Analysis

The results presented in this section are based on two complementary stages of DWA development and validation. The initial performance evaluation was conducted using a custom test stand developed during the first two years of my PhD, while I was based at Harvard, prior to being stationed at the University of Manchester. While no photographs of the original Harvard setup are available, a functionally equivalent test stand was later reconstructed at the University of Manchester, and its Computer-Aided Design (CAD) model is shown in Figure 3.14. The Manchester test stand reproduced the key elements of the original configuration and was used to extend the performance validation to new operational regimes.

Most of the results in the following subsections are drawn from the earlier study conducted at Harvard and documented in [74], while the performance limitations and extended characterization are newly performed at Manchester and presented here for the first time.

The following subsections evaluate the DWA system's performance through controlled



Figure 3.14: The DWA test stand replicating the APA setup for performance validation. The wires are soldered onto headboards identical to those deployed in actual DUNE APAs, enabling realistic testing of mechanical and electrical performance.

bench tests and production deployment. These tests assess continuity detection, tension measurement precision, and limitations related to wire length and environmental conditions.

3.6.1 Continuity and Isolation Tests

To test electrical continuity and isolation, a frequency sweep was conducted from 100 Hz to 1 kHz using a 50 Hz step size. Prior to sampling, a 0.2-second stimulus duration was applied to allow signal stabilization. A DAC output amplitude of 512 mV and a digital potentiometer resistance of 43 kΩ were used uniformly. The results, presented in Figure 3.15, show high reproducibility across repeated measurements. Noise was below the marker resolution threshold and did not affect the continuity/isolation classification.

As discussed in Section 3.3.2, the shape of the amplitude response is governed by the high-pass filter formed by the wire capacitance and input resistance of the VGA. The total capacitance includes contributions from both the wire and internal parasitic components, such as the switch matrix and flex cable routing. Differences in internal

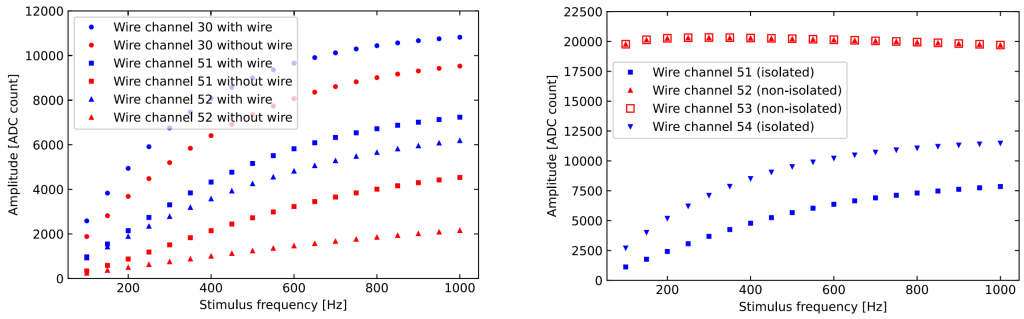


Figure 3.15: Continuity and isolation test results obtained using the DWA system. Left: Amplitude response for channels 30, 51, and 52 with and without wires connected. The increased signal amplitude in connected cases highlights the system's sensitivity to wire presence and continuity. Right: Isolation tests for wire channels 51–54. Channels 52 and 53 were intentionally shorted with a jumper wire, resulting in elevated, flat amplitude profiles characteristic of non-isolated wires. In contrast, channels 51 and 54 display typical filtered responses, indicating proper isolation. These results demonstrate the DWA's ability to distinguish electrically continuous and isolated wires via simple thresholding and pattern recognition.

capacitance and gain across channels result in baseline variations. To illustrate this, the left panel of Figure 3.15 presents responses from selected channels both with and without wire connections. A clear contrast is observed, enabling channel-by-channel diagnosis of wire continuity.

In the right panel, channels 52 and 53 were deliberately shorted using a jumper wire. Their flat and elevated amplitude response clearly differentiates them from electrically isolated wires, indicating the DWA's sensitivity to inter-wire coupling and effective isolation detection via threshold-based classification.

3.6.2 Tension Measurements

To validate tension measurements, eight wires were tested with expected resonance frequencies near 200 Hz—at the high end of the DWA's operational range. Previous studies [75] found that resonance amplitudes diminish at higher frequencies due to

increasing stiffness and internal damping of the wire, making excitation and detection more challenging. Figure 3.16 illustrates this attenuation effect.

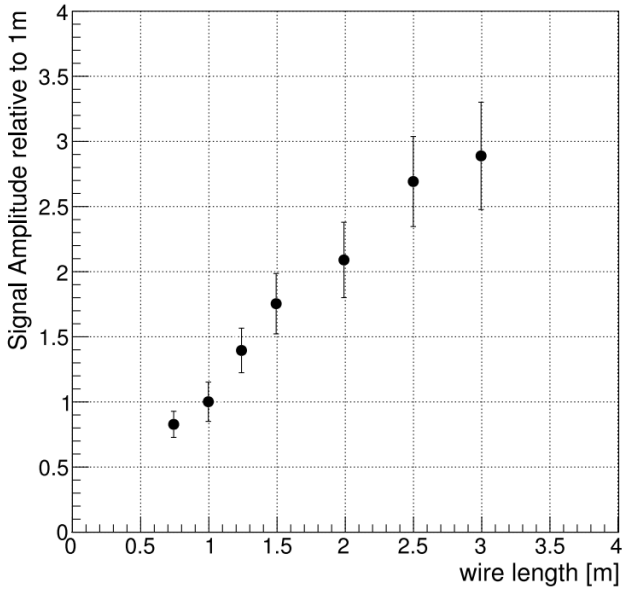


Figure 3.16: Measured signal amplitude as a function of wire length, normalized to the response at 1 m. Plot is taken from [75]. The increasing trend highlights the enhanced detectability of longer wires, while shorter wires exhibit reduced amplitudes due to lower capacitive coupling and diminished oscillation amplitudes, especially at high resonance frequencies.

The DWA was configured with a 0.125 Hz step size, 1 s stimulus duration, 2048 mV DAC amplitude, 53 kΩ resistance, 32 ADC samples per AC cycle, and ±1.6 kV DC bias. Figure 3.17 shows the resulting processed amplitude scans. The fundamental resonance frequencies, ranging from 192.1 Hz to 199.4 Hz, are clearly resolved despite the reduced capacitive coupling from the 4.8 mm wire pitch (larger than the 3 mm in [75]). The DWA's ability to measure higher frequencies is enabled by increased DC bias and enhanced noise filtering. Since wire tension T is proportional to ${f_0}^2$ (see Equation 3.1), this high-frequency performance extends the measurable tension range.

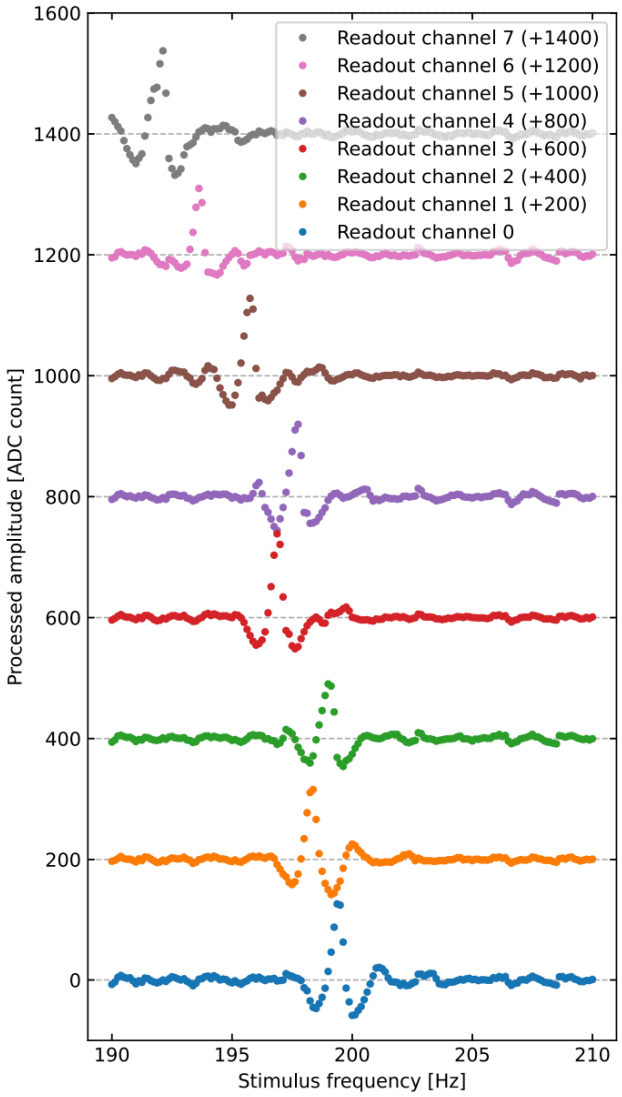


Figure 3.17: Processed amplitude scans from eight DWA readout channels using 0.125 Hz frequency steps and 1 s stimulus duration. Vertical offsets are added for clarity. Each trace shows a clear resonance dip, with frequencies ranging from 192.1 Hz to 199.4 Hz, corresponding to wire tensions between 5.8 and 6.2 N. Despite the reduced capacitive coupling from the 4.8 mm wire pitch, resonances are well resolved due to increased DC bias and improved noise filtering. The scan demonstrates the DWA's capability for high-frequency tension measurement with sub-percent repeatability.

3.6.2.1 Frequency Detection Accuracy

To validate frequency detection, DWA results were compared to a laser–photodiode apparatus (Figure 3.1) on a separate set of 6 m wires tensioned to 6.5 N (approx. 17 Hz). Agreement within 0.1 Hz was observed, corresponding to 1% tension accuracy. Further comparison using a force gauge and laser system on 1 m wires showed a systematic 0.3 N offset in laser-derived tension due to wire density tolerance. After applying a correction for this effect, the laser and force gauge measurements agreed with the DWA results to within 1%, providing strong cross-validation of the DWA's accuracy using multiple independent techniques.

3.6.2.2 Tension Extraction and Timing Bias

Using the measured wire density, tension values from Figure 3.17 range from 5.8 to 6.2 N. The dominant source of systematic uncertainty—approximately 0.3 N—arises from a 1 cm uncertainty in wire length. Repeated scans show tension variation below 0.1%, indicating excellent statistical precision and high repeatability of the method.

The total scan duration for Figure 3.17 was about 3 minutes, while continuity scans in Figure 3.15 took 5 seconds. Measurement time depends on frequency range, step size, stimulus duration, and ADC sampling. If the stimulus duration is too short, the wire cannot fully respond, resulting in frequency shifts. Figure 3.18 shows the bias introduced by a zero-second stimulus duration, compared to a laser baseline. A calibration factor of 0.975 corrects this bias. Fast scans using this correction achieve the speedup by the factor of 10 while maintaining 1% accuracy.

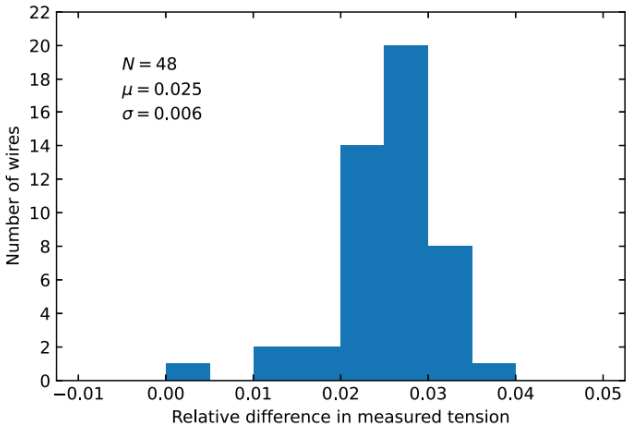


Figure 3.18: Distribution of relative differences in measured wire tension between fast scans (0 s stimulus duration) and a laser-based baseline. This systematic offset, attributed to incomplete wire excitation, is corrected by applying a global calibration factor of 0.975.

3.6.3 Operational Limitations

Environmental effects such as humidity can influence DWA performance. High humidity has been observed to introduce leakage currents at Daresbury Laboratory, complicating data collection. These effects can be mitigated by using reference scans acquired under similar environmental conditions.

In addition to environmental factors, physical constraints on the testable wire length were systematically investigated during the extended characterization work conducted at Manchester. This study analyzed the signal-to-noise ratio (SNR) of the DWA as a function of wire length, providing a quantitative basis for understanding operational limitations.

To extract the overall shape of the frequency scan while minimizing the impact of rapid fluctuations, a moving average filter was applied to the absolute value of the original scan following processing with the same filtering method used in the DWA software, along with an additional low-pass filter. The window size for the moving average was

set to half of the total frequency range, ensuring that the smoothing process captured the broader features of the scan while reducing localized variations. The moving average was implemented using a simple averaging kernel, which was convolved with both the amplitude and frequency arrays. Since the filter operates on the absolute value of the signal, it effectively removes oscillatory components while preserving the overall envelope of the waveform. This approach suppresses noise and small-scale fluctuations, facilitating a clearer identification of large-scale signal structures without distorting the general shape of the scan.

Figure 3.19 presents the results of this filtering pipeline. The left panel shows the effect of applying a low-pass filter and absolute-value transformation to the data shown in the right image of Figure 3.12. The right panel then shows the result after applying a moving average, effectively smoothing and extracting the signal envelope.

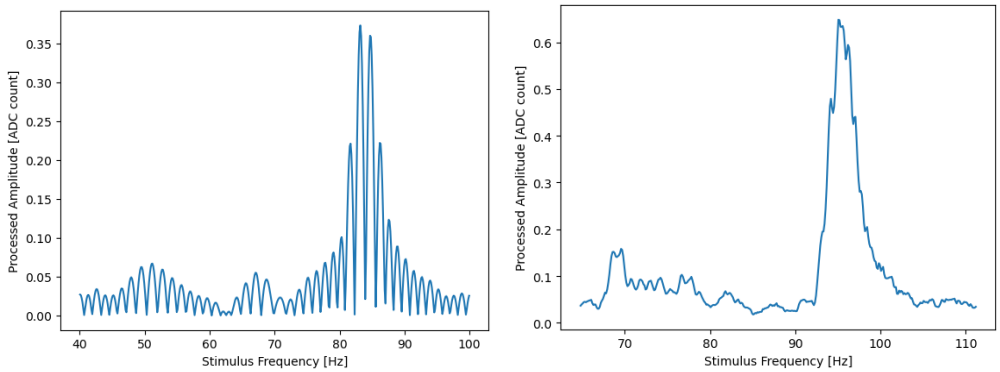


Figure 3.19: Signal envelope extraction process for SNR analysis. Left: The raw scan is processed using a low-pass filter followed by an absolute-value transformation, preserving the resonance shape while suppressing oscillatory noise. Right: The resulting signal is further smoothed using a moving average filter with a window size equal to half the frequency range, revealing the overall scan envelope. This approach enables robust extraction of signal amplitude for subsequent SNR calculation.

To determine the signal amplitude, a Gaussian function was fitted around the expected location of the resonance peak. The signal amplitude A_{signal} was taken as the

average within one σ of the fitted peak. For noise estimation, the same frequency window was applied in a region without resonance, yielding A_{noise}. The signal-to-noise ratio (SNR) was then calculated as: $\text{SNR} = \frac{A_{\text{signal}}}{A_{\text{noise}}}$.

The results of this Manchester-based study are shown in Figure 3.20. The data points indicate that wires shorter than approximately 50 cm yield SNR values close to 1, suggesting that resonance detection is unreliable in this regime due to the insufficient signal response. This aligns with the practical limitation of the DWA, which requires wires to be at least 50 cm long for any meaningful resonance measurement to be observed. Above 90 cm, SNR increases sharply, though uncertainty also rises, likely due to damping or minor tension variations. This result confirms that the DWA performs optimally for wire lengths greater than 50 cm, with improved resonance detection for longer wires due to their more pronounced oscillatory response.

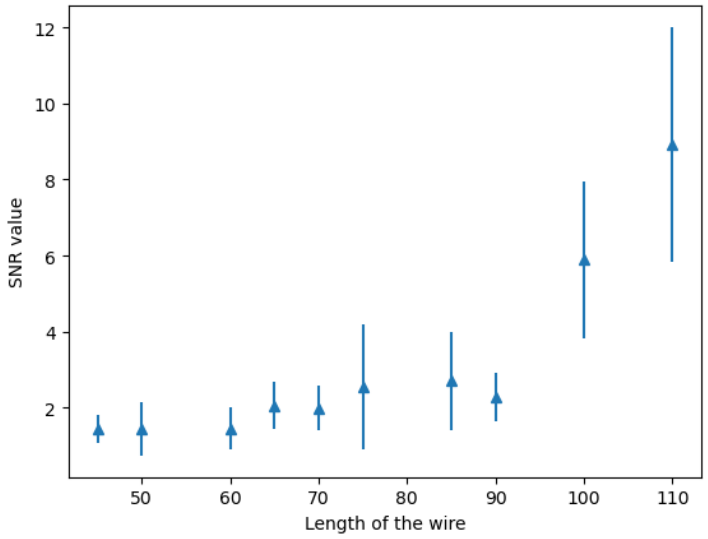


Figure 3.20: SNR as a function of wire length. Wires shorter than 50 cm exhibit SNR values near unity, making resonance detection unreliable in this regime. Beyond 90 cm, SNR increases sharply, though with larger uncertainties, likely due to damping or tension non-uniformities.

3.6.4 On-APA Validation of DWA

Figure 3.21 presents a comparison between DWA and laser-based tension measurements performed on an APA produced at Daresbury Laboratory. The top panel shows per-wire tensions across all wire planes and sides (GA to XB), with results from the DWA (blue) and laser system (red). Shaded regions denote the nominal (blue) and acceptance (orange) tension ranges. The two methods show excellent agreement across all planes. Slightly larger discrepancies in the U and V layers reflect the more complex wire geometries, where multiple wire segments are mapped to a single readout channel, introducing additional uncertainty in the laser measurement.

The bottom panel of Figure 3.21 shows histograms of the difference $T_{\text{Laser}} - T_{\text{DWA}}$ for each plane. The distributions are centered near zero with standard deviations below 0.5 N, confirming that the DWA delivers consistent and precise measurements. X and G planes show the narrowest spread, while the broader spread in U and V is consistent with the increased mapping complexity.

3.7 Summary

DWA has revolutionized the QA/QC process for APA production, addressing the limitations of previous methods while ensuring the structural and electrical integrity of APAs throughout their assembly, transport, and deployment. By enabling automated, high-precision wire tension measurements, DWA streamlines a previously labor-intensive process, reducing human intervention and enhancing reproducibility. Its ability to assess wire continuity and isolation further establishes it as an indispensable diagnostic tool for APA mass production at Daresbury, the University of Chicago, and other facilities involved in DUNE construction.

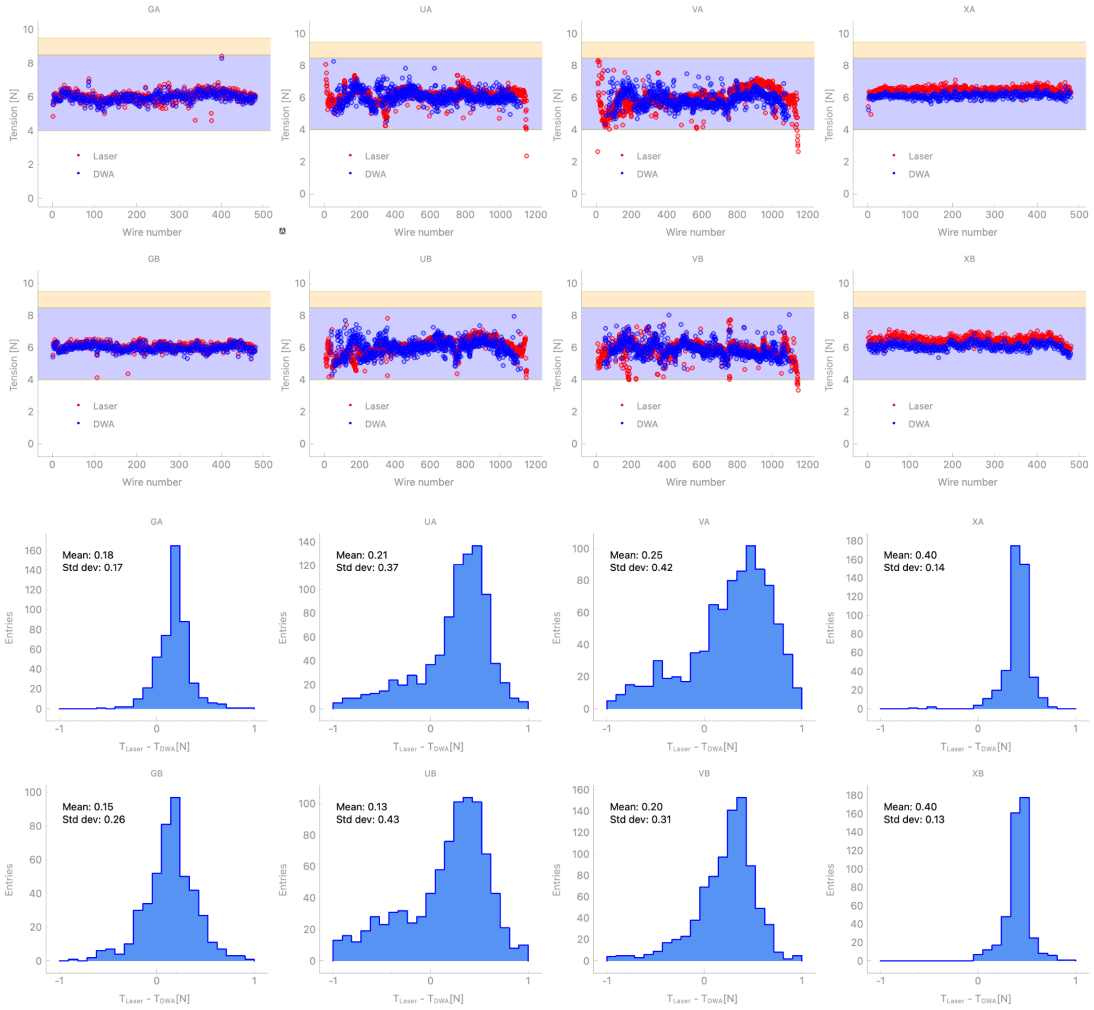


Figure 3.21: Comparison of DWA and laser-based tension measurements for APA13. Top: Tension measurements from the DWA (blue) and laser system (red) across all APA planes and sides. Shaded bands indicate nominal (blue) and acceptable (orange) tension ranges. Strong correlation is observed across all layers. Larger differences in the U and V planes stem from complex geometries where multiple segments are routed to a single channel. Bottom: Histograms of the difference $T_{\text{Laser}} - T_{\text{DWA}}$ by plane. Distributions are centered near zero with sub-0.5 N standard deviation, confirming the accuracy and precision of DWA measurements.

The performance validation of the DWA has demonstrated its high accuracy and reliability, with systematic comparisons to laser-based measurements confirming consistency within 1% precision. The method's robustness against environmental fluctuations,

such as temperature and humidity variations, further solidifies its reliability in diverse testing environments. Additionally, studies on SNR have established the operational limits of DWA, confirming its capability to measure wires beyond 50 cm in length while maintaining strong signal fidelity.

Following its successful validation, the DWA has been integrated into routine APA QA/QC procedures at major production and testing sites including Daresbury Laboratory, the University of Chicago, Fermilab, and CERN. It is now a standard tool for both incoming and outgoing APA inspections, supporting efficient, high-throughput verification with minimal operator intervention. Twelve DWA units are currently in production to meet the demands of DUNE's large-scale APA assembly.

By bridging the gap between precision metrology and large-scale detector construction, the DWA has become a cornerstone technology in modern neutrino physics experiments. Its success exemplifies how innovative instrumentation can significantly improve detector performance and reliability, setting new standards for large-scale physics experiments like DUNE.

It has been a privilege to play a leading role in the development and implementation of the DWA, guiding the project from early prototyping through to mass deployment. My responsibilities encompassed circuit design iterations, system integration, software refinement, and the establishment of a production line to support large-scale usage. I also developed training materials for use across multiple testing sites, delivered hands-on instruction, and formalized standardized testing protocols—now adopted as routine practice. These efforts enabled the successful scaling of the DWA into a fully integrated QA/QC tool for APA production. To ensure long-term sustainability, I have personally trained a growing user base, including five PhD students, three postdoctoral researchers, and two staff scientists in Manchester. Additional training programs are planned to

maintain technical continuity throughout the DUNE construction phase in the near future.

Although the DWA has enabled significant advancements, there are still ways to improve wire based LArTPCs. While these detectors have played a crucial role in neutrino physics, their inherent limitations—high channel counts, complex signal readout, and scalability constraints—pose growing obstacles to further advancements. Rather than refining wire-based LArTPCs indefinitely, it is worth considering whether a fundamentally different approach could unlock new possibilities. The next chapter explores one such alternative: Q-Pix.

Simplicity is the ultimate sophistication.

Leonardo da Vinci

4

Q-Pix

As LArTPCs evolve into larger and more ambitious instruments, the nature of their performance changes. Traditional wire-based readout systems are like classical compositions—structured, continuous, and deliberate in how they record every note of a particle's passage. However, as detectors scale toward Kilotons, this rigid approach begins to falter. The sheer complexity of the signal space demands a new kind of instrumentation —one that can adapt, improvise, and respond only when there is something truly worth

hearing.

Q-Pix introduces a different philosophy of detection. It is not a piano string waiting to be plucked, but a digital jazz musician, listening in silence and responding only when the rhythm demands it. Each pixel in the array acts autonomously, integrating charge over time and emitting a data "note" only when a tune is worth recording. This time-to-charge encoding transforms the detector into an asynchronous, sparse, and highly scalable system—less like a continuous recording and more like an improvisational score built from moments of significance.

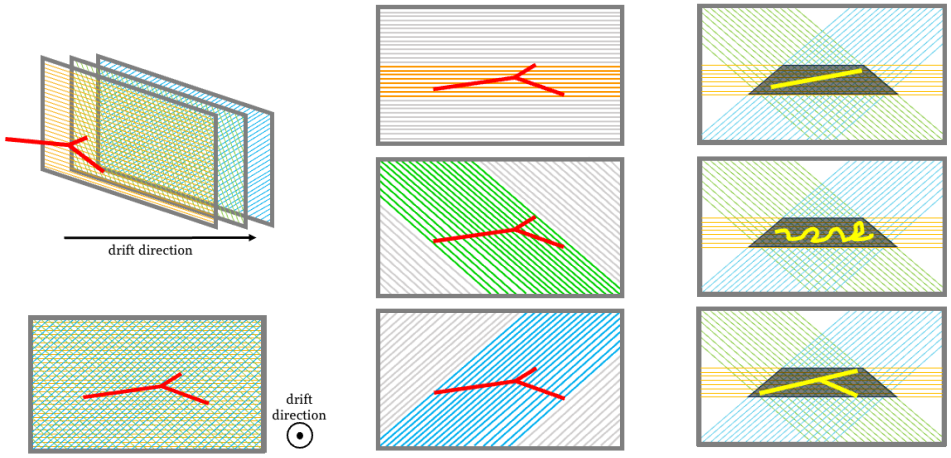
This chapter presents the motivation for developing a pixel-based readout, the principles underpinning the Q-Pix architecture, and the results of the experimental demonstrations of its core functionality.

4.1 Challenges of wire-based technology

Wire-based technology has a rich history in LArTPC experiments, as evidenced by its successful implementation in ICARUS [54], ArgoNeuT [55], Liquid Argon In A Testbeam (LArIAT) [78], Cryogenic Apparatus for Precision Tests of Argon Interactions with Neutrinos (CAPTAIN) [79], and MicroBooNE [56]. The DUNE far detector's first module also utilizes this technology in its APA design describe in Subsection 2.4.1. However, a fundamental limitation of wire-based readout is the inherent reduction of dimensionality: the 3D evolution of ionization is projected onto 2D wire planes. This dimensional compression introduces ambiguities that significantly complicate the reconstruction of complex or overlapping events.

Figure 4.1 vividly illustrates this challenge with a scenario where a track is oriented nearly parallel to the APA planes and perpendicular to the electric field. Panel (a)

depicts this track (in red) relative to the three wire planes (orange, green, and blue). Due to this orientation, as shown in panel (b), the ionization electrons drift simultaneously towards all three wire planes, causing every intersected wire to receive a signal at the same time. This results in a highly degenerate configuration where each wire plane records a signal cluster devoid of relative timing information crucial for resolving the track's structure along the drift direction. Consequently, as highlighted in panel (c), the only spatial constraint derivable from the combined wire signals is that the true track must lie within the overlapping shaded region. This example underscores the fundamental ambiguity arising from the 2D projection, severely limiting the ability to uniquely reconstruct the original 3D trajectory even for relatively simple events.



(a) Track Example **(b)** Projection to APA **(c)** Possible Reconstruction

Figure 4.1: Example of a degenerate track configuration in a wire-based LArTPC readout. (a) A charged particle track (red) is oriented nearly parallel to the APA planes and perpendicular to the electric field direction. (b) Projections onto the three wire planes show that ionization electrons arrive at all wires simultaneously, producing signal clusters without relative timing differences. (c) The only spatial constraint inferred from the combined wire signals is that the track must lie within the shaded overlapping region, illustrating the inherent ambiguity in reconstructing such track orientations from 2D projections.

This inherent reconstruction problem escalates rapidly with the number of simul-

taneously activated wires. In densely ionizing or high-multiplicity events, the lack of temporal separation among numerous coincident signals leads to a combinatorial explosion of possible 3D interpretations consistent with the 2D wire data. This can render entire regions of the detector difficult to interpret. Furthermore, large-scale wire-based systems like the DUNE APAs amplify this issue. Here, a single readout channel can be connected to multiple wire segments stacked along the drift direction, meaning a single charge signal can originate from several discrete spatial locations, further hindering accurate 3D reconstruction.

Beyond these ambiguities rooted in the event topology and readout geometry, wire-based systems are also susceptible to single-point hardware failures [80, 81, 82]. Each wire and its associated electronics chain represents an independent point of failure. A malfunction in any of these components can lead to the loss of signal from an entire readout channel, potentially affecting a significant volume of the detector. In APAs, where a single channel can correspond to extended wire segments or multiple drift locations, the failure of even one channel can noticeably reduce the efficiency of reconstructing events across a broad area. Ensuring robustness against such failures is a critical engineering consideration for large detectors with millions of channels, impacting their long-term reliability and data quality.

The limitations of wire-based readout, while qualitatively evident through examples like the degenerate track configuration, have also been quantitatively assessed. Studies comparing 2D and 3D readout architectures, such as the one presented in Ref. [83], demonstrate that the loss of 3D spatial information inherent to wire-based systems leads to significant inefficiencies in event reconstruction. This dimensional reduction obscures fine details of the ionization pattern. The quantitative analysis in Ref. [83] provides a valuable framework for understanding these limitations and underscores the

potential advantages of adopting 3D readout schemes like pixelated architectures, which will be discussed in the following section.

4.2 Simulation Study of 2D vs. 3D Readout Geometries

To quantitatively evaluate the potential benefits of a true 3D charge readout for LArT-PCs [83] conducted a comparative simulation study between a conventional 2D projective wire readout and a fully pixelated 3D readout scheme. This study assessed how readout geometry affects neutrino event classification using deep learning techniques. Convolutional neural networks (CNNs) were trained on identical datasets, formatted for both 2D and 3D geometries, to evaluate differences in classification performance without bias from reconstruction software.

Table 4.1 summarizes the classification accuracy of the trained networks for the 3D readout configuration.

Category	**3D Accuracy [%]**
Neutrino Interaction	94
Proton Multiplicity	91
Charge Pion Presence	94
Neutral Pion Presence	95

Table 4.1: Accuracy in the validation set for the best 3D network to correctly classify neutrino events.

The subsequent physics case analysis utilizes this classification accuracy results by applying the trained networks to a realistic, flux-weighted DUNE far detector dataset. This allows for the evaluation of physics performance metrics like efficiency, purity, and background rejection for key event topologies using the network outputs as selection variables, directly relevant to long-baseline neutrino oscillation studies. By optimizing

thresholds for both 2D and 3D networks to achieve equivalent target purity or efficiency, a fair comparison of their relative classification performance under realistic analysis conditions is conducted.

The first analysis examines ν_e CC event selection, essential for oscillation studies. Figure 4.2 shows the resulting efficiency and purity as a function of neutrino energy. At 85% efficiency, the 3D network achieves 90.6% purity, while the 2D network reaches only 62.7%. Fixing purity at 96%, the 3D configuration maintains 78% efficiency versus 34% for 2D.

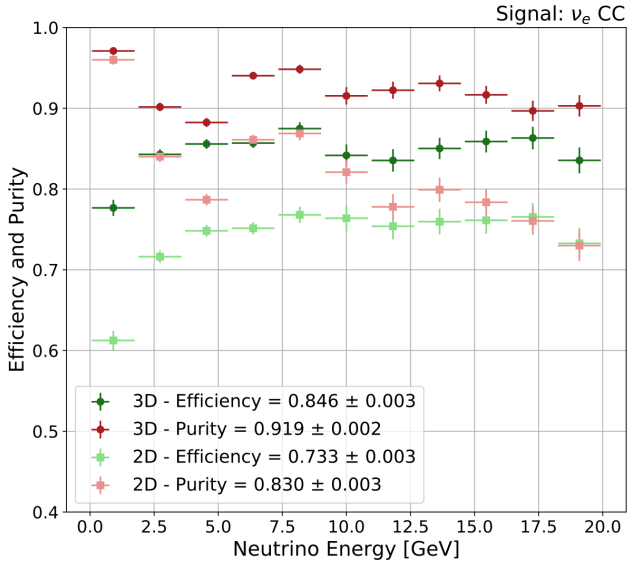


Figure 4.2: Efficiency and purity for inclusive ν_e CC event selection as functions of neutrino energy, for both 2D and 3D readouts. Figure from [83].

The second analysis focuses on neutral current π^0 production, a major background for ν_e CC selection. As shown in Figure 4.3, the 3D readout achieves 93.1% purity at 85% efficiency, compared to 83.5% for 2D. At 98% purity, the 3D network retains 63% efficiency, versus 43% for 2D.

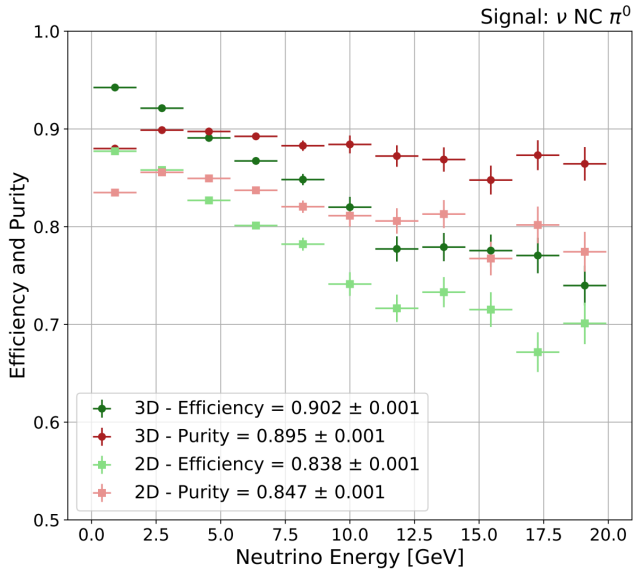


Figure 4.3: Efficiency and purity for neutral current π^0 event selection as functions of neutrino energy, for both 2D and 3D readouts. Figure from [83].

The third analysis evaluates ν_μ CC selection, for which both readouts reach $\sim 99.6\%$ purity when tuned for 99% background rejection. Figure 4.4 shows the 3D network achieves an average efficiency of 72%, compared to 65% for 2D.

Together, these three classification studies demonstrate the significant advantages of a 3D pixel-based readout over the conventional 2D projective wire configuration across a range of neutrino interaction topologies. For complex signatures such as ν_e CC and NC π^0 events, the 3D readout provides substantially higher purity at fixed efficiency and retains significantly more signal events under high-purity selection requirements. Even for the relatively straightforward ν_μ CC selection, the 3D readout consistently achieves better efficiency without sacrificing background rejection. These results highlight the physics potential of a true 3D readout architecture, particularly in the context of large-scale LArTPCs aiming to push the limits of signal identification and background

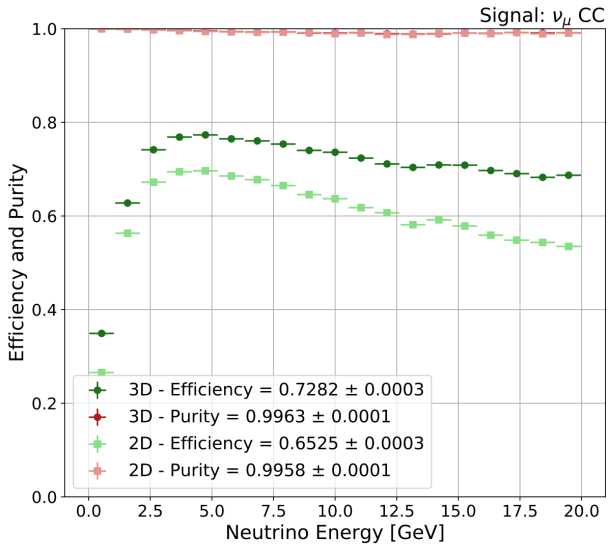


Figure 4.4: Efficiency and purity for ν_μ CC event selection as functions of neutrino energy, with 99% background rejection. Figure from [83].

suppression. However, realizing such a readout in practice poses several technical and engineering challenges, particularly in scaling pixel-based systems to the size and complexity required for next-generation detectors. The following section outlines these challenges and introduces the Q-Pix concept as a promising solution to enable low-power, scalable, and fully 3D charge readout for future LArTPCs.

4.3 Q-Pix Principle

Q-Pix is a novel pixel-based readout architecture originally proposed by Dave Nygren in collaboration with Yuan Mei [84]. It was developed to meet the stringent demands of low-energy, high-resolution LArTPC applications while preserving the advantages of true 3D charge imaging.

Q-Pix employs a network of self-triggering charge-integrate/reset (CIR) blocks, each

equipped with a free-running local clock. These blocks digitize the time intervals between charge resets locally, enabling compact encoding of both charge and timing information. This asynchronous, sparse data acquisition approach significantly reduces the overall data volume. In addition, Q-Pix incorporates a dynamically reconfigurable, fault-tolerant network topology, mitigating the impact of single-point failures—a key concern in large-scale deployments.

One of the primary concerns is the significantly increased data volume associated with pixel-based charge readout, largely driven by the higher channel count compared to traditional wire-based systems—especially in large-scale detectors like the DUNE FD. Moreover, in a large LArTPC, the vast majority of the detector volume is inactive most of the time, with no interesting physics signals occurring. As a result, an effective readout system must adhere to an "electronic principle of least action", which can minimize activity and power consumption under normal conditions, while remaining capable of rapid and responsive data acquisition when a signal does appear.

The following section introduces the Q-Pix concept in more detail and explores how it addresses the challenges of scalability and power efficiency in pixel-based readout systems for next-generation LArTPC detectors.

4.4 Q-Pix Schematic Designs

Building on the foundational concept introduced above, the detailed implementation of Q-Pix revolves around how charge signals are digitized and time-stamped at the pixel level. Two primary circuit-level schemes have been proposed to realize this functionality, as illustrated in Figure 4.5. The first, known as the reset scheme, formed the basis of the original Q-Pix design and relies on detecting the moment when an integrated

charge exceeds a predefined threshold, triggering a reset and time-stamp recording. More recently, a refined approach called the replenishment scheme has been introduced to address several limitations of the reset model, including improved charge-time linearity and better compatibility with low-leakage electronics. The following subsections describe these two schemes in detail, outlining their operating principles and their implications for large-scale deployment in LArTPCs.

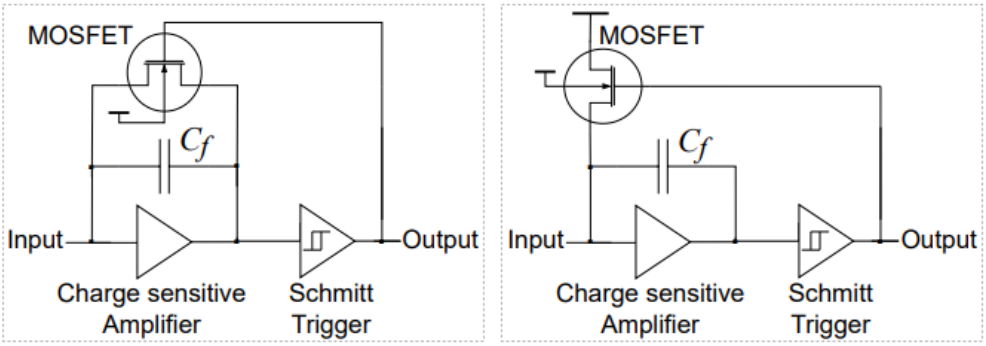


Figure 4.5: Circuit schematics of the two Q-Pix charge digitization schemes. Left: the original reset-based scheme, in which the capacitor is fully discharged once the comparator threshold is crossed. Right: the replenishment-based scheme, where only a fixed charge quantum is removed, preserving the remaining charge on the capacitor. Figure taken from [85].

4.4.1 Reset Scheme

The foundational implementation of Q-Pix is based on a CIR circuit, illustrated schematically in the left image of Figure 4.5. This design uses a self-triggering mechanism for charge detection and is paired with a time-stamping strategy similar to the one successfully deployed in the IceCube experiment [86]. When charge carriers arrive at the circuit input, they are first amplified by a charge-sensitive amplifier (CSA) and continuously integrated onto a feedback capacitor. Once the accumulated charge exceeds a predefined threshold set by a regenerative comparator (typically a

Schmitt trigger), the circuit initiates a rapid discharge of the capacitor resetting its state, and records a time-stamp based on the local free-running clock. The pixel is immediately ready to begin integrating charge again, enabling fully asynchronous, triggerless operation in which each pixel responds only to meaningful signal activity.

A key feature of the reset scheme is that the entire charge stored on the capacitor is removed during each reset, which simplifies the circuit design but also introduces a potential limitation. If additional charge arrives during the brief reset interval, it is discharged along with the pre-threshold charge and effectively lost, leading to a slight undercounting of the total collected charge. Despite this, the reset time difference (RTD) —the time interval between successive resets—serves as the core unit of information for each pixel. Each RTD reflects the time required to accumulate a fixed charge quantum, ΔQ, as set by the comparator threshold. Because the average input current I is inversely proportional to the RTD, it can be reconstructed using the relation $I \propto 1/\text{RTD}$, with $I \cdot \Delta T = \Delta Q$. This allows a sparse and efficient reconstruction of current waveforms without full waveform digitization. An example of waveform reconstruction using RTDs is shown in Figure 4.6.

4.4.2 Enhanced Q-Pix Design: Replenishment Scheme

The replenishment scheme is a refinement of the original reset-based Q-Pix architecture illustrated schematically in the left image of Figure 4.5, introduced to address a subtle but important limitation in the charge integration process. Like the reset scheme, it is built around the same fundamental principle: a capacitor accumulates charge from incoming ionization signals, and when a threshold is reached, a time-stamp is recorded. The difference lies in what happens during the discharge phase. In the original reset scheme, the capacitor is fully discharged once the threshold is exceeded, which means

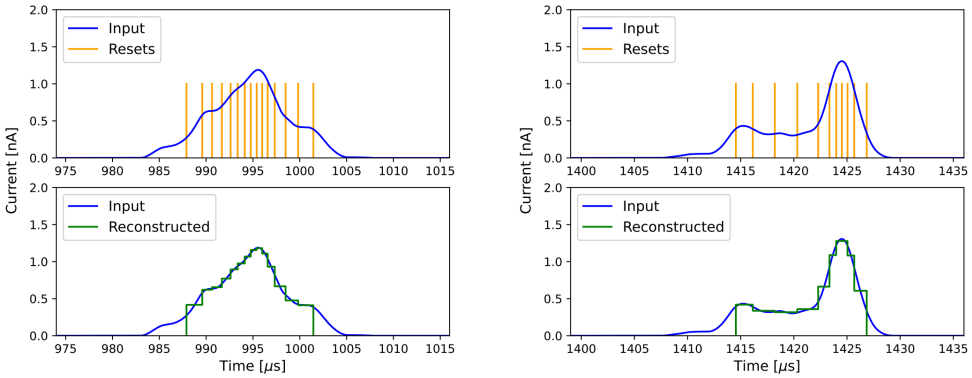


Figure 4.6: Examples of waveform reconstruction from RTDs. The input currents are the results of charge integration simulation for two different pixels near the vertex of simulated neutrino interaction. The blue lines show the current arriving to the pixel. The orange vertical lines in both of the top images show the reset signals that were produced by the input current in each case. The green lines on the bottom images show the reconstructed current using the RTDs. For this simulation, ΔQ was chosen to be 1 fC (6250 electrons, or equivalently, 147.5 keV in LAr). Figures taken from [87].

any additional charge entering the system during the brief discharge window is lost and cannot be accounted for. This leads to a small but systematic underestimation of total collected charge, particularly in the presence of rapidly arriving signals.

The replenishment scheme resolves this issue by replacing the full reset with a controlled, partial discharge using a calibrated current source. Rather than draining the entire accumulated charge, the system removes a known fixed amount of charge, ΔQ, and records the time at which this action occurs. This preserves the ability to reconstruct current using the same principle as the reset scheme—namely, that $I \propto 1/\text{RTD}$, where RTD is now the time between replenishment events. However, because only a fixed and well-defined amount of charge is removed, any additional charge arriving during the brief discharge interval remains on the capacitor and is included in the subsequent measurement. This improves the fidelity of the current reconstruction, reduces distortion due to signal pile-up, and enhances overall charge accounting. In effect, the replenishment

scheme retains the simplicity and asynchronous nature of the reset architecture, while offering a more precise treatment of dynamic charge input—an important consideration for accurately capturing the detailed time structure of neutrino interactions in large LArTPCs.

Feature	**Reset Scheme**	**Replenishment Scheme**
Discharge Method	Full capacitor reset upon threshold crossing	Fixed charge removal using calibrated current source
Residual Charge Handling	Lost during reset	Preserved and carried over to the next cycle
Charge Accounting	Approximate; overlapping signal charge during reset is discarded	Precise; only known amount removed, enabling better charge fidelity
Circuit Complexity	Simpler	Slightly more complex due to current source control
Response to Signal Overlap	May discard additional charge arriving during reset	Retains charge arriving during discharge period
Current Reconstruction	$I \propto 1/\text{RTD}$, with possible underestimation	$I \propto 1/\text{RTD}$, with improved accuracy

Table 4.2: Comparison of the Reset and Replenishment Schemes in Q-Pix

4.5 Q-Pix Hardware Development

The successful implementation of the Q-Pix architecture requires rigorous hardware validation to demonstrate the feasibility of its core design principles in practice. So far, our Q-Pix collaboration has undertaken a series of prototyping efforts focused on realizing and testing essential functionalities. These efforts represent a critical step in bridging the gap between the conceptual design and a deployable readout system suitable for large-scale LArTPCs. This section reviews two key milestones in the ongoing hardware development, as reported in Refs.[85, 88], with each of the following subsections dedi-

cated to summarizing and contextualizing the results of these studies within the broader development trajectory of the Q-Pix readout system.

4.5.1 Demonstration of Q-Pix reconstruction mechanism

To validate the core design principles of the Q-Pix readout architecture, our collaboration developed and characterized a prototype front-end implementation based on predominantly Commercial Off-The-Shelf (COTS) components [85]. This prototype demonstrates the feasibility of realizing a sub-fC scale pixelated readout in hardware, requiring only a single custom n-type Metal-Oxide-Semiconductor (NMOS) transistor, with the remaining elements being mature commercial parts. This minimal reliance on custom components makes the design highly attractive for scalable deployment, suggesting that a low-power, sub-fC sensitive, pixelated charge readout –a foundational technology for large-scale 3D LArTPCs –can be constructed using predominantly readily available components and just one bespoke device.

This study, which focused on the replenishment scheme, addressed the challenge in the stabilization of the quantized charge unit ΔQ through the introduction of a clocked reset mechanism. The experimental setup employed discrete Operational Amplifier (OpAmps), NMOS transistors, and an FPGA-controlled reset circuit, as illustrated in Figure 4.7. This system enabled precise pulse-width modulation for the reset control, ensuring consistent quantization in the presence of parasitic capacitances and environmental noise.

By tuning the NMOS current and reset pulse width, the prototype demonstrated reliable charge quantization down to $\Delta Q \approx 0.46$ fC equivalent to 50 keV signal detection, a value well-matched to the requirements of LArTPC applications. The performance was quantified through measurements of the reset frequency as a function of input current,

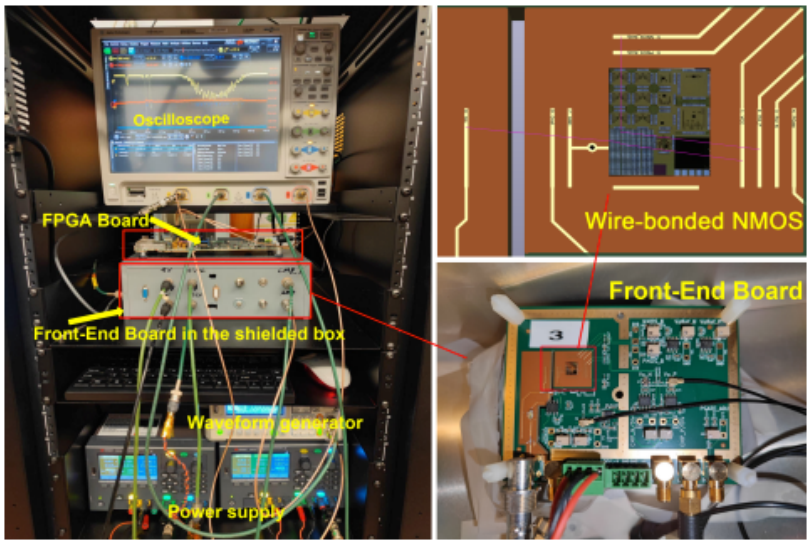


Figure 4.7: Photograph and schematic of the Q-Pix front-end demonstration setup. The circuit is implemented with discrete COTS components, including OpAmps and a wire-bonded NMOS transistor. Measures were taken to minimize leakage current and parasitic capacitance, including shielding, mechanical PCB modifications, and careful connector selection. Figures taken from [85].

revealing excellent time-to-charge linearity across a wide dynamic range. The results can be seen in Figure 4.8, which shows a linear fit to the measured data and confirms the effectiveness of the Q-Pix encoding mechanism at picoampere-scale currents.

Beyond validating charge quantization, the study also confirmed that the real hardware reproduces the expected dynamic response to typical ionization current signals. Figure 4.9 presents a comparison between simulated and measured Q-Pix reset waveforms for a representative input current profile. The post-improvement hardware setup (bottom panel) closely matches the simulated behavior, demonstrating successful signal capture and reset pulse generation with a reduced ΔQ of 0.46 fC. This marks the first experimental observation of full waveform behavior in a Q-Pix-like system, providing confidence in its ability to encode ionization topologies for later reconstruction.

These results show that despite the complexity traditionally associated with 3D pix-

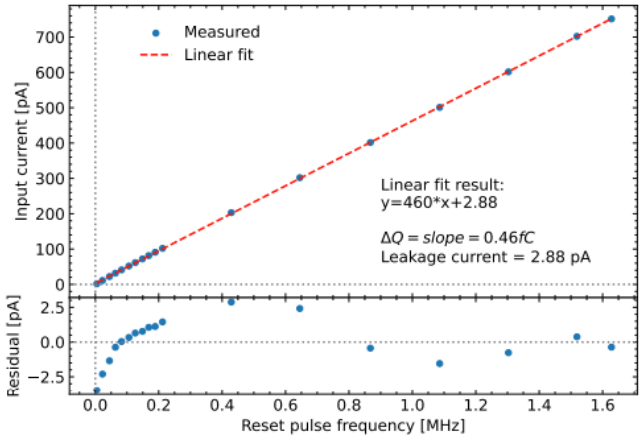


Figure 4.8: Measured input current vs. reset frequency for the Q-Pix COTS prototype. The extracted $\Delta Q = 0.46$ fC demonstrates excellent time-to-charge linearity down to a few pA, validating the core principle of the Q-Pix architecture. Figure taken from [85].

elated readouts, the practical implementation of Q-Pix may only require the design and fabrication of a single custom transistor. With the rest of the circuitry built from widely available components, the prototype lays a compelling foundation for a scalable, cost-effective, and low-power front-end for large liquid argon detectors like DUNE.

4.5.2 Demonstration of Q-Pix Charge Quantization and Readout Capabilities

To evaluate the potential of Q-Pix for performing precision physics measurements, the collaboration developed a fully COTS multi-channel prototype and applied it to a controlled study of electron transport in a gaseous TPC [88]. Operating in gas provided a stable and accessible platform to investigate charge transport without the added complexity of a cryogenic environment. Specifically, the Simplified Analog Q-Pix (SAQ) system, composed of 16 analog front-end channels and a digital FPGA-based back-end, was used to measure the transverse diffusion of electrons in P-10 gas (90% Ar, 10% CH_4). This marks the first physics result obtained using a Q-Pix prototype, establish-

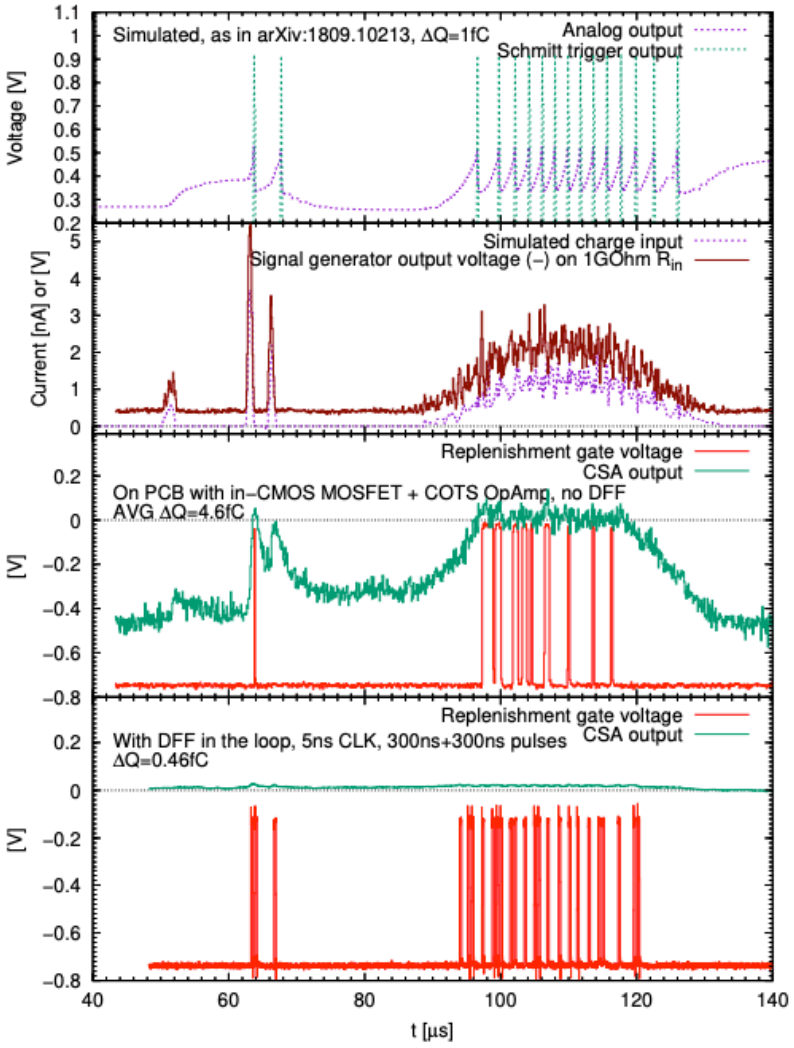


Figure 4.9: Comparison of simulated and measured Q-Pix reset waveforms for a typical ionization current input. The improved hardware setup (bottom panel) reproduces the expected signal shape with a reduced ΔQ of 0.46 fC, demonstrating successful waveform capture by the replenishment scheme. Figures taken from [85].

ing its viability as a low-threshold, self-triggered, and high-resolution ionization imaging device.

The experimental apparatus consisted of a vacuum TPC with a gold photocathode

illuminated by pulsed UV light from a xenon flashlamp to produce a well-defined electron swarm. The electrons drifted under a uniform electric field toward a segmented anode composed of 16 concentric annular electrodes, each coupled to a channel of the SAQ readout. Figure 4.10 illustrates the system configuration, including the geometry of the TPC and the anode-readout integration.

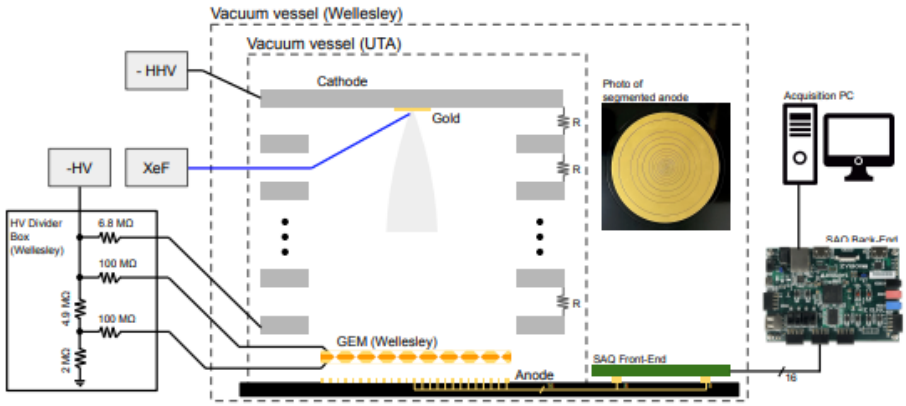


Figure 4.10: System diagram of the TPC and SAQ electronics [88]. A UV light pulse from a xenon flashlamp produces electrons at a gold photocathode. These drift toward a 16-channel segmented anode, where the SAQ front-end records reset pulses corresponding to integrated charge. The readout architecture enables reconstruction of the transverse distribution of the electron cloud. Figure taken from [88].

To interpret the measured charge distributions $\tilde{Q}(r)$ across the segmented anode, the collaboration developed a set of simulations modeling the expected response of the Q-Pix readout under various illumination conditions. As shown in Figure 4.11, these simulations account for fiber alignment offsets and angular tilts relative to the photocathode, which can introduce asymmetries in the radial charge profiles. While such effects complicate the extraction of transverse diffusion, they are well-characterized and incorporated into the analysis as constrained nuisance parameters. This modeling enables robust comparisons between measurement and theory across a range of pressures

and drift fields.

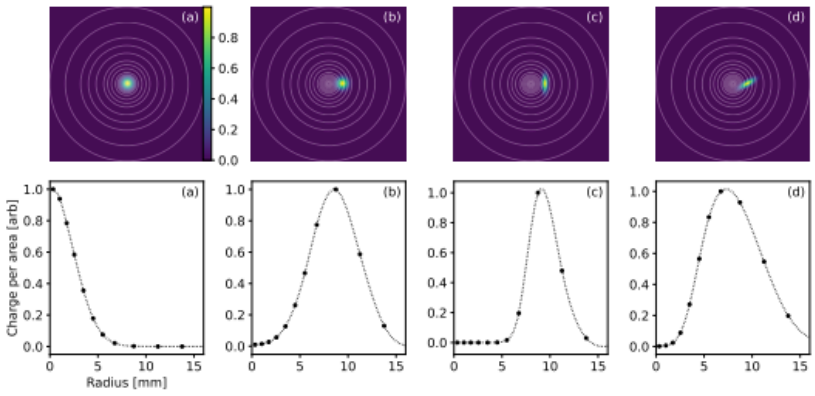


Figure 4.11: Simulated charge cloud distributions and corresponding radial profiles $\tilde{Q}(r)$ for various fiber orientations and positions. These models are used to account for systematic effects in the geometry and illumination of the TPC, enabling accurate extraction of transverse diffusion from the Q-Pix reset data. Figure taken from [88].

By monitoring the reset rates in each channel, the spatial distribution of the charge cloud arriving at the anode could be reconstructed. The width of this distribution reflects the degree of transverse diffusion experienced during drift. Calibrated measurements were performed across a range of gas pressures (200–1500 Torr) and electric fields (50–500 V/cm). The reconstructed charge profiles showed the expected narrowing with increasing pressure, and no significant dependence on field strength, in agreement with electron transport simulations using PyBoltz [89]. These results are summarized in Figure 4.12, which compares the extracted transverse diffusion coefficients to simulation and previous experimental data.

These results confirm that Q-Pix's time-to-charge encoding not only functions reliably in multi-channel configurations, but also enables quantitative reconstruction of transport phenomena within a TPC. When considered alongside earlier waveform reconstruction studies [85], this demonstration underscores Q-Pix's potential as a scalable,

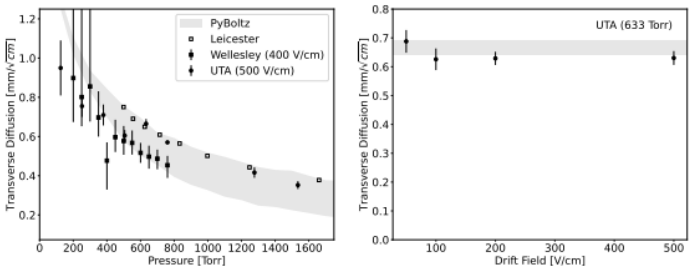


Figure 4.12: Measured transverse diffusion σ_T as a function of gas pressure (left) and drift field (right), compared with expectations from PyBoltz simulation and prior experimental data. Results from both the Wellesley and UTA systems show good agreement with theory, confirming that the Q-Pix readout enables quantitative reconstruction of transport properties in a TPC. Figure taken from [88].

physics-grade readout system for LArTPCs and other ionization-based detectors.

4.5.3 Toward Cryogenic Operation: Compact One-Channel Prototypes

A critical next step in the Q-Pix hardware development program is the validation of a multi-channel system operating in liquid argon. While previous work has demonstrated the core functionality of the Q-Pix readout architecture using COTS components in room-temperature gas TPCs, its operation under cryogenic conditions remains untested. To address this, the collaboration is pursuing a staged approach, beginning with the design and characterization of a compact one-channel prototype intended to serve as the basic unit of a larger, cryo-compatible multi-channel array.

The "Pill Board (PB)" prototype encapsulates the analog front-end of a single Q-Pix channel into a compact, modular unit. Unlike previous designs that implemented a more complex 64-channel interface from the outset, this architecture simplifies system integration and modular testing by enabling the use of identical one-channel units. The current design remains scalable, with support for expansion to a full 64-channel system interfaced to a shared digital readout back-end. To characterize the performance of the

PB and validate its response to known input currents, a circuit analysis was conducted at the University of Texas at Arlington (UTA). The measurements utilized a custom-built nanoampere-scale current source developed at UTA, capable of delivering highly stable, low-current signals appropriate for Q-Pix calibration.By sweeping the input current and recording reset time intervals, the effective ΔQ for the PB was extracted under various operating conditions, providing a foundational calibration for future cryogenic testing.

4.5.3.1 Design Strategy: Modular One-Channel "PB" Prototype

The PB implements the replenishment-based CIR architecture in a fully self-contained format. Its design prioritizes modularity, simplicity, and cryogenic compatibility, making it an ideal unit for calibration, testing, and tiling into a larger system. Figure 4.13 shows both a photograph of the PB and a simplified schematic of its core analog logic, highlighting the connection between the circuit design and its physical implementation.

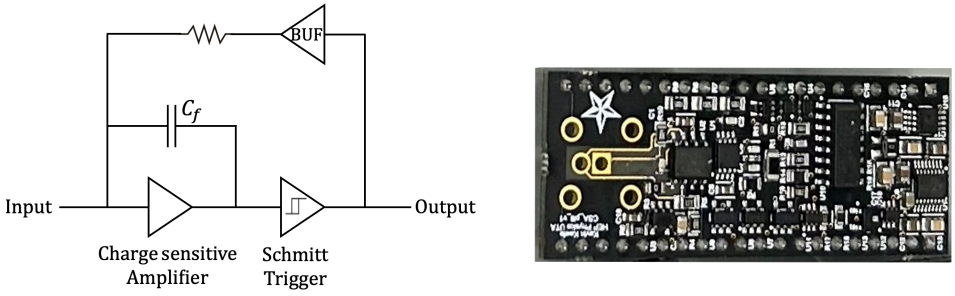


Figure 4.13: Schematic (left) and photograph (right) of the Q-Pix PB designed by Kevin Keefe, The University of Texas at Arlington. The design implements the replenishment-based CIR scheme in a compact and modular form factor. Together, these images highlight the connection between the circuit architecture and its physical realization.

At the core of the PB is a CSA implemented using a low-leakage operational amplifier. Input current from the anode electrode is integrated until the output voltage crosses a threshold set by a comparator, which then triggers a charge replenishment. This signal,

corresponding to the quantized charge ΔQ, is the key observable in the Q-Pix encoding scheme. What is particularly notable about this implementation is its use of a simple replenishment mechanism based on a voltage buffer and resistor—effectively using Ohm's law (V/R) to deliver a controlled charge subtraction. This approach avoids the need for a regulated current source or custom transistor and contrasts with the more sophisticated replenishment circuit used in the COTS prototype introduced in subsection 4.5.1, which employed a four-terminal NMOS device to inject a fixed charge with greater precision. The simplicity of the V/R approach offers a pragmatic path toward modular testing, even if it sacrifices some control over charge quantization compared to dedicated current-source designs.

The analog front-end is complemented by a digital slow control system, which allows in situ tuning of critical operating parameters. Two I^2C-controlled digital potentiometers adjust the reference voltage (V_{ref}) and common-mode voltage (V_{cm}), while a dual-channel DAC (AD5339) supplies biasing voltages with high precision. This configuration supports automated calibration workflows and enables stable operation in cryogenic environments-where manual tuning is impractical. The design also includes careful grounding and filtering to minimize noise and leakage current. Guard-ring structures and shielding capacitors are used to further suppress noise.

One of the key advantages of the PB architecture is its scalability. Each unit can be treated as a standalone channel, allowing for straightforward replication and tiling into a 64-channel readout system. This modular approach reduces design complexity and facilitates both system integration and debugging. By abstracting each readout channel into an independent unit, the PB serves as a versatile building block for the next-generation Q-Pix system aimed at cryogenic deployment.

4.5.3.2 Circuit Characterization and Calibration Infrastructure

To enable precise calibration of the PB prototype, a dedicated low-noise current source board was developed to supply well-defined nanoampere-scale input currents. The circuit is based on a quad op-amp configured to generate a programmable current output of -1A to 1A, with the input voltage of -10V to 10V. A trim stage allows fine-tuning of the current level to sub-nanoampere precision. The current source was carefully designed to be symmetric with respect to ground, supporting both positive and negative current delivery. This allows bidirectional testing of the PB response and full characterization of its linearity. The system is powered using isolated ± 2.5 V supplies to minimize noise pickup.

The board was calibrated using a nanoammeter and tested across a range of expected current values. Repeated measurements showed excellent linearity and reproducibility, as shown in Figure 4.14. The RMS variation between measurements was negligible across the tested range, confirming the current source as a reliable input reference for PB calibration. This infrastructure enables precise extraction of the effective ΔQ for each PB, as well as characterization of noise performance, integrator stability, and replenishment timing.

The PB prototype was calibrated by injecting the controlled current from the nanoampere current source (described above) at room temperature and observing the output of the charge-integrate and reset logic using a digital oscilloscope. The goal of this procedure was to validate that the replenishment-based Q-Pix mechanism functions as expected and that the RTD encodes the input current in a predictable and repeatable manner.

Figure 4.15 shows oscilloscope traces captured during the test, with input currents of

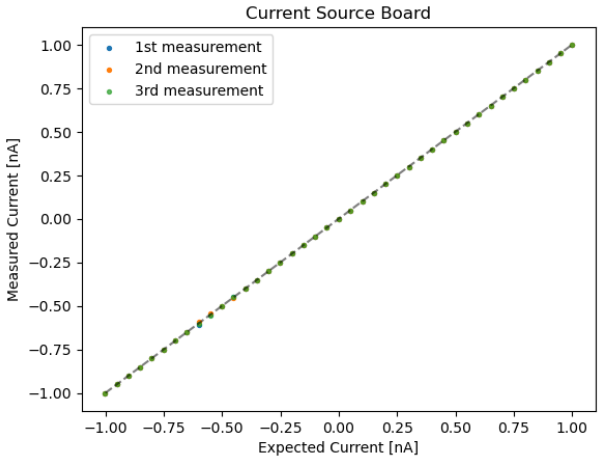


Figure 4.14: Calibration of the nanoampere current source board. Three independent measurements confirm excellent linearity between expected and measured current values over a range of ±1 nA. This stability enables high-precision characterization of the PB readout circuit. The error bars are smaller than the data point markers and are not visible at this scale.

approximately 0.65 nA and 0.90 nA. The yellow trace corresponds to the output of the integrator, which exhibits a sawtooth-like waveform as the input current charges the integrator until it crosses the threshold. The blue trace shows the output of the Schmitt trigger comparator, which generates a replenishment pulse each time the threshold is crossed. As expected, the time between reset pulses decreases as the input current increases, indicating a larger quantity of charge accumulated over a shorter time interval.

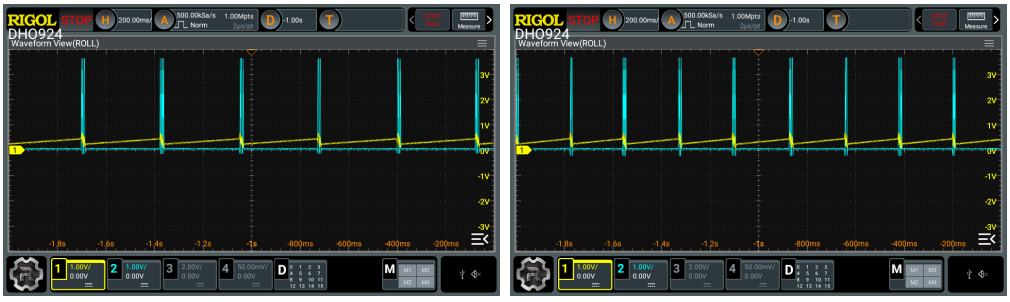


Figure 4.15: Oscilloscope capture of the PB response to 0.65 nA (left) and 0.95 nA (right) input current. The RTD shortens compared to the 0.65 nA case, as expected from increased input current.

To quantify the performance of the circuit, the inverse of the measured RTD (1/RTD) was plotted against the expected current from the calibrated current source. As shown in Figure 4.16, the relationship is approximately linear, consistent with the Q-Pix operating principle: a constant input current results in a regular reset interval inversely proportional to the current magnitude. This measurement confirms that the PB circuit performs the time-to-charge conversion accurately and consistently across a representative current range.

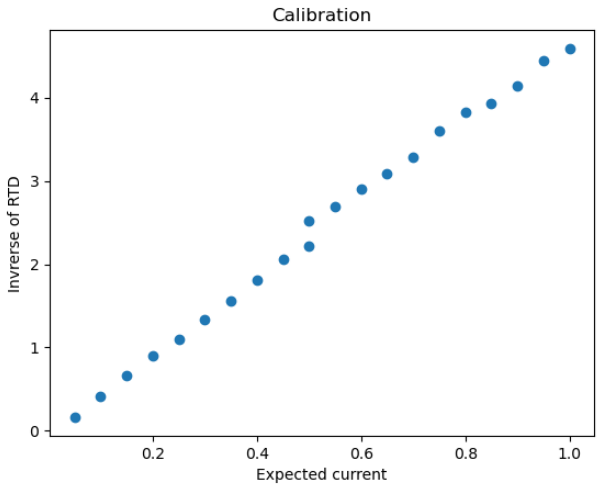


Figure 4.16: Calibration curve for the PB prototype. The inverse of the RTD shows an approximately linear relationship with the expected input current from the calibrated nanoampere source, confirming the validity of the time-to-charge encoding mechanism. The error bars are smaller than the data point markers and are not visible at this scale.

These calibration measurements were performed at room temperature to establish baseline performance of the PB circuit prior to cryogenic deployment. The observed linearity and repeatability of the replenishment timing behavior confirm that the circuit performs reliably under controlled conditions and is ready for further validation in liquid argon. This warm test campaign serves as an essential intermediate step, ensuring that the analog front-end and time-to-charge encoding mechanism are well-understood before

subjecting the system to the challenges of cryogenic operation.

4.5.3.3 Toward Multi-Channel and Cryogenic Deployment

With the successful validation of the PB prototype at room temperature, the next stage of development is focused on scaling the system to a 64-channel Q-Pix-ASIC prototype and demonstrating its performance in liquid argon. This ongoing effort is planned to be carried out using the UTA-Harvard (UTAH) TPC, a vertically oriented cylindrical time projection chamber designed for precision detector R&D in cryogenic environments. A photograph of the assembled system is shown in Figure 4.17, along with a set of detailed CAD views of the field cage and mounting infrastructure.

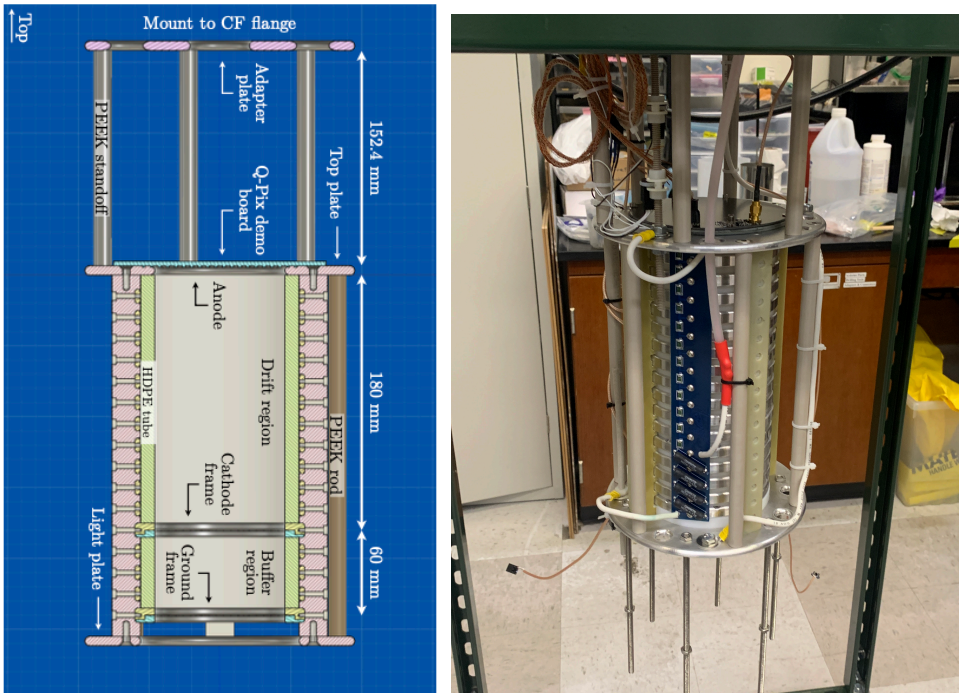


Figure 4.17: Left: Schematics diagram of the UTAH TPC field cage. Right: Photograph of the UTAH TPC, a vertically mounted cylindrical time projection chamber for LAr R&D. Modular field-shaping rings and mounting structures accommodate a 64-channel Q-Pix readout system.

The UTAH TPC features a cylindrical field cage with a 92 mm inner radius and a total drift length of 255 mm. The cage consists of field-shaping rings spaced along the vertical drift axis. The rings are connected via a resistive divider chain to maintain a uniform drift field, nominally operated at 500 V/cm. A mesh cathode sits at the base of the drift volume, while an anode mesh and signal collection region are located at the top. Simulations confirm that the electric field is uniform to within 1% across the active region, ensuring reliable charge transport.

The cryogenic deployment is supported by a well-characterized LAr fill and purification procedure developed for the UTAH TPC. The TPC is lifted into position using a crane and seated on a thermal insulation platform, while an environmental fans are used to prevent condensation around the signal interface. This infrastructure enables stable cooldown and high-purity conditions for extended operation. For the planned tests, the nominal drift length of approximately 12.8 cm and an operating drift field of 100 V/cm correspond to a maximum drift time of roughly 80 μs, which defines the expected reset pulse interval range for the Q-Pix system during cosmic muon and α-source calibration studies.

The physics-readout capability of the Q-Pix system in LAr will be tested with two main event sources; ^{241}Am source and cosmic-ray muons. For the ^{241}Am source, a thin, needle-like encapsulation will be inserted into the drift volume. The α particles emitted by this source will produce short, localized ionization clusters. In addition, the vertical geometry of the TPC makes it well suited to capture cosmic-ray muons, which generate extended ionization tracks traversing the full drift region. These complementary signals will provide clear benchmarks to evaluate spatial resolution, temporal stability, and event reconstruction using Q-Pix's time-to-charge encoding.

The development of the PB prototype and its ongoing integration into the UTAH

TPC mark a pivotal point in the experimental realization of Q-Pix. The modular architecture, validated calibration methodology, and upcoming cryogenic deployment collectively demonstrate the feasibility of scaling Q-Pix from a conceptual circuit to a functioning, physics-capable readout system.

These efforts provide the foundational hardware needed to explore Q-Pix's strengths in low-energy ionization signal detection—particularly in the context of rare-event physics. In the next chapter, this potential is examined through a detailed study of Q-Pix's sensitivity to supernova neutrino bursts, where the architecture's fine-grained temporal resolution and self-triggered design offer unique advantages in capturing low-energy, time-structured signals.

Remember to look up at the stars and not down at your feet. Try to make sense of what you see and wonder about what makes the universe exist. Be curious.

Stephen Hawking

5

Q-Pix Supernovae studies

Stars have always captivated us with their brilliance, quietly twinkling in the night sky. For most of their lives, they shine with a steady rhythm, fusing lighter elements into heavier ones in a slow, burning harmony. They have guided sailors across oceans and inspired stories sung across generations. Some stars, like our Sun, will one day dim and fade in silence, transitioning gracefully into white dwarfs—a quiet coda to a long-lived stellar symphony. But others, those with at least eight times the mass of our Sun, are

destined for a far more dramatic finale. These massive stars end not in fading light, but in a final, resonant crescendo: a core-collapse supernova, the dying chord of a stellar life played at full cosmic volume.

This chapter is devoted to those fleeting neutrinos. We explore how Q-Pix, with its quiet vigilance and exquisite timing, is uniquely suited to capture the earliest whispers of a supernova burst. These are not the high-energy collisions of accelerator beams, but subtle impressions from deep space—low-energy, untriggered events that unfold over tens of seconds, requiring a detector that listens patiently and responds precisely.

Building on the architectural foundation laid in the previous chapter, we now consider how Q-Pix can elevate DUNE's sensitivity to supernova neutrinos. Q-Pix's time-to-charge encoding, low detection threshold, and continuous readout make it an ideal instrument for this rare but information-rich phenomenon. The study presented here forms the basis of my co-published work [87] and demonstrates how, in the hands of Q-Pix, DUNE becomes not just a long baseline neutrino experiment, but an astrophysical observatory—attuned to the dying notes of distant stars.

5.1 Supernova explosion

The path to this final crescendo is forged through nuclear fusion. Over the course of millions of years, massive stars evolve through a series of nuclear burning stages, using progressively heavier elements as fuel: hydrogen, helium, carbon, neon, oxygen, and silicon. In each stage, these elements fuse into heavier ones, causing the star's core to grow increasingly hot and dense. The energy from these nuclear reactions provide an outward pressure that counterbalances the inward pull of gravity. When one type of fuel is exhausted, the star contracts, heats up, and ignites the next fuel source, typically

the fusion product of the previous stage. While hydrogen and helium burning can last millions of years, the final burning phase with silicon only lasts for about two weeks. Silicon burning produces iron-group nuclei, marking the last exothermic fusion process. From this point on, no further fusion can release energy. As the core temperature continues to rise, high-energy gamma rays begin to break down iron nuclei into lighter components—a process known as photodisintegration. This reaction absorbs energy, further reducing the pressure within the core and accelerating its collapse. With no fusion left to sustain the star and energy being actively consumed by nuclear disintegration, the core—now a dense mass of iron—collapses under its own weight at nearly a quarter of the speed of light. The collapse is abruptly halted by the short-range repulsive nuclear force, sending a shock wave surging outward. This rebounding shock is the true identity of a core-collapse supernova, unleashing a torrent of energy that briefly rivals the combined luminosity of an entire galaxy [90]. Though not the most energetic explosion in the universe, it is among the most luminous and most revealing—an astrophysical event where gravity, quantum mechanics, and nuclear physics collide in a single moment. This is the iron-core collapse supernova, the dominant pathway for the death of massive stars.

Alternative collapse scenarios exist. One such example is the electron-capture supernova (ECSN), in which a degenerate oxygen-neon-magnesium core succumbs not to photodisintegration, but to electron capture. These ECSN models—such as those developed by the Garching group—present distinct dynamics and neutrino emission signatures, which will be explored in detail in Section 5.3.1.

Starting from the core collapse of the star, approximately 99% of the gravitational binding energy will be carried away by neutrinos, totaling around 3×10^{53} ergs (3×10^{46} jouls) over about 10 seconds—equivalent to 2×10^{12} times the Sun's total energy

output over one year [91]. The vast majority of these neutrinos escape the star and travel across the universe, offering a unique glimpse into the supernova's core processes before any light signal arrives at Earth. The sequence of events leading to a core-collapse supernova is visually depicted in Figure 5.1.

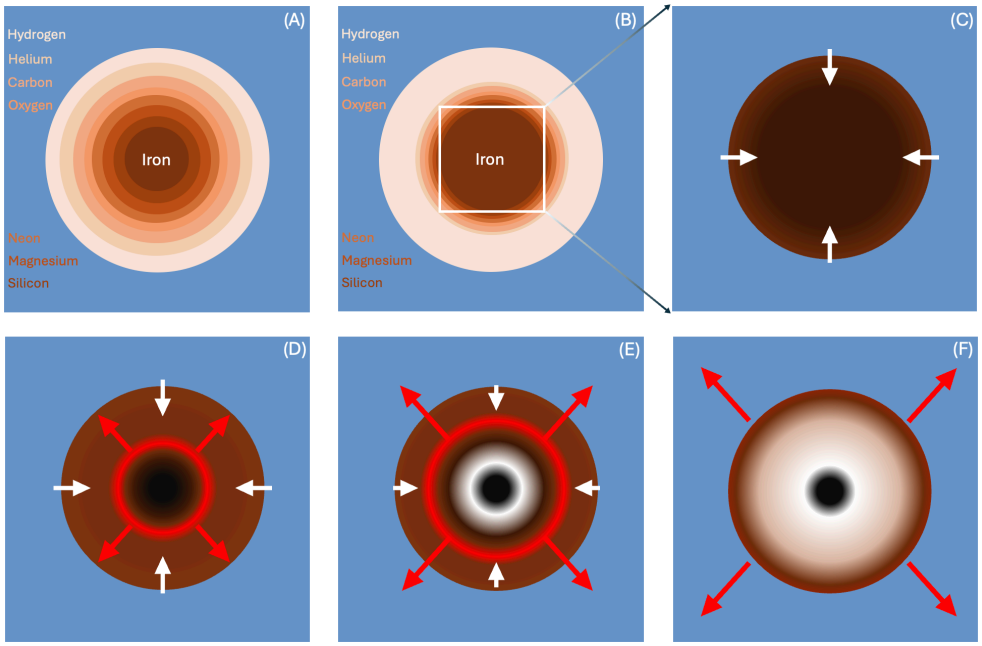


Figure 5.1: Illustration of the core-collapse supernova mechanism. (A) A massive star evolves through successive nuclear burning stages, forming an onion-like structure with progressively heavier elements toward the center. (B) As silicon burning ceases, an inert iron core forms and continues to grow. (C) With no fusion left to support it and photodisintegration of iron nuclei removing thermal pressure, the core becomes unstable. (D) The core collapses at relativistic speeds until halted by nuclear repulsion in the inner core. (E) This abrupt halt generates a rebounding shock wave that propagates outward through infalling material. (F) The shock wave, potentially revived by neutrino heating, ejects the outer layers in a supernova explosion.

5.2 Supernovae Neutrinos

The journey to the first discovery of supernova neutrinos began with a silent signal that arrived before dawn on February 23, 1987. At 16:35:35 JST, the Kamiokande

experiment in Japan recorded a sudden burst of neutrinos—lasting just 13 seconds—originating from a stellar explosion in the Large Magellanic Cloud. At the time, however, the event did not trigger any immediate alarms or recognition; the signal was quietly logged without being flagged as unusual. It wasn't until February 25, when a faxed message from the University of Pennsylvania reached the University of Tokyo (see Figure 5.2, left), that the significance of this fleeting signal came to light. Prompted by this external alert, the Kamiokande team began a detailed re-analysis of their data on February 27—discovering that they had, unknowingly, recorded the first glimpse of supernova neutrinos, hours before the light from the explosion was observed on earth.

In a small personal twist of fate, that date—February 27—would become my birthday exactly ten years later. Just as Kamiokande turned its eye to the data and unearthed a new window into the cosmos, so too has that date marked the beginning of my own journey into neutrino physics. The serendipity of it is hard to ignore.

As shown in the right panel of Figure 5.2, the burst signal reveals a sharp peak and, just before it, a two-minute gap—caused by a brief maintenance downtime. Had that pause lasted any longer, the discovery might never have happened. Instead, this remarkable event revealed that neutrinos precede light in a supernova, offering humanity both a deeper understanding of stellar collapse and a powerful early warning mechanism for future cosmic events [92].

These neutrinos, emitted during the collapse of a massive star, typically carry energies in the range of a few to several tens of MeV—distinctly higher than those of solar neutrinos but well below the GeV-scale neutrinos studied in accelerator experiments. This intermediate energy regime presents both a challenge and an opportunity: it requires detection technologies capable of low thresholds, fine time resolution, and efficient background suppression, especially when aiming to extract information beyond

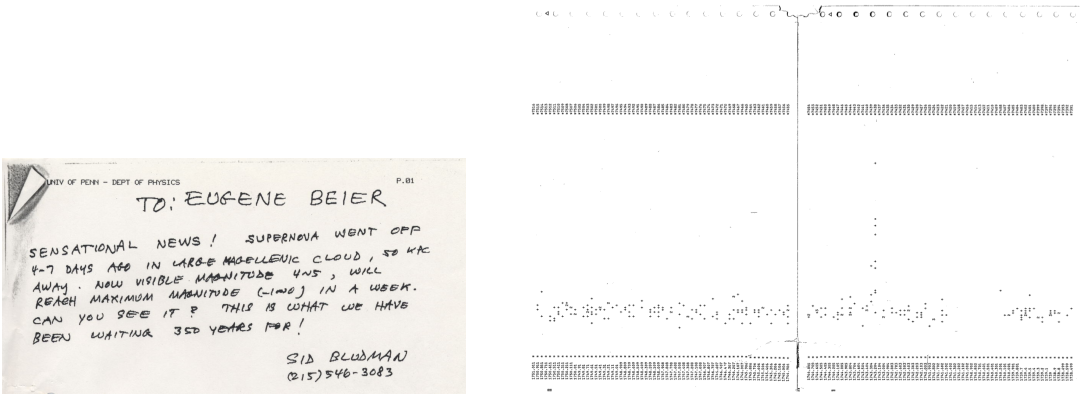


Figure 5.2: The left photo shows the faxed message sent from the University of Pennsylvania to the University of Tokyo on February 25, 1987, alerting the Kamiokande team to the recent observation of supernova SN1987A. In response, the team requested the relevant data, which was subsequently sent via physical mail and arrived two days later. The right image displays this mailed data printout, showing the burst of neutrino events detected on February 23. The events are read from right to left, with a pronounced peak followed by a quiet two-minute gap that occurs just a few minutes prior. This gap corresponds to a scheduled detector maintenance pause. Remarkably, had this maintenance been delayed by just four additional minutes, Kamiokande would likely have missed the entire neutrino burst. Photos taken from [93].

the mere presence of a supernova.

Despite the great opportunities that early supernova detection would provide, those neutrinos can be more than just an indicator of the occurring of supernovae-they could be an effective probe in astrophysics and particle physics. Thus far, the direct detection of neutrinos from SN 1987A by three experiments, Kamiokande [92], Irvine-Michigan-Brookhaven (IMB) detector [94], and Baksan underground scintillation telescope [95], confirmed several aspects of supernova astrophysics and demonstrated how such observations can deepen our understanding of fundamental neutrino properties. The unique dying star environment that supernova neutrinos travel through of the exploding star cannot be reproduced in terrestrial experiments. The interior consists of multiple layers of stellar material with wildly varying densities, reaching $\rho \sim 10^{12}\mathrm{g/cm}^3$ at its maximum , to be compared to the density of Earth, $\rho \sim 3\mathrm{g/cm}^3$. The extreme environment

induces complex interaction effects, including the intense matter effect and collective neutrino-neutrino interactions, which simultaneously influence the full range of neutrino flavor evolution [96].

Detecting the energy spectra and fluxes of these neutrinos provides a rare opportunity to test our understanding of physics under such extraordinary conditions, far beyond the reach of current terrestrial experiments [97, 98, 99, 100]. In the era of multi-messenger astronomy, advanced neutrino detection technologies is essential to achieve a high-statistics characterization of the supernova neutrino burst, which will enables deeper insights into such studies of the behaviour of neutrinos.

A future galactic supernova, plausibly occurring within the coming decades, would offer an unparalleled opportunity to significantly improve measurements such as neutrino mass ordering [101], the neutrino halo model [102], and the neutrino magnetic moment [103]. Unlike SN 1987A, which was detected primarily via inverse β decay in water Cherenkov detectors, the next-generation neutrino experiments such as DUNE will provide sensitivity to the charged-current interactions of electron neutrinos with argon nuclei, enabling an independent and complementary view of supernova neutrino physics. To fully exploit such an event, next-generation neutrino experiments must be capable of precisely measuring the energy, timing structure, and flavor composition of the supernova neutrino spectrum, enabling unprecedented insights into both astrophysical and fundamental neutrino properties [104, 105, 106, 107, 108]. In the following sections, I examine the role of Q-Pix as a candidate technology for the next-generation DUNE experiment. By leveraging its intrinsic 3D spatial resolution and low-noise capabilities, Q-Pix has the potential to improve event reconstruction efficiency, background discrimination, and supernova burst triggering, making it a compelling alternative to traditional wire-based readout systems. The feasibility of Q-Pix is explored to en-

able high-precision measurements of low-energy events such as supernova neutrinos, contributing to the broader effort of multi-messenger astrophysics and the real-time detection of the next nearby supernova, such as SNEWS (SuperNova Early Warning System).

5.3 Simulation Framework for Supernova Neutrino Studies

A key area of interest for multi-kiloton-scale LArTPC experiments is the exploration of low-energy (<100 MeV) physics, which can significantly expand the scientific reach of LArTPC detectors [109, 110]. Measurements of MeV-scale activity from accelerator neutrino interactions [111], radiogenic backgrounds [112, 113], and Michel electrons [114, 115, 116] have already been conducted by the ArgoNeuT [117], LArIAT [118], MicroBooNE [119], and ICARUS[120] experiments. The potential for low-energy physics of large LArTPCs has been studied for solar neutrinos[121, 122], accelerator neutrinos [123, 109], hidden sector particles [124, 125], Weakly Interacting Massive Particles (WIMPs) searches [126], $0\nu\beta\beta$ [127], and supernova neutrinos [106, 109]—the primary focus of study presented in this chapter.

The following subsections detail the simulation framework used to quantify the enhanced physics reach by Q-Pix, compared to a traditional wire-based readout. Subsection 5.3.1 provides an overview of the supernova neutrino event generator and supernova neutrino model employed in the analysis. Sub-section 5.3.2 describes the characterization of radiogenic backgrounds in the detector that can mimic supernova neutrino signatures. Finally, sub-section 5.3.3 details the Q-Pix readout simulation.

5.3.1 Supernova Neutrino Signal Modeling

The simulation of supernova neutrino events in this study is based on the supernova luminosity, energy, and time distributions provided by the "Garching" electron-capture supernova model [128]. This type of supernova occurs less frequent, and is triggered by electron-capture. In this type of process, the star is supported by the electron degeneracy pressure of the core. When those electrons start to be captured by ^{20}Ne, the number of electron reduces decreasing the degeneracy pressure, which then triggers the core-collapse. This scenario involves a lower core mass compared to iron-core collapse supernovae, leading to a weaker explosion and a shorter-duration neutrino burst. Because the Garching model predicts the lowest number of neutrino interactions among standard supernova models, it was selected as a conservative benchmark for this study. Rather than performing a dedicated simulation with **SNOwGLoBES** (SuperNova Observatories with GLoBES) [129], we adopted event rates and spectra from previous DUNE studies [106] that utilized this tool. SNOwGLoBES is a widely used software package for simulating expected neutrino signals from core-collapse supernovae across various detector technologies, including LArTPCs. It extends the General Long Baseline Experiment Simulator (GLoBES) framework to provide detailed predictions of event rates, energy spectra, and time-dependent signals. Following common practice in the literature [130, 131, 132, 133], a supernova distance of 10 kiloparsecs (kpc) is assumed, yielding the event rates listed in Table 5.1. The corresponding energy and timing distributions, shown in Figure 5.3, are used as inputs for the subsequent event reconstruction analysis.

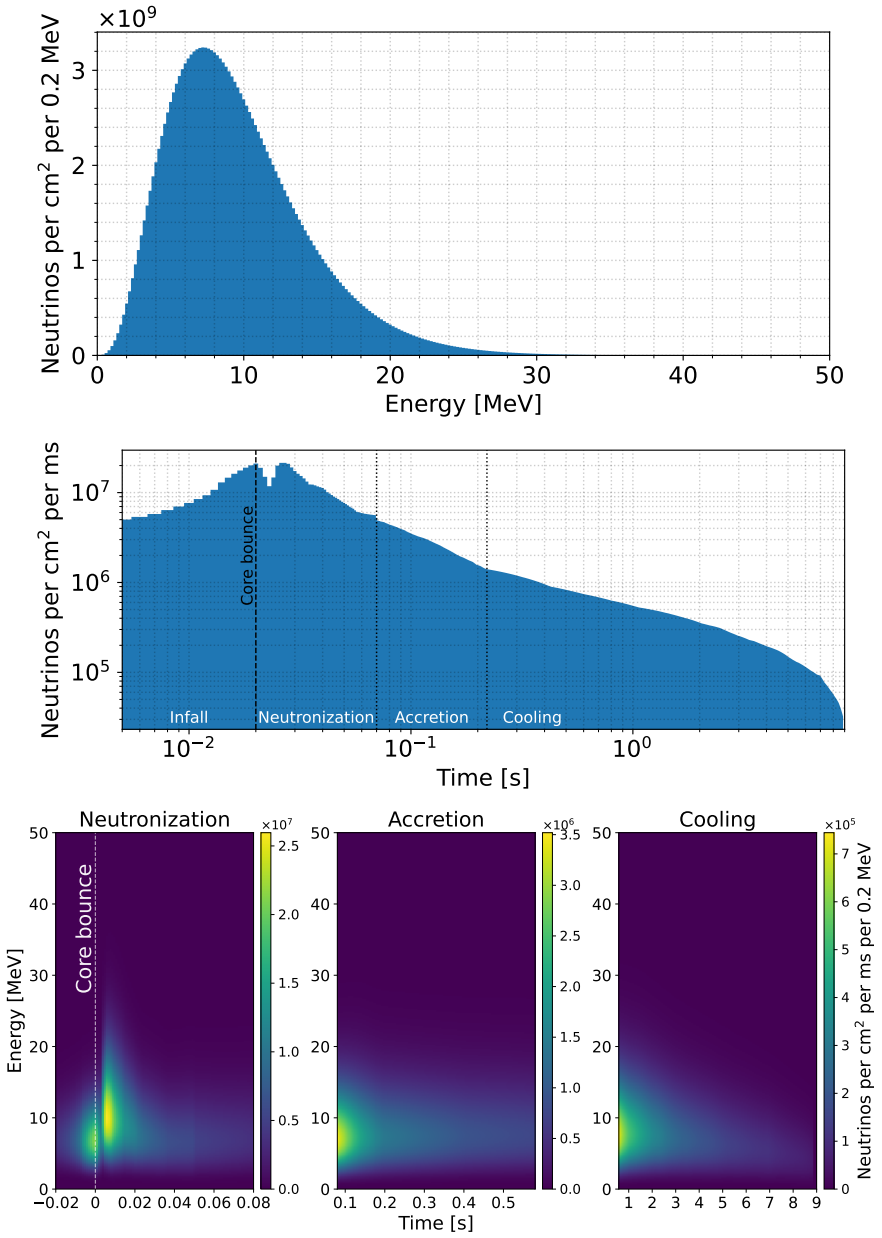


Figure 5.3: Simulated neutrino emission from a core-collapse supernova at 10 kpc, based on the Garching electron-capture model. Top: Total neutrino fluxes as a function of time for all flavors. Middle: Time-integrated energy spectra of ν_e neutrinos separated by emission phase (neutronization, accretion, and cooling). Bottom: Time evolution of the ν_e flux, showing the characteristic temporal structure of each phase. These spectra serve as input for evaluating Q-Pix's sensitivity to supernova neutrinos.

Interaction channel	Type	Number of events
$\nu_e + {}^{40}\mathrm{Ar} \to e^- + {}^{40}\mathrm{K}^*$	CC	220
$\bar{\nu}_e + {}^{40}\mathrm{Ar} \to e^+ + {}^{40}\mathrm{Cl}^*$	CC	5
$\nu_e + e^- \to \nu_e + e^-$	ES	19
$\bar{\nu}_e + e^- \to \bar{\nu}_e + e^-$	ES	4
$\nu_\mu + e^- \to \nu_\mu + e^-$	ES	3
$\bar{\nu}_\mu + e^- \to \bar{\nu}_\mu + e^-$	ES	2
$\nu_\tau + e^- \to \nu_\tau + e^-$	ES	3
$\bar{\nu}_\tau + e^- \to \bar{\nu}_\tau + e^-$	ES	2

Table 5.1: Predicted number of events for each interaction channel in 10 kton of liquid argon for a core-collapse supernova at 10 kpc, based on SNOwGLoBES simulations. Interaction types are labeled as CC (charged current) or ES (elastic scattering).

These event rates can also be visualized in terms of the total deposited energy, as shown in Figure 5.4. The ν_e CC events dominate the overall yield, but the much rarer elastic scattering (ES) events, shown in blue, are of particular importance due to their directional sensitivity, as will be discussed later.

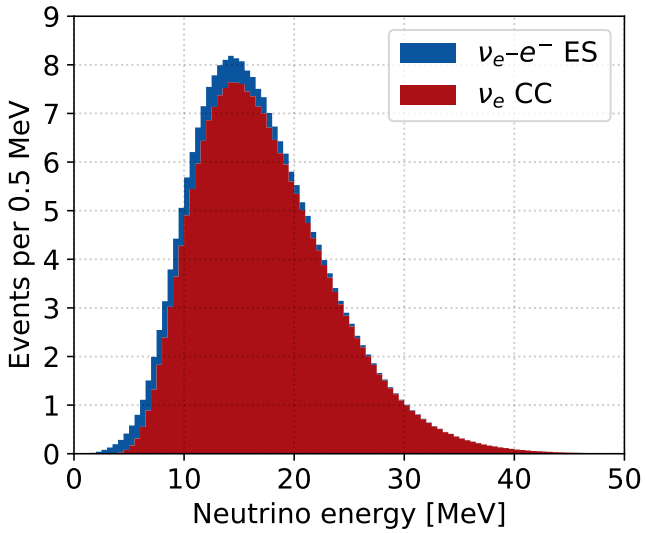


Figure 5.4: Stacked energy spectrum of supernova neutrino interaction with 220 ν_e CC (red) and 19 ν_e–e^- ES events (blue) in 10 kton of liquid argon computed using SNOwGLoBES. Plot taken from Ref.[87].

Once the predicted event rates from a SN are obtained, the interactions of these

neutrinos need to be simulated. For the simulation of supernova neutrino–nucleus interactions, this study employs the **MARLEY** (Model of Argon Reaction Low Energy Yields) event generator [134, 135], which simulates the initial neutrino-nucleus interactions as well as the subsequent nuclear de-excitation, producing a list of final-state observable particles. In this analysis, only ν_e CC interactions and ν_e–e^- ES events were considered:

$$\begin{aligned} \nu_e + {}^{40}\mathrm{Ar} &\rightarrow e^- + {}^{40}\mathrm{K}^* \qquad \text{(Charged Current)} \\ \nu_e + e^- &\rightarrow \nu_e + e^- \qquad \text{(Elastic Scattering)} \end{aligned} \tag{5.1}$$

Electron antineutrino ($\bar{\nu}e$) interactions, as well as NC interactions from all neutrino flavors—including muon and tau neutrinos ($\nu\mu$, ν_τ) and their antiparticles—were not included in this study. This choice was made conservatively to focus on the dominant detection channels: ν_e CC and ν_e–e^- ES interactions. While these neglected channels contribute non-negligibly to the total signal, especially through NC excitation of ^{40}Ar, their event rates are significantly lower than those of ν_e CC and ES in the context of a Garching electron-capture supernova. Their inclusion would only serve to enhance the total signal, thereby improving sensitivity beyond what is reported here.

5.3.2 Radiogenic Background Modeling

For evaluating supernova burst detection capabilities, it is essential to account for background events originating from radiogenic sources within both the detector materials and the bulk liquid argon. Previous DUNE studies [106, 136] applied a minimum energy threshold of 5 MeV, effectively excluding most radiogenic backgrounds. However, a detailed analysis of low-energy detection performance necessitates an explicit treatment of these backgrounds, in order to properly evaluate supernova bursts.

An initial estimate of relevant isotopes and their activities was obtained from [137] and is summarized in Table 5.2. Given that a typical supernova neutrino burst unfolds over approximately 10 seconds (see Figure 5.3), background rates were evaluated over the same time window. Simulations incorporated approximately 842,000 primary radioactive decays randomly distributed in time across this interval. To model equilibrium conditions, all isotopes were assumed to be in secular equilibrium at t=0 s.

Isotope	Rate [Bq/kg]	Region	Region mass [kg]	Rate [Bq]	Number of decays (per 10 s window)
^{210}Po	0.2	PD [Bq/m^2]	2.46856	0.493712	5
^{60}Co	0.0455	CPA	90	4.095	41
^{40}K	0.49	APA	258	1,264.2	12,642
^{39}Ar	1.010	bulk LAr	∼70,000	70,700	707,000
^{42}Ar	0.000092	bulk LAr	∼70,000	6.44	64
^{42}K	0.000092	bulk LAr	∼70,000	6.44	64
^{222}Rn	0.04	bulk LAr	∼70,000	2,800	28,000
^{214}Pb	0.01	bulk LAr	∼70,000	700	7,000
^{214}Bi	0.01	bulk LAr	∼70,000	700	7,000
^{85}Kr	0.115	bulk LAr	∼70,000	8,050	80,500

Table 5.2: Summary of radiogenic background sources considered in this study, based on activity estimates from [137]. Only the principal isotopes from major decay chains are included, providing a first-order approximation appropriate for evaluating supernova neutrino detection sensitivity. More detailed study is needed for solar neutrino studies as detailed in Section 6.4.

Each decay was spatially generated based on the physical origin of the emitting material. For isotopes within the liquid argon, decays were distributed uniformly throughout the active volume. For backgrounds originating from structural components such as the cathode and anode, event locations were sampled according to the geometry of DUNE FD, detailed in [29]. When isotopes produced unstable daughters, such as in the decay chain of ^{214}Bi to ^{210}Po, subsequent decays were included with their characteristic lifetimes to capture time-correlated activity.

The pixel-based readout introduces additional material, including PCBs as potential sources of radiogenic backgrounds. However, in addition with the feasibility of producing

low-background PCBs [138, 139, 140], the enhanced discrimination capabilities offered by the Q-Pix readout, suggest that these backgrounds will be small and can be effectively mitigated.

Figure 5.5 shows the energy and timing spectra of both the signal and background events simulated in this analysis.

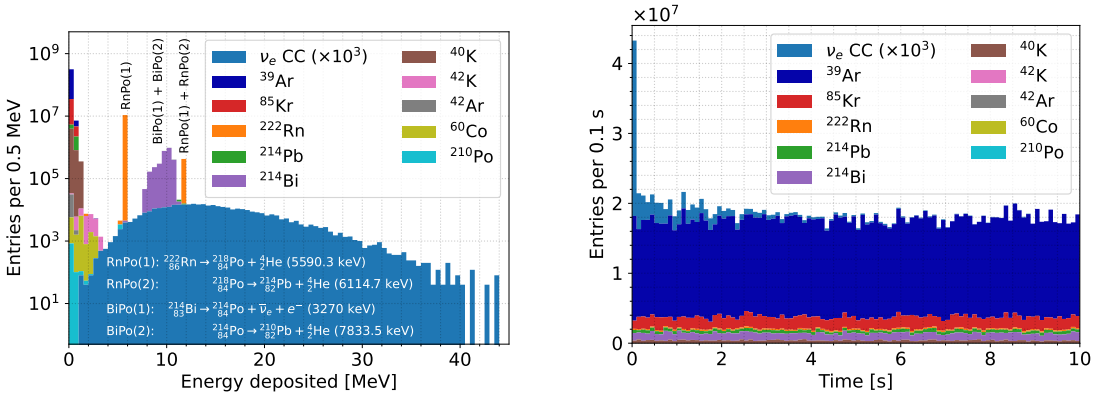


Figure 5.5: Left: stacked histogram of the simulated deposited energy of the signal event, ν_e CC (magnified by $\times 10^3$) in a typical supernova simulation over 10 seconds and of the simulated radiogenic background events. Right: stacked histogram of the timing profile of events hits from simulated supernova signal and radiogenic background events. Figures taken from Ref.[87].

5.3.3 Q-Pix Response Simulation

The Q-Pix simulation framework consists of two primary `C++`-based packages, simulating single DUNE APA drift volumes (one volume consists of a 2.3×6 m^2 charge collection/readout plane with a 3.6 m drift length). The first is a Geant4-based package [141, 142, 143] that simulates particle interactions and energy depositions within a liquid argon volume. Its output consists of trajectory segments, referred to as "hits", each recording spatial coordinates, timing, and deposited energy. The second is a Q-Pix-specific package that processes these hits by converting them into ionization electrons,

which are then propagated to a simulated pixelated anode plane to simulate the response of the Q-Pix electronics with the Rest Scheme as described in Section 4.4.1. This stage includes modeling of relevant detector effects such as recombination (via the modified box model), electron lifetime attenuation, and drift-time-induced diffusion. Once electrons reach the anode, the pixel response is simulated by calculating RTDs: each pixel integrates incoming charge and resets when a threshold is exceeded. The final output is a set of RTDs and pixel addresses, corresponding to the digitized output that a real Q-Pix system would produce.

This process is done by converting Geant4 hits into ionization electrons using an assumed average energy required to create an ion pair in LAr, which is 23.6 eV per electron. The simulation then applies recombination effects, where electrons emitted by ionization get thermalized by interactions with the surrounding LAr and recombine with nearby ions. The "modified box" model [144, 55] is used to remove recombined electrons from further consideration. The remaining ionization electrons are uniformly distributed in time between the start and end of the Geant4 hit. Next, the drift time of each electron was computed in order to determine the attenuation of arriving signal due to electron's lifetime and position smearing arouse from longitudinal and transverse diffusion. This process was performed for every ionization electron associated with each Geant4 hit in each event. The electrons are then sorted by drift time, and their final positions are obained. They are then grouped based on their positions on pixel collection plane, in terms of the $4 \times 4\text{mm}^2$ pixels. The resulting output is an array of hit pixels, each containing an array of time-sorted electrons.

Q-Pix resets are produced by integrating the charge on each pixel within a 10 ns time step. This time step was assumed to be exact for simplicity, which is small enough compared to microseconds-level events. At each time step, equivalent noise charge is

added to the signal to simulate the behavior of the Q-Pix front-end electronics in Reset Sceheme, mimicking the expected performance of the ASIC. The leakage current present in the front-end electronics is considered a sub-leading noise component. Since no prototype ASIC had been produced at the time of this study, the leakage was assumed to be 100 aA, a value chosen based on the measured leakage current of the LArPix ASIC [145], which shares similar technological and geometric considerations with Q-Pix. Additionally, this simulation assumes that no charge is lost or perturbed during a reset. This assumption is supported by the feasibility of implementing charge-conserving techniques in the ASIC design, such as charge-pump front-end architectures as Replenishment scheme discussed discussed in Subsection 4.4.2. Any potential charge loss can ultimately be calibrated and corrected, making this a reasonable approximation.

When a pixel accumulates a sufficient number of electrons to trigger a reset (i.e., 6250 electrons, or 1 fC), the time stamp and pixel ID are logged, and the charge is drained from the pixel. This simulation steps closely mirrors the actual response of the electronics and replicates the expected data format. The pixel ID and reset times are then stored in the same **ROOT** file as the Geant4 information [146]. The various parameter values used in this study are summarized in Table 5.3. Additionally, the RTD code can be configured to generate current profiles, which can be exported to be used in external simulation software. An example of such a current profile, along with the corresponding reset timestamps, is shown in Figure 5.6, illustrating the response of an identical event placed at two different drift distances, at 10 cm and 150 cm. The difference in drift distance has a large effect on the charge collection and electronics response, as can be infered from the differences in the visualized current profile and the corresponding number and frequency of resets.

Parameter	Value
W-value for ionization in LAr	23.6 eV/e^-
Drift electric field	500 V/cm
Drift velocity	164,800 cm/s
Longitudinal diffusion	6.8223 cm^2/s
Transverse diffusion	13.1586 cm^2/s
Electron lifetime	0.1 s
Reset threshold	1 fC (6250 e^-, or 147.5 keV in LAr)
Sampling time	10 ns

Table 5.3: Summary of the physical parameters used in this study for Q-Pix simulations.

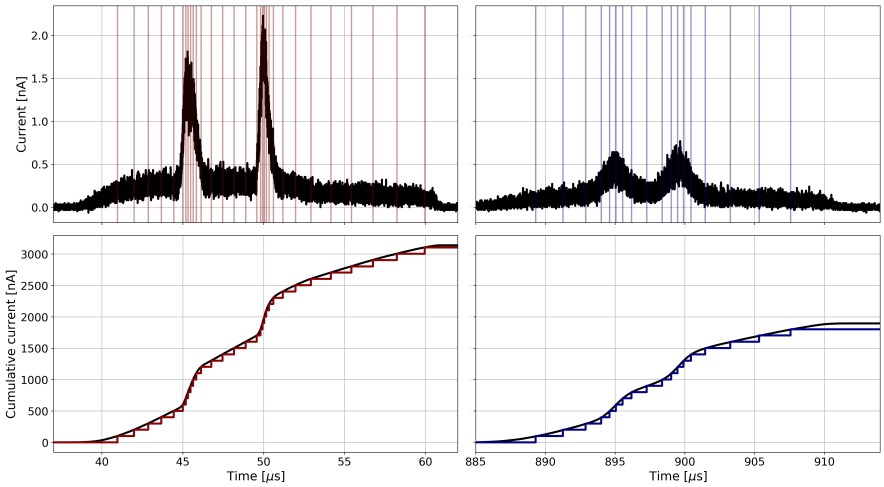


Figure 5.6: Examples of the current profiles (black lines) produced with the Q-Pix simulation package. The corresponding resets can be seen as the vertical lines on the top plots, each representing a 1 fC accumulation. The left plots and right plots represent the drift distance of 10 cm and 150 cm, respectively. Plots taken from Ref.[87].

5.4 Performance of Q-Pix Readout for Supernova Neutrino Detection

In this section, the results of this study are discussed. Subsection 5.4.1 presents the improvements in energy reconstruction offered by Q-Pix, with a particular emphasis on low-energy events below 5 MeV, which wasn't explored by previous DUNE studies [106, 136]. This section presents a comprehensive study of Q-Pix's capabilities for detecting

supernova neutrinos. It outlines the clustering algorithm developed to isolate burst-like activity from background, describes how the asynchronous architecture naturally suppresses data rates, and evaluates the feasibility of using Q-Pix as part of the SuperNova Early Warning System (SNEWS). The analysis also examines Q-Pix's potential to identify the onset of a supernova burst and to reconstruct the direction of the incoming neutrinos using its intrinsic three-dimensional tracking.

5.4.1 Low-Energy Energy Reconstruction with Q-Pix

In order to enable direct comparison with other studies, an energy reconstruction procedure was developed to relate the charge collected via Q-Pix resets to the true neutrino energy. The reconstructed energy depends sensitively on several factors, including 3D event topology, drift length, and diffusion effects. To account for these, a correction matrix was constructed based on a detailed simulation of electron tracks in liquid argon. This procedure follows the approach outlined in previous supernova studies by DUNE [106].

Single electrons were simulated isotropically at various energies relevant to supernova neutrino interactions, and at multiple drift distances throughout the detector. From these data, a conversion matrix was derived to map the number of observed Q-Pix resets to the true deposited energy, as a function of drift distance. The simulation was performed with 0.1 MeV steps in electron energy and 50 cm increments in drift distance, allowing for fine-grained correction across the detection volume, especially at low energies (<5 MeV). This correction process serves as an effective calibration, compensating for the charge loss and temporal smearing that occur during drift and diffusion.

In the reconstruction studies, it was assumed that an external photon detection sys-

tem could provide drift distance measurements with an uncertainty of ±25 cm, enabling event-by-event application of the correction matrix. The correction was applied solely to facilitate comparisons with other studies by adjusting for drift-dependent attenuation and improving energy linearity.

As shown in Figure 5.7, the uncorrected reconstructed energy displays a linear trend but underestimates the true neutrino energy, particularly at higher energies. The application of the correction matrix improves the agreement by aligning the slope with the true energy scale. A small residual offset remains, which could be further reduced through more refined calibration strategies.

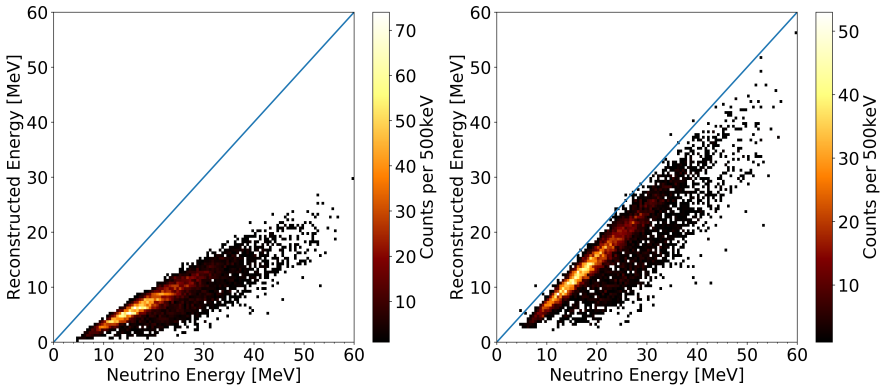


Figure 5.7: Left: Reconstructed energy for supernova events as a function of true neutrino energy without energy correction. Right: Reconstructed energy after applying the correction matrix. The correction acts as an effective calibration that restores linearity between observed charge and neutrino energy. Plots adapted from [87].

5.4.2 Event Reconstruction Efficiency

To evaluate the Q-Pix readout's performance, this study adopts two complementary efficiency metrics: event reconstruction efficiency and event identification efficiency. Event reconstruction efficiency is defined as the fraction of supernova neutrino events

for which the total deposited energy exceeds a specified threshold and produces a reconstructable signal in the detector. It reflects the intrinsic sensitivity of the system to low-energy interactions, regardless of background.

In contrast, event identification efficiency (introduced in the next subsection) is defined at the reset level within each event—quantifying the fraction of signal-induced resets that are correctly grouped into clusters and retained after background rejection. Together with event identification purity, these metrics evaluate how effectively the reconstruction algorithm distinguishes signal from radiogenic background based on track topology.

Figure 5.8 shows the event reconstruction efficiency for two minimum energy thresholds (1 MeV and 5 MeV), demonstrating that Q-Pix maintains high efficiency even at lower neutrino energies compared to the DUNE wire-based readout [106].

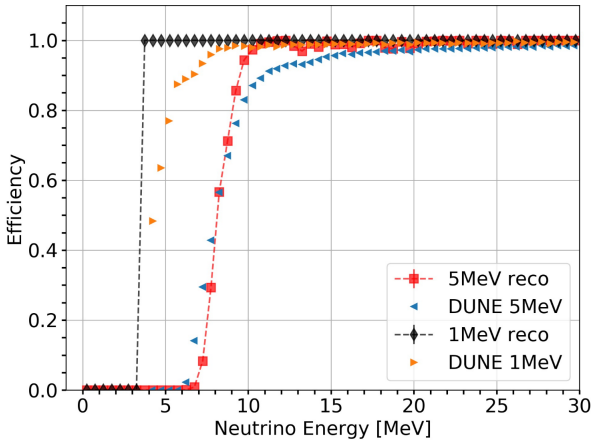


Figure 5.8: Supernova event reconstruction efficiency as a function of true neutrino energy is shown. Red and black represents for the minimum total deposited energy requirements, 5 MeV and 1 MeV respectively. For comparison, the efficiencies for DUNE from Ref. [106] are shown in blue triangles for a minimum of 5 MeV deposited and in orange triangles for a minimum of 1 MeV deposited. Plots taken from Ref.[87].

This advantage is attributed to Q-Pix's fine-grained 3D charge readout and low ef-

fective threshold, which together enhance sensitivity to faint signals.

5.4.3 Event Discrimination and Clustering Performance

In this work, radiogenic backgrounds have been explicitly included to make the supernova burst analysis more realistic. This addition necessitated the development of an event identification scheme capable of distinguishing background events from true supernova neutrino interactions. The Q-Pix readout provides both fine 3D spatial resolution and unique time-encoded charge information, which were leveraged to implement a clustering algorithm that reconstructs 3D tracks from resets. The algorithm was designed to discriminate events based on differences in track topology, using three tunable parameters: (1) the spatial clustering rule, (2) the RTDs, and (3) the minimum number of resets required to define a track. These parameters were jointly optimized to maximize background rejection without compromising sensitivity to low-energy neutrino signals.

The spatial clustering algorithm employed a simple nearest-neighbor rule, in which only adjacent pixels were considered part of the same cluster. This approach ensures that spatially or temporally separated energy depositions are reconstructed as distinct tracks. However, because this study prioritized enhancing the discrimination power between signal and background, this clustering choice came at the cost of some energy reconstruction efficiency. The main challenge lies in associating spatially displaced energy depositions within the same event. For instance, de-excitation photons produced in supernova neutrino interactions can travel significant distances from the primary electron track. As a result, resets triggered by these photons may form a separate cluster and be excluded from the energy reconstruction, leading to a systematic underestimation of the event energy.

To optimize the RTD threshold and the minimum cluster size, a dataset of 10,000 radiogenic background events and 10,000 supernova neutrino interactions was generated within a single DUNE-like volume. These samples were analyzed independently to tune the selection for maximal performance. As shown in Figure 5.5 (left), radiogenic background contributions are most significant below ∼5 MeV of deposited energy. Therefore, the optimization primarily targeted events with total energy ≤5 MeV, where the distinction between signal and background is most critical.

The event identification efficiency was defined as

$$\text{Event identification efficiency} = \frac{\text{Number of reconstructed signal resets}}{\text{True number of signal resets}} \tag{5.2}$$

within an event. The number of signal resets in a time window was calculated by summing the resets from all clusters that exceed the given reset threshold. In the similar manner, the event identification purity was defined as well, as

$$\text{Event identification purity} = \frac{\text{Number of reconstructed signal resets}}{\text{Number of reconstructed signal + background resets}} \tag{5.3}$$

within an event.

The efficiency and purity as a function of reset thresholds is shown in Figure 5.9, where each colored line represents a different reset threshold used for track reconstruction.

From this result, any time window from 2 μs to any significantly longer value could be used without affecting efficiency or purity. However, anchoring the threshold to the physical scale of longitudinal diffusion provides a natural and optimal choice.

For the DUNE APA configuration, with a maximum drift distance of 3.6 m and an electric field of $E = 500$ V/cm, the corresponding electron drift velocity is approximately

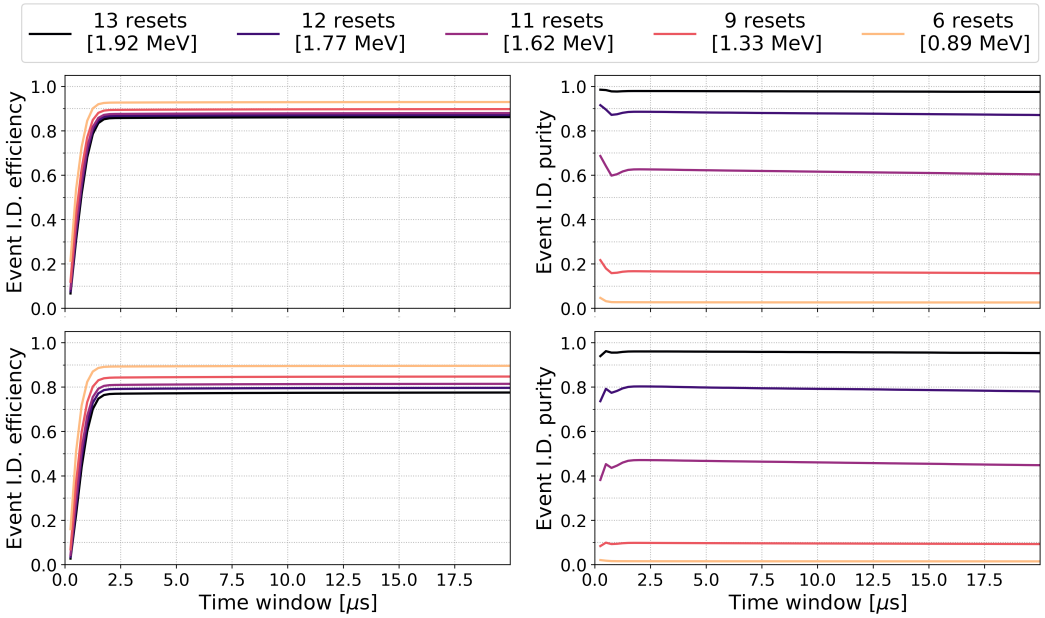


Figure 5.9: Top row: event ID efficiency (left) and purity (right) for the full supernova energy spectrum. The colors represent different reset thresholds. Bottom row: same as above, but only considering events with less than 5 MeV of energy in order to optimize the background reduction. Both are plotted as a function of the cluster time window. Plots taken from Ref.[87].

$v_d = 1.6$ mm/μs [147]. The longitudinal diffusion coefficient D_L can be estimated using the Einstein relation:

$$D_L = \frac{k_B T}{e}\mu, \tag{5.4}$$

where $T = 87$ K is the temperature of liquid argon and $\mu = v_d/E$ is the electron mobility. Substituting values gives:

$$D_L = \frac{1.38 \times 10^{-23}\ \text{J/K} \times 87\ \text{K}}{1.6 \times 10^{-19}\ \text{C}} \times \frac{1.6\ \text{mm}/\mu\text{s}}{500\ \text{V/cm}} \approx 7.2\ \text{cm}^2/\text{s}. \tag{5.5}$$

The corresponding temporal spread in arrival time due to diffusion, for a drift distance

$L = 360$ cm, is given by:

$$\sigma_t = \sqrt{\frac{2D_L L}{v_d^3}}. \tag{5.6}$$

Plugging in the values:

$$3\sigma_t = 3\sqrt{\frac{2 \times 7.2 \text{ cm}^2/\text{s} \times 360 \text{ cm}}{(1.6 \text{ mm}/\mu\text{s})^3}} \approx 3 \times 1.125 \ \mu\text{s} \approx 3 \ \mu\text{s}. \tag{5.7}$$

This 3 μs window defines the characteristic timescale over which resets from the same interaction are expected to arrive, justifying its use as the RTD threshold. As discussed previously, the remaining $\sim$10% of resets not captured by this clustering are predominantly due to de-excitation photons spatially separated from the primary track (see Figure 5.9). While more advanced clustering algorithms may improve efficiency, the chosen parameters were found to balance simplicity and background rejection effectively for the purposes of this analysis.

With the optimal 3 μs time window established based on diffusion considerations, the next step was to define the minimum number of resets required for a cluster to be considered a valid signal. Using this 3 μs time window, the event identification efficiency and purity as a function of the reset threshold was computed, as shown in Figure 5.10.

For events with $\leq$5 MeV of total deposited energy, a purity of >95% was achieved while maintaining an efficiency of around 80%, by setting the threshold to 13 resets, which corresponds to approximately 1.85 MeV of deposited energy. This final optimization step can be further tuned depending on the specific analysis requirements, allowing for different trade-offs between purity and efficiency based on the scientific objectives of the study.

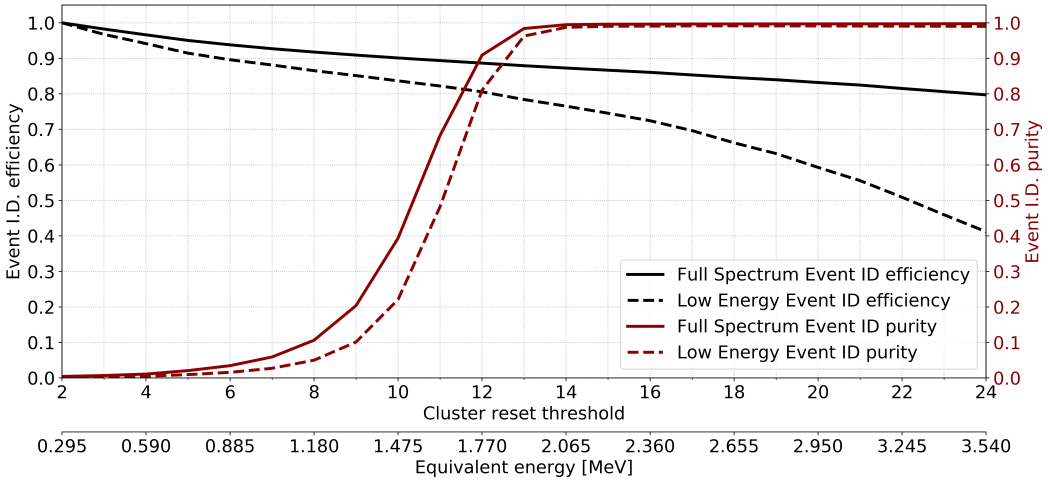


Figure 5.10: Event ID efficiency (black) and purity (red) as a function of minimum number of resets per cluster for the 3μs time window. Results are shown for the full energy spectrum (solid line) and for the low-energy events ($\leq$5 MeV) (dashed line). Plots taken from Ref.[87].

5.4.4 Data Rates

A unique challenge posed in supernova detection with a kiloton-scale LArTPC is managing data rates while maintaining a low-energy threshold of <10 MeV. One of the most significant advantages of the Q-Pix readout is its ability to achieve low-energy thresholds while maintaining very low data rates from the fact that recorded data are in the form of time-stamps only. Figure 5.11 shows the expected data rate per volume equipped with Q-Pix, as a function of reset threshold to be used for clustering algorithm, on the radiogenic background rates outlined in Table 5.2.

This data rate is derived based on the average number of resets observed in one APA over the 10 seconds time window, with the 10,000 uniquely simulated radiogenic background events. The number of resets are shown on the left y-axis, while the corresponding data size is shown on the right y-axis. The data rate is calculated assuming resets are encoded by 64 bits of information. Even with the lowest clustering threshold

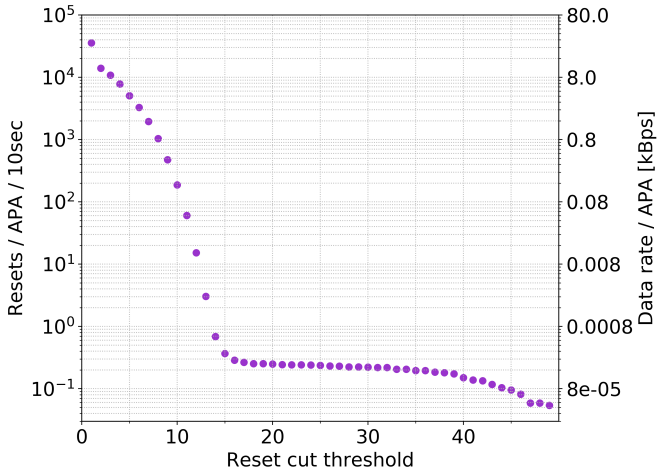


Figure 5.11: The data rates shown here are the average of 10,000 unique 10-second-long APA drift volumes as a function of the threshold on the number of resets. Data rates for one APA from radiogenic background events will be a function of the threshold on the number of resets. The rates are shown in number of resets per APA per 10 seconds (left axis) and the corresponding data rate (right axis). Plots taken from Ref.[87].

possible for Q-Pix, which is 1 reset and equivalent to 147 keV of deposited energy, the total data rate for the full 10-kton module is 5.7 MB/s. If 7 resets are used for the clustering threshold, which is equivalent to 1 MeV of deposited energy, the data rate can be further reduced by two orders of magnitude. Since the rates of radiogenic backgrounds are much larger than that of supernova neutrino interaction, the estimated data rate remains largely unchanged even after the supernova burst events are included. This demonstrates that the Q-Pix readout system can efficiently handle low-energy thresholds while maintaining manageable data rates, making it a highly effective solution for supernova neutrino detection in large-scale LArTPCs.

To compare this data rate to that of current DUNE design with APA, some details have to be taken into consideration. First point is the difference in the number of channels. The envisioned Q-Pix 10-kton module (consisting of 200 APAs with a 4 mm pixel pitch) would require approximately 172 million readout channels, compared to

384,000 channles used in the wire readout for the same module. Second, the APA data rates [148] assumes 100 seconds of readout with a threshold of 10 MeV of true neutrino energy (roughly corresponds to 5 MeV of deposited energy) for the one year time window. On the other hand, what has been presented so far for Q-Pix in this work was calculated for one second window, with much lower energy threshold than 5 MeV. For the purpose of making a comparison, data rate for Q-Pix with the threshold of 10 MeV true energy (corresponds to 5 MeV deposited energy, equivalent to 34 reset threshold) for one year time window was calculated. The data rate from the dominant source of radiogenic background events was estimated to be 16.5×10^{-5} kB/s/APA. For the 10kton module with 200 APAs, this is equivalent to 0.032kB/s/10kton, which is 1.03GB/year/10kton. For the similar scenario, DUNE FD data rates is expected to be less than 2PB/year/10kton, which is six orders of magnitude larger. The comparison can be seen in Table 5.4.

System	**Data rate per 10 kton per year (petabytes)**	**Data rate per channel per second (kilobytes)**
Q-Pix 10 kton pixel readout	1.03×10^{-6}	1.9×10^{-10}
DUNE 10 kton projective readout	<2	1.6

Table 5.4: Comparison of data rates between a 10-kton DUNE projective readout as described in Ref. [148] and a Q-Pix 10-kton module described in this work. In both cases, a 10 MeV energy threshold is assumed.

Although the detailed comparisons require further simulations, this shows that the Q-Pix architecture can vastly reduce the data rate for the detection of supernova neutrinos while maintaining much lower energy threshold compared to the previous technologies. The capability of Q-Pix technology as a continuous readout will be further explored in the Subsection 6.5.5.

This low data rate can be suppressed further with a DAQ scheme, where the resets

can be stored locally in an ASIC chip until they are read out. This approach preserves sensitivity to low-energy signals while minimizing bandwidth—an essential feature for long-term supernova monitoring. Beyond precision measurements, however, a supernova burst also demands a prompt, coordinated alert. In the next section, we explore how Q-Pix's self-triggered design could contribute to the global SNEWS, enabling timely notification of such rare astrophysical events.

5.4.5 SuperNova Early Warning System

The SNEWS is an international collaboration designed to provide early alerts of core-collapse supernovae in our galaxy and nearby galaxies through the detection of neutrinos. Unlike photons, which take hours to days to escape the star's core after a supernova explosion depending on the density of the star, neutrinos interact weakly with matter, allowing them to escape much faster. This allows neutrinos to arrive on earth earlier than photons, enabling it to be used as a tool for providing an early warning. The SNEWS network links multiple neutrino observatories worldwide, such as Super-Kamiokande [149], IceCube [150], Kamioka Liquid Scintillator Antineutrino Detector (KamLAND) [151], Borexino [152], Cubic Kilometer Neutrino Telescope (KM3NeT) [153], and Helium and Lead Observatory (HALO) [154]. By requiring coincident neutrino detections across multiple detectors, SNEWS aims to minimize false alarms and maximize the reliability of alerts sent to the astronomical community. These alerts enable rapid follow-up observations across the electromagnetic spectrum, enhancing our understanding of supernova mechanisms and nucleosynthesis processes. The detection of neutrinos from SN1987A marked the first and, to date, only observation of neutrinos from an extragalactic supernova. These detections were able to constrain the supernova models but were limited by the very small number of observed

neutrino events. A future galactic supernova would yield thousands of neutrino detections across modern observatories, enabling unprecedented insight into the neutrino emission spectrum, flavor transformations, and core-collapse physics. For a neutrino detector to be able to contribute to SNEWS, it must be sensitive to the sudden increase in MeV-scale neutrino interactions within the detector volume and be able to quickly determine whether it is supernova burst (SNB) event with high confidence. Moreover, it needs to have ability to determine the direction of the SNB from the reconstructed neutrino events. In the following subsections, the triggering mechanism to generate an alert from a real-time analysis, and directionality determination within the Q-Pix readout will be discussed.

5.4.6 Supernova Neutrino Burst Triggering

The identification of SNB event with Q-Pix will be initiated by the clustering algorithm (explained in subsection 5.4.3), which can extract a high purity sample of neutrino interactions. The clustering algorithm used for this process is based on Density-Based Spatial Clustering of Applications with Noise (DBSCAN) [155] with a Chebyshev metric [156]. This allows efficient processing of up to 500 independent 10-second time windows per minute, which is more than sufficient for near real-time SNB detection. It is important to note that the clustering algorithm in this section is applied to mixed samples of both signal and background events, unlike the approach described in the subsection 5.4.3, for a realistic optimization. Thus, the RTD was optimized at 6 μs, and the number of resets required for clustering to be 14, which is equivalent to 2.065 MeV energy deposition. An example of reset time profile in a single 10-kton Q-Pix detector module before and after the clustering algorithm is shown in Figure 5.12. It shows that algorithm allows radiogenic background events (in blue) to be largely suppressed, while preserving the

supernova neutrino interactions (in orange). In this example, the SNB reset clustering efficiency is $\frac{7002}{8196} \approx 85\%$ and purity is $\frac{7002}{7002+38} \approx 99\%$, demonstrating the strong potential of the Q-Pix architecture for real-time supernova detection.

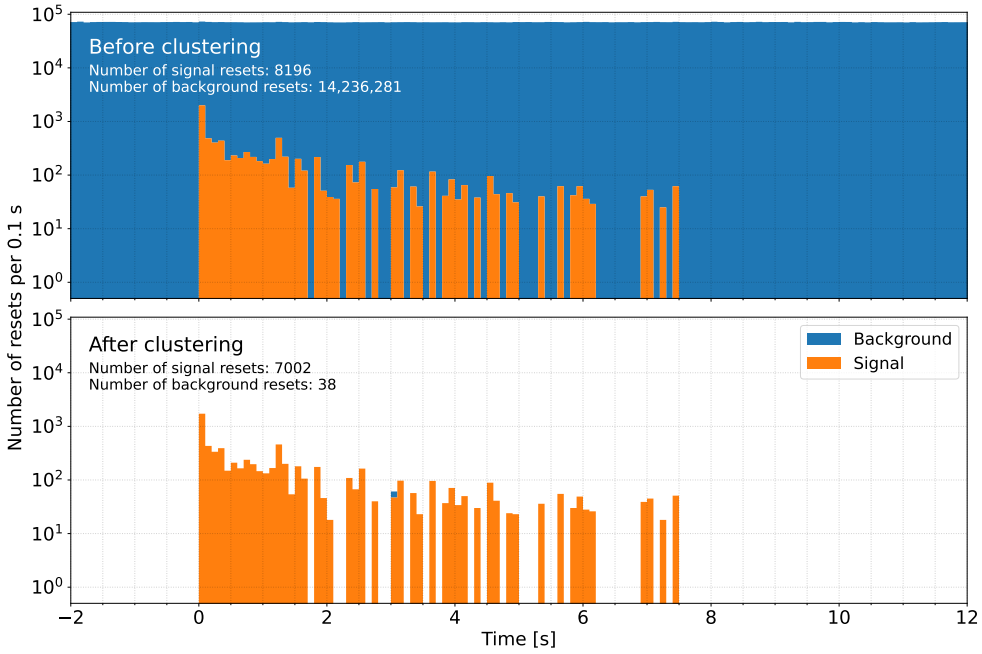


Figure 5.12: Number of resets in duration of times in a 10-kton Q-Pix detector module before (top) and after (bottom) clustering for a supernova burst simulated at 10 kpc. Figures taken from [87].

Next, Q-Pix's ability to alert for SNBs were quantified. This was done by computing the burst triggering efficiency, defined as

$$\text{Alert Efficiency} = \frac{\text{Number of identified SNBs}}{\text{Total number of SNBs simulated}}. \tag{5.8}$$

This efficiency is heavily dependent on the number of neutrino interactions detected from one SNB event, as the larger the number of interactions, the easier it is to identify SNBs. Figure 5.13 shows comparison of the burst triggering efficiency as a function

of number of neutrino interactions from a supernova burst, between different detector technologies for DUNE.

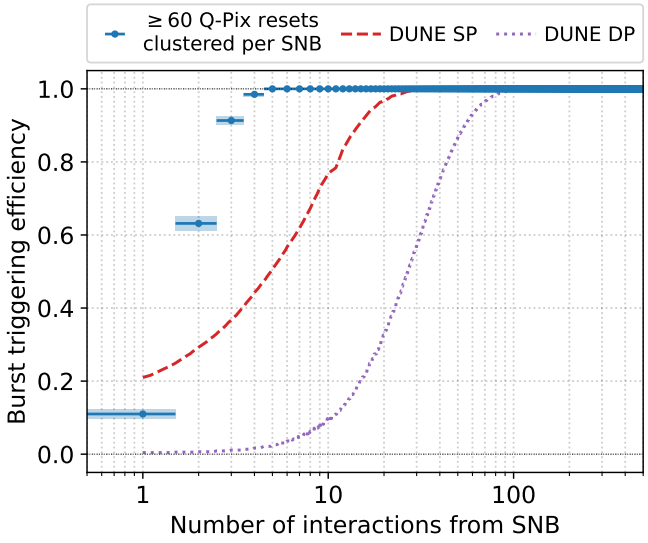


Figure 5.13: Supernova burst triggering efficiency as a function of the number of ν_e interactions in a 10-kton Q-Pix-enabled detector module. The blue points indicate the case where the total number of Q-Pix resets after clustering within a 10-second window is required to be at least 60 (∼8.85 MeV). The DUNE SP (single-phase) and DP (dual-phase) efficiencies are shown for comparison and are taken from [106]. Figure taken from [87].

It was determined that with a minimum threshold of 60 resets per cluster within a 10 second time, equivalent to 8.85 MeV deposited energy, the false trigger rate can be suppressed to less than one per month. This presents a large improvement on the supernova burst detection efficiency with 10kton module, compared to the baseline DUNE single-phase (SP) and dual-phase (DP)* detectors described in Ref. [106]. Additionally, due to the increased efficiency achieved by Q-Pix, supernova burst can be detected with fewer number of neutrino interactions compared to the other technologies. Since further SNBs

*DP LArTPC technology, which extracts and amplifies ionization charge in a gaseous layer above the liquid argon, was explored in early R&D but is no longer part of DUNE's detector design.

produce less neutrino interactions in the detector, this means that maximum detectable distance of SNBs can be extended with Q-Pix. For example, in order to achieve close to 100% burst triggering efficiency, Q-Pix only requires 4 neutrino interactions, while DUNE SP would have require 30 neutrinos. This number of interaction corresponds to 80 kpc and 30 kpc respectively, demonstrating the Q-Pix's ability to extend the reach of DUNE to SNB detection.

5.4.7 Directionality Determination

One powerful tool that is enhanced by the intrinsic 3D information captured in a pixel-based readout is the ability to determine the 3D spatial topology of the events. When coupled with the low-energy thresholds available with the Q-Pix readout, there is an opportunity to attempt to reconstruct the direction from where the neutrinos originate from.

This subsection demonstrate for the first time how such a pointing analysis can be done with a LArTPC, equipped with the Q-Pix readout. The ability to determine the incoming direction of neutrinos, neutrino pointing, plays a crucial role in enabling multi-messenger astronomy by providing directional information to astronomers. As mentioned, neutrinos are emitted on short time scale of $\mathcal{O}$(seconds), compared to that of electromagnetic signal, which emerges over much longer time scale of $\mathcal{O}$(hours to days) during a core-collapse supernova. This time difference allows neutrino detectors to issue an early warning through SNEWS, enabling telescopes to observe the supernova at the earliest stages of its electromagnetic emission. Additionally, neutrino pointing can be informative when identifying supernovae that may lack a detectable electromagnetic radiation. Certain core-collapse events, referred to as "failed" supernovae, can produce a copious amount of neutrinos without generating an observable electromagnetic signa-

ture [157]. Using directional information from neutrino observations, the area of search for such events can be narrowed down. By evaluating the neutrinos' trajectories, oscillations in flavor composition due to interactions with Earth can be observed, providing additional constraints on neutrino oscillation parameters.

For the analysis presented in this work, the focus is on reconstructing the primary electron track resulting from ν_eCC interactions and ν_e–e^- ES interactions, which dominate the signal channels as shown in Table 5.1. In the energy range of supernova neutrinos (1–50 MeV), only the ES channel retains strong directional correlation with the incoming neutrino, while the direction of the primary electron in CC events is largely uncorrelated, as shown in Figure 5.14.

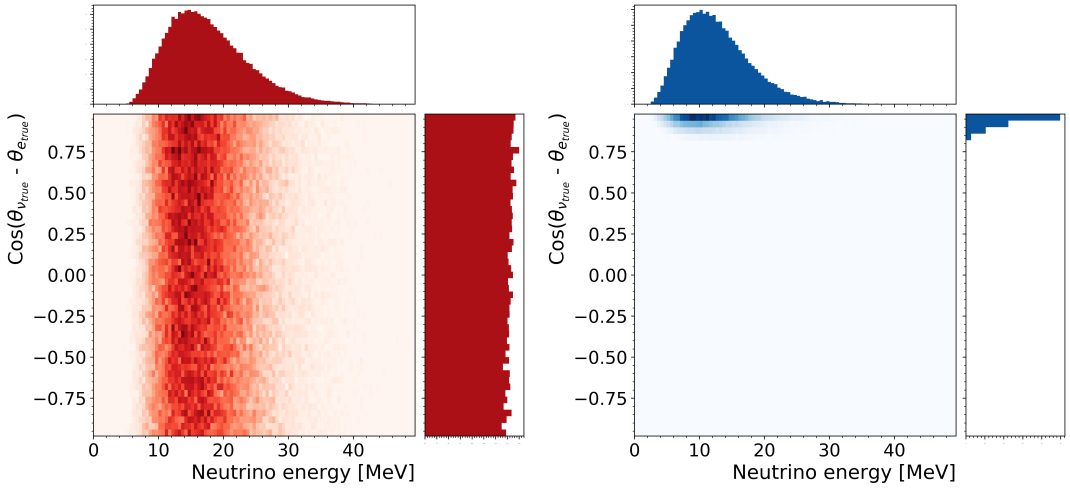


Figure 5.14: Histogram of the true neutrino energy as a function of cosine of the difference in the true neutrino angle ($\theta_{\nu_{\text{true}}}$) minus the true electron angle ($\theta_{e_{\text{true}}}$) for ν_e CC events (left) and for ν_e–e^- ES (right). The z-axis color scale units are events per 0.5 MeV per 0.04. Plots taken from Ref.[87].

This contrast arises from the underlying interaction mechanisms. While both processes are mediated by the weak interaction, CC events occur on nucleons bound within a heavy argon nucleus. The complex nuclear environment, including Fermi motion,

nucleon binding energy, and final-state interactions, introduces significant smearing of the outgoing lepton direction. As a result, electrons from ν_e CC interactions exhibit an approximately isotropic angular distribution, as seen on the left in Figure 5.14.

In contrast, ν_e–e^- ES is a two-body interaction with a loosely bound atomic electron and is dominated by well-defined kinematics. The outgoing electron is strongly forward-peaked, preserving the incident neutrino's direction. Consequently, ES events serve as the primary handle for performing directional reconstruction of supernova neutrinos.

To reconstruct the electron track for a candidate event, clustering algorithm was applied with the reset threshold of 13 resets. As it has been explained in subsection 5.4.3, this criteria ensures less than 1% contamination from radiogenic backgrounds while maintaining a relatively high signal detection efficiency of approximately 90%. The collection of 3D reset positions for each event is then analyzed using the Random Sample Consensus (RANSAC) algorithm [158]. RANSAC is a robust statistical model fitting method used to identify inliers and outliers within a dataset by fitting a model to the data. The algorithm operates iteratively: in each iteration, it randomly selects a minimal subset of data points sufficient to estimate the model parameters. The resulting model is then tested against the full dataset to determine how many points—within a predefined tolerance—agree with it (inliers). By repeating this process multiple times, RANSAC identifies the model with the largest consensus set, inherently reducing the influence of outliers. In the context of this study, RANSAC is employed to distinguish resets that align with the trajectory of the primary electron (inliers) from those resulting from secondary radiative processes, such as de-excitation photons, which deviate from the main track (outliers). A graphical representation of the RANSAC process is shown in the left of Figure 5.15. Once the inliers were identified, a RANSAC-based linear fit was applied to determine the axis of the electron track, which will be the basis for

direction reconstruction. Based on this line, the furthest pair of inlier reset points was identified to define the track endpoints. While this linear fit provides the directional axis, an inherent ambiguity remains as to which end corresponds to the starting reset point (SRP) and which to the ending reset point (ERP)—a distinction illustrated in the right image of Figure 5.15. Resolving this ambiguity is essential for accurately reconstructing the incoming neutrino direction, a key component in neutrino pointing analyses.

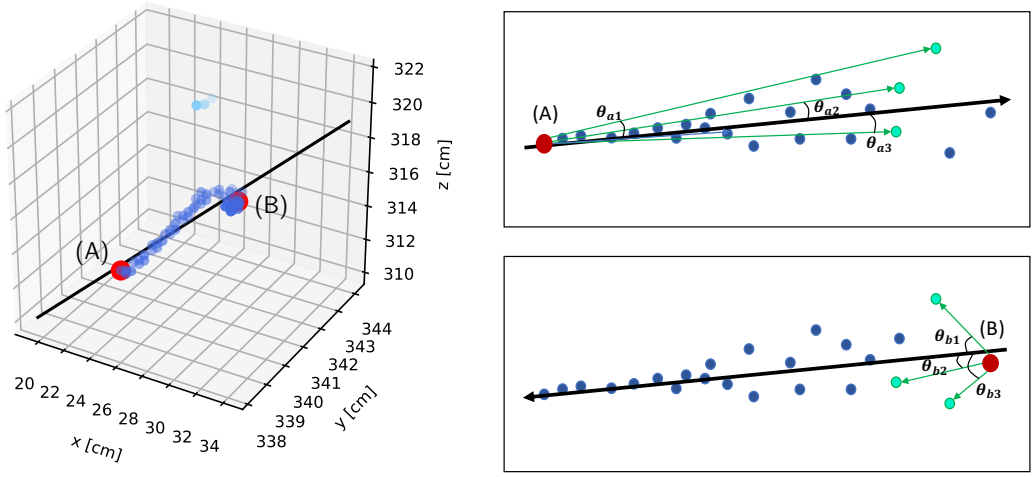


Figure 5.15: Left: Hits produced by the outgoing electron in an example supernova neutrino event. The black line is the linear RANSAC fit. The darker blue points and lighter blue points represent the inlier and outlier reset points identified by the RANSAC algorithm respectively. The two red dots (A) and (B) are the farthest reset points apart from each other among the inlier reset points. Right: 2D cartoon representation of inlier reset points. The two red dots are the left-most and right-most point among the inlier reset points. The black line represents the linear RANSAC fit performed to find the trajectory and the cyan points and green lines illustrate inlier reset points to identify the direction of travel of the electron. Images taken from Ref.[87].

This ambiguity can be resolved using a topological approach based on the energy loss and scattering behavior of the primary electron as it propagates through the liquid argon. As the primary electron travels through argon, it will keep depositing energy in its journey, losing energy. Since electrons with less energy tends to get scattered with

larger angle, the spacial spread of reset points toward the end of its trajectory gets wider. The right image of Figure 5.15 shows the 2D projection of the method to distinguish the SRP and ERP by quantifying the spacial spread of resets. The process begins by drawing a central line between the two farthest inlier reset points. Then additional lines are drawn from the assumed SRP and ERP to each inlier reset point, and the cosine of the angles between each of those lines and the central line was calculated. Since the beginning of the track should have localized resets, the angles will be smaller, and the its cosine value will be larger. Therefore, by choosing the track endpoint that makes the cumulative sum of cosine values larger, we can determine SRP, ensuring that the track is correctly oriented in the direction of increasing scattering and energy loss.

Figure 5.16 shows the performance of the directional reconstruction algorithm for ES events. It plots the cosine of the angle between the true neutrino direction and the reconstructed direction of the primary electron, as a function of neutrino energy. Since elastic scattering is forward-peaked, a correctly reconstructed electron direction should closely align with the incoming neutrino direction—yielding values of $\cos(\theta_{\nu_{\text{true}}} - \theta_{\text{reco}})$ near 1. The strong peak near 1 in Figure 5.16 indicates that this method correctly reconstructs the primary electron direction in more than 70% of events, validating its effectiveness for neutrino pointing in a Q-Pix-enabled detector.

Figure 5.17 further demonstrates the impact of the track-fitting correction procedure applied to enhance directionality. It compares the distribution of reconstructed directions before and after the correction is applied. The sharper peak in the corrected distribution confirms the improved alignment with the true electron direction. Compared to this, the peak in Figure 5.16 appears slightly broader, as it reflects the difference between the reconstructed electron direction and the true neutrino direction, rather than the true electron itself.

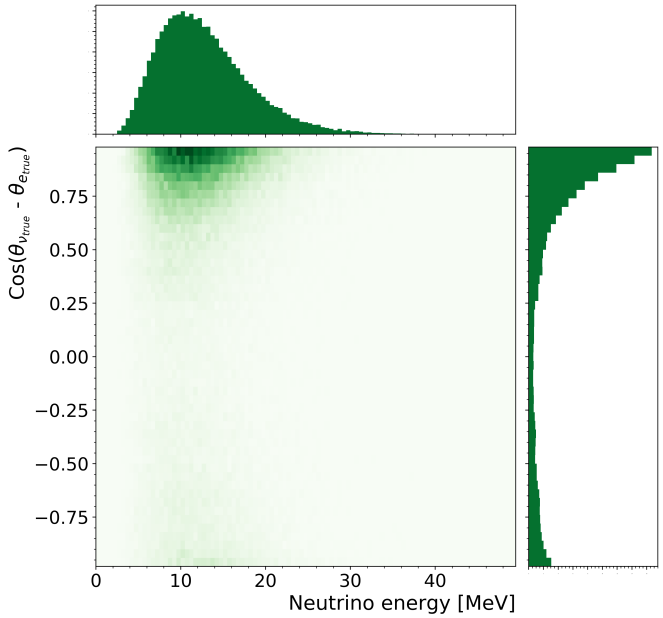


Figure 5.16: 2D histogram of the cosine of the difference between the true direction of the neutrino and the true direction of the electron track produced in the interaction, as a function of the true neutrino energy. Plot taken from Ref.[87].

Now that the event-by-event directionality reconstruction method has been established, the next step is to apply this algorithm to an entire simulated SNB. The Garching benchmark model was used for this study again, yielding 220 CC events and 19 ES events, as summarized in Table 5.1. The corresponding energy spectrum of these events is shown in Figure 5.4. For each neutrino interaction, the directionality of the outgoing primary electron was reconstructed. While earlier analyses often quantify directional performance using a single angular deviation (i.e., the angle between true and reconstructed direction vectors), this scalar representation cannot capture the full 3D orientation of reconstructed tracks. To more faithfully visualize and analyze the angular distribution of the reconstructed directions, we instead adopt a spherical coordinate representation, projecting each direction vector onto a (θ, φ) plane. This allows for a

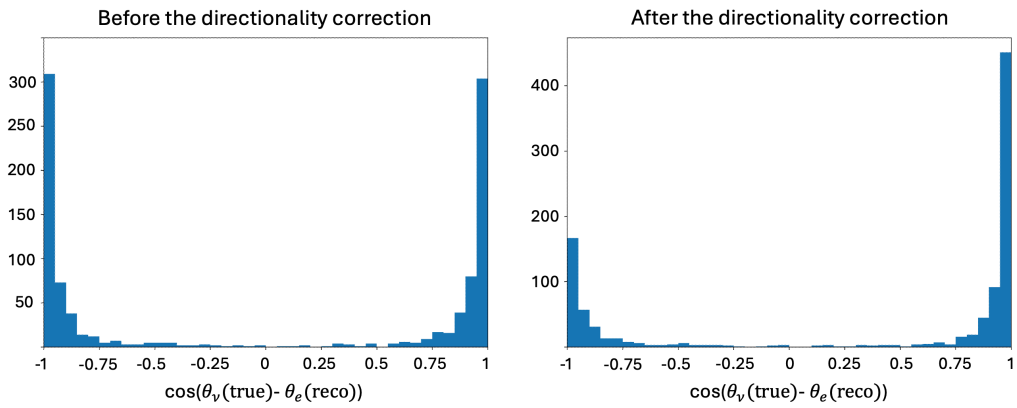


Figure 5.17: Histogram of the cosine of the angle between the reconstructed and true directions of the primary electron track. The left panel shows the distribution before applying the topological directionality analysis. Peaks at both -1 and $+1$ indicate that while the track axis is reconstructed correctly, its direction is ambiguous. The right panel shows the result after applying the direction-resolving algorithm, which significantly reduces the ambiguity and enhances the forward-direction reconstruction. A residual peak at -1 remains, indicating cases where the ambiguity was not fully resolved.

more complete characterization of the pointing performance and reveals features such as backward misreconstructions or lateral dispersion that would be otherwise hidden in one-dimensional summaries.

The resulting (θ, φ) distribution is shown in Figure 5.18. To extract the dominant direction of the reconstructed neutrino flux, principal component analysis (PCA) [159] was applied to the collection of reconstructed direction vectors. PCA is a statistical method that identifies the directions in which data varies the most and reduces dimensionality while preserving structure. In this context, PCA determines the principal axis through the densest region of reconstructed vectors, effectively identifying the most likely incoming neutrino direction. As seen in Figure 5.18, CC events (red) exhibit a broadly isotropic distribution due to their complex nuclear kinematics, whereas ES events (blue) retain strong directionality aligned with the incoming neutrinos. Consequently, when

both event types are combined, PCA naturally identifies the ES-dominated region as the dominant direction of the ensemble, providing a robust estimate of the supernova origin.

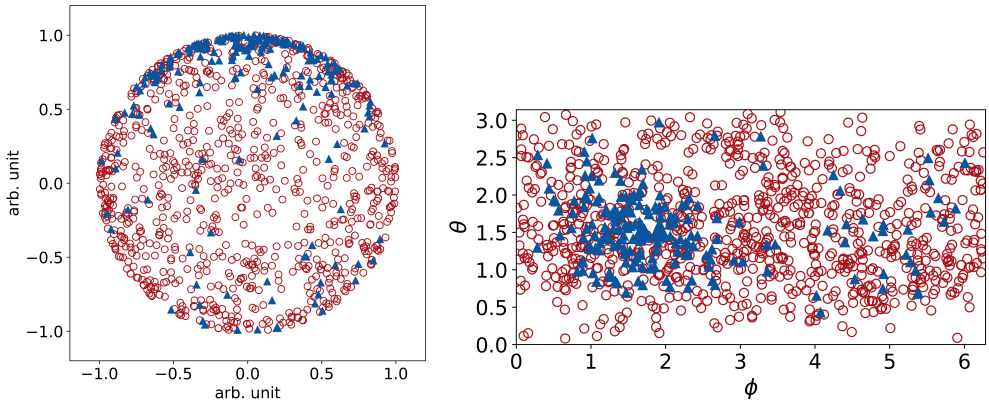


Figure 5.18: Representation of the direction vector reconstructed for each neutrino interaction in a simulated supernova burst event shown on a unit sphere (left) and projected onto a θ–φ plane. Solid blue triangles (▲) represent events from ν_e–e^- ES interactions and hollow red circles (○) represent events from ν_e CC interactions. Plot taken from Ref.[87].

With the primary axis determined through principal component analysis, by identifying the most prominent point in the distribution of reconstructed directions, we can specify the inferred direction from which the supernova burst originated from.

To evaluate the precision of this approach, a unique sample of 10,000 SNBs with randomly distributed origins were simulated, and analyzed. The results show that the reconstructed direction successfully identifies the SNB position for approximately 80% of the events, with an angular deviation of $(\theta_{\text{reco}} - \theta_{\text{true}}) < 25°$. The remaining 20% of cases resulted in "backward" reconstructions, where the direction was reconstructed to be opposite to the actual supernova origin. With the primary axis determined through principal component analysis, by identifying the most prominent point in the distribution of reconstructed directions, we can specify the inferred direction from which the

supernova burst originated. Despite this ambiguity in a fraction of cases, the restriction of the search area in the sky provided by this reconstruction method offers a powerful tool for astronomical observations during supernova burst searches.

Figure 5.19 shows the angular resolution achieved by this directionality reconstruction method, in terms of the angular differences between the true and reconstructed directions of SNBs. As can be seen in the right image of Figure 5.18, the projection of vector to the φ and θ space spans for $0 < \theta < \pi$ and $0 < \varphi < 2\pi$. Since Figure 5.19 shows the difference of two vectors, it spans for $-\pi < \theta < \pi$ and $-2\pi < \varphi < 2\pi$.

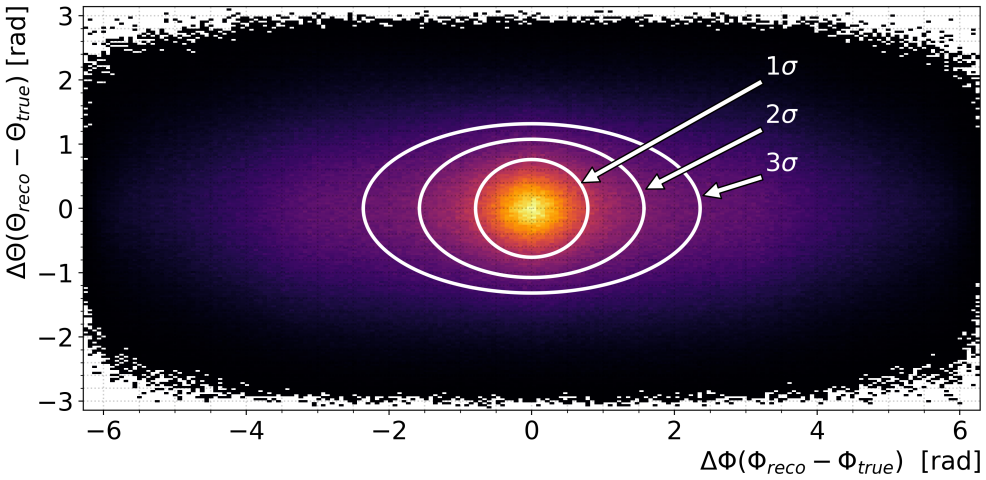


Figure 5.19: Angular resolution for the supernova pointing in terms of θ and φ. The σ bands correspond to a 2D Gaussian fit to the peak to reduce the bias from the tails from poorly reconstructed events. A clear peak at $\Delta\theta = \Delta\varphi = 0$ can be observed. Plot taken from Ref.[87].

A bright and clear peak can be seen at $\Delta\theta = \Delta\varphi = 0$, indicating that the majority of reconstructed directions align closely with the true supernova neutrino direction. The φ projection of the resolution plot follows a Gaussian distribution, while the θ projection has two additional shoulders around $\theta = \pi$ and $\theta = -\pi$, corresponding to cases where the reconstructed direction points opposite to the true neutrino source resulting from the previously discussed directional ambiguity. Additionally, 1σ, 2σ, and 3σ contours

of 2D Gaussian fit were overlaid, to quantitatively characterize the pointing resolution of the method. The fit results show that the 10 kpc SNB can be reconstructed with $\theta = 33^\circ$ and $\varphi = 45^\circ$ at 1σ, and $\theta = 99^\circ$ and $\varphi = 135^\circ$ at 3σ.

The DUNE Collaboration recently published a study on the supernova pointing capabilities of its single-phase wire-based LArTPC far detector module [160]. In that analysis, they assumed perfect classification between ES and CC events, and simulated performance with a 40-kiloton fiducial mass. Under these idealized conditions, DUNE achieved an angular resolution of approximately 3.4° at the 1σ level for a supernova located 10 kpc away. However, in their most conservative scenario—where no distinction is made between ES and CC events, as is also assumed in the present work—the reported pointing resolution degraded significantly to 102°. Despite the simplicity of the initial reconstruction strategy developed for this Q-Pix-based study three years ago, the results presented here already comparable to the recent DUNE baseline, underscoring the strength and promise of the Q-Pix architecture for supernova directionality.

Several strategies offer potential for further improvement. For instance, machine learning algorithms trained on the full 3D charge topology may enhance directionality by exploiting subtle spatial asymmetries in track development. Additionally, integrating Q-Pix charge information with scintillation light timing from a photon detection system could provide an absolute time reference, breaking degeneracies in track orientation and improving backward rejection. It is also important to emphasize that, in this analysis, no attempt was made to distinguish ES from CC events. However, CC interactions could be identified through the presence of associated de-excitation photons.

Future work will focus on isolating and removing these non-pointing CC events, which is expected to substantially improve angular resolution and further enhance Q-Pix's potential for multi-messenger astrophysics. This strategy will be revisited, in the context

of solar neutrino studies, in the following chapter.

5.5 Summary

The opportunity to observe neutrinos from the next core-collapse supernova presents a unique laboratory for testing particle physics under some of the most extreme astrophysical conditions. It will produce a significant amount of neutrinos of MeV scale, carrying important information to answer many astrophysical questions. Additionally, time difference between the emergence of neutrino and electromagnetic photons from a supernova enables neutrinos to be used as an early warning tool. Such early detection is pivotal for multi-messenger astronomy, offering a more complete understanding of the core-collapse process.

By combining fine spatial resolution with sufficient data handling, Q-Pix enhances the physics potential of large-scale LArTPC while potentially reducing the overall DUNE data rate by orders of magnitude and preserving full 3D event reconstruction capabilities. This technology addresses key challenges in detecting low-energy neutrinos, such as those from supernova bursts, and enhances the ability to perform precision measurements critical for both particle physics and astrophysics.

The Q-Pix readout has demonstrated improved low-energy detection and reconstruction capabilities compared to those achieved with the conventional projective wire-based readout currently envisioned for the DUNE experiment. Notably, the Q-Pix architecture produces higher efficiency and higher purity in individual supernova neutrino event identification even after incorporating radiogenic background estimates from both the bulk liquid argon and detector materials.

One of the key advantages of the pixel-based readout lies in its preservation of full

3D event information, which facilitates precise angular reconstruction of the incoming neutrino direction. The analysis presented here shows that within a single 10-kton Q-Pix-enabled module, an angular resolution of approximately 33° in the θ direction and 45° in the φ direction can be achieved at the 1σ confidence level. Such directional capabilities are essential for enabling neutrino pointing and contributing to early-warning systems like SNEWS.

The physics reach offered by the Q-Pix readout, particularly in the realm of low-energy neutrino physics, highlights the compelling case for further development and deployment of this technology in kiloton-scale LArTPCs.

The Sun, with all those planets revolving around it and dependent on it, can still ripen a bunch of grapes as if it had nothing else in the universe to do.

Galileo Galilei

6

Solar studies with Q-Pix

In the previous chapter, we examined supernova neutrinos—produced in the violent crescendo of stellar death, where massive stars collapse and explode in a cataclysmic finale. These neutrinos arrive like a thunderous chord, sudden and fleeting, announcing the end of a symphonic movement written in gravitational fury.

Yet not all neutrinos enter the cosmic stage with such grandeur. Some emerge as subtle, sustained tones—more akin to the gentle hum of a pianissimo passage than

the crashing cadence of a finale. Solar neutrinos, born in the quiet heartbeat of the Sun's core, arrive not in bursts but as a continuous stream. They are the undertone beneath the cosmos' orchestration: ever-present, softly voiced, yet rich with information, preserving the rhythm of our nearest star's inner workings—measured, understated, and indispensable to the harmony of the whole. However, extracting their signal requires rigorous background suppression and innovative readout technologies that can amplify the faintest trace without distorting the melody.

In this final chapter, we explore the prospects for observing solar neutrinos in a LArTPC instrumented with Q-Pix. By combining its high spatial resolution with a scalable, triggerless readout, Q-Pix design allows us to hear what was once inaudible: the delicate timbre of low-energy events emerging from the persistent background. This effort is not only an inquiry into the nuclear musical score playing within the Sun's core, but also a movement toward expanding the repertoire of neutrino physics—refining oscillation models, probing neutrino-matter interactions, and extending the dynamic range of precision measurements in LArTPCs.

6.1 Fusion Processes and Solar Neutrinos

In the core of the sun where temperatures reach approximately 15 million Kelvin and pressures are immense, nuclear fusion occurs. These reactions not only produce the energy that powers the Sun but also generate electron neutrinos, which, due to their extremely weak interactions with matter, escape unimpeded and provide real-time insight into the nuclear processes at the heart of the Sun. These solar neutrinos have become vital tools for investigating fundamental properties of neutrinos, including flavour oscillations, the mass ordering, and possible other interactions beyond the Standard Model.

The dominant fusion mechanism in the Sun is the proton–proton (pp) chain, responsible for roughly 99% of solar energy production [161]. This sequence begins with the fusion of two protons into deuterium (^{2}H), releasing a positron and an electron neutrino:

$$p + p \rightarrow {}^2\mathrm{H} + e^+ + \nu_e. \tag{6.1}$$

The deuterium can then fuse with another proton to create helium-3 (^{3}He):

$${}^2\mathrm{H} + p \rightarrow {}^3\mathrm{He} + \gamma. \tag{6.2}$$

From here, several branches are possible: in the pp-I chain, two ^{3}He nuclei combine to form helium-4 (^{4}He) and release two protons:

$${}^3\mathrm{He} + {}^3\mathrm{He} \rightarrow {}^4\mathrm{He} + 2p. \tag{6.3}$$

In the pp-II and pp-III chains, ^{3}He reacts with ^{4}He to form beryllium-7 (^{7}Be):

$${}^3\mathrm{He} + {}^4\mathrm{He} \rightarrow {}^7\mathrm{Be} + \gamma, \tag{6.4}$$

which can further undergo electron capture to emit monoenergetic neutrinos

$${}^7\mathrm{Be} + e^- \rightarrow {}^7\mathrm{Li} + \nu_e \tag{6.5}$$

or form boron-8 (^{8}B)

$${}^7\mathrm{Be} + p \rightarrow {}^8\mathrm{B} + \gamma, \tag{6.6}$$

which decays to produce high-energy neutrinos (B8 neutrinos)

$$^{8}\mathrm{B} \rightarrow {}^{8}\mathrm{Be}^{*} + e^{+} + \nu_{e}, \tag{6.7}$$

followed by $^{8}\mathrm{Be}^{*} \rightarrow 2\,^{4}\mathrm{He}$ [162]. Additional reactions, such as the pep

$$p + e^{-} + p \rightarrow {}^{2}\mathrm{H} + \nu_{e} \tag{6.8}$$

and hep

$$^{3}\mathrm{He} + p \rightarrow {}^{4}\mathrm{He} + e^{+} + \nu_{e} \tag{6.9}$$

processes, occur less frequently. Among them, hep neutrinos are the most energetic solar neutrinos, with endpoint energies near 18 MeV [163]—though they have not yet been observed. Each of these neutrino components has a unique energy spectrum, enabling precision studies of solar fusion and neutrino oscillations, including the matter-induced MSW effect in the Sun's dense interior [164, 165]. These processes' energy spectra are shown in Figure 6.1 along with the illustration of processes in Figures 6.2.

Alongside the pp-chain, the Sun also hosts the carbon–nitrogen–oxygen (CNO) cycle—a catalytic fusion process that plays a dominant role in more massive stars but contributes less than 1% of the Sun's energy [167]. In this cycle, hydrogen is fused into helium using carbon, nitrogen, and oxygen as catalysts. The cycle progresses through a series of reactions and beta decays, ultimately regenerating the initial carbon nucleus while releasing two positrons and two electron neutrinos in each cycle. The neutrinos are emitted during the beta decays of nitrogen-13, oxygen-15, and fluorine-17 (^{13}N, ^{15}O, ^{17}F), each producing characteristic energy spectra [168]. Although the CNO neutrino flux is lower than that of the pp-chain, it is especially valuable because its rate is

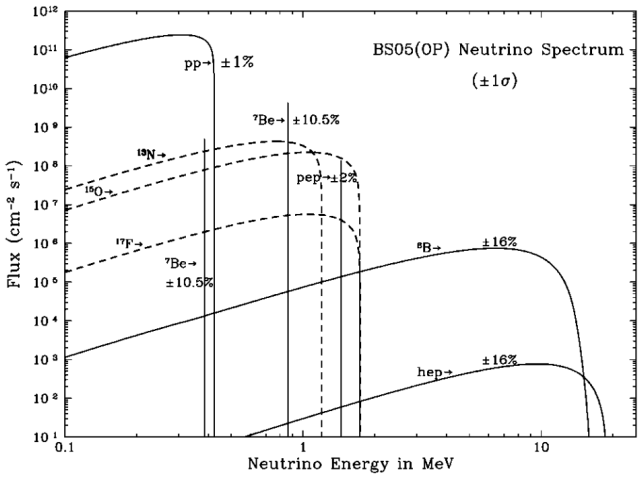


Figure 6.1: Energy spectra of solar neutrinos produced from various fusion reactions within the Sun. Taken from [166].

directly sensitive to the abundance of heavy elements within the solar core, commonly referred to as solar metallicity. Unlike surface spectroscopy or helioseismology, which rely on indirect measurements, CNO neutrino detection offers a direct probe of the Sun's internal composition [169].

Solar neutrino observations have historically played a pivotal role in particle physics, most notably in the discovery of neutrino oscillations by experiments such as SNO [170], Super-Kamiokande [171], and Borexino [172]. These results provided compelling evidence that neutrinos have mass and change flavor as they traverse through space and matter. Precise measurements of solar neutrino fluxes are used to test the predictions of the Standard Solar Model (SSM), which describes the Sun's energy generation, structure, and evolution [173]. One key parameter in the SSM is solar metallicity, the proportion of the Sun's mass made up of elements heavier than hydrogen and helium. Metallicity affects the opacity of the solar interior, which in turn alters the radiative energy transport, temperature gradient, and the depth of the convective zone. Be-

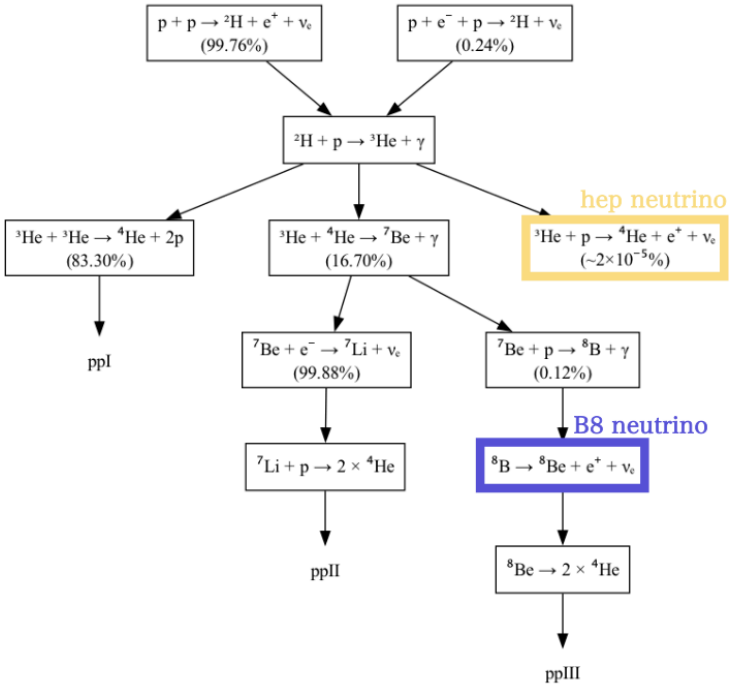


Figure 6.2: Visualization of the proton–proton (pp) chain, the dominant energy production mechanism in the Sun. The yellow box highlights the hep branch, in which $^3\mathrm{He} + \mathrm{p} \rightarrow {}^4\mathrm{He} + \mathrm{e}^+ + \nu_e$ generates the most energetic solar neutrinos known, despite its extremely low branching ratio ($\sim 2\times10^{-5}$). The blue box indicates the B8 production, where ^{8}B decays into ^{8}Be, emitting an energetic ν_e—a key target in solar neutrino experiments due to its higher energy and distinctive signature.

cause nuclear fusion rates are temperature-dependent particularly in the CNO cycle, metallicity also influences the spectrum and flux of solar neutrinos [161].

Helioseismic measurements from experiments such as Global Oscillation Network Group (GONG) [174] and the Michelson Doppler Imager instrument [175]on the The Solar and Heliospheric Observatory (SOHO) spacecraft [176] have historically agreed well with high-metallicity (high-Z) models, accurately predicting sound-speed profiles, convective zone depths, and surface helium abundance [177, 178]. Similarly, solar neutrino

measurements—like the ^{8}B flux observed by SNO—matched high-Z model predictions once neutrino oscillations were included [166]. However, recent advances in 3D spectroscopic modeling, which account for non-local thermodynamic equilibrium effects, have led to a downward revision of the Sun's surface metallicity, creating significant discrepancies with helioseismological observations [179, 180]. This tension is referred to as the solar metallicity problem. Beyond stellar modeling, the Sun's metallicity also influences broader astrophysical studies, including the evolution of stars and the chemical history of our galaxy [181].

Solar neutrinos also probe outstanding questions in neutrino physics. One such issue is the tension between the solar-determined and reactor-determined values of the mass-squared difference Δm^2_{21}, with KamLAND reporting a best-fit value about 1.5σ higher than that inferred from solar experiments [182, 183]. In addition, solar neutrinos offer sensitivity to NSIs that might arise from physics beyond the Standard Model. Consequently, precision measurements of solar neutrinos are essential not only for solar modeling but also for testing fundamental principles in particle physics.

Despite their importance, detecting solar neutrinos is challenging. Although the solar neutrino flux is approximately as large as $6 \times 10^{10} \mathrm{cm}^{-2}\mathrm{s}^{-1}$, the low energies of these neutrinos result in small interaction rates [166]. Their energies typically range from a few hundred keV up to about 18 MeV, with the B8 and hep processes providing the highest-energy neutrinos [184]. This is significantly lower than neutrinos from accelerators or supernovae, making their detection difficult. Successfully observing solar neutrinos requires detectors with very low-energy thresholds, fine tracking resolution, and the ability to reject background radiation in the 1–20 MeV range.

In this chapter, we assess the sensitivity of a 10-kiloton LArTPC, equipped with Q-Pix readout, to solar neutrinos. We consider deployment in an underground site such as

SURF and evaluate two detector configurations: a baseline design similar to DUNE's far detector modules introduced in Section 2.2.2, and a low-background scenario inspired by the Sanford Underground Low background Module (SLoMo) proposal [185].

6.2 Experimental Consideration

This section outlines the experimental assumptions and simulation setup used to evaluate solar neutrino sensitivity in two distinct detector configurations: a *baseline scenario*, representing a conventional liquid argon detector filled with atmospheric argon (standard LAr used for experiments) and equipped with enhanced photon detection, and a *low-background scenario*, optimized for rare-event searches using underground argon (UAr) and improved shielding. Sourced from deep geological reservoirs shielded from cosmic rays, UAr contains three to four orders of magnitude less ^{39}Ar than atmospheric argon [186]. With a half-life of 269 years, ^{39}Ar undergoes beta decay with an endpoint energy of approximately 565 keV, making it a major source of internal background in detectors using atmospheric argon. Its suppression in UAr significantly enhances sensitivity to low-energy events such as solar neutrinos. The following subsections describe the shared detector geometry, the defining features of each scenario, and the assumed cavern environment.

6.2.0.1 Detector setup

Both configurations use a 17.5 kiloton LArTPC with a 10 kiloton fiducial volume measuring $12.0 \times 14.0 \times 58.2$ m^3. The active volume is divided into four drift regions of 3.5 m length each, oriented along the z-axis as can be seen in Figure 6.3. A uniform electric field of 500 V/cm is applied, and ionization electrons are readout by modular anode

planes composed of contiguous 4×4 mm^2 Q-Pix pixels arranged in 6×2.3 m^2 panels. The mechanical support structure is envisioned to minimize inactive material, but is not simulated in this work. Event propagation use a Geant4-based framework, and reconstruction is performed using the same clustering and reset-based energy algorithms developed for supernova neutrino studies in Section 5.4.3.

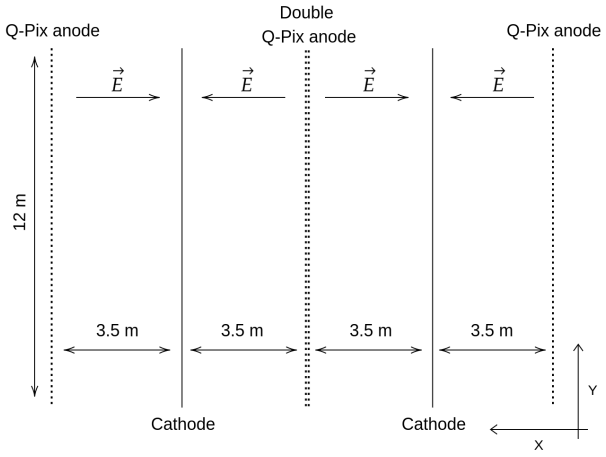


Figure 6.3: Schematic cross section of the detector model used in this study. The z axis runs parallel to the readout planes, each facing an individual drift volume. Figure taken from our forthcoming study [187].

The *baseline scenario* uses atmospheric argon as the active medium. The full anode plane is assumed to be sensitive to photons, providing a 37% effective photon coverage. A photon detection efficiency of 15% is adopted, corresponding to the performance of commercial photodetectors operating at 128 nm. Although ambitious, this configuration serves as a benchmark to evaluate the potential impact of enhanced scintillation light detection systems. It also motivates continued research into integrated charge-light readout technologies [188, 189].

The *low-background* scenario follows design principles proposed by the SLoMo collaboration [185]. It retains the same geometry and readout scheme as the baseline

but is filled with UAr. Additional background suppression is achieved through neutron shielding, implemented using a water shield or borated cryostat. Fast neutrons are moderated via hydrogen scattering and captured by ^{10}B, which has a high thermal neutron capture cross section. These reactions release only short-range particles, reducing the probability of background contamination. Furthermore, radon-induced backgrounds are suppressed by three orders of magnitude using specialized argon purification and recirculation systems.

6.2.0.2 Cavern

Both detector configurations are assumed to be installed in a deep underground cavern at SURF. The dimensions match those of the DUNE experiment: 144.5 m (length) $\times$ 19.8 m (width) $\times$ 28.0 m (height) [29]. While cosmic-ray fluxes are significantly reduced at this depth, radiation from the surrounding rock and construction materials still contributes to the background.

To mitigate this, the cavern walls are lined with specially selected low-radioactivity concrete or shotcrete. The elemental compositions of the native rock and these engineered materials are shown in Table 6.1. These compositions inform the simulations of external gamma and neutron backgrounds from uranium, thorium, and potassium decay chains.

6.3 Solar Neutrino Prediction

This analysis focuses on the detection of B8 neutrinos and hep neutrinos through both CC and ES interactions. These two neutrino sources are particularly relevant in the context of this study: B8 neutrinos provide the dominant solar neutrino flux above

Atomic percentage [%]		
Element	Rock	Concrete/ Shotcrete
O	58.74	56.538
Fe	1.50	0.132
Mn	0.03	0.001
Ca	0.11	21.061
K	1.55	0.283
Si	19.85	4.173
Al	4.94	0.514
Mg	3.58	0.382
Na	0.69	0.120
N	-	0.067
C	-	12.005
H	9.00	4.724

Table 6.1: Atomic composition of cavern rock and assumed low-radioactivity concrete and shotcrete used to line the detector cavern walls. Data taken from [190].

2 MeV, while hep neutrinos represent the highest energy component predicted by the SSM, with endpoint energies extending to approximately 18 MeV. To date, hep neutrinos have not been experimentally observed; existing measurements have only set upper limits on their flux [191, 192]. Detecting these rare, high-energy neutrinos would be an important discovery and would provide a stringent test of the SSM.

The predicted signal rates for each interaction channel are summarized in Table 6.2, with the corresponding input spectra shown in Figure 6.4.

Interaction Channel	Events / (10 kton × year)
$\nu_e + {}^{40}\mathrm{Ar} \rightarrow e^- + {}^{40}\mathrm{K}^*$ (^{8}B CC)	14380
$\nu_e + e^- \rightarrow \nu_e + e^-$ (^{8}B ES)	9160
$\nu_e + {}^{40}\mathrm{Ar} \rightarrow e^- + {}^{40}\mathrm{K}^*$ (hep CC)	86
$\nu_e + e^- \rightarrow \nu_e + e^-$ (hep ES)	23

Table 6.2: Expected number of ν_e interactions from B8 and hep solar neutrinos in a 10-kiloton-year exposure, separated by interaction channel. Both CC and ES interactions are included.

These estimates are based on the solar neutrino fluxes from the BS05(OP) Standard Solar Model [166] shown in Figure 6.1, combined with neutrino-argon interaction

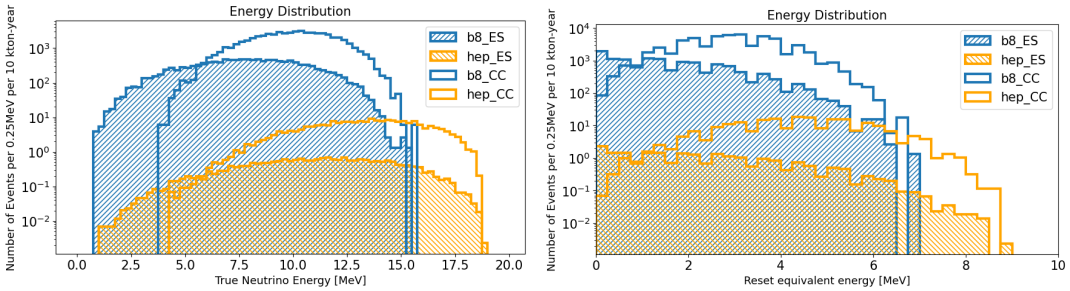


Figure 6.4: Energy spectra of B8 and hep neutrino interactions in a 10-kiloton LArTPC per year. The plot on the left shows distributions as a function of true neutrino energy; the plot on the right shows corresponding spectra reconstructed using reset-equivalent energy, as measured by the Q-Pix readout.

cross sections from Ref. [106], which are derived using the MARLEY simulation framework [193] shown in Figure 6.5.

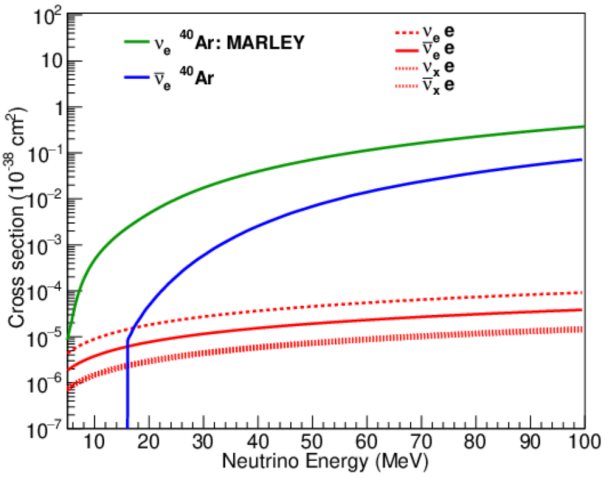


Figure 6.5: Neutrino interaction cross sections on ^{40}Ar. Figure taken from [106].

6.4 Background Prediction

Solar neutrinos primarily interact via CC or ES interactions producing single recoiling electrons in the sub-MeV to low-MeV energy range. These signals are rare and subtle,

and are often indistinguishable from backgrounds that also produce lone electrons, such as beta decays and Compton-scattered electrons from external gamma rays. As shown in Figure 6.4, the relevant energy window extends up to about 20 MeV, covering signals from both B8 and hep neutrinos. Within this window, a wide variety of background processes must be carefully considered in order to assess the sensitivity.

Previous experiments, such as SNO [194] and Borexino [195, 182], have shown that precise solar neutrino measurements are possible, but only if all relevant backgrounds are well understood and tightly controlled. In the context of a 10-kiloton LArTPC like DUNE's far module, the background conditions differ significantly from those targeting low energy as prime research goals. The radiopurity, geometric structure, and reconstruction techniques of a LArTPC create both opportunities and challenges for background mitigation.

Unlike supernova bursts, which produce a transient signal lasting only around ten seconds, solar neutrino detection relies on continuous readout over long time periods —months or even years. This extended integration time makes it essential to account for radioactive decays that occur on timescales far longer than what is relevant for burst detection. As a result, even long-lived isotopes that are negligible in the context of supernova neutrino detection can become significant background sources for solar neutrino measurements, particularly as their decay products accumulate over time. This accumulation poses a serious challenge to solar neutrino detection, where the signal is both rare and low in energy. The backgrounds relevant to solar neutrino detection are divided into two main categories based on their point of origin, relative to detector: internal and external, as detailed in the following subsections.

A comprehensive overview of all background isotopes, including half-lives, decay modes, energies, daughter products, branching ratios, and expected rates, is presented

in Table 6.5 at the end of this section for reference.

6.4.1 Internal Backgrounds

We begin by examining internal backgrounds—radioactive processes originating within the active volume including intrinsic radioactivity in the liquid argon and contaminants within detector components. These sources, intrinsic to the argon medium or introduced via detector components and materials, represent some of the most challenging and persistent backgrounds for low-energy solar neutrino studies. Table 6.3 shows the brief summary of these relevant processes.

Source	**Process Type**	**Mechanism**	**Impact on Analysis**
Intrinsic Ar Isotopes (^{39}Ar, ^{42}Ar, ^{85}Kr)	β decay	Beta particles emitted from intrinsic cosmogenic isotopes	Produce electrons that mimic solar signals
Intrinsic Rn Isotopes (^{222}Rn, ^{220}Rn, ^{219}Rn)	α and β decays	Sequential radioactive decay in LAr from radon daughters	β decays produce high-energy electrons that mimic solar signals
α from Rn chains	α capture on Ar	α particles excite ^{36,38,40}Ar nuclei, emitting 1–18 MeV γ cascades	γ-induced electrons (Compton/pair production) mimic solar signals; significant above 5 MeV
α from Rn chains	(^{40}Ar(α,n)) reactions	α induces neutron emission with coincident γ rays	Neutron and γ energies are low; interaction rates subdominant —excluded in this study
Detector material radioactivity	$\alpha/\beta/\gamma$ from U/Th chains, ^{60}Co, ^{40}K	Emissions from support structures, electronics, etc.	Not included in this study due to minimal Q-Pix material; contributions expected to be negligible

Table 6.3: Summary of internal background sources, processes, and their impact on solar neutrino signal identification in a liquid argon detector.

6.4.1.1 Argon radioactivity: ^{39}Ar, ^{42}Ar, and ^{85}Kr

Commercially available argon is primarily derived from the Earth's atmosphere through cryogenic fractional distillation of liquefied air, a process used in large-scale industrial

air separation units. In this method, atmospheric air is compressed, cooled, and liquefied, and its components are separated based on their boiling points. Argon, which boils at 87.4 K, is isolated taking advantage of the difference in boiling points of nitrogen (77.4 K) and oxygen (90.2 K). It is then purified and stored either as a compressed gas or cryogenic liquid. The isotopic composition of atmospheric argon is dominated by the stable isotope ^{40}Ar, which makes up 99.6% of the total, with smaller contributions from stable isotopes ^{36}Ar (0.34%) and ^{38}Ar (0.06%) [196]. The isotope ^{40}Ar is the one exploited in LArTPC experiments due to its favorable physical and nuclear properties. While these isotopes are not problematic for high-energy physics applications, atmospheric argon also contains several radioactive isotopes, notably ^{37}Ar, ^{39}Ar, and ^{42}Ar, with estimated abundances of approximately 3×10^{-19}, 8×10^{-13}, and 1×10^{-19} atoms per atom of argon, respectively. These isotopes are particularly concerning for low-energy studies such as solar neutrino detection.

These radioactive isotopes originate through cosmic-ray interactions in the atmosphere and during neutron activation processes. ^{39}Ar is produced through several processes, including the ^{40}Ar(n,2n)^{39}Ar reaction induced by fast neutrons, as well as spallation from cosmic rays and secondary reactions involving neutron capture and beta decay. ^{39}Ar undergoes beta decay with a half-life of 269 years and a Q_β = 565 keV. ^{37}Ar, on the other hand, is primarily produced via spallation reactions on argon [197]. It has a relatively short half-life of 35 days and decays via electron capture, producing a low-energy signal of Q_β=0.813 MeV. Finally, ^{42}Ar, a rare isotope with a half-life of 32.9 years, is produced mainly through α capture of ^{40}Ar or two-step neutron capture of ^{40}Ar [198]. It decays to ^{42}K producing energy of Q_β=0.599 MeV. Although ^{37}Ar undergoes electron capture, both ^{39}Ar and ^{42}Ar decay via beta emission, producing electrons that propagate within the detector, which can closely mimic the electron sig-

nals expected from solar neutrino interactions. In contrast, ^{37}Ar is not considered in this study, as its short half-life of 35 days ensures that its activity will have decayed well before data taking begins. Moreover, once atmospheric argon is extracted, purified, and stored underground—shielded from further cosmic-ray exposure—no additional ^{37}Ar is produced, preventing any replenishment of this isotope.

Activities of ^{39}Ar and ^{42}Ar in liquid argon have been measured by several experiments, including WARP [199], GERDA [200], DEAP-600 [201], and DBA [202], which reported values of approximately 1 Bq/kg and 50–100 μBq/kg, respectively. In this study, we assume activities of 1 Bq/kg for ^{39}Ar and 100 μBq/kg for ^{42}Ar. In addition to these intrinsic argon isotopes, another background source of concern is ^{85}Kr. It is a radioactive noble gas introduced into the environment primarily through nuclear fuel reprocessing and atmospheric fallout from weapons testing, or due to neutron capture reactions of cosmic ray neutrons with ^{84}Kr in the atmosphere [203]. Despite the fact that krypton is chemically distinct from argon, trace amounts can be present in commercial argon due to its similar physical properties and the difficulty of separating noble gases. ^{85}Kr has a half-life of 10.7 years and beta-decays with $Q_\beta = 0.687$ MeV. Depending on the argon purity, it can vary up to factor of three. The activity level of 0.1 Bq/kg was assumed in this study [182, 199].

The daughter isotopes resulting from the decay of ^{39}Ar and ^{85}Kr are stable. However, ^{42}Ar decays into an unstable isotope, ^{42}K, which subsequently undergoes beta decay with half-life of 12 hours, with the energy of Q_β=3.525 MeV. Approximately 82% of these decays proceed directly to the ground state of ^{42}Ca, and the remaining 18% transition to an excited state ^{42}Ca*, emitting an additional 1.524 MeV gamma ray.

In principle, if the ^{42}K ion remains positively charged ($^{42}K^+$), the background from this decay chain could be reduced, as the positively charged ions might drift toward

the cathode and out of the fiducial volume before it decays. However, there are no measurements made for the ion survival probability of $^{42}K^{+}$ in liquid argon. At these energies, a substantial amount of any potential reduction in background due to ion drift is expected to be negligible. Thus, the conservative assumption was made such that the daughter nucleus activities is the same as those of their parent isotopes.

As detailed in the SLoMo proposal [185] and mentioned in section 6.2.0.1, the UAr can significantly reduce internal radioactive backgrounds. The activities of ^{39}Ar and ^{85}Kr in UAr have been measured by the DarkSide collaboration to be approximately 0.73 mBq/kg and 2 mBq/kg, respectively [204, 205], reporting reductions by roughly three orders of magnitude. Although direct measurements of ^{42}Ar activity in UAr have not yet been performed, a three-order-of-magnitude suppression relative to atmospheric argon was assumed, to be consistent with assumptions made in previous studies [185, 206].

6.4.1.2 Radon decay chains: ^{119}Rn. ^{220}Rn, ^{222}Rn

Radon isotopes are generated from the decay of uranium and thorium in detector components and surrounding materials such as cavern rock, concrete, and shotcrete, and can diffuse into the detector's active volume. Radon isotopes and their decay daughters were classified as internal backgrounds in this study, as their decays primarily occur within the detector. Following Ref. [207], activity of 1 mBq/kg was assumed for ^{222}Rn, which originates from the ^{238}U decay chain. Because the measured abundance of ^{232}Th is typically 1.5 to 5 times higher than that of ^{238}U in surrounding materials [208, 209, 210, 211], and considering that ^{220}Rn is a decay product of ^{232}Th, and given that ^{220}Rn is a decay product of ^{232}Th, we conservatively assume a ^{220}Rn activity of 5 mBq/kg. Finally, for ^{219}Rn which arises from the ^{235}U decay chain, an activity of 7 mBq/kg was

estimated based on the relative isotopic abundance of uranium [212].

Each radon isotope generates a radioactive decay chain such as alpha and beta decays with varying energies. The specific decay chains considered in this study are visualized in Figure 6.6 and Figure 6.7, and detailed in Table 6.5. The expected number of events for each decay within these chains is calculated assuming secular equilibrium, where the decay rate of each daughter isotope is determined by multiplying the parent's decay rate by the branching ratio and accounting for its probability to decay within a one-year time window. For long-lived isotopes such as ^{210}Pb, accumulation over extended periods could increase their activity. However, as will be demonstrated later, the sensitivity results presented here do not significantly depend on these particular decays or their subsequent radioactive daughter isotopes.

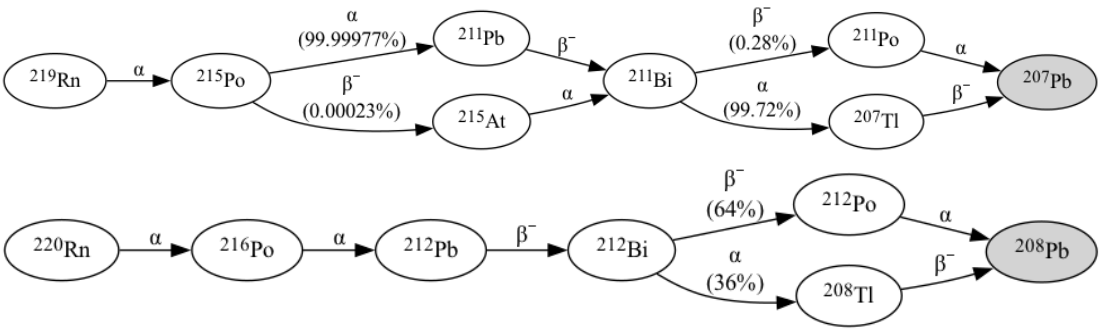


Figure 6.6: Decay chains of ^{219}Rn (top) and ^{220}Rn (bottom), originating from the ^{235}U and ^{232}Th series, respectively. Each chain illustrates sequential alpha and beta decays leading to stable lead isotopes (^{207}Pb and ^{208}Pb). Branching ratios are labeled where relevant, highlighting both dominant and subdominant pathways.

As previously mentioned, beta-emitting isotopes and solar neutrino interactions both generate one primary electron that propagates within the detector. Although most beta emitters yield electrons with energies below approximately 2–3 MeV, two thallium isotopes, ^{208}Tl and ^{210}Tl, exhibit significantly higher energies Q_β of 5.0 MeV and 5.4 MeV, respectively. The beta electron emitted from ^{208}Tl decays can carry energies

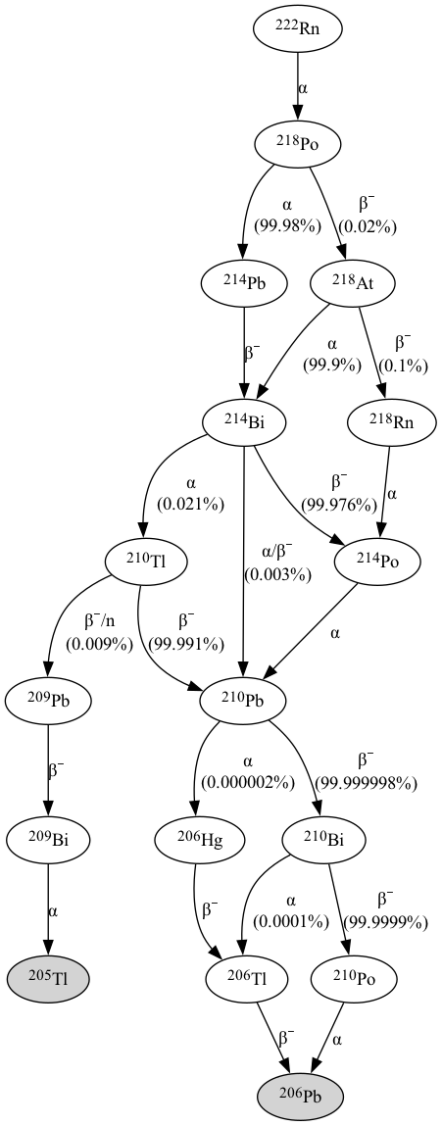


Figure 6.7: Decay chain of ^{222}Rn, part of the ^{238}U series. This chain proceeds through a series of alpha and beta decays with occasional branching, ultimately terminating at stable ^{206}Pb. Minor branches and rare decay modes are shown alongside their branching fractions.

up to 2.38 MeV, with the remaining decay energy emitted as gamma rays, whereas ^{210}Tl decays produce electrons with energies extending up to 4.40 MeV. This presents an irreducible background for detecting solar neutrino events below 4.40 MeV, as we estimate approximately 10^7 ^{210}Tl decays occurring within the active detector volume, two orders of magnitude higher than the total expected number of solar neutrino events.

Regarding alpha decays, the ionization tracks produced by alpha particles do not pose a significant problem, as they are morphologically distinct from those of solar neutrino-induced electrons. However, alpha particles can also be captured by argon isotopes (^{36}Ar, ^{38}Ar, and ^{40}Ar) via "giant resonance" processes, in which the incoming alpha particle excites the nucleus to a high-energy collective state involving the coherent motion of protons against neutrons. These resonantly excited nuclei subsequently de-excite by emitting gamma rays with energies ranging from approximately 1 to 17 MeV [213]. These gamma rays represent a significant background for solar neutrino detection, as they can produce electrons within the active volume through Compton scattering or pair production, thereby mimicking solar neutrino signatures.

Currently, alpha-capture cross sections in argon have only been measured with limited precision, exhibiting approximately 30% uncertainty and with limited parameter space [213]. These cross sections were measured at 90° for alpha energies between 6 and 15 MeV. The average cross section was then calculated by integrating over the full solid angle, assuming isotropic emission.

Given the potential impact of this background on solar neutrino studies, the rate has been estimated based on these past measurements on alpha capture's cross section [213]. The estimated alpha-capture rate is approximately 10^6 events per 10 kiloton per year. This rate is independently verified through simulations using Q-Pix Geant4 (QPixG4), which modeled isotropic alpha emission within the detector volume using the energies

and branching fractions listed in Table 6.5, and yielded consistent results. The resulting gamma-ray energy spectrum from alpha-capture events is shown in Figure 6.8.

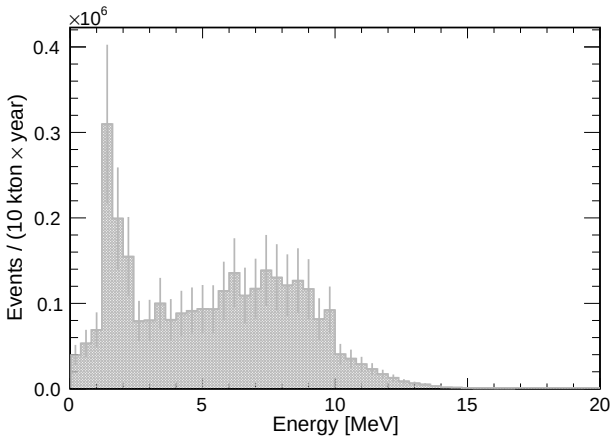


Figure 6.8: Simulated energy spectrum of gamma rays produced from alpha-capture reactions in argon. The error bars reflect uncertainties in the measured cross sections. Taken from our forthcoming study [187].

The spectrum spans a wide energy range, with a substantial number of events occurring between 5 and 10 MeV, and a non-negligible tail extending beyond 12 MeV. This overlap directly affects the energy window for B8 solar neutrinos and partially overlaps with that of hep neutrinos. While the high-energy tail is less populated, it remains especially problematic due to the low expected event rate of hep neutrinos. Moreover, the underlying cross sections used in the simulation carry large uncertainties, and much of the existing data is sparse or incomplete. This introduces considerable uncertainty into the background model. As a result, improving the precision of alpha-capture measurements in argon is crucial for reducing model uncertainties and enabling robust solar neutrino sensitivity estimates.

Alpha particles can also interact with argon nuclei through the alpha-induced neutron emission, where ^{40}Ar interacts with an α particle, emit a neutron and gamma rays,

resulting on the formation of ^{43}Ca [214]. Based on the simulation, this process rate can be estimated to be pproximately 10^7 such reactions per year. The resulting gamma energies span from 0.3 to 6.2 MeV, consistent with previously reported measurements [215], and the neutron energies extend up to 3.6 MeV. Since these energies are below those of external neutron and gamma rays discussed in the following sections, and their reaction rates are significantly lower, their contributions are not considered in this analysis. Additionally, beta-delayed neutron emission from the radon daughter ^{210}Tl may occur. In this process, ^{210}Tl undergoes beta decay, transforming into ^{210}Pb. Normally, this transition would result in the emission of a beta particle and a neutrino.

However, in some cases, the beta decay populates excited states in the daughter nucleus (^{210}Pb*) that lie above the neutron separation energy. When this happens, the nucleus is energetically unstable and can release a neutron in addition to the beta particle. For ^{210}Tl, the emitted neutron in such decays can carry an energy of up to 5.189 MeV, corresponding to the energy difference between the excited state and the neutron emission threshold. The occurrence of this process depends on the branching ratio to those high-lying excited states, which is typically small. Thus, while this mechanism contributes neutrons that fall within the energy range of relevance to solar neutrino backgrounds, the expected rate of this decay is extremely low compared to the dominant external neutron backgrounds and is therefore also excluded from our analysis.

Table 6.5 summarizes all considered radioactive decays originating from radon isotopes, along with their respective activities and half-lives. As previously discussed for ^{42}K$^+$, certain daughter nuclei produced by radioactive decays may remain positively charged and potentially be removed if their half-lives exceed the drift time. Experimental results from Enriched Xenon Observatory 200 (EXO-200) [216] indicate ion survival

probabilities in liquid xenon of approximately 50% for $^{218}Po^{+}$ (produced via alpha decay) and 75% for $^{214}Bi^{+}$ (produced via beta decay). However, measurements in liquid argon by DarkSide [217] report a significantly lower survival probability of roughly 37% for $^{218}Po^{+}$. Although this effect might contribute to a reduction in background rates, we adopt the conservative assumption that each daughter nucleus has the same activity as its parent, considering that potential reductions are negligible relative to the overall background-to-signal ratio. For instance, it requires four sequential decays such as $^{220}Rn \rightarrow {}^{216}Po \rightarrow {}^{212}Pb \rightarrow {}^{212}Bi \rightarrow {}^{208}Tl$ to produce ^{208}Tl. Even with a hypothetical 50% ion survival probability and complete ion collection prior to decay, the resulting ^{208}Tl activity would decrease from approximately 10^{12} to $\sim 10^{10}$ decays per year, still five orders of magnitude greater than the expected number of solar neutrino events.

In the low-background scenario, the implementation of a dedicated radon purification system, along with rigorous detector fabrication and installation protocols is assumed. This can reduce radon-related backgrounds by three orders of magnitude [185], which have already been achieved by dark matter experiments, including DarkSide [218] and DEAP-600 [219]. Thus, in the low-background scenario, a three-order-of-magnitude reduction in all radon-induced radioactive decays were conservatively assumed.

6.4.1.3 Radioactivity from detector components

Radiocontaminants present within detector components were considered as potential sources of internal background. Detector materials typically contain considerable amounts of radioactive isotopes such as ^{238}U, ^{235}U, ^{232}Th, ^{60}Co, and ^{40}K, which can generate background events. However, since the Q-Pix readout system is expected to require significantly less material and simpler mechanical support structures compared to conventional APAs or CRPs, radioactive decays from detector components were not

considered in this study. Additionally, while isotopes such as ^{238}U, ^{235}U, and ^{232}Th give rise to the radon decay chains discussed previously, ^{60}Co and ^{40}K only emit low-energy beta particles with energies below 1.5 MeV. Thus, these decays contributions are not included either.

6.4.2 Time Integration and Decay Chain Modeling

To quantify these contributions, especially for long-lived isotopes and their daughter particles, time-dependent modeling is essential. The time evolution of each decay chain is modeled using the standard exponential decay law:

$$N_{\text{decayed}}(t) = N_0 \left(1 - e^{-\lambda t}\right), \tag{6.10}$$

where $N_{\text{decayed}}(t)$ is the number of decayed nuclei at time t, N_0 is the initial number, and $\lambda = \frac{\ln 2}{T_{1/2}}$ is the decay constant, with $T_{1/2}$ being the half-life. Since the rates are calculated for a 1-year exposure of a 10-kiloton detector module, $t = 1$ year was used. This allows the estimation not just of the primary isotope's decay, but also of the expected number of daughter nuclei that form and decay over the same period. In cases where the half-lives are much shorter than one year, secular equilibrium is assumed between parent and daughter activities, after adjusting for branching ratios and decay probabilities.

6.4.3 External backgrounds

External backgrounds originate from the surrounding cavern environment—such as rock, concrete, shotcrete, and the cryostat—and enter the fiducial volume primarily as neutrons and gamma rays. A summary of external background sources is provided in Table 6.4, listing the relevant processes, mechanisms, and their impact on solar neu-

trino signal identification. Alpha and beta particles from these external materials do not contribute to this study, as their ranges are too short to penetrate into the detector.

Source	**Process Type**	**Mechanism**	**Impact on Analysis**
Neutrons (E>1.46 MeV)	Inelastic scattering on ^{40}Ar	Excitation of ^{40}Ar followed by γ cascades (1.46–11.77 MeV)	γ produces electrons via Compton scattering or pair production, mimicking solar signals
Neutrons (E<1.46 MeV)	Elastic scattering and capture	Neutrons thermalize and are captured by ^{40}Ar or ^{36}Ar, emitting γ (6.1 MeV, 8.8 MeV)	γ again leads to electrons that mimic solar signals
γ from cavern	γ interaction (Compton/pair production)	External γ from rock/concrete penetrates cryostat and interacts in LAr	Produce signal-like electrons directly; highly challenging to distinguish from solar signals

Table 6.4: Summary of external background processes relevant to solar neutrino detection in liquid argon detectors. All mechanisms produce secondary electrons that can mimic solar neutrino signatures.

6.4.3.1 Neutrons

Neutrons are produced mainly through fission process and alpha-induced nuclear reactions. These neutrons are primarily produced through alpha-induced nuclear reactions and spontaneous fission, driven by isotopes in the ^{232}Th and ^{238}U decay chains happening in the cavern. The neutron rate and associated energy spectrum were estimated based on the material compositions listed in Table 6.1. For neutrons produced via (α, n) reactions, the neutron energy spectra are generated using the **NeuCBOT** software package [220], which simulates alpha interactions with elements found in the cavern materials based on their measured elemental abundances. The resulting spectrum includes both the energy distribution and the total yield of neutrons generated through this mechanism. Additionally, a significant component of the neutron background arises from spontaneous fission of ^{238}U. This contribution is modeled using a Watt fission spectrum, an empirical representation of the energy distribution of fission neutrons. The

Watt spectrum takes the form:

$$N(E) \propto e^{-E/a} \sinh\left(\sqrt{bE}\right) \tag{6.11}$$

where E is the energy of neutron, and a and b are parameters that characterize the shape of the spectrum and are specific to the fissioning isotope [221]. In this study, neutron yield per fission was taken be 2, as was done in [208]. These combined inputs provide a realistic prediction of the total neutron background relevant for solar neutrino analyses. The combined neutron energy spectrum is presented in Figure 6.9, and was used in this study. These neutrons are then propagated within the detector volume using the QPixG4 simulation framework.

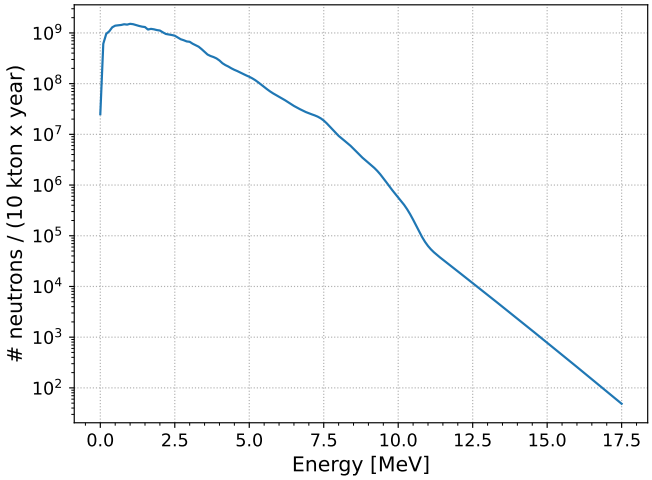


Figure 6.9: Energy spectrum of neutrons simulated from radioactive processes in cavern wall materials. Taken from our forthcoming study [187].

In argon, neutrons with energies above 1.46 MeV can undergo inelastic scattering [222, 223], exciting the ^{40}Ar. This will result in the de-excitation of gamma rays – gamma-ray cascades with energies in the range of 1.46 to 11.77 MeV [222]. Using the experimentally measured neutron-argon inelastic cross sections [223], the neutron flux estimated from

radiological assays of rock and shotcrete samples reported by DUNE [207], and our own QPixG4 simulations,the neutron inelastic scattering frequency was approximated to be 0.3 Hz per 10 kiloton. Below 1.46 MeV, neutrons will no longer have enough energy to excite ^{40}Ar and trigger innelastic scattering. Instead, they will mainly undergo elastic scattering, until it loses energy through multiple elastic scatterings until its kinetic energy is comparable to the thermal energy of the liquid argon (thermalization). As the energy level is far below MeV range, their contributions are considered negligible.

Once thermalized, neutrons can become candidates to be captured by argon nuclei. In this process, gamma cascades with maximum energies of 6.1 MeV and 8.8 MeV from captures on ^{40}Ar and ^{36}Ar, respectively are expected [224, 225]. Neutron capture on impurities, such as ^{14}N, can yield gamma-rays with even higher energies [226], but given the anticipated purity levels of liquid argon [57], these contributions are considered negligible. To estimate the neutron capture rate, 3 Hz per 10 kiloton reported in a study of potential for solar neutrino detection in DUNE [190] were used, and the gamma cascades from neutron capture was simulated with QPixG4. Finally, the output was re-weighted to match experimental measurements from neutron resonance study [227]. For the low-background scenario, a 50-cm water shield combined with a borated cryostat were considered, and reduced neutron backgrounds by four orders of magnitude, as detailed in Ref. [185]. Thus, neutron-induced backgrounds in low-background case was calculated by reducing the simulated neutron rate shown in Figure 6.9 by a factor of 10^4.

6.4.3.2 Gammas

Gamma rays interacting in liquid argon often produce single electrons through processes like Compton scattering or pair production. These interactions produce indistinguish-

able signals from solar neutrino events and are therefore particularly challenging to reject. Therefore, accurately estimating gamma-ray rates from external sources, referred as "external gammas" here, is crucial for solar neutrino detection studies. Gamma rays emitted by radioactive decays in cavern walls typically reach energies up to approximately 3 MeV. Additionally, neutrons produced through fission and (α,n) reactions may be captured by nuclei in surrounding materials such as cavern rock, concrete, shotcrete, and cryostat walls, generating higher-energy gamma rays, reaching energies up to about 11.5 MeV [228]. Furthermore, alpha particles from radioactive decay chains and fission processes can also interact or induce alpha-capture reactions in materials like magnesium and silicon, leading to gamma-ray emissions with energy exceeding 17 MeV [229]. Unlike neutrons, gamma rays penetrate the cryostat walls with minimal attenuation and can propagate tens to hundreds of centimeters into the liquid argon.

Given the significance of external gamma backgrounds, a detailed review of measured gamma-ray spectra from existing underground experiments was conducted, independently from simulations, which carry uncertainties. While the local geological composition affects the gamma flux, the substantial consistency observed among different underground laboratories provides confidence in the spectrum adopted here.

The gamma-ray spectrum from the DUNE experiment [207, 230] was adopted as baseline in this study, which estimates total external gamma flux of approximately 21 MHz reaching to the surface of liquid argon. This value is consistent, within an order of magnitude, with measurements performed at various underground facilities, including Gran Sasso [231], SNOLAB [232], YangYang [233], Jinping [234], and Kamiokande [235]. The fraction of gamma rays above 5 MeV in the DUNE-based spectrum (shown in Figure 6.10) is approximately 9.6×10^{-8} of the total flux. This fraction also varies significantly across other reported spectra, ranging from 10^{-8} to 10^{-5}. Such variation

in high-energy gamma estimates is particularly relevant, since if gamma rates above 5 MeV is higher than anticipated, this could severely impact the detection of both B8 and hep solar neutrinos. Therefore, dedicated measurements of external gamma-ray spectra, particularly at energies above 5 MeV, will be crucial for precise solar neutrino sensitivity estimates.

Finally, it is important to highlight that existing gamma-ray measurements rarely provide information of spectrum beyond approximately 11 MeV. Since materials like magnesium and silicon inside the cavern can produce gamma rays with energies above 17 MeV, the higher energy range of gamma-ray spectrum was obtained by extrapolating the spectrum given in Refs. [207, 230]. This extrapolated spectrum is presented along with the spectrum from the DUNE experiment in Figure 6.10, and was used as the final gamma-ray spectrum.

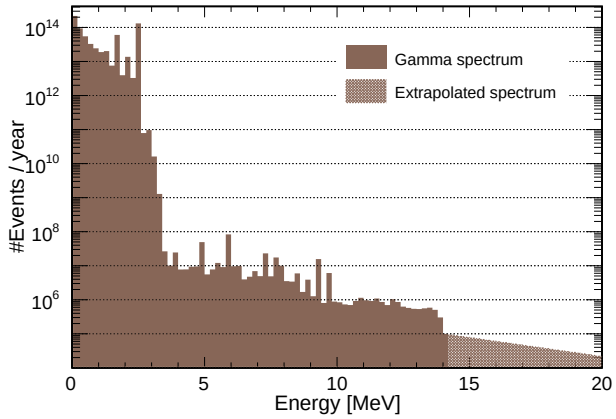


Figure 6.10: External gamma-ray spectrum at the LAr surface estimated by DUNE [207, 230]. The spectrum shows a steep decline above 4 MeV. The dashed tail indicates the extrapolated high-energy component. Taken from our forthcoming study [187].

Since external gammas were not addressed in the SLoMo proposal [185], no reduction is considered for the low-background scenario of study as well, and the predicted rates

discussed in this section were used.

Isotope	Half-life (s)	Decay	Q (MeV)	Daughter Isotope	BR (%)	Rate (Bq/kg)	Expected events	Low-bkg events
Argon and Krypton								
^{39}Ar	8.5×10^{9}	β	0.565	^{39}K	100	1.1	$\sim 10^{14}$	$\sim 10^{11}$
^{42}Ar	1.0×10^{9}	β	0.599	^{42}K	100	1.0×10^{-4}	$\sim 10^{10}$	$\sim 10^{7}$
^{42}K	4.5×10^{4}	β	3.525	^{42}Ca	100	1.0×10^{-4}	$\sim 10^{10}$	$\sim 10^{7}$
^{85}Kr	3.9×10^{4}	β	0.687	^{85}Rb	100	1.0×10^{-1}	$\sim 10^{13}$	$\sim 10^{10}$
^{219}Rn decay chain								
^{219}Rn	4.0	α	6.946	^{215}Po	100	7.0×10^{-6}	$\sim 10^{9}$	$\sim 10^{6}$
^{215}Po	1.8×10^{-3}	α	7.526	^{211}Pb	99.99977	7.0×10^{-6}	$\sim 10^{9}$	$\sim 10^{6}$
^{215}Po	1.8×10^{-3}	β	0.721	^{215}At	0.00023	1.6×10^{-11}	$\sim 10^{3}$	$\sim 10^{0}$
^{211}Pb	0.6	β	1.367	^{211}Bi	100	7.0×10^{-6}	$\sim 10^{9}$	$\sim 10^{6}$
^{215}At	1.0×10^{-4}	α	8.178	^{211}Bi	100	1.6×10^{-11}	$\sim 10^{3}$	$\sim 10^{0}$
^{211}Bi	3.6×10^{-2}	α	6.750	^{207}Tl	99.72	7.0×10^{-6}	$\sim 10^{9}$	$\sim 10^{6}$
^{211}Bi	3.6×10^{-2}	β	0.574	^{211}Po	0.28	2.0×10^{-8}	$\sim 10^{6}$	$\sim 10^{3}$
^{207}Tl	7.9×10^{-2}	β	1.418	^{207}Pb	100	7.0×10^{-6}	$\sim 10^{9}$	$\sim 10^{6}$
^{211}Po	0.5	α	7.594	^{207}Pb	100	2.0×10^{-8}	$\sim 10^{6}$	$\sim 10^{3}$
^{220}Rn decay chain								
^{220}Rn	55.6	α	6.404	^{216}Po	100	5.0×10^{-3}	$\sim 10^{12}$	$\sim 10^{9}$
^{216}Po	0.1	α	6.906	^{212}Pb	100	5.0×10^{-3}	$\sim 10^{12}$	$\sim 10^{9}$
^{212}Pb	3.8×10^{4}	β	0.569	^{212}Bi	100	5.0×10^{-3}	$\sim 10^{12}$	$\sim 10^{9}$
^{212}Bi	3.6×10^{3}	α	2.251	^{208}Tl	64	3.2×10^{-3}	$\sim 10^{12}$	$\sim 10^{9}$
^{212}Bi	3.6×10^{3}	α	6.207	^{212}Po	36	1.8×10^{-3}	$\sim 10^{11}$	$\sim 10^{8}$
^{208}Tl	1.8×10^{2}	β	4.999	^{208}Pb	100	3.2×10^{-3}	$\sim 10^{12}$	$\sim 10^{9}$
^{212}Po	3.0×10^{-7}	α	8.954	^{208}Pb	100	1.8×10^{-3}	$\sim 10^{11}$	$\sim 10^{8}$
^{222}Rn decay chain								
^{222}Rn	3.3×10^{5}	α	5.590	^{218}Po	100	1.0×10^{-3}	$\sim 10^{11}$	$\sim 10^{8}$
^{218}Po	1.9×10^{2}	α	6.114	^{214}Pb	99.98	1.0×10^{-3}	$\sim 10^{11}$	$\sim 10^{8}$
^{218}Po	1.9×10^{2}	β	0.259	^{218}At	0.02	2.0×10^{-7}	$\sim 10^{7}$	$\sim 10^{4}$
^{214}Pb	1.6×10^{3}	β	1.018	^{214}Bi	100	1.0×10^{-3}	$\sim 10^{11}$	$\sim 10^{8}$
^{218}At	1.3	α	6.874	^{214}Bi	99.9	2.0×10^{-7}	$\sim 10^{7}$	$\sim 10^{4}$
^{218}At	1.3	β	2.881	^{218}Rn	0.1	2.0×10^{-10}	$\sim 10^{4}$	$\sim 10^{1}$
^{218}Rn	2.1×10^{3}	α	7.262	^{214}Po	100	2.0×10^{-10}	$\sim 10^{4}$	$\sim 10^{1}$
^{214}Bi	1.2×10^{3}	β	3.269	^{214}Po	99.97	1.0×10^{-3}	$\sim 10^{11}$	$\sim 10^{8}$
^{214}Bi	1.2×10^{3}	α	5.621	^{210}Tl	0.021	2.1×10^{-7}	$\sim 10^{7}$	$\sim 10^{4}$
^{214}Bi	1.2×10^{3}	α/β	3.270	^{210}Pb	0.003	3.0×10^{-8}	$\sim 10^{6}$	$\sim 10^{3}$
^{214}Po	1.6×10^{-4}	α	7.883	^{210}Pb	100	1.0×10^{-3}	$\sim 10^{11}$	$\sim 10^{8}$
^{210}Tl	78.0	β	5.483	^{210}Pb	99.991	2.1×10^{-7}	$\sim 10^{7}$	$\sim 10^{4}$
^{210}Tl	78.0	β/n	0.294	^{209}Pb	0.009	1.9×10^{-11}	$\sim 10^{3}$	$\sim 10^{0}$
^{209}Pb	1.2×10^{4}	β	0.644	^{209}Bi	100	1.9×10^{-11}	$\sim 10^{3}$	$\sim 10^{0}$
^{209}Bi	6.3×10^{26}	α	3.137	^{205}Tl	100	0.0	$\sim 10^{0}$	$\sim 10^{0}$
^{210}Pb	7.0×10^{8}	β	0.063	^{210}Bi	99.999998	3.1×10^{-5}	$\sim 10^{9}$	$\sim 10^{6}$
^{210}Pb	7.0×10^{8}	α	3.792	^{206}Hg	0.000002	5.8×10^{-13}	$\sim 10^{2}$	$\sim 10^{-1}$
^{206}Hg	4.9×10^{2}	β	1.308	^{206}Tl	100	5.8×10^{-13}	$\sim 10^{2}$	$\sim 10^{-1}$
^{210}Bi	4.3×10^{5}	α	5.036	^{206}Tl	0.0001	3.1×10^{-11}	$\sim 10^{3}$	$\sim 10^{0}$
^{210}Bi	4.3×10^{5}	β	1.162	^{210}Po	99.9999	3.1×10^{-5}	$\sim 10^{9}$	$\sim 10^{6}$
^{206}Tl	2.5×10^{2}	β	1.532	^{206}Pb	100	5.8×10^{-13}	$\sim 10^{2}$	$\sim 10^{-1}$
^{210}Po	1.2×10^{7}	α	5.407	^{206}Pb	100	2.6×10^{-5}	$\sim 10^{9}$	$\sim 10^{6}$
Other								
α-capture	—	—	—	—	—	—	$\sim 10^{6}$	$\sim 10^{3}$
Neutron inelastic	—	—	—	—	—	—	$\sim 10^{7}$	$\sim 10^{3}$
Neutron capture	—	—	—	—	—	—	$\sim 10^{7}$	$\sim 10^{3}$
Cavern Gammas	—	—	—	—	—	—	$\sim 10^{13}$	$\sim 10^{13}$

Table 6.5: Summary of backgrounds contributing to solar neutrino detection for a 10 kt·yr exposure. Backgrounds are grouped by origin. Expected event counts are computed assuming secular equilibrium.

6.5 Results

This section presents simulation results for solar neutrino signals and associated backgrounds, based on the assumptions detailed in Sections 6.3 and 6.4. Multiple background reduction strategies are explored to assess the feasibility of solar neutrino detection in a liquid argon detector. In addition, the expected data rates for the Q-Pix data acquisition system are evaluated, demonstrating its capacity for continuous, low-threshold readout —a critical requirement for capturing low-energy, time-distributed solar neutrino events.

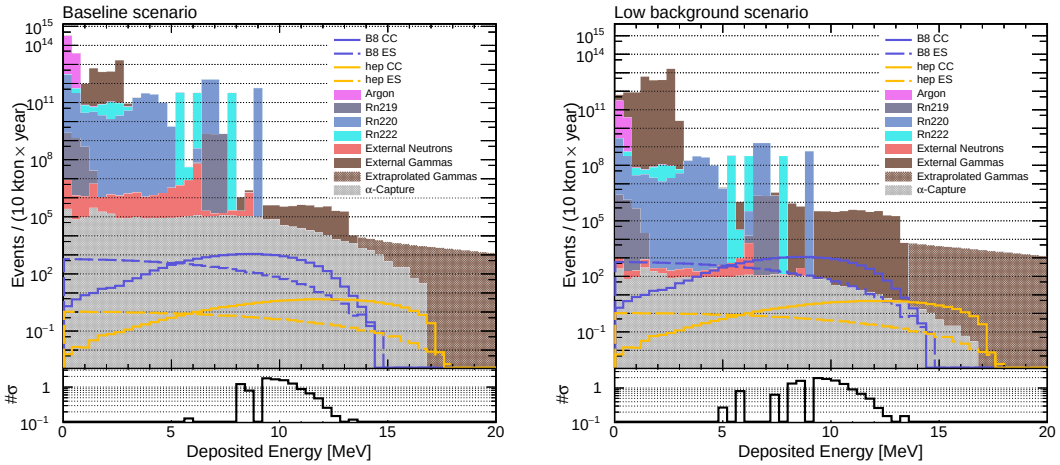


Figure 6.11: Simulated deposited energy spectra of solar neutrinos (B8 and hep) and backgrounds for a 10 kt·yr exposure. The baseline scenario and low-background scenario are shown in left and right, respectively. Stacked histograms show dominant internal and external background contributions, while lines indicate the total solar neutrino spectrum. The sensitivity curves below each plot show statistical significance ($\#\sigma$) as a function of energy, calculated under a background-only hypothesis. Plots follow the format our forthcoming study [187], but the data shown are newly generated under different background assumptions provided by DUNE experiment.

The left top histogram of Figure 6.11 shows the energy spectra deposited by B8 and hep solar neutrino interactions, along with all backgrounds considered in the baseline scenario (described in Section 6.4). Below it, the sensitivity of the combined neutrino channels as a function of deposited energy is shown. The sensitivity ($\#\sigma$) is computed

as $\#\sigma = \Phi^{-1}(1-p)$, where Φ^{-1} is the inverse cumulative distribution function (quantile function) of the standard normal distribution, and p is the p-value associated with the background-only hypothesis. The p-value represents the probability of observing a signal-like fluctuation, or a more extreme result, assuming that no true signal is present.

The results indicate that the detection of solar neutrinos below approximately 8 MeV is essentially infeasible due to the overwhelming background rates from radioactive decays, exceeding the expected solar neutrino signal by up to 11 orders of magnitude in the 2–6 MeV range. Above 8 MeV, the dominant backgrounds arise from gamma-ray interactions, particularly those originating from external sources and from alpha-capture reactions within the detector. Within the energy window of 8–12 MeV, solar neutrino detection may be possible, but it will critically depend on precise constraints of these backgrounds by experiments.

The right histpgram of Figure 6.11 presents the same deposited energy spectra, but for the low-background scenario. While this scenario has significantly lower rates across most of the backgrounds, cavern gamma-rays are irreducible as discussed in Section 6.4.3.2, and gamma rays from alpha-capture reactions remain a significant and uncertain background component. This shows the necessity for dedicated in-situ measurements of these background sources.

In the following subsections, the strategies for further reducing these backgrounds were investigated through software-level techniques, such as event reconstruction strategies (Section 6.5.1), fiducialization (Section 6.5.2), directionality studies (Section 6.5.3), and photon detection capabilities (Section 6.5.4).

6.5.1 Background rejection with Q-Pix clustering

The first strategy explored was to apply the clustering algorithm introduced in Section 5.4.3, leveraging differences in topological signatures and energy depositions among particle types. Of all the particle types considered, only alpha interactions produce significantly different topologies. In contrast, beta decays, gamma-ray interactions (via Compton scattering or pair production), and neutron interactions (via neutron capture or inelastic scattering leading to gamma emission) all predominantly result in single-electron events that topologically mimic solar neutrino interactions.

Gamma and neutron interactions can occasionally produce additional isolated energy depositions, which could potentially be exploited to identify and veto these backgrounds. In the case of gamma rays, such deposition may arise from secondary Compton scatterings, where the gamma deposits energy at multiple spatially separated points. Additionally, for gamma energies above 1.022 MeV, pair production may occur, resulting in the creation of an electron–positron pair. While both particles can produce visible ionization tracks, the positron eventually annihilates, emitting two 511 keV gamma rays. These annihilation gammas can travel some distance before undergoing secondary interactions, leading to further isolated energy depositions. For neutrons, inelastic scattering or capture processes can lead to the emission of high-energy gamma rays, which in turn may create additional energy depositions away from the primary event.

In all cases, these processes can result in multi-site topologies, distinct from the signal expected from solar neutrino interactions: a single, isolated electron track with no additional spatially correlated energy deposits. In this study, the effectiveness of applying different clustering thresholds was investigated as a preliminary strategy to reject some backgrounds. Given the overwhelming background event rates, detailed

topological identification and rejection strategies are deferred to future work and not addressed in this study.

Alpha particles, which stop and deposit their energy rapidly and locally within liquid argon, yield distinctively short clusters compared to electron-induced events. This analysis indicates that alpha interactions are clustered with a maximum of approximately 4 resets, equivalent to the number of resets produced by an electron of about 1 MeV in our detector configuration.

This reset-based clustering threshold can be used to exclude regions of the energy spectrum where solar neutrino signals are entirely obscured by backgrounds, particularly below approximately 3 MeV, as can be seein in Figure 6.11. Therefore, a reset threshold cut of 12 is adopted for the remainder of this study, corresponding to a deposited energy of approximately 3 MeV, effectively removing all events below this threshold.

6.5.2 Fiducialization

External radiation constitutes the dominant background. This subsection investigates the effectiveness of fiducialization in mitigating cavern gamma rays and neutron-induced gamma backgrounds. Figure 6.12 shows the survival probability of external gamma-rays as a function of their initial energy and distance from the cryostat walls. As anticipated, gamma-induced events are exponentially suppressed with increasing fiducialization distance, whereas the solar neutrino signal, being uniformly distributed within the detector, experiences only a linear reduction. To quantify the practical benefits of this effect, a specific fiducialization strategy was implemented.

To illustrate the potential of fiducialization alone, a straightforward yet stringent strategy was considered in this subsection. Using four meters of argon as passive shielding on all sides. This reduces the active detector volume to the innermost two TPC

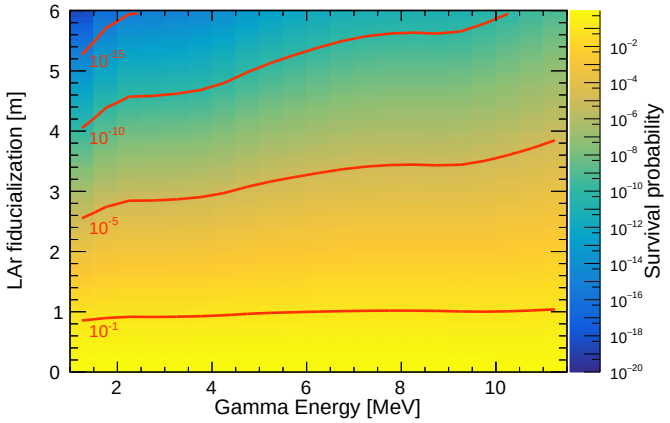


Figure 6.12: Survival probability of external gamma rays as a function of their initial energy and the thickness of liquid argon used as passive shielding. The 10^{-1}, 10^{-5}, 10^{-10}, 10^{-15} contours are shown in red. Plot adopted from our forthcoming study [187].

sections (see Figure 6.3), retaining a region approximately 6 m high and 54 m long, corresponding to roughly 20% of the total active argon mass (approximately 2.3 kilotonnes). This aggressive fiducialization scenario retains approximately $\mathcal{O}(10^4)$ solar neutrino events per year, compared to approximately $\mathcal{O}(10^6)$ gamma-ray events and $\mathcal{O}(1)$ neutron inelastic scattering event per year.

As shown in Figure 6.13, this stringent fiducialization substantially enhances the visibility of the solar neutrino signal across a broader energy range, including the hep neutrino component, which becomes potentially observable.

Unambiguous identification of the hep neutrino component will require precise characterization of alpha-capture gamma rays from argon, as well as precise understanding of external gamma-rays at energies above 11 MeV. Furthermore, achieving adequate energy resolution will be critical for identifying hep neutrino events within the ∼15–18 MeV region. This simplified fiducialization analysis serves as general guidance for future solar neutrino studies, while detailed optimization involving combined background

rejection techniques will still be essential in dedicated analyses and is beyond the scope of this work.

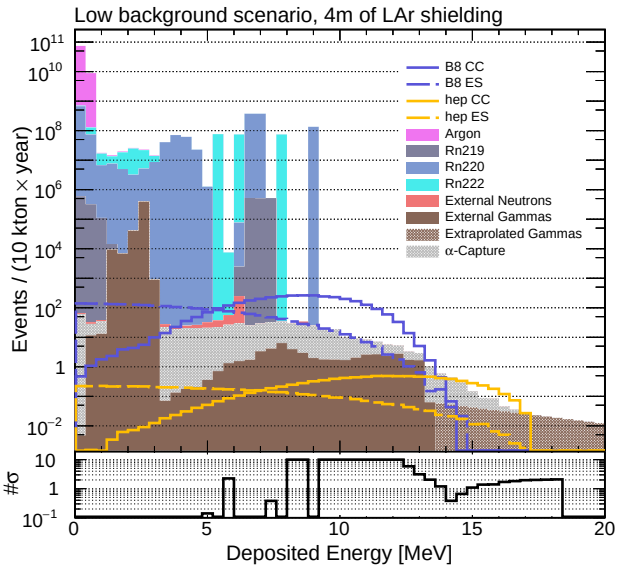


Figure 6.13: Deposited energy spectra for signal and background sources in the low-background scenario, assuming 4 m of liquid argon as passive shielding. The bottom panel shows the signal sensitivity as a function of deposited energy. Plot taken from our forthcoming study [187].

6.5.3 Background rejection with directionality

A key distinguishing feature of solar neutrino events is their known source direction, the Sun, which sets them apart from most background processes. While CC interactions do not preserve directional information of the incoming neutrino, ES events do, as has been described in Section 5.4.7.

In the previous subsection, it was demonstrated that Q-Pix has ability to reconstruct the directions of electrons produced by low-energy ES neutrino interactions, hence reconstruct the direction of incoming neutrinos [87]. In this study, the potential of using directionality was investigated as an additional tool for discriminating solar neutrino

signals from backgrounds.

We assume a Q-Pix clustering threshold set at 12 resets, corresponding to a minimum deposited energy threshold of approximately 3 MeV. Electron directions from ES events are reconstructed following the procedure established in the previous chapter 5.

Unlike the case of supernova neutrino detection, where the transient burst nature and tight time coincidence of events dramatically suppress the background, solar neutrino signals are embedded in a steady background over long exposures. As such, a more rigorous statistical approach is needed to separate signal from noise. To address this challenge, we employ a likelihood-based hypothesis testing framework that combines directional and energy information to assess whether the observed angular distribution is consistent with a solar signal atop background, or background alone. The null hypothesis ($\mathcal{H}_0$) assumes that the observed data come solely from background, while the alternative hypothesis ($\mathcal{H}_1$) allows for contributions from both signal and background.

For each energy bin of interest, simulated pseudo-experiments are generated by drawing events from representative distributions of both signal and background as a function of $\cos\theta$, where θ is defined as the angle between the reconstructed electron direction and the known direction of the incoming neutrino. The absolute value $|\cos\theta|$ is used, since the position of the Sun is known at all times, eliminating the forward–backward ambiguity present in supernova neutrino analyses. This allows directional sensitivity to be characterized more simply and robustly.

The background distribution is modeled as isotropic in $|\cos\theta|$, reflecting the uniform directional behavior expected from gamma rays and neutron-induced backgrounds, which lack any correlation with the solar direction. The total number of background events is evenly divided across a fixed number of angular bins, and the number of events in each bin is drawn from a Poisson distribution with the expected bin mean.

This captures the natural statistical fluctuations inherent in event rates—an especially important consideration in the low-statistics regime of solar neutrino detection—and ensures that the simulated background samples reflect realistic detector behavior and uncertainty.

Signal events, in contrast, exhibit a distinct peak due to the kinematics of elastic scattering. The simulated angular distribution of signal events is first binned and converted into a cumulative distribution function (CDF). Uniformly distributed random numbers are then sampled and mapped onto this CDF, allowing for the generation of events in proportion to the underlying signal probability density. Each sampled event is assigned the midpoint of the corresponding angular bin, yielding a dataset that statistically reproduces the expected signal distribution while naturally incorporating Poisson fluctuations in both the total rate and angular structure. An example illustrating the original signal distribution and the combined signal-plus-background angular distribution is shown in Figure 6.14.

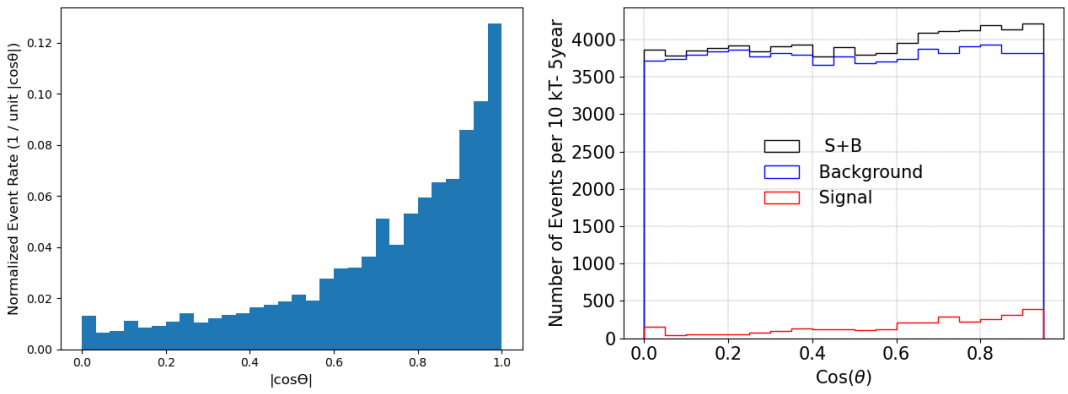


Figure 6.14: Left: Example CDF of pseudo-experiment for the events with reconstructed energy between 6 and 12 MeV in 10kT for a period of 5 years. Right: The angular distributions of signal, background, and total events are shown in red, blue, and black, respectively. Here, θ denotes the angle between the Sun's direction and that of the reconstructed primary electron. The simulation assumes a low-background scenario and a 4 m fiducial volume cut.

To test each hypothesis, a binned Poisson likelihood function is constructed. Under the signal+background hypothesis ($\mathcal{H}_1$), the expected number of events in bin i is modeled as a weighted sum of signal and background contributions:

$$\mathcal{L}(s, b) = \prod_i \frac{(sS_i + bB_i)^{n_i}}{n_i!} e^{-(sS_i + bB_i)}, \tag{6.12}$$

where n_i is the observed number of events in bin i, and S_i and B_i are the normalized signal and background distributions in that bin. The parameters s and b scale the total expected signal and background rates and are adjusted to maximize the likelihood. For the background-only hypothesis ($\mathcal{H}_0$), the signal contribution is fixed to zero ($s = 0$) and the background normalization b is re-optimized.

The test statistic used to quantify the support for the presence of a signal is the log-likelihood ratio:

$$\lambda = -2 \ln \left(\frac{\mathcal{L}_{\mathcal{H}_0}}{\mathcal{L}_{\mathcal{H}_1}} \right), \tag{6.13}$$

where $\mathcal{L}_{\mathcal{H}_0}$ and $\mathcal{L}_{\mathcal{H}_1}$ are the maximum likelihood values under the background-only and signal+background hypotheses, respectively. This procedure is repeated across many pseudo-experiments for both hypotheses, yielding distributions of the test statistic that characterize each scenario. Figure 6.15 shows an example of these distributions: the blue histogram represents test statistics computed under the background-only hypothesis $\mathcal{H}_0$, while the orange histogram corresponds to pseudo-experiments generated under the signal+background hypothesis $\mathcal{H}_1$. The degree of separation between these two distributions directly reflects the statistical sensitivity of the analysis to detecting a directional neutrino signal.

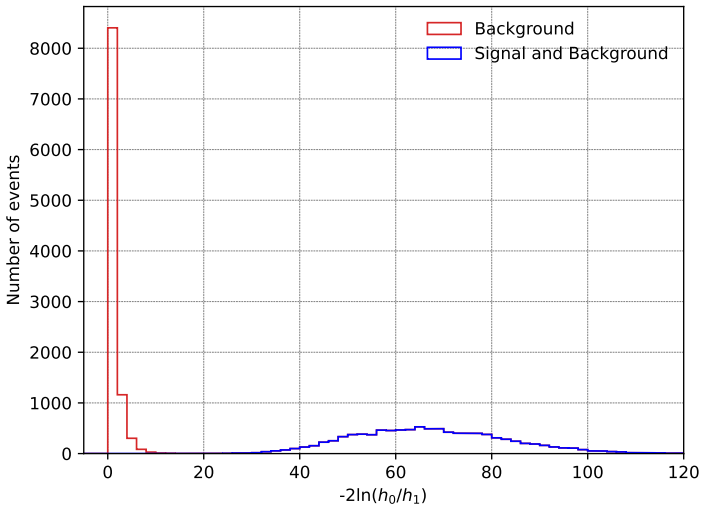


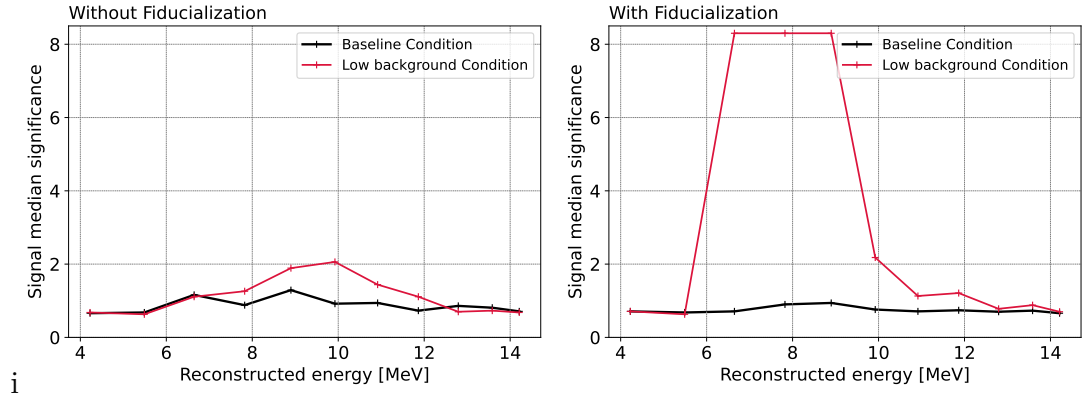
Figure 6.15: Distributions of the log-likelihood ratio test statistic for background-only (blue) and signal+background (red) hypotheses. The separation between the two distributions quantifies the statistical power of the analysis to distinguish the presence of a directional solar neutrino signal from isotropic backgrounds. The degree of overlap directly impacts the computed p-value and resulting significance.

The sensitivity is quantified by calculating the p-value, defined as the fraction of background-only pseudo-experiments yielding a test statistic greater than the median value observed under the signal+background hypothesis. This p-value is then translated into a significance using the inverse cumulative distribution function of the standard normal distribution. The final result characterizes how effectively directional information can distinguish solar neutrino signals from isotropic backgrounds, taking into account statistical fluctuations and limitations imposed by detector performance.

While directionality was previously shown to be a powerful tool for identifying neutrinos from supernova events, the results of this study indicate that its effectiveness in the context of solar neutrinos is significantly reduced due to the overwhelming background rates. As shown in Figure 6.16, the signal median significance remains below 2σ across all energies in both the baseline and low-background scenarios when fiducialization is

not applied, underscoring the challenge of isolating directional information under such high background conditions.

Combining directional reconstruction with a stringent 4 m fiducial volume cut in the low-background scenario, a notable improvement is observed, with sensitivities reaching above 5σ in the 6–12 MeV range. This demonstrates that fiducialization is essential to suppress external gamma and neutron backgrounds sufficiently for directionality to become a viable tool in solar neutrino detection. Without fiducialization, or under the baseline background assumptions, the directional discrimination power is effectively lost.



i

Figure 6.16: Median significance of directional sensitivity to solar neutrinos as a function of energy, with and without fiducialization. The left shows the median significance over a five-year exposure for the non-fiducialized case, where external backgrounds dominate and limit sensitivity to below 2σ across all energies. The right shows the same analysis with a 4 m fiducial volume cut applied, where sensitivity exceeds 5σ in the 6–12 MeV range under the low-background scenario.

6.5.4 Background rejection with light detection

Light detection in LArTPC can significantly enhance event reconstruction by providing complementary information such as precise t_0, improved spatial localization, and additional energy constraints. This section examines specific scenarios in which a robust

photon detection system offers distinct advantages over charge-only measurements.

The results presented are based on a Geant4-based toy simulation incorporating the full detector geometry, with explicit modeling of photon production and propagation. Individual photosensors were not simulated, but this study assumes an idealized photon detection system providing full (100%) light sensitivity across the pixel readout planes, to be consistent with a proposed dual charge-light readout scheme using Q-Pix technology by UTA [189].

This setup corresponds to an overall detector photon coverage of approximately 37%. A conservative photon detection efficiency of 15% is adopted, consistent with current performance benchmarks of commercially available photosensors designed for vacuum-ultraviolet wavelengths [188], and a timing resolution better than 10 ns is assumed. These generalized assumptions enable the evaluation of background rejection performance that could be achieved with an advanced photon detection system, without reliance on specific hardware implementations.

Two particular techniques are explored in this subsection: pulse-shape discrimination to distinguish solar neutrino signals from gamma-ray backgrounds arising from alpha-capture events and identification of delayed photon emissions associated with the de-excitation of ^{40}K* nuclei produced in charged-current interactions ($\nu_e + {}^{40}\mathrm{Ar} \rightarrow {}^{40}\mathrm{K}^{*} + e^{-}$).

6.5.4.1 Pulse-Shape Discrimination Analysis

Pulse-shape discrimination (PSD) techniques exploit the fact that gamma rays generated by alpha-capture reactions in liquid argon produce scintillation light profiles that differ from those of electron recoils, due to the distinct ionization history preceding gamma emission. Specifically, when an alpha particle is emitted—such as from a radon

decay chain—it traverses a short path in the detector due to its high mass and charge, depositing energy densely along its track. In some cases, the alpha particle is captured by an argon nucleus before fully stopping, exciting the nucleus and resulting in the emission of one or more gamma rays.

Although the final detectable particle is a gamma ray, the dense ionization trail of the preceding alpha fundamentally alters the local excitation environment. This results in a time profile of scintillation light that is faster and more prompt-heavy than that of electrons or standard gamma interactions. The recombination dynamics of the ion-electron pairs and the excitation of argon atoms into molecular states are affected by the high ionization density.

Alpha particles tend to produce a larger proportion of fast-decaying singlet states compared to triplet states, in contrast to lower-ionizing particles like electrons. As a result, the scintillation light signal from an alpha-capture event exhibits a faster time profile and a higher ratio of prompt to delayed light. This behavior was first characterized in detail in the work which measured time profiles of scintillation light in liquid argon [236]. It demonstrated clear differences between alpha- and electron-induced signals due to differing singlet/triplet production ratios, as can be seen in Figure 6.17.

This altered time structure enables the use of PSD techniques to statistically differentiate gamma rays produced by alpha-capture from those originating in solar neutrino interactions, which typically result in electron recoils with more uniform, low-density ionization profiles. PSD, therefore, offers a powerful tool to suppress one of the most poorly constrained and potentially irreducible backgrounds in low-energy solar neutrino studies, especially in the context of large LArTPC.

To distinguish between electron recoils from solar neutrino interactions and gamma

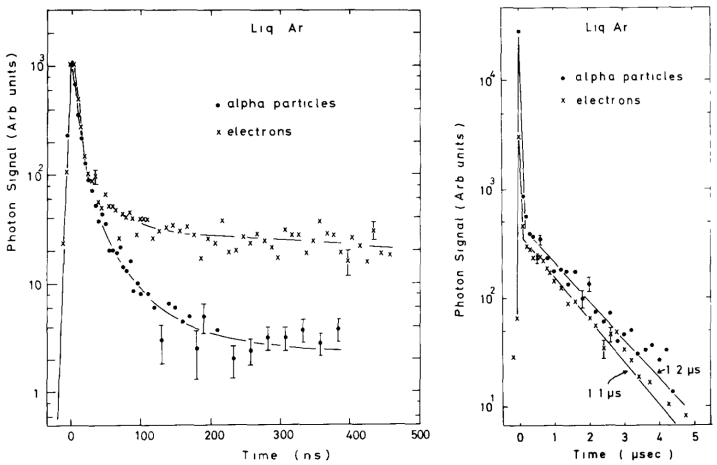


Figure 6.17: Time evolution of scintillation light intensity in liquid argon for alpha particles (solid circles) and electrons (crosses). The left panel shows the photon signal on a nanosecond timescale, highlighting the larger prompt light component produced by alpha particles. The right panel extends the time window to several microseconds, revealing the differing contributions from singlet (fast) and triplet (slow) excimer states. Alpha-induced events exhibit a significantly faster decay due to enhanced singlet-state production, providing the basis for pulse-shape discrimination between alpha- and electron-induced signals in liquid argon detectors. Taken from [236].

rays produced by alpha-capture processes, a PSD analysis was performed using simulated photon arrival time distributions. For each event, the time profile of detected scintillation photons was recorded, taking into account the characteristic differences in light emission between highly ionizing alpha-induced processes and minimally ionizing electron tracks. Two time integration windows were defined: a fast window spanning the first 50 nanoseconds, and a total window encompassing the full event duration (typically several microseconds). The PSD parameter was then calculated as the ratio of light collected in the fast window to the total light:

$$\text{PSD parameter} = \frac{Q_{\text{fast}}}{Q_{\text{total}}} \tag{6.14}$$

This procedure was applied to large samples of both electron and alpha-capture

gamma events. The resulting distributions, normalized to unit area, reveal a clear separation between the two populations. Electron-induced events exhibit a lower PSD value due to the higher fraction of delayed scintillation light, while alpha-capture events generate a relatively larger prompt component, because of the preceding dense ionization.

This distinction enables statistical discrimination between signal and background, as demonstrated in Figure 6.18, and provides a valuable handle for suppressing one of the most problematic backgrounds in solar neutrino analyses. Our results indicate that by applying a PSD cut of <0.4, it is possible to retain 99% of electron-induced signal events while rejecting approximately 99% of alpha-capture gamma events with preceding alpha ionization.

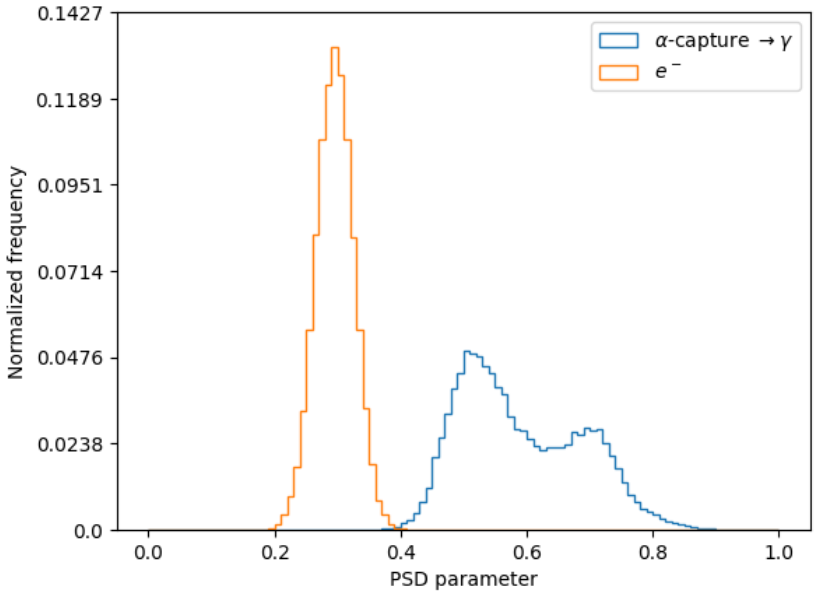


Figure 6.18: Distribution of the ratio of fast and slow scintillation light (PSD parameter) for electrons (orange) and alpha-capture gammas (blue). Plot taken from our forthcoming study [187].

It is important to note limitations uncovered in the Geant4 simulation of alpha par-

ticle transport within the 1.1–8.9 MeV range. Specifically, Geant4 simulations report zero ionization for more than 60% of alpha-capture events. This behavior is likely unphysical, as alpha particles in this energy range are expected to deposit substantial ionization in liquid argon. Given this discrepancy, dedicated experimental measurements of alpha-capture processes in liquid argon are crucial for accurately characterizing this background and determining the practical effectiveness of PSD techniques.

6.5.4.2 Delayed-Light Coincidence Tagging of Solar Neutrino CC Events

CC interactions of solar neutrinos on argon,

$$\nu_e + {}^{40}\mathrm{Ar} \rightarrow e^- + {}^{40}\mathrm{K}^*, \tag{6.15}$$

can be further isolated from background by detecting a delayed scintillation pulse emitted during the de-excitation of the ^{40}K* nucleus [237]. For a fraction of such CC interactions, as shown in Figure 6.19, the resulting ^{40}K* nucleus decays by emitting a 1.64 MeV gamma ray with a half-life of 336 ns [222]. This half-life is too short to produce a distinct charge signal, but it is long enough to yield a temporally separable delayed light signal that can be detected independently of the prompt electron scintillation.

The left panel of Figure 6.19 shows the fraction of CC events that produce delayed gammas as a function of incoming solar neutrino energy. The right panel shows the expected number of detected photons from these delayed 1.64 MeV gammas as a function of emission position relative to the photon detection plane. It shows the number of photons detected by the assumed photon detection system placed at the anode plane, for isotropically emitted 1.64 MeV gamma-rays within the detector.

Even when the delayed emission occurs at the maximum drift distance of 3.5 meters,

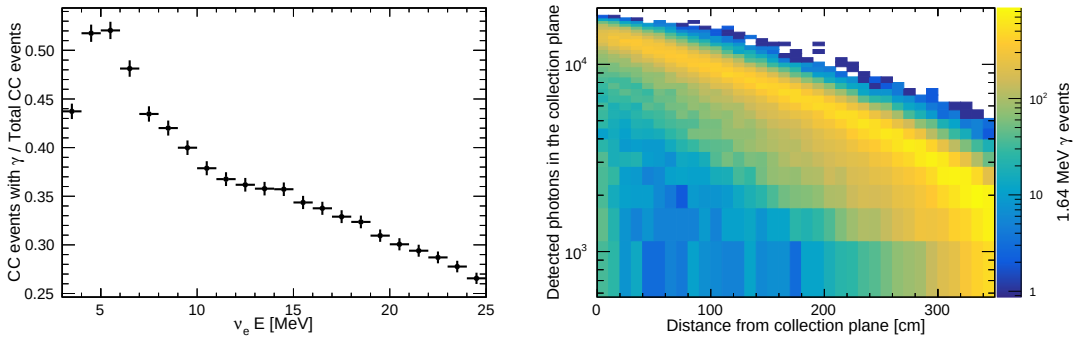


Figure 6.19: The left plot shows the fraction of CC events generating a delayed gamma as a function of the energy of the incoming solar neutrino. The right shows the expected number of detected photons from the delayed gammas as a function of distance from the collection panel. Plot adopted from our forthcoming study [187].

photons can be typically detected with the order of thousands, demonstrating the feasibility of detecting these delayed scintillation signals. For identifying signal coincidences, we define a conservative time window of 1500 ns, encompassing more than 99% of the delayed gamma-ray emissions. To estimate the likelihood of accidental background coincidences within a delayed-light time window, each background source listed in Table 6.5 is modeled as a Poisson process. For a fixed coincidence window of 1500 ns—chosen to encompass more than 99% of the delayed 1.64 MeV gamma-ray emissions from ^{40}K* de-excitations—the expected number of events from background source i is denoted by $\mu_{\mathrm{bkg},i}$. The probability that no such background event occurs in the coincidence window is then given by the Poisson probability of observing zero events:

$$P(\mu_{\mathrm{bkg},i}, 0) = e^{-\mu_{\mathrm{bkg},i}}. \tag{6.16}$$

Assuming that background sources are independent, the total probability of observing

zero coincidences across all sources is the product of individual probabilities:

$$P(0) = \prod_i P(\mu_{\mathrm{bkg},i}, 0) = \exp\left(-\sum_i \mu_{\mathrm{bkg},i}\right). \tag{6.17}$$

This expression gives the overall likelihood that no background process produces a coincident signal in the defined window. A lower value of $P(0)$ corresponds to a higher risk of accidental coincidence, which could obscure the delayed gamma-ray signature associated with genuine CC solar neutrino interactions.

In this calculation, it is assumed that the background processes are temporally uncorrelated and spatially independent, and that contributions from different detector drift volumes can be neglected. These assumptions are reasonable given the detector design and low per-volume rates of relevant background processes, especially in the low-background scenario with fiducialization. This analysis provides a conservative yet informative estimate of the expected false positive rate for background coincidences in the presence of delayed gamma signatures.

For the baseline scenario, using the full 10-kton active mass, the probability of observing at least one random coincidence is approximately 99%. In contrast, in the low-background scenario, this probability drops significantly to 33%. Introducing a stringent fiducialization strategy (4 meters of passive argon shielding) further reduces the random coincidence probability to approximately 87% and 0.1% for the baseline and low-background scenarios, respectively.

The clustering threshold was set to 12 resets, corresponding to an energy cut of approximately 3 MeV, before applying the delayed photon coincidence criterion. Table 6.6 summarizes the expected number of CC events from B8 and hep neutrinos, as well as the estimated number of background coincidences under the various detector scenarios.

Here, "background coincidences" are defined as background events that accompanied electron events of above ∼3 MeV that are followed by a delayed scintillation flash from another background event. Figure 6.20 demonstrates the combined effects of fiducialization and delayed-light detection on the significance of the solar neutrino signals (hep and B8). When both methods are employed in the low-background scenario, the solar neutrino signal becomes discernible over a wide range of reconstructed energies, despite the comparatively low absolute number of solar neutrino events per year.

Background scenario	B8 CC Events	hep CC Events	Background coincidences
Baseline	3797	13	1.71×10^9
Low background	3797	13	1.19×10^7
Baseline with 4 m fiducialization	893	3	3.42×10^8
Low background with 4 m fiducialization	893	3	796

Table 6.6: Expected B8 and hep CC events and background coincidences per year under different background scenarios using the light coincidence technique in the considered active volume per year.

6.5.5 Expected data rates

Unlike supernova neutrino bursts, which occur over a brief and well-defined time window of approximately 10 seconds, solar neutrino detection requires continuous data acquisition over long periods—spanning several years, in order to accumulate sufficient statistics. This fundamental difference imposes significantly stricter demands on data handling and storage infrastructure.

For supernovae, the shortness of the signal duration enables data reduction strategies based on short-term buffering or triggering, dramatically limiting the volume of recorded data. In contrast, solar neutrino analyses must retain a wide energy spectrum of low-rate, untriggered events in real time, including both signal and background. This requires a data acquisition system capable of continuous, high-fidelity recording without

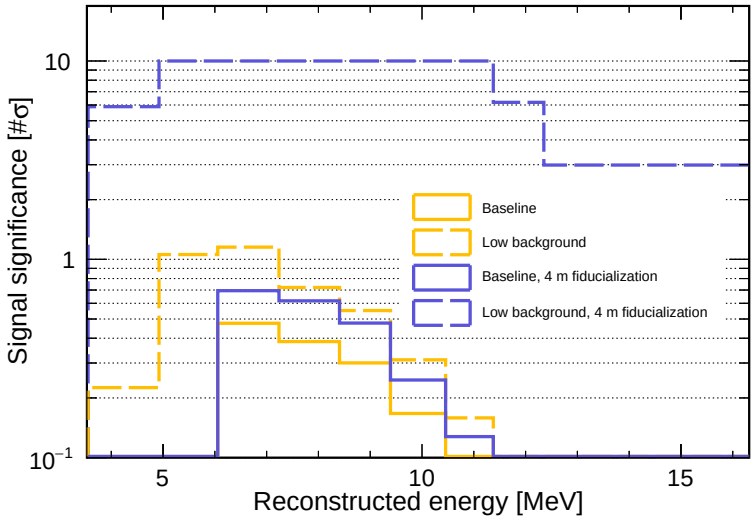


Figure 6.20: Estimated detection significance for solar neutrino CC events under different scenarios. Solid lines indicate results from delayed-light tagging alone, while hatched lines show the improvement when combined with 4 m fiducialization. Yellow curves represent the baseline background scenario; blue curves represent the low-background scenario. Plot adopted from our forthcoming study [187].

overwhelming computing or storage resources. The Q-Pix architecture, with its intrinsically sparse and scalable data structure, offers a compelling solution to this challenge.

Figure 6.21 presents the estimated data rates with Q-Pix for solar neutrino events and dominant background sources under both the baseline and low-background scenarios. A pre-selection threshold of at least 12 resets per event (corresponding to a deposited energy of approximately 3 MeV) was applied. In Q-Pix, each reset stores 8 bytes, and the data rate is computed by counting the number of resets per event. Under these assumptions, the total data volume needed to record all events depositing more than 3 MeV is approximately 1 TB per year per 10-kton detector module, an amount well within the capabilities of current storage systems.

If extending readout to lower energy thresholds is desired, Q-Pix can also continuously

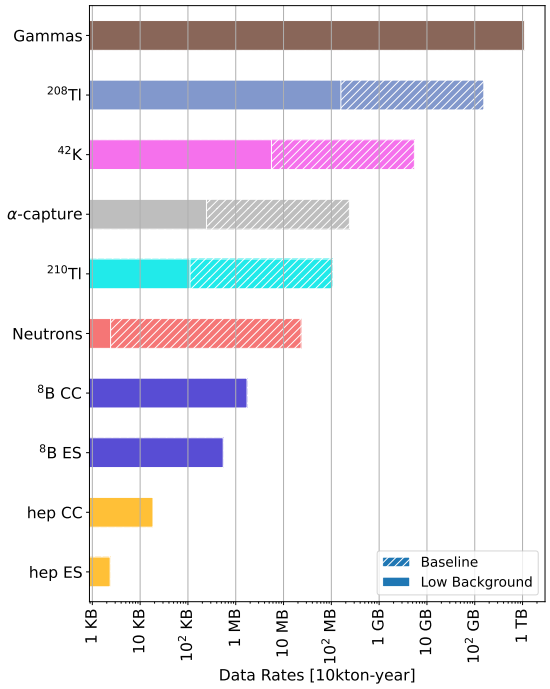


Figure 6.21: Estimated data rates with Q-Pix readout for solar neutrino signals and background sources in a 10 kiloton-year exposure. Full bar lengths represent the baseline background scenario, while hatched regions denote the component suppressed in the low-background scenario. A clustering threshold of 12 resets (corresponding to ∼3 MeV) was applied to all events. Plot adopted from our forthcoming study [187].

record all events with at least one reset (approximately 0.15 MeV threshold), resulting in a total annual data volume of about 1 PB, which still remains feasible with current data storage technologies.

In contrast, conventional APA-based or CRP-based LArTPC modules produce significantly larger data volumes. Given the combined signal and background rate for events depositing more than 3 MeV is roughly 300 Hz, nearly every drift window would include at least one potentially relevant event. Continuous readout at this rate would produce roughly 10^5 PB of data per year. For example, reading out an entire 10-kton DUNE module yields approximately 6.5 GB per event for a wire-based detector operating with a 5.4 ms waveform acquisition window [148], and about 8.0 GB per event for a CRP-based detector using a 4.25 ms window [238]. Even employing advanced triggering techniques—such as selective readout of individual APAs or CRPs—can at most reduce the data volume by two orders of magnitude, which still remains several orders higher than the corresponding Q-Pix output. This highlights the unique advantage of Q-Pix's asynchronous, sparse readout structure for long-term, low-energy solar neutrino studies.

6.6 Summary

This study presents a comprehensive assessment of the feasibility of detecting solar neutrinos in a LArTPC equipped with Q-Pix pixelated readout technology. A detailed simulation-based evaluation of background sources, both internal and external, was carried out, assuming a detector located in an underground environment. Internal backgrounds, including intrinsic argon radioisotopes, radon decay chains, and their daughters, pose major challenges for low-energy solar neutrino detection. In the sub-5 MeV energy regime, beta and gamma decays dominate the background landscape,

with event rates that surpass the solar neutrino signal by 8 to 11 orders of magnitude.

These conclusions hold even under optimistic mitigation assumptions, such as ion drift or recombination effects, and remain valid when excluding minor contributions from radiocontaminants in support structures. Even in a low-background scenario incorporating underground argon and radon mitigation strategies, internal background levels remain too high to enable meaningful solar neutrino measurements at low energies.

At higher energies (above 5 MeV), two primary background sources emerge: gamma rays produced via alpha-capture on argon nuclei, and high-energy external gammas originating from cavern walls. The former arises from radon chain and remains one of the most poorly constrained backgrounds due to limited measurements of alpha-capture cross sections in argon. While PSD offers partial suppression of this background, the associated modeling uncertainty remains a major sensitivity limitation. External gamma rays, on the other hand, can penetrate several meters into the detector volume and are effectively suppressed only through aggressive fiducialization. Both backgrounds introduce significant systematic uncertainty and represent critical targets for future experimental study.

The findings of this work highlight the urgent need for dedicated measurements of alpha-capture cross sections and in-situ surveys of cavern gamma-ray fluxes to robustly quantify solar neutrino sensitivity in LArTPCs. Several background rejection techniques were explored to address these challenges. These include fiducialization, pulse-shape discrimination, tagging of delayed scintillation light from $^{40}K^{*}$ de-excitation following CC interactions, and directional reconstruction of electron recoils from ES events. When implemented in combination, particularly under a low-background configuration with 4-meter passive shielding, these techniques significantly improve the signal-to-background

ratio in the 6–12 MeV range- opening the door to precision measurements of B8 solar neutrinos and potentially enables the first observation of hep neutrinos in liquid argon.

Directional sensitivity, in particular, was shown to provide added statistical power, especially when paired with fiducialization. Nonetheless, the overall feasibility of solar neutrino studies remains tightly coupled to the ability to constrain backgrounds with high precision and to achieve excellent reconstruction fidelity.

Finally, this study highlights the formidable challenges posed by solar neutrino detection in large-scale LArTPCs like DUNE. Unlike supernova bursts, which require data acquisition over a 10 second window, solar neutrino detection demands uninterrupted collection of low-energy events over many months or years. Traditional triggered readout systems, such as those based on wire planes or wire planes alike, are not well-suited to this task due to the vast data volumes generated by unfiltered background activity. This work shows that a radical shift in readout strategy, such as with Q-PIX, is needed in order to understand solar neutrino measurement in DUNE.

In this context, the Q-Pix architecture—based on sparse, asynchronous, and reset-driven readout—enables continuous recording with dramatically reduced data volume. With an energy threshold of approximately 3 MeV (12 resets), the annual data load is on the order of 1 TB, and even at the lowest thresholds (1 reset), remains below 1 PB/year. These rates are orders of magnitude lower than conventional readouts, even when optimized with selective triggering. While this design alone does not resolve all the background and reconstruction challenges, it provides a necessary technological foundation. With such innovations, precision solar neutrino measurements in DUNE-scale detectors will soon become reachable.

Whereof we can speak,

thereof we must seek—and speak.

Inspired by Ludwig Wittgenstein

7

Conclusion

Neutrinos, once dubbed "the invisible particles", have persistently challenged our ability to observe and understand them. Yet, it is precisely this elusiveness that has driven the continuous evolution of curiosity and detection technologies—pushing the boundaries of experimental physics. This dissertation has been a journey through that evolution, demonstrating how advancing detector capabilities transforms not only what we can see, but what we can know about the universe allowing us to hear the faintest notes in

the cosmic symphony.

At the heart of this work lies a singular vision: to bring neutrino interactions into sharper focus—to achieve high-definition neutrino physics with LArTPCs. From foundational questions about neutrino mass and oscillation to the practical challenges of building and operating detectors at scale, this thesis has engaged with both the physics that composes the melody and the instrumentation required to hear it.

The story began with an exploration of the theoretical and experimental landscape of neutrino physics, setting the stage for why precision detection is indispensable. DUNE emerged as the embodiment of this ambition—a flagship experiment designed to play in the grand register of discovery, orchestrated across 1300 kilometers and performed by an ensemble of massive LArTPC buried deep underground. However, as the symphony grew in scale and complexity, so too did the need for harmony among its components.

The development of the Digital Wire Analyzer exemplified how automation and precision engineering could safeguard the integrity of wire-based LArTPCs. By transforming quality assurance from a labor-intensive process into an efficient, scalable system, the DWA ensured that each "string" of the detector played its part faithfully.

Production development and workflow management are not typically considered central to a physics PhD. However, this work provided invaluable experience in systems engineering, cross-institutional collaboration, and real-world project management—skills essential to long-term engagement in experimental particle physics. It has been deeply rewarding to see my effort evolve from a small prototype into a formally adopted DUNE technology, now entering mass production. Guiding the DWA project through every phase of its lifecycle remains one of the most meaningful accomplishments of my PhD.

Yet, even as wire-based systems were perfected, their inherent limitations became clear. This realization prompted a shift from refining existing technologies to reimag-

ining them altogether. Where traditional readouts operated like classical notation, recording every line in sequence, Q-Pix introduced a more agile form: an asynchronous, self-triggering architecture that listens in silence and speaks only when the physics calls for it. Through hardware prototyping and simulation studies, this thesis also demonstrated how Q-Pix could revolutionize low-energy neutrino detection, offering true three-dimensional imaging, self-triggering capabilities, and enhanced background rejection allowing us to discern the quietest passages with unprecedented clarity.

The application of Q-Pix to supernova and solar neutrino studies served as a proof-of-concept for this paradigm shift. By capturing faint, low-energy signals with unprecedented clarity, Q-Pix-enabled detectors show promise not only in advancing astrophysical observations but also in broadening the scientific reach of LArTPCs into domains previously constrained by current technological limits.

As experiments strive to detect ever rarer events and probe deeper into the fabric of the Standard Model and beyond, the demand for precise, scalable, and intelligent detectors will only continue to grow. Q-Pix represents distinct yet converging visions of how pixelated readouts can redefine the capabilities of LArTPCs—whether through continuous listening for cosmic whispers or handling high interaction rates with efficiency and precision.

In conclusion, this dissertation has charted a course from the challenges of wire-based LArTPCs to the horizon of pixelated detection. It reflects a broader narrative within experimental physics: that progress is driven not just by asking new questions, but by developing the tools capable of answering them.

When I began this journey, I was captivated by how experimental physics extends the boundaries of human perception—transforming the invisible into the observable. In my Statement of Purpose submitted for my PhD application to Harvard, I reflected on

Ludwig Wittgenstein's view, expressed in his *Tractatus Logico-Philosophicus*, that "the world is the totality of facts," and his famous caution: "Whereof one cannot speak, thereof one must be silent." Wittgenstein suggested that language is inherently limited to what can be empirically verified; beyond this, meaningful discourse is no longer possible.

These developments, however, are not an endpoint but part of a broader landscape of innovation. As I transition to Lawrence Berkeley National Laboratory (LBNL), my research will focus on advancing LArPix—a parallel low-power, pixelated readout technology similar in spirit to Q-Pix. I will continue to contribute to ongoing research and development, with an emphasis on improving performance, scalability, and integration with future large-scale LArTPCs. The future of neutrino physics hinges on such complementary innovations.

Science operates precisely within this realm of the speakable—seeking, verifying, and articulating facts about the world. Through experimental inquiry, we do not cross into the unspeakable; rather, we expand the domain of what can be spoken about by uncovering new facts. We transform previously unknown aspects of reality into part of the describable, empirical world. With each advancement in detection technology, we push outward the frontier of facts, deepening humanity's ability to meaningfully engage with the universe.

Now, at the conclusion of my PhD journey, that conviction remains stronger than ever. The pursuit of high-definition neutrino physics is not merely about refining instruments—it is about expanding the domain of truths we can uncover and articulate.

To paraphrase my earlier reflection: Whereof we can speak, thereof we must seek—and speak. With innovations like Q-Pix, we continue to give voice to the faint whispers of the universe's most elusive messengers. The once-invisible world of neutrinos is

coming ever more vividly into view—and with it, so too does our understanding of nature deepen.

Bibliography

[1] Mary K. Gaillard, Paul D. Grannis, and Frank J. Sciulli. "The Standard model of particle physics". In: *Rev. Mod. Phys.* 71 (1999), S96–S111. doi: 10.1103/RevModPhys.71.S96. arXiv: hep-ph/9812285.

[2] Georges Aad et al. "Observation of a new particle in the search for the Standard Model Higgs boson with the ATLAS detector at the LHC". In: *Phys. Lett. B* 716 (2012), pp. 1–29. doi: 10.1016/j.physletb.2012.08.020. arXiv: 1207.7214 [hep-ex].

[3] Frederick Reines. *'Foreword' to Spaceship Neutrino by Christine Sutto.* 1992.

[4] C. L. Cowan et al. "Detection of the Neutrino". In: *Science* 118.3058 (1953), pp. 218–219. doi: 10.1126/science.118.3058.218.

[5] F. Reines and C. L. Cowan. "Detection of the Free Neutrino". In: *Phys. Rev.* 92 (3 Nov. 1953), pp. 830–831. doi: 10.1103/PhysRev.92.830. url: https://link.aps.org/doi/10.1103/PhysRev.92.830.

[6] G. Danby et al. "Observation of High-Energy Neutrino Reactions and the Existence of Two Kinds of Neutrinos". In: *Phys. Rev. Lett.* 9 (1 July 1962), pp. 36–44. doi: 10.1103/PhysRevLett.9.36. url: https://link.aps.org/doi/10.1103/PhysRevLett.9.36.

[7] K. Kodama et al. "The DONuT Experiment and the First Direct Observation of the Tau Neutrino". In: *Nuclear Physics B - Proceedings Supplements* 168 (2008), pp. 336–338. doi: 10.1016/j.nuclphysbps.2007.12.138.

[8] K. Kodama et al. “Final tau-neutrino results from the DONuT experiment”. In: *Phys. Rev. D* 78 (5 Sept. 2008), p. 052002. doi: 10.1103/PhysRevD.78.052002. url: https://link.aps.org/doi/10.1103/PhysRevD.78.052002.

[9] M. Acciarri et al. “Determination of the number of light neutrino species from single photon production at LEP”. In: *Physics Letters B* 431.1 (1998), pp. 199–208. issn: 0370-2693. doi: https://doi.org/10.1016/S0370-2693(98)00519-X. url: https://www.sciencedirect.com/science/article/pii/S037026939800519X.

[10] C. S. Wu et al. “Experimental Test of Parity Conservation in Beta Decay”. In: *Physical Review* 105.4 (1957), pp. 1413–1415. doi: 10.1103/PhysRev.105.1413.

[11] M. Goldhaber, L. Grodzins, and A. W. Sunyar. “Helicity of Neutrinos”. In: *Physical Review* 109.3 (1958), pp. 1015–1017. doi: 10.1103/PhysRev.109.1015.

[12] R. Davis Jr., D. S. Harmer, and K. C. Hoffman. “Search for Neutrinos from the Sun”. In: *Physical Review Letters* 20.21 (1968), pp. 1205–1209. doi: 10.1103/PhysRevLett.20.1205.

[13] J. N. Bahcall, N. A. Bahcall, and G. Shaviv. “Present Status of the Theoretical Predictions for the Cl37 Solar-Neutrino Experiment”. In: *Physical Review Letters* 20.21 (1968), pp. 1209–1212. doi: 10.1103/PhysRevLett.20.1209.

[14] K. S. Hirata et al. “Observation of B^8 Solar Neutrinos in the Kamiokande-II Detector”. In: *Physical Review Letters* 63.1 (1989), pp. 16–19. doi: 10.1103/PhysRevLett.63.16.

[15] K. S. Hirata et al. “Observation of a Small Atmospheric ν_μ/ν_e Ratio in Kamiokande”. In: *Physics Letters B* 280 (1992), pp. 146–152. doi: 10.1016/0370-2693(92)90775-3.

[16] P. Anselmann et al. “Solar neutrinos observed by GALLEX at Gran Sasso”. In: *Physics Letters B* 285 (1992), pp. 376–389. doi: 10.1016/0370-2693(92)91408-4.

[17] T. Kajita, E. Kearns, and M. Shiozawa. “Establishing atmospheric neutrino oscillations with Super-Kamiokande”. In: *Nuclear Physics B* 908 (2016). Neutrino Oscillations: Celebrating the Nobel Prize in Physics 2015, pp. 14–29. issn: 0550-3213. doi: https://doi.org/10.1016/j.nuclphysb.2016.04.017. url: https://www.sciencedirect.com/science/article/pii/S0550321316300554.

[18] B. Aharmim et al. “Independent Measurement of the Total Active ^{8}B Solar Neutrino Flux Using an Array of ^{3}He Proportional Counters at the Sudbury Neutrino Observatory”. In: *Phys. Rev. Lett.* 101 (11 Sept. 2008), p. 111301. doi: 10.1103/PhysRevLett.101.111301. url: https://link.aps.org/doi/10.1103/PhysRevLett.101.111301.

[19] Z. Maki, M. Nakagawa, and S. Sakata. “Remarks on the Unified Model of Elementary Particles”. In: *Progress of Theoretical Physics* 28.5 (1962), pp. 870–880. doi: 10.1143/PTP.28.870.

[20] J. A. Casas and A. Ibarra. “Oscillating neutrinos and $\mu \to e, \gamma$”. In: *Nucl. Phys. B* 618 (2001), pp. 171–204. doi: 10.1016/S0550-3213(01)00475-8. arXiv: hep-ph/0103065.

[21] S. F. King. “Neutrino mass models”. In: *Reports on Progress in Physics* 67 (2004), pp. 107–158. doi: 10.1088/0034-4885/67/2/R01.

[22] R. N. Mohapatra et al. “Theory of neutrinos: a white paper”. In: *Reports on Progress in Physics* 70 (2007), pp. 1757–1867. doi: 10.1088/0034-4885/70/11/R02.

[23] S. Weinberg. “Baryon- and Lepton-Nonconserving Processes”. In: *Physical Review Letters* 43 (1979), pp. 1566–1570. doi: 10.1103/PhysRevLett.43.1566.

[24] M. C. Gonzalez-Garcia and M. Maltoni. "Phenomenology with Massive Neutrinos". In: *Physics Reports* 460 (2008), pp. 1–129. doi: 10.1016/j.physrep.2007.12.004.

[25] F. Granena et al. "NEXT, a HPGXe TPC for neutrinoless double beta decay searches". In: (July 2009). arXiv: 0907.4054 [hep-ex].

[26] A. D. Sakharov. "Violation of CP Invariance, C Asymmetry, and Baryon Asymmetry of the Universe". In: *JETP Lett.* 5 (1967), pp. 24–27.

[27] W. Buchmüller, R. D. Peccei, and T. Yanagida. "Leptogenesis as the Origin of Matter". In: *Annual Review of Nuclear and Particle Science* 55 (2005), pp. 311–355. doi: 10.1146/annurev.nucl.55.090704.151558.

[28] S. Davidson, E. Nardi, and Y. Nir. "Leptogenesis". In: *Physics Reports* 466 (2008), pp. 105–177. doi: 10.1016/j.physrep.2008.06.002.

[29] Babak Abi et al. "Deep Underground Neutrino Experiment (DUNE), Far Detector Technical Design Report, Volume IV: Far Detector Single-phase Technology". In: *JINST* 15.08 (2020), T08010. doi: 10.1088/1748-0221/15/08/T08010. arXiv: 2002.03010 [physics.ins-det].

[30] F. An et al. (JUNO Collaboration). "Neutrino Physics with JUNO". In: *Journal of Physics G: Nuclear and Particle Physics* 43 (2016), p. 030401. doi: 10.1088/0954-3899/43/3/030401.

[31] K. Abe et al. (T2K Collaboration). "The T2K Experiment". In: *Nuclear Instruments and Methods in Physics Research Section A* 659 (2011), pp. 106–135. doi: 10.1016/j.nima.2011.06.067.

[32] D. S. Ayres et al. (NOvA Collaboration). *NOvA: Proposal to Build a 30 Kiloton Off-Axis Detector to Study Neutrino Oscillations in the Fermilab NuMI Beamline*. 2004. arXiv: hep-ex/0503053 [hep-ex].

[33] K. Abe et al. (T2K Collaboration). "Constraint on the matter–antimatter symmetry-violating phase in neutrino oscillations". In: *Nature* 580 (2020), pp. 339–344. doi: 10.1038/s41586-020-2177-0.

[34] M. A. Acero et al. (NOvA Collaboration). "An Improved Measurement of Neutrino Oscillation Parameters by the NOvA Experiment". In: *Physical Review D* 104 (2021), p. 012020. doi: 10.1103/PhysRevD.104.012020.

[35] KATRIN Collaboration† et al. "Direct neutrino-mass measurement based on 259 days of KATRIN data". In: *Science* 388.6743 (2025), pp. 180–185. doi: 10.1126/science.adq9592. eprint: https://www.science.org/doi/pdf/10.1126/science.adq9592. url: https://www.science.org/doi/abs/10.1126/science.adq9592.

[36] Elena Giusarma et al. "Constraints on neutrino masses from Planck and Galaxy Clustering data". In: *Phys. Rev. D* 88.6 (2013), p. 063515. doi: 10.1103/PhysRevD.88.063515. arXiv: 1306.5544 [astro-ph.CO].

[37] N. Abgrall et al. "The Large Enriched Germanium Experiment for Neutrinoless Double Beta Decay (LEGEND)". In: *AIP Conf. Proc.* 1894.1 (2017). Ed. by Osvaldo Civitarese, Ivan Stekl, and Jouni Suhonen, p. 020027. doi: 10.1063/1.5007652. arXiv: 1709.01980 [physics.ins-det].

[38] E. Armengaud et al. "The CUPID-Mo experiment for neutrinoless double-beta decay: performance and prospects". In: *Eur. Phys. J. C* 80.1 (2020), p. 44. doi: 10.1140/epjc/s10052-019-7578-6. arXiv: 1909.02994 [physics.ins-det].

[39] S. Al Kharusi et al. "nEXO Pre-Conceptual Design Report". In: (May 2018). arXiv: 1805.11142 [physics.ins-det].

[40] A. Aguilar et al. "Evidence for neutrino oscillations from the observation of $\overline{\nu}_e$ appearance in a $\overline{\nu}_\mu$ beam". In: *Phys. Rev. D* 64 (11 Nov. 2001), p. 112007. doi: 10.1103/PhysRevD.64.112007. url: https://link.aps.org/doi/10.1103/PhysRevD.64.112007.

[41] A. A. Aguilar-Arevalo et al. "Improved Search for $\overline{\nu}_\mu \to \overline{\nu}_e$ Oscillations in the MiniBooNE Experiment". In: *Phys. Rev. Lett.* 110 (16 Apr. 2013), p. 161801. doi: 10.1103/PhysRevLett.110.161801. url: https://link.aps.org/doi/10.1103/PhysRevLett.110.161801.

[42] P. Abratenko et al. (MicroBooNE Collaboration). "Search for an Excess of Electron Neutrino Interactions in MicroBooNE Using Multiple Final State Topologies". In: *Physical Review Letters* 128 (2022), p. 241801. doi: 10.1103/PhysRevLett.128.241801.

[43] R. Acciarri et al. "A Proposal for a Three Detector Short-Baseline Neutrino Oscillation Program in the Fermilab Booster Neutrino Beam". In: (Mar. 2015). arXiv: 1503.01520 [physics.ins-det].

[44] J. Rout, K. Bora, and N. Sinha. "Physics prospects with the second oscillation maximum at the Deep Underground Neutrino Experiment". In: *Phys. Rev. D* 103 (2021), p. 116003. doi: 10.1103/PhysRevD.103.116003.

[45] V. Hewes et al. "Deep Underground Neutrino Experiment (DUNE) Near Detector Conceptual Design Report". In: *Instruments* 5.4 (2021), p. 31. doi: 10.3390/instruments5040031. arXiv: 2103.13910 [physics.ins-det].

[46] B. Abi et al. (DUNE Collaboration). "Deep Underground Neutrino Experiment (DUNE), Far Detector Technical Design Report, Volume II: DUNE Physics". In: *Journal of Instrumentation* 15 (2020), T08010. doi: 10.1088/1748-0221/15/08/T08010.

[47] J. M. Berryman et al. "Beyond the Standard Model Physics at DUNE". In: *Reports on Progress in Physics* 85 (2022), p. 044201. doi: 10.1088/1361-6633/ac4138.

[48] DUNE Collaboration. *The Deep Underground Neutrino Experiment (DUNE) Website*. https://www.dunescience.org/. [Accessed 6 May 2025].

[49] Vaia Papadimitriou et al. "Design of the LBNF Beamline". In: *7th International Particle Accelerator Conference*. 2016, TUPMR025. doi: 10.18429/JACoW-IPAC2016-TUPMR025. arXiv: 1704.04471 [physics.acc-ph].

[50] Babak Abi et al. "Deep Underground Neutrino Experiment (DUNE), Far Detector Technical Design Report, Volume IV: Far Detector Single-phase Technology". In: *JINST* 15.08 (2020), T08010. doi: 10.1088/1748-0221/15/08/T08010. arXiv: 2002.03010 [physics.ins-det].

[51] W.J. Willis and V. Radeka. "Liquid-argon ionization chambers as total-absorption detectors". In: *Nuclear Instruments and Methods* 120.2 (1974), pp. 221–236. issn: 0029-554X. doi: https://doi.org/10.1016/0029-554X(74)90039-1. url: https://www.sciencedirect.com/science/article/pii/0029554X74900391.

[52] Carlo Rubbia. *The liquid-argon time projection chamber: a new concept for neutrino detectors*. Tech. rep. Geneva: CERN, 1977. url: https://cds.cern.ch/record/117852.

[53] D. R. Nygren. "The Time Projection Chamber: A New 4π Detector for Charged Particles". In: *Proceedings of The 1974 PEP Summer Study* (Berkeley, California). Ed. by J. Kadyk et al. University of California, 1974, pp. 58–78.

[54] M. Antonello et al. "Operation and performance of the ICARUS-T600 cryogenic plant at Gran Sasso underground Laboratory". In: *JINST* 10.12 (2015), P12004. doi: 10.1088/1748-0221/10/12/P12004. arXiv: 1504.01556 [physics.ins-det].

[55] C. Anderson et al. "The ArgoNeuT Detector in the NuMI Low-Energy beam line at Fermilab". In: *JINST* 7 (2012), P10019. doi: 10.1088/1748-0221/7/10/P10019. arXiv: 1205.6747 [physics.ins-det].

[56] R. Acciarri et al. "Design and Construction of the MicroBooNE Detector". In: *JINST* 12.02 (2017), P02017. doi: 10.1088/1748-0221/12/02/P02017. arXiv: 1612.05824 [physics.ins-det].

[57] A. Abed Abud et al. "Design, construction and operation of the ProtoDUNE-SP Liquid Argon TPC". In: *JINST* 17.01 (2022), P01005. doi: 10.1088/1748-0221/17/01/P01005. arXiv: 2108.01902 [physics.ins-det].

[58] R. Acciarri et al. "Design and Construction of the MicroBooNE Detector". In: *JINST* 12.02 (2017), P02017. doi: 10.1088/1748-0221/12/02/P02017. arXiv: 1612.05824 [physics.ins-det].

[59] R. Acciarri et al. "Construction and Assembly of the Wire Planes for the MicroBooNE Time Projection Chamber". In: *JINST* 12.03 (2017),

T03003. doi: 10.1088/1748-0221/12/03/T03003. arXiv: 1609.06169 [physics.ins-det].

[60] R. Stephenson and J.E. Bateman. "A non-contact method for measuring MWPC wire tensions". In: *Nuclear Instruments and Methods* 171.2 (1980), pp. 337–338. issn: 0029-554X. doi: https://doi.org/10.1016/0029-554X(80)90511-X. url: https://www.sciencedirect.com/science/article/pii/0029554X8090511X.

[61] K Lang, J Ting, and V Vassilakopoulos. "A technique of direct tension measurement of a strung fine wire". In: *Nuclear Instruments and Methods in Physics Research Section A: Accelerators, Spectrometers, Detectors and Associated Equipment* 420.3 (1999), pp. 392–401. issn: 0168-9002. doi: https://doi.org/10.1016/S0168-9002(98)01184-X. url: https://www.sciencedirect.com/science/article/pii/S016890029801184X.

[62] C. Bacci et al. "A method for measuring the wire tension in drift chambers using neodymium permanent magnets". In: *1995 IEEE Nuclear Science Symposium and Medical Imaging Conference Record*. Vol. 1. 1995, 469–473 vol.1. doi: 10.1109/NSSMIC.1995.504269.

[63] I. D'Antone, M. Lolli, and G. Torromeo. "An automatic tension measurement system of MWPC wires". In: *Nuclear Instruments and Methods in Physics Research Section A: Accelerators, Spectrometers, Detectors and Associated Equipment* 317.1 (1992), pp. 155–160. issn: 0168-9002. doi: https://doi.org/10.1016/0168-9002(92)90604-3. url: https://www.sciencedirect.com/science/article/pii/0168900292906043.

[64] Malcolm Coupland. "A method for measuring the wire tensions in proportional and drift chambers". In: *Nuclear Instruments and Methods in Physics Research* 211.2 (1983), pp. 369–370. issn: 0167-5087. doi: https://doi.org/10.1016/0167-5087(83)90261-2. url: https://www.sciencedirect.com/science/article/pii/0167508783902612.

[65] M. Calvetti et al. "A computer-aided system for MWPC wire tension control". In: *Nuclear Instruments and Methods* 174.1 (1980), pp. 285–289. issn: 0029-554X. doi: https://doi.org/10.1016/0029-554X(80)90443-

7. url: https://www.sciencedirect.com/science/article/pii/0029554X80904437.

[66] Richard T. Jones. "An automated method for measuring wire tensions in multiwire chambers". In: *Nuclear Instruments and Methods in Physics Research Section A: Accelerators, Spectrometers, Detectors and Associated Equipment* 269.3 (1988), pp. 550–553. issn: 0168-9002. doi: https://doi.org/10.1016/0168-9002(88)90132-5. url: https://www.sciencedirect.com/science/article/pii/0168900288901325.

[67] T. Ohama et al. "Electrical measurement of wire tension in a multi-wire drift chamber". In: *Nuclear Instruments and Methods in Physics Research Section A: Accelerators, Spectrometers, Detectors and Associated Equipment* 410.2 (1998), pp. 175–178. issn: 0168-9002. doi: https://doi.org/10.1016/S0168-9002(98)00224-1. url: https://www.sciencedirect.com/science/article/pii/S0168900298002241.

[68] B. Koene and L. Linssen. "A method for tension control of MWPC wires". In: *Nuclear Instruments and Methods in Physics Research* 190.3 (1981), pp. 511–514. issn: 0167-5087. doi: https://doi.org/10.1016/0029-554X(81)90950-2. url: https://www.sciencedirect.com/science/article/pii/0029554X81909502.

[69] Duncan Carlsmith and Sergei Lusin. "Drift tube wire tension monitoring". In: *Nuclear Instruments and Methods in Physics Research Section A: Accelerators, Spectrometers, Detectors and Associated Equipment* 364.1 (1995), pp. 79–89. issn: 0168-9002. doi: https://doi.org/10.1016/0168-9002(95)00273-1. url: https://www.sciencedirect.com/science/article/pii/0168900295002731.

[70] Bradley Brinkley, J. Busenitz, and Gyula Zilizi. "Wire tension measurement using voltage switching". In: *Nuclear Instruments and Methods in Physics Research Section A: Accelerators, Spectrometers, Detectors and Associated Equipment* 373.1 (1996), pp. 23–29. issn: 0168-9002. doi: https://doi.org/10.1016/0168-9002(95)01489-6. url: https://www.sciencedirect.com/science/article/pii/0168900295014896.

[71] P. Ciambrone et al. “Automated wire tension measurement system for LHCb muon chambers”. In: *Nuclear Instruments and Methods in Physics Research Section A: Accelerators, Spectrometers, Detectors and Associated Equipment* 545.1 (2005), pp. 156–163. issn: 0168-9002. doi: https://doi.org/10.1016/j.nima.2004.12.039. url: https://www.sciencedirect.com/science/article/pii/S0168900205004936.

[72] A.D. Volkov. “Wire tension monitor for proportional chambers of the ANKE spectrometer”. In: *Nuclear Instruments and Methods in Physics Research Section A: Accelerators, Spectrometers, Detectors and Associated Equipment* 701 (2013), pp. 80–85. issn: 0168-9002. doi: https://doi.org/10.1016/j.nima.2012.10.068. url: https://www.sciencedirect.com/science/article/pii/S0168900212012181.

[73] A. Andryakov et al. “Electrostatic digital method of wire tension measurement for KLOE drift chamber”. In: *Nuclear Instruments and Methods in Physics Research Section A: Accelerators, Spectrometers, Detectors and Associated Equipment* 409.1 (1998), pp. 63–64. issn: 0168-9002. doi: https://doi.org/10.1016/S0168-9002(97)01237-0. url: https://www.sciencedirect.com/science/article/pii/S0168900297012370.

[74] Sebastien Prince et al. “Digital Wire Analyzer of Mechanical Tension, Electrical Continuity, and Isolation”. In: *IEEE Trans. Instrum. Measur.* 71 (2022), p. 2006612. doi: 10.1109/TIM.2022.3214606. arXiv: 2206.00125 [physics.ins-det].

[75] Diego Garcia-Gamez et al. “A Novel Electrical Method to Measure Wire Tensions for Time Projection Chambers”. In: *Nucl. Instrum. Meth. A* 915 (2019), pp. 75–81. doi: 10.1016/j.nima.2018.09.031. arXiv: 1804.05941 [physics.ins-det].

[76] IPC. *IPC-2222B: Sectional Design Standard for Rigid Organic Printed Boards*. https://shop.ipc.org/ipc-2222/ipc-2222-standard-only. Revision B. Association Connecting Electronics Industries (IPC), 2020.

[77] A. Savitzky and M. J. E. Golay. “Smoothing and differentiation of data by simplified least squares procedures”. In: *Analytical Chemistry* 36 (Jan. 1964), pp. 1627–1639. doi: 10.1021/ac60214a047.

[78] Roberto Acciarri et al. "The Liquid Argon In A Testbeam (LArIAT) Experiment". In: *JINST* 15.04 (2020), P04026. doi: 10.1088/1748-0221/15/04/P04026. arXiv: 1911.10379 [physics.ins-det].

[79] Jianming Bian. "The CAPTAIN Experiment". In: *Meeting of the APS Division of Particles and Fields*. Sept. 2015. arXiv: 1509.07739 [physics.ins-det].

[80] R. Acciarri et al. "Design and construction of the MicroBooNE detector". In: *JINST* 12 (2017), P02017. doi: 10.1088/1748-0221/12/02/P02017.

[81] MicroBooNE Collaboration. *MicroBooNE TPC Design Overview*. https://cds.cern.ch/record/2824019/files/2203.00740.pdf.

[82] MicroBooNE Collaboration. *Reconstruction performance and event displays*. https://microboone.fnal.gov/wp-content/uploads/MICROBOONE-NOTE-1083-PUB.pdf.

[83] Corey Adams et al. "Enhancing neutrino event reconstruction with pixel-based 3D readout for liquid argon time projection chambers". In: *JINST* 15.04 (2020), P04009. doi: 10.1088/1748-0221/15/04/P04009. arXiv: 1912.10133 [physics.ins-det].

[84] David Nygren and Yuan Mei. "Q-Pix: Pixel-scale Signal Capture for Kiloton Liquid Argon TPC Detectors: Time-to-Charge Waveform Capture, Local Clocks, Dynamic Networks". In: (Sept. 2018). arXiv: 1809.10213 [physics.ins-det].

[85] Peng Miao et al. "Demonstrating the Q-Pix front-end using discrete OpAmp and CMOS transistors". In: (Nov. 2023). arXiv: 2311.09568 [physics.ins-det].

[86] M. G. Aartsen et al. "The IceCube Neutrino Observatory: Instrumentation and Online Systems". In: *JINST* 12.03 (2017), P03012. doi: 10.1088/1748-0221/12/03/P03012. arXiv: 1612.05093 [astro-ph.IM].

[87] S. Kubota et al. "Enhanced low-energy supernova burst detection in large liquid argon time projection chambers enabled by Q-Pix". In: *Phys. Rev.*

D 106.3 (2022), p. 032011. doi: 10.1103/PhysRevD.106.032011. arXiv: 2203.12109 [hep-ex].

[88] Nora Hoch et al. "First operation of a multi-channel Q-Pix prototype: measuring transverse electron diffusion in a gas time projection chamber". In: *JINST* 19.06 (2024), P06007. doi: 10.1088/1748-0221/19/06/P06007. arXiv: 2402.05734 [hep-ex].

[89] jrheling. *pybotz: A python interface to the web UI of APC's Netbotz 500 monitoring hardware*. https://github.com/jrheling/pybotz. Retrieved from https://github.com/jrheling/pybotz. 2025.

[90] Hans-Thomas Janka. "Explosion Mechanisms of Core-Collapse Supernovae". In: *Annual Review of Nuclear and Particle Science* 62 (2012), pp. 407–451. doi: 10.1146/annurev-nucl-102711-094901.

[91] Hans A. Bethe. "Supernova Mechanisms". In: *Reviews of Modern Physics* 62 (1990), pp. 801–866. doi: 10.1103/RevModPhys.62.801.

[92] K. Hirata et al. "Observation of a neutrino burst from the supernova SN1987A". In: *Phys. Rev. Lett.* 58 (14 Apr. 1987), pp. 1490–1493. doi: 10.1103/PhysRevLett.58.1490. url: https://link.aps.org/doi/10.1103/PhysRevLett.58.1490.

[93] The University of Tokyo Institute for Cosmic Ray Research. 超新星爆🄵ニュ🄵トリノ🄵出から *35* 年を迎えました. url: https://www-sk.icrr.u-tokyo.ac.jp/news/detail/401/ (visited on 02/23/2022).

[94] R. M. Bionta et al. "Observation of a Neutrino Burst in Coincidence with Supernova SN 1987a in the Large Magellanic Cloud". In: *Phys. Rev. Lett.* 58 (1987), p. 1494. doi: 10.1103/PhysRevLett.58.1494.

[95] E.N. Alekseev et al. "Detection of the neutrino signal from SN1987A in the LMC using the INR Baksan underground scintillation telescope". In: *Phys. Lett. B* 205 (1988), pp. 209–214. doi: 10.1016/0370-2693(88)91651-6.

[96] H. Duan, G. M. Fuller, and Y.-Z. Qian. "Collective Neutrino Oscillations". In: *Ann. Rev. Nucl. Part. Sci.* 60 (2010), pp. 569–594. doi: 10.1146/annurev.nucl.012809.104524. arXiv: 1001.2799 [hep-ph].

[97] G. M. Fuller et al. "Resonant Neutrino Oscillations and Stellar Collapse". In: *Astrophys. J.* 322 (Nov. 1987), p. 795. doi: 10.1086/165772.

[98] Huaiyu Duan and James P Kneller. "Neutrino flavour transformation in supernovae". In: *J. Phys. G* 36 (2009), p. 113201. doi: 10.1088/0954-3899/36/11/113201. arXiv: 0904.0974 [astro-ph.HE].

[99] Cecilia Lunardini. "Theory and phenomenology of supernova neutrinos". In: *AIP Conf. Proc.* 1666.1 (2015). Ed. by Ed Kearns, p. 070001. doi: 10.1063/1.4915560.

[100] Heamin Ko et al. "Comprehensive Analyses of the Neutrino-Process in the Core-collapsing Supernova". In: (Mar. 2022). arXiv: 2203.13365 [nucl-th].

[101] Kate Scholberg. "Supernova Signatures of Neutrino Mass Ordering". In: *J. Phys. G* 45.1 (2018), p. 014002. doi: 10.1088/1361-6471/aa97be. arXiv: 1707.06384 [hep-ex].

[102] John F. Cherry et al. "Halo Modification of a Supernova Neutronization Neutrino Burst". In: *Phys. Rev. D* 87 (2013), p. 085037. doi: 10.1103/PhysRevD.87.085037. arXiv: 1302.1159 [astro-ph.HE].

[103] Sudip Jana, Yago P. Porto-Silva, and Manibrata Sen. "Exploiting a future galactic supernova to probe neutrino magnetic moments". In: (Mar. 2022). arXiv: 2203.01950 [hep-ph].

[104] Fengpeng An et al. "Neutrino Physics with JUNO". In: *J. Phys. G* 43.3 (2016), p. 030401. doi: 10.1088/0954-3899/43/3/030401. arXiv: 1507.05613 [physics.ins-det].

[105] K. Abe et al. "Hyper-Kamiokande Design Report". In: (May 2018). arXiv: 1805.04163 [physics.ins-det].

[106] B. Abi et al. "Supernova neutrino burst detection with the Deep Underground Neutrino Experiment". In: *Eur. Phys. J. C* 81.5 (2021), p. 423. doi: 10.1140/epjc/s10052-021-09166-w. arXiv: 2008.06647 [hep-ex].

[107] K. Abe et al. "Supernova Model Discrimination with Hyper-Kamiokande". In: *Astrophys. J.* 916.1 (2021), p. 15. doi: 10.3847/1538-4357/abf7c4. arXiv: 2101.05269 [astro-ph.IM].

[108] Angel Abusleme et al. "JUNO Physics and Detector". In: (Apr. 2021). arXiv: 2104.02565 [hep-ex].

[109] W. Castiglioni et al. "Benefits of MeV-scale reconstruction capabilities in large liquid argon time projection chambers". In: *Phys. Rev. D* 102.9 (2020), p. 092010. doi: 10.1103/PhysRevD.102.092010. arXiv: 2006.14675 [physics.ins-det].

[110] D. Caratelli et al. "Low-Energy Physics in Neutrino LArTPCs". In: *2022 Snowmass Summer Study*. Mar. 2022. arXiv: 2203.00740 [physics.ins-det].

[111] R. Acciarri et al. "Demonstration of MeV-Scale Physics in Liquid Argon Time Projection Chambers Using ArgoNeuT". In: *Phys. Rev. D* 99.1 (2019), p. 012002. doi: 10.1103/PhysRevD.99.012002. arXiv: 1810.06502 [hep-ex].

[112] The MicroBooNE Collaboration. *Study of Reconstructed ^{39}Ar Beta Decays at the MicroBooNE Detector*. Tech. rep. June 2018. doi: 10.2172/1573057. url: https://www.osti.gov/biblio/1573057.

[113] P. Abratenko et al. "Observation of Radon Mitigation in MicroBooNE by a Liquid Argon Filtration System". In: (Mar. 2022). arXiv: 2203.10147 [physics.ins-det].

[114] S. Amoruso et al. "Measurement of the mu decay spectrum with the ICARUS liquid argon TPC". In: *Eur. Phys. J. C* 33 (2004), pp. 233–241. doi: 10.1140/epjc/s2004-01597-7. arXiv: hep-ex/0311040.

[115] R. Acciarri et al. “Michel Electron Reconstruction Using Cosmic-Ray Data from the MicroBooNE LArTPC”. In: *JINST* 12.09 (2017), P09014. doi: 10.1088/1748-0221/12/09/P09014. arXiv: 1704.02927 [physics.ins-det].

[116] W. Foreman et al. “Calorimetry for low-energy electrons using charge and light in liquid argon”. In: *Phys. Rev. D* 101.1 (2020), p. 012010. doi: 10.1103/PhysRevD.101.012010. arXiv: 1909.07920 [physics.ins-det].

[117] Roxanne Guenette. “The ArgoNeuT experiment”. In: *Meeting of the APS Division of Particles and Fields*. Oct. 2011. arXiv: 1110.0443 [physics.ins-det].

[118] F. Cavanna et al. “LArIAT: Liquid Argon In A Testbeam”. In: (June 2014). arXiv: 1406.5560 [physics.ins-det].

[119] R. Acciarri et al. “Design and Construction of the MicroBooNE Detector”. In: *JINST* 12.02 (2017), P02017. doi: 10.1088/1748-0221/12/02/P02017. arXiv: 1612.05824 [physics.ins-det].

[120] P. Abratenko et al. “ICARUS at the Fermilab Short-Baseline Neutrino program: initial operation”. In: *Eur. Phys. J. C* 83.6 (2023), p. 467. doi: 10.1140/epjc/s10052-023-11610-y. arXiv: 2301.08634 [hep-ex].

[121] Francesco Capozzi et al. “DUNE as the Next-Generation Solar Neutrino Experiment”. In: *Phys. Rev. Lett.* 123.13 (2019), p. 131803. doi: 10.1103/PhysRevLett.123.131803. arXiv: 1808.08232 [hep-ph].

[122] Saba Para et al. “SoLAr: Solar Neutrinos in Liquid Argon”. In: *2022 Snowmass Summer Study*. Mar. 2022. arXiv: 2203.07501 [hep-ex].

[123] Alexander Friedland and Shirley Weishi Li. “Understanding the energy resolution of liquid argon neutrino detectors”. In: *Phys. Rev. D* 99.3 (2019), p. 036009. doi: 10.1103/PhysRevD.99.036009. arXiv: 1811.06159 [hep-ph].

[124] Roni Harnik, Zhen Liu, and Ornella Palamara. “Millicharged Particles in Liquid Argon Neutrino Experiments”. In: *JHEP* 07 (2019), p. 170. doi: 10.1007/JHEP07(2019)170. arXiv: 1902.03246 [hep-ph].

[125] R. Acciarri et al. “Improved Limits on Millicharged Particles Using the ArgoNeuT Experiment at Fermilab”. In: *Phys. Rev. Lett.* 124.13 (2020), p. 131801. doi: 10.1103/PhysRevLett.124.131801. arXiv: 1911.07996 [hep-ex].

[126] A. Avasthi et al. “Low Background kTon-Scale Liquid Argon Time Projection Chambers”. In: *2022 Snowmass Summer Study*. Mar. 2022. arXiv: 2203.08821 [physics.ins-det].

[127] A. Mastbaum, F. Psihas, and J. Zennamo. “Xenon-Doped Liquid Argon TPCs as a Neutrinoless Double Beta Decay Platform”. In: (Mar. 2022). arXiv: 2203.14700 [physics.ins-det].

[128] L. Hudepohl et al. “Neutrino Signal of Electron-Capture Supernovae from Core Collapse to Cooling”. In: *Phys. Rev. Lett.* 104 (2010). [Erratum: Phys.Rev.Lett. 105, 249901 (2010)], p. 251101. doi: 10.1103/PhysRevLett.104.251101. arXiv: 0912.0260 [astro-ph.SR].

[129] Kate Scholberg. “SNOwGLoBES: SuperNova Observatories with GLoBES”. In: *APS April Meeting Abstracts*. Vol. 2011. APS Meeting Abstracts. Apr. 2011, p. L11.006.

[130] Yudai Suwa et al. “Observing Supernova Neutrino Light Curves with Super-Kamiokande: Expected Event Number over 10 s”. In: *Astrophys. J.* 881 (2019), p. 139. doi: 10.3847/1538-4357/ab2e05. arXiv: 1904.09996 [astro-ph.HE].

[131] Rafael F. Lang et al. “Supernova neutrino physics with xenon dark matter detectors: A timely perspective”. In: *Phys. Rev. D* 94.10 (2016), p. 103009. doi: 10.1103/PhysRevD.94.103009. arXiv: 1606.09243 [astro-ph.HE].

[132] A. Odrzywolek and T. Plewa. “Probing thermonuclear supernova explosions with neutrinos”. In: *Astron. Astrophys.* 529 (2011), A156. doi: 10.1051/0004-6361/201015133. arXiv: 1006.0490 [astro-ph.SR].

[133] Shaquann Seadrow et al. “Neutrino Signals of Core-Collapse Supernovae in Underground Detectors”. In: *Mon. Not. Roy. Astron. Soc.* 480.4

(2018), pp. 4710–4731. doi: 10.1093/mnras/sty2164. arXiv: 1804.00689 [astro-ph.HE].

[134] Steven Gardiner et al. "MARLEY: Model of Argon Reaction Low Energy Yields". In: *APS Division of Nuclear Physics Meeting Abstracts*. Vol. 2015. APS Meeting Abstracts. Oct. 2015, PD.007.

[135] Steven Gardiner. "Simulating low-energy neutrino interactions with MARLEY". In: *Comput. Phys. Commun.* 269 (2021), p. 108123. doi: 10.1016/j.cpc.2021.108123. arXiv: 2101.11867 [nucl-th].

[136] B. Abi et al. "Deep Underground Neutrino Experiment (DUNE), Far Detector Technical Design Report, Volume II: DUNE Physics". In: (Feb. 2020). arXiv: 2002.03005 [hep-ex].

[137] Jingyuan Shi. "Studies of Radiological Backgrounds in The Dune Far Detector and The Sensitivity to The Solar Neutrino Day-Night Effect Using The Photon-Detector System". PhD thesis. The University of Manchester (United Kingdom), 2019.

[138] S. Cebrián et al. "Radiopurity assessment of the tracking readout for the NEXT double beta decay experiment". In: *JINST* 10.05 (2015), P05006. doi: 10.1088/1748-0221/10/05/P05006. arXiv: 1411.1433 [physics.ins-det].

[139] D. S. Akerib et al. "Design and performance of a modular low-radioactivity readout system for cryogenic detectors in the CDMS experiment". In: *Nucl. Instrum. Meth. A* 591 (2008), pp. 476–489. doi: 10.1016/j.nima.2008.03.103.

[140] F. J. Iguaz et al. "TREX-DM: a low-background Micromegas-based TPC for low-mass WIMP detection". In: *Eur. Phys. J. C* 76.10 (2016), p. 529. doi: 10.1140/epjc/s10052-016-4372-6. arXiv: 1512.01455 [physics.ins-det].

[141] S. Agostinelli et al. "Geant4—A simulation toolkit". In: *Nucl. Instrum. Meth. A* 506 (2003), pp. 250–303. doi: 10.1016/S0168-9002(03)01368-8.

[142] J. Allison et al. “Geant4 Developments and Applications”. In: *IEEE Trans. Nucl. Sci.* 53 (2006), p. 270. doi: 10.1109/TNS.2006.869826.

[143] J. Allison et al. “Recent developments in Geant4”. In: *Nucl. Instrum. Meth. A* 835 (2016), pp. 186–225. doi: 10.1016/j.nima.2016.06.125.

[144] R Acciarri et al. “A study of electron recombination using highly ionizing particles in the ArgoNeuT Liquid Argon TPC”. In: *Journal of Instrumentation* 8.08 (Aug. 2013), P08005. doi: 10.1088/1748-0221/8/08/P08005. url: https://dx.doi.org/10.1088/1748-0221/8/08/P08005.

[145] D. A. Dwyer et al. “LArPix: Demonstration of low-power 3D pixelated charge readout for liquid argon time projection chambers”. In: *JINST* 13.10 (2018), P10007. doi: 10.1088/1748-0221/13/10/P10007. arXiv: 1808.02969 [physics.ins-det].

[146] R. Brun and F. Rademakers. “ROOT: An object oriented data analysis framework”. In: *Nucl. Instrum. Meth. A* 389 (1997). Ed. by M. Werlen and D. Perret-Gallix, pp. 81–86. doi: 10.1016/S0168-9002(97)00048-X.

[147] Brookhaven National Laboratory. *Properties of LAr*. url: https://www.phy.bnl.gov/~chao/docs/Properties-of-LAr-v9a-thorn.pdf (visited on 02/20/2025).

[148] Babak Abi et al. “Deep Underground Neutrino Experiment (DUNE), Far Detector Technical Design Report, Volume III: DUNE Far Detector Technical Coordination”. In: *JINST* 15.08 (2020), T08009. doi: 10.1088/1748-0221/15/08/T08009. arXiv: 2002.03008 [physics.ins-det].

[149] S. Fukuda et al. “The Super-Kamiokande detector”. In: *Nucl. Instrum. Meth. A* 501 (2003), pp. 418–462. doi: 10.1016/S0168-9002(03)00425-X.

[150] IceCube Collaboration, M. G. Aartsen, et al. “The IceCube Neutrino Observatory: Instrumentation and Online Systems”. In: *JINST* 12 (2017), P03012. doi: 10.1088/1748-0221/12/03/P03012. arXiv: 1612.05093.

[151] K. Eguchi et al. “First results from KamLAND: Evidence for reactor antineutrino disappearance”. In: *Phys. Rev. Lett.* 90 (2003), p. 021802. doi: 10.1103/PhysRevLett.90.021802.

[152] G. Alimonti et al. “The Borexino detector at the Laboratori Nazionali del Gran Sasso”. In: *Nucl. Instrum. Meth. A* 600 (2009), pp. 568–593. doi: 10.1016/j.nima.2008.11.076.

[153] S. Adrián-Martínez et al. “Letter of intent for KM3NeT 2.0”. In: *J. Phys. G* 43 (2016), p. 084001. doi: 10.1088/0954-3899/43/8/084001.

[154] M. B. Andrade et al. “The Helium and Lead Observatory (HALO) at SNOLAB”. In: *Nucl. Instrum. Meth. A* 582 (2007), pp. 93–96. doi: 10.1016/j.nima.2007.08.161.

[155] Martin Ester et al. “A density-based algorithm for discovering clusters in large spatial databases with noise”. In: *KDD’96: Proceedings of the Second International Conference on Knowledge Discovery and Data Mining* (Portland, Oregon). Ed. by Evangelos Simoudis, Jiawei Han, and Usama Fayyad. AAAI Press, 1996, pp. 226–231.

[156] C. D. Cantrell. *Modern Mathematical Methods for Physicists and Engineers*. USA: Cambridge University Press, 2000. isbn: 0521598273.

[157] Ken’ichiro Nakazato et al. “Supernova Neutrino Light Curves and Spectra for Various Progenitor Stars: From Core Collapse to Black Hole Formation”. In: *Astrophys. J. Suppl.* 205 (2013), p. 2. doi: 10.1088/0067-0049/205/1/2.

[158] M. Fishler and R. C. Bolles. “Random sample consensus: a paradigm for model fitting with applications to image analysis and automated cartography”. In: *Communications of the ACM* 24 (1981), pp. 381–395. doi: 10.1145/358669.358692.

[159] I.T. Jolliffe. *Principal Component Analysis*. Springer Series in Statistics. New York, NY: Springer, 2002. isbn: 9780387954424. url: https://doi.org/10.1007/b98835.

[160] Adam Abed Abud et al. “Supernova Pointing Capabilities of DUNE”. In: (July 2024). arXiv: 2407.10339 [hep-ex].

[161] John N. Bahcall, M. H. Pinsonneault, and Sarbani Basu. “Solar models: Current epoch and time dependences, neutrinos, and helioseismological properties”. In: *Astrophys. J.* 555 (2001), pp. 990–1012. doi: 10.1086/321493. arXiv: astro-ph/0010346.

[162] W. C. Haxton, Aldo Serenelli, and Carlos Peña-Garay. “Solar Neutrinos: Status and Prospects”. In: *Annu. Rev. Astron. Astrophys.* 51 (2013), pp. 21–61. doi: 10.1146/annurev-astro-081811-125539. arXiv: 1208.5723 [astro-ph.SR].

[163] John N. Bahcall and Marc H. Pinsonneault. “Solar models with helium and heavy element diffusion”. In: *Rev. Mod. Phys.* 67 (1995), pp. 781–808. doi: 10.1103/RevModPhys.67.781.

[164] R.G.H. Robertson. “Solar neutrinos: Status and prospects”. In: *Rev. Mod. Phys.* 83 (2011), pp. 171–180. doi: 10.1103/RevModPhys.83.171. arXiv: 1201.2199 [hep-ex].

[165] Aldo M. Serenelli. “Alive and well: a short review about standard solar models”. In: *Astrophys. Space Sci.* 328 (2010), pp. 13–21. doi: 10.1007/s10509-009-0201-1. arXiv: 1109.4996 [astro-ph.SR].

[166] John N. Bahcall, Aldo M. Serenelli, and Sarbani Basu. “New Solar Opacities, Abundances, Helioseismology, and Neutrino Fluxes”. In: *The Astrophysical Journal* 621.1 (Jan. 2005), p. L85. doi: 10.1086/428929. url: https://dx.doi.org/10.1086/428929.

[167] Eric G. Adelberger et al. “Solar fusion cross sections. II. The pp chain and CNO cycles”. In: *Rev. Mod. Phys.* 83 (2011), pp. 195–245. doi: 10.1103/RevModPhys.83.195. arXiv: 1004.2318 [nucl-ex].

[168] W. C. Haxton, A. M. Serenelli, and C. Peña-Garay. “CN-cycle solar neutrinos and the Sun’s primordial core metalicity”. In: *Astrophys. J.* 687 (2008), pp. 678–691. doi: 10.1086/591925.

[169] M. Agostini et al. “Experimental evidence of neutrinos produced in the CNO fusion cycle in the Sun”. In: *Nature* 587 (2020), pp. 577–582. doi: 10.1038/s41586-020-2934-0.

[170] Q. R. Ahmad et al. “Direct Evidence for Neutrino Flavor Transformation from Neutral-Current Interactions in the Sudbury Neutrino Observatory”. In: *Phys. Rev. Lett.* 89 (1 June 2002), p. 011301. doi: 10.1103/PhysRevLett.89.011301. url: https://link.aps.org/doi/10.1103/PhysRevLett.89.011301.

[171] K. Abe et al. “Solar Neutrino Measurements in Super-Kamiokande-IV”. In: *Phys. Rev. D* 94.5 (2016), p. 052010. doi: 10.1103/PhysRevD.94.052010. arXiv: 1606.07538 [hep-ex].

[172] G. Bellini et al. “Final results of Borexino Phase-I on low-energy solar neutrino spectroscopy”. In: *Phys. Rev. D* 89 (11 June 2014), p. 112007. doi: 10.1103/PhysRevD.89.112007. url: https://link.aps.org/doi/10.1103/PhysRevD.89.112007.

[173] D. B. Guenther et al. “Standard Solar Model”. In: *Astrophysical Journal* 387 (Mar. 1992), p. 372. doi: 10.1086/171090.

[174] John W. Harvey et al. “The Global Oscillation Network Group (GONG) project”. In: *Science* 272.5266 (1996), pp. 1284–1286. doi: 10.1126/science.272.5266.1284.

[175] P. H. Scherrer et al. “The Solar Oscillations Investigation –Michelson Doppler Imager”. In: *Solar Physics* 162 (1995), pp. 129–188. doi: 10.1007/BF00733429.

[176] V. Domingo, B. Fleck, and A. I. Poland. “The SOHO Mission: An Overview”. In: *Solar Physics* 162 (1995), pp. 1–37. doi: 10.1007/BF00733425.

[177] J. W. Harvey et al. “The Global Oscillation Network Group (GONG) Project”. In: *Science* 272.5266 (1996), pp. 1284–1286. issn: 00368075, 10959203. url: http://www.jstor.org/stable/2889785 (visited on 01/13/2025).

[178] P. H. Scherrer et al. “The Solar Oscillations Investigation - Michelson Doppler Imager”. In: *Solar Physics* 162.1-2 (Dec. 1995), pp. 129–188. doi: 10.1007/BF00733429.

[179] Sarbani Basu and H. M. Antia. “Constraining Solar Abundances Using Helioseismology”. In: *apjl* 606.1 (May 2004), pp. L85–L88. doi: 10.1086/421110. arXiv: astro-ph/0403485 [astro-ph].

[180] J. Montalbán et al. “Solar Model with CNO Revised Abundances”. In: *SOHO 14 Helio- and Asteroseismology: Towards a Golden Future*. Ed. by D. Danesy. Vol. 559. ESA Special Publication. Oct. 2004, p. 574. doi: 10.48550/arXiv.astro-ph/0408055. arXiv: astro-ph/0408055 [astro-ph].

[181] Tobias Fischer et al. “Neutrinos and nucleosynthesis of elements”. In: *Prog. Part. Nucl. Phys.* 137 (2024), p. 104107. doi: 10.1016/j.ppnp.2024.104107. arXiv: 2308.03962 [astro-ph.HE].

[182] A. Gando et al. “Reactor On-Off Antineutrino Measurement with KamLAND”. In: *Phys. Rev. D* 88.3 (2013), p. 033001. doi: 10.1103/PhysRevD.88.033001. arXiv: 1303.4667 [hep-ex].

[183] Rasmi Hajjar, Sergio Palomares-Ruiz, and Olga Mena. “Shedding light on the Δm212 tension with supernova neutrinos”. In: *Phys. Lett. B* 854 (2024), p. 138719. doi: 10.1016/j.physletb.2024.138719. arXiv: 2307.09509 [hep-ph].

[184] L. Hüdepohl et al. “Neutrino Signal of Electron-Capture Supernovae from Core Collapse to Cooling”. In: *Physical Review Letters* 104.25, 251101 (June 2010), p. 251101. doi: 10.1103/PhysRevLett.104.251101. arXiv: 0912.0260 [astro-ph.SR].

[185] T Bezerra et al. “Large low background kTon-scale liquid argon time projection chambers”. In: *Journal of Physics G: Nuclear and Particle Physics* 50.6 (May 2023), p. 060502. doi: 10.1088/1361-6471/acc394. url: https://dx.doi.org/10.1088/1361-6471/acc394.

[186] P. Agnes et al. “Low Radioactivity Argon Dark Matter Search with the DarkSide-50 Detector”. In: *Phys. Rev. D* 93 (2016), p. 081101. doi: 10.1103/PhysRevD.93.081101. arXiv: 1510.00702 [physics.ins-det].

[187] M. Á. García-Peris et al. “Potential for solar neutrino detection in a large liquid argon detector instrumented with Q-Pix”. In preparation. 2025.

[188] HPK. https://hamamatsu.su/files/uploads/pdf/3_mppc/s13370_vuv4-mppc_b_(1).pdf.

[189] M. Rooks et al. “Development of a novel, windowless, amorphous selenium based photodetector for use in liquid noble detectors”. In: *Journal of Instrumentation* 18.01 (Jan. 2023), P01029. doi: 10.1088/1748-0221/18/01/P01029. url: https://dx.doi.org/10.1088/1748-0221/18/01/P01029.

[190] Aran Borkum. “Solar neutrinos at DUNE”. PhD thesis. Sussex U., University of Sussex, Sussex U., 2023.

[191] B. Aharmim et al. “Search for *hep* solar neutrinos and the diffuse supernova neutrino background using all three phases of the Sudbury Neutrino Observatory”. In: *Phys. Rev. D* 102.6 (2020), p. 062006. doi: 10.1103/PhysRevD.102.062006. arXiv: 2007.08018 [hep-ex].

[192] M. Agostini et al. “Improved measurement of ^{8}B solar neutrinos with $1.5 kty$ of Borexino exposure”. In: *Phys. Rev. D* 101.6 (2020), p. 062001. doi: 10.1103/PhysRevD.101.062001. arXiv: 1709.00756 [hep-ex].

[193] Steven Gardiner. “Simulating low-energy neutrino interactions with MARLEY”. In: *Computer Physics Communications* 269 (2021), p. 108123. issn: 0010-4655. doi: https://doi.org/10.1016/j.cpc.2021.108123. url: https://www.sciencedirect.com/science/article/pii/S0010465521002356.

[194] M. Anderson et al. “Measurement of the ^{8}B solar neutrino flux in SNO+ with very low backgrounds”. In: *Phys. Rev. D* 99.1 (2019), p. 012012. doi: 10.1103/PhysRevD.99.012012. arXiv: 1812.03355 [hep-ex].

[195] D. Basilico et al. “Final results of Borexino on CNO solar neutrinos”. In: *Phys. Rev. D* 108 (10 Nov. 2023), p. 102005. doi: 10.1103/PhysRevD.108.102005. url: https://link.aps.org/doi/10.1103/PhysRevD.108.102005.

[196] Juris Meija et al. “Isotopic compositions of the elements 2013 (IUPAC Technical Report)”. In: *Pure and Applied Chemistry* 88.3 (2016), pp. 293–306. doi: 10.1515/pac-2015-0305.

[197] Bradley G. Fritz et al. *Measurement of Argon-37 Background Concentrations in the Atmosphere*. Tech. rep. PNNL-30583. Richland, WA: Pacific Northwest National Laboratory, 2020. url: https://www.pnnl.gov/main/publications/external/technical_reports/PNNL-30583.pdf.

[198] A. S. Barabash, R. R. Saakyan, and V. I. Umatov. “On concentration of ^{42}Ar in the Earth’s atmosphere”. In: *Nucl. Instrum. Meth. A* 839 (2016), pp. 39–42. doi: 10.1016/j.nima.2016.09.042. arXiv: 1609.08890 [nucl-ex].

[199] P. Benetti et al. “Measurement of the specific activity of ar-39 in natural argon”. In: *Nucl. Instrum. Meth. A* 574 (2007), pp. 83–88. doi: 10.1016/j.nima.2007.01.106. arXiv: astro-ph/0603131.

[200] M. Agostini et al. “The background in the $0\nu\beta\beta$ experiment GERDA”. In: *Eur. Phys. J. C* 74.4 (2014), p. 2764. doi: 10.1140/epjc/s10052-014-2764-z. arXiv: 1306.5084 [physics.ins-det].

[201] A. S. Barabash, R. R. Saakyan, and V. I. Umatov. “On concentration of ^{42}Ar in the Earth’s atmosphere”. In: *Nucl. Instrum. Meth. A* 839 (2016), pp. 39–42. doi: 10.1016/j.nima.2016.09.042. arXiv: 1609.08890 [nucl-ex].

[202] R. Ajaj et al. “Electromagnetic backgrounds and potassium-42 activity in the DEAP-3600 dark matter detector”. In: *Phys. Rev. D* 100.7 (2019), p. 072009. doi: 10.1103/PhysRevD.100.072009. arXiv: 1905.05811 [nucl-ex].

[203] Martin Stute. *85 Kr (krypton-85)*. Accessed: 2025-03-23. 2025. url: https://www.ldeo.columbia.edu/~martins/isohydro/kr85.html.

[204] P. Agnes et al. “Results From the First Use of Low Radioactivity Argon in a Dark Matter Search”. In: *Phys. Rev. D* 93.8 (2016). [Addendum: Phys.Rev.D 95, 069901 (2017)], p. 081101. doi: 10.1103/PhysRevD.93.081101. arXiv: 1510.00702 [astro-ph.CO].

[205] P. Agnes et al. “Separating ^{39}Ar from ^{40}Ar by cryogenic distillation with Aria for dark-matter searches”. In: *Eur. Phys. J. C* 81.4 (2021), p. 359. doi: 10.1140/epjc/s10052-021-09121-9. arXiv: 2101.08686 [physics.ins-det].

[206] Sagar Poudel et al. “Low-Radioactivity Argon for Rare-Event Searches”. https://indico.sanfordlab.org/event/29/papers/487/files/133-low_radioactivity_argon_proceedings_Dec6.pdf.

[207] Juergen Reichenbacher. “Radiological Backgrounds in DUNE Far Detectors”. https://indico.sanfordlab.org/event/68/contributions/1523/attachments/813/2044/cossurf24_westerdale.pdf.

[208] Francesco Capozzi et al. “DUNE as the Next-Generation Solar Neutrino Experiment”. In: *Phys. Rev. Lett.* 123.13 (2019), p. 131803. doi: 10.1103/PhysRevLett.123.131803. arXiv: 1808.08232 [hep-ph].

[209] Kevin T. Lesko et al. “Deep Underground Science and Engineering Laboratory - Preliminary Design Report”. In: (Aug. 2011). arXiv: 1108.0959 [hep-ex].

[210] Jaret Heise. “The Sanford Underground Research Facility at Homestake”. In: *J. Phys. Conf. Ser.* 606.1 (2015). Ed. by Iris Abt et al., p. 012015. doi: 10.1088/1742-6596/606/1/012015. arXiv: 1503.01112 [physics.ins-det].

[211] Y.D. Chan et al. “The ”Low-Background Construction of Laboratories at the 4850 ft Level Davis Campus””. https://sanfordlab.org/news/low-background-construction-laboratories-4850-ft-level-davis-campus.

[212] IAEA. https://www.iaea.org/topics/spent-fuel-management/depleted-uranium.

[213] G.S. Foote et al. "Alpha capture to the giant dipole resonances of 42Ca, 44Ca and 52Cr". In: *Nuclear Physics A* 263.2 (1976), pp. 349–364. issn: 0375-9474. doi: https://doi.org/10.1016/0375-9474(76)90177-9. url: https://www.sciencedirect.com/science/article/pii/0375947476901779.

[214] N. G. Alenius et al. "Structure of 43Ca from the 40Ar(, n)43Ca reaction". In: *Il Nuovo Cimento A (1965-1970)* 8 (1972). doi: 10.1007/BF02728760.

[215] Balraj Singh and Jun Chen. "Nuclear Data Sheets for A = 43". In: *Nuclear Data Sheets* 126 (2015), pp. 1–150. issn: 0090-3752. doi: https://doi.org/10.1016/j.nds.2015.05.001. url: https://www.sciencedirect.com/science/article/pii/S0090375215000125.

[216] J. B. Albert et al. "Measurements of the ion fraction and mobility of α- and β-decay products in liquid xenon using the EXO-200 detector". In: *Phys. Rev. C* 92.4 (2015), p. 045504. doi: 10.1103/PhysRevC.92.045504. arXiv: 1506.00317 [nucl-ex].

[217] Alissa Erin Monte. "Alpha Radiation Studies and Related Backgrounds in the DarkSide-50 Detector". PhD thesis. Massachusetts U., Amherst, Massachusetts U., Amherst, 2018. doi: 10.7275/12757774.

[218] C. E. Aalseth et al. "DarkSide-20k: A 20 tonne two-phase LAr TPC for direct dark matter detection at LNGS". In: *Eur. Phys. J. Plus* 133 (2018), p. 131. doi: 10.1140/epjp/i2018-11973-4. arXiv: 1707.08145 [physics.ins-det].

[219] R. Ajaj et al. "Search for dark matter with a 231-day exposure of liquid argon using DEAP-3600 at SNOLAB". In: *Phys. Rev. D* 100.2 (2019), p. 022004. doi: 10.1103/PhysRevD.100.022004. arXiv: 1902.04048 [astro-ph.CO].

[220] Shawn Westerdale. https://github.com/shawest/neucbot.

[221] H. Wulandari et al. "Neutron flux underground revisited". In: *Astropart. Phys.* 22 (2004), pp. 313–322. doi: 10.1016/j.astropartphys.2004.07.005. arXiv: hep-ex/0312050.

[222] Jun Chen. "Nuclear Data Sheets for A=40". In: *Nuclear Data Sheets* 140 (2017), pp. 1–376. issn: 0090-3752. doi: https://doi.org/10.1016/j.nds.2017.02.001. url: https://www.sciencedirect.com/science/article/pii/S0090375217300169.

[223] Sean Patrick MacMullin. "Elastic and Inelastic Scattering of Neutrons from Neon and Argon: Impact on Neutrinoless Double-Beta Decay and Dark Matter Experimental Programs". PhD thesis. North Carolina U., 2013. doi: 10.17615/1bgs-yt67.

[224] C. D. Nesaraja and E. A. McCutchan. "Nuclear Data Sheets for A = 41". In: *Nucl. Data Sheets* 133 (2016), pp. 1–220. doi: 10.1016/j.nds.2016.02.001.

[225] John Cameron et al. "Nuclear Data Sheets for A = 37". In: *Nucl. Data Sheets* 113 (2012), pp. 365–514. doi: 10.1016/j.nds.2012.02.001.

[226] E. T. Jurney et al. "Thermal-neutron capture by ^{14}N". In: *Phys. Rev. C* 56 (1 July 1997), pp. 118–134. doi: 10.1103/PhysRevC.56.118. url: https://link.aps.org/doi/10.1103/PhysRevC.56.118.

[227] Said F Mughabghab. *Atlas of Neutron Resonances: Resonance Parameters and Thermal Cross Sections. Z=1-100; 5th ed.* San Diego, CA: Elsevier, 2006. url: https://cds.cern.ch/record/1086969.

[228] IAEA. https://www-nds.iaea.org/capgam/index.htmlx.

[229] L. Meyer-Schützmeister et al. "The giant dipole resonance excited by -capture". In: *Nuclear Physics A* 108.1 (1968), pp. 180–208. issn: 0375-9474. doi: https://doi.org/10.1016/0375-9474(68)90153-X. url: https://www.sciencedirect.com/science/article/pii/037594746890153X.

[230] Juergen Reichenbacher. "Backgrounds for Supernova Neutrino Detection with Underground Detectors (Liquid Argon)". https://indico.slac.stanford.edu/event/7400/contributions/6432/attachments/3156/8655/Backgrounds_SNBnuDetection_CCSNe_workshop_NPN_SLAC_12July2023_JR.pdf.

[231] M. Haffke et al. “Background measurements in the Gran Sasso Underground Laboratory”. In: *Nuclear Instruments and Methods in Physics Research Section A: Accelerators, Spectrometers, Detectors and Associated Equipment* 643.1 (2011), pp. 36–41. issn: 0168-9002. doi: https://doi.org/10.1016/j.nima.2011.04.027. url: https://www.sciencedirect.com/science/article/pii/S0168900211007650.

[232] *High Energy Gamma-Rays measurements in the SNO cavity*. https://sno.phy.queensu.ca/str/SNO-STR-97-009.pdf.

[233] A. Agrawal et al. “Background study of the AMoRE-pilot experiment”. In: *Astropart. Phys.* 162 (2024), p. 102991. doi: 10.1016/j.astropartphys.2024.102991. arXiv: 2401.07476 [nucl-ex].

[234] YangPing Shen et al. “Measurement of gamma detector backgrounds in the energy range of 3–8 MeV at Jinping underground laboratory for nuclear astrophysics”. In: *Science China Physics, Mechanics & Astronomy* 60.10 (2017), pp. 1869–1927. issn: 10.1007/s11433-017-9049-3. doi: https://doi.org/10.1007/s11433-017-9049-3.

[235] S. Fukuda et al. “The Super-Kamiokande detector”. In: *Nuclear Instruments and Methods in Physics Research Section A: Accelerators, Spectrometers, Detectors and Associated Equipment* 501.2 (2003), pp. 418–462. issn: 0168-9002. doi: https://doi.org/10.1016/S0168-9002(03)00425-X. url: https://www.sciencedirect.com/science/article/pii/S016890020300425X.

[236] Shinzou Kubota, Masahiko Hishida, and Akira Nohara. “Variation of scintillation decay in liquid argon excited by electrons and alpha particles”. In: *Nuclear Instruments and Methods* 150.3 (1978), pp. 561–564. issn: 0029-554X. doi: https://doi.org/10.1016/0029-554X(78)90128-3. url: https://www.sciencedirect.com/science/article/pii/0029554X78901283.

[237] R. S. Raghavan. “Inverse β^- decay of ^{40}Ar: A new approach for observing MeV neutrinos from laboratory and astrophysical sources”. In: *Phys. Rev. D* 34 (7 Oct. 1986), pp. 2088–2091. doi: 10.1103/PhysRevD.34.2088. url: https://link.aps.org/doi/10.1103/PhysRevD.34.2088.

[238] Adam Abed Abud et al. “The DUNE Far Detector Vertical Drift Technology. Technical Design Report”. In: *JINST* 19.08 (2024), T08004. doi: 10.1088/1748-0221/19/08/T08004. arXiv: 2312.03130 [hep-ex].